STABILITY AND MORPHING CHARACTERISTICS OF BISTABLE COMPOSITE LAMINATES

A Dissertation
Presented to
The Academic Faculty

by

Samer A. Tawfik

In Partial Fulfillment
of the Requirements for the Degree
Doctor of Philosophy in the
School of Aerospace Engineering

Georgia Institute of Technology
August 2008

STABILITY AND MORPHING CHARACTERISTICS OF BISTABLE COMPOSITE LAMINATES

Approved by:

Dr. Erian Armanios, Advisor
School of Aerospace Engineering
Georgia Institute of Technology

Dr. D. Stefan Dancila
Dancila LLC.

Dr. Juan R. Cruz
Atmospheric Flight and Entry System Branch
NASA Langley Research Center

Dr. Rami Haj-Ali
School of Civil & Environmental Engineering
Georgia Institute of Technology

Dr. Massimo Ruzzene
School of Aerospace Engineering
Georgia Institute of Technology

Date Approved: May 9, 2008

To my father, Anwar
For being a role model in words and deeds

To my mother, Marcelle
For her love, caring and teaching

To my brother, Tawfik
My intelligent tutor and best friend

ACKNOWLEDGEMENTS

An African proverb states that “It takes a whole village to raise a child”. I experienced the full meaning of this proverb throughout the years I spent at GA Tech as a graduate student. I could not have possibly survived the many hours of hard work without the help of some special individuals; they are contributors to my success. They gained my respect due to their constructive input into my work and life qualities.

I would like to express my deepest gratitude to my dear advisor Dr. Erian Armanios. I believe that Dr. Armanios is the most caring and understanding professor. He always takes the time to patiently listen to, and help everyone. He always provides simpler ways to explain ideas and complex concepts, and suggests unique ways to resolve issues. To him I owe many opportunities I had, and for him I have great respect. I feel both honored and blessed to graduate as one of his students. He is surely a wise counselor, and a friendly mentor.

I am also grateful to Dr. D. Stefan Dancila for always providing the advice when most needed. I still remember vividly his valuable words to me in many occasions on how to better myself. I acknowledge his immeasurable contributions into my work and character.

I would like to acknowledge Dr. Juan R. Cruz who with lots of patience and in a very friendly manner listened, discussed, explained and advised.

I would like to thank Dr. Rami Haj-Ali and Dr. Massimo Ruzzene for their willingness to serve on my thesis committee.

Many thanks are due to my dear friends and labmates Dr. Roxana Vasilescu, Dr. Serkan Ozbay and Xinyuan Tan for their unfailing support and cooperation throughout the years. I would also like to thank my dear friends Mr. Sam Patterson, Roussislava Zaharieva, Michael Tadros, Vin Sharma, Henry Won, and Chang-Yong Lee, their abundantly honest companionship and help made all the difference. I appreciate the fruitful conversations with Nick Burgess, Anthony Cella, and Eric Lynch. I am indebted to Mr. Andrew Carignan, the Machine Shop Manager, for his practical suggestions and for building the required apparatus in a remarkably short time.

I would also like to acknowledge New Way® Air Bearing for providing a generous educational discount.

Special words of recognition are due for my parents for their never ending love and patience. Thanks for providing the utmost example of love and sacrifice. Thanks to my dear brother, for his wise and motivating words. Thanks to my family for being special and close despite the distance.

Above all there is ONE; to Him all praise is due. “The LORD is my strength and my song; he has become my salvation. He is my God, and I will praise him, my father's God, and I will exalt him” (Exodus 15:2)

TABLE OF CONTENTS

LIST OF TABLES

LIST OF FIGURES

SUMMARY

The focus of the current research is to investigate the potential of using bistable unsymmetric cross-ply laminated composites as a means for achieving structures with morphed characteristics. To this end, an investigation of the design space for laminated composites exhibiting bistable behavior is undertaken and the key parameters controlling their behavior are identified. For this purpose a nonlinear Finite Element methodology using ABAQUS™ code is developed to predict both the cured shapes and the stability characteristics of unsymmetric cross-ply laminates. In addition, an experimental program is developed to validate the analytically predicted results through comparison with test data.

A new method is proposed for attaching piezoelectric actuators to a bistable panel in order to preserve its favorable stability characteristics as well as optimizing the actuators performance. The developed nonlinear FE methodology is extended to predict the actuation requirements of bistable panels. Actuator requirements, predicted using the nonlinear FE analysis, are found to be in agreement with the test results.

The current research also explores the potential for implementing bistable panels for Uninhabited Aerial Vehicle (UAV) wing configuration. To this end, a set of bistable panels is manufactured by combining symmetric and unsymmetric balanced and unbalanced stacking sequence and their stability characteristics are predicted. A preliminary analysis of the aerodynamic characteristics of the manufactured panels is carried out and the aerodynamic benefits of manufactured bistable panel are noted.

CHAPTER 1

INTRODUCTION

This research aims at defining the design space for laminated composites exhibiting bistable behavior and identifying the key parameters controlling their behavior. Accordingly, both analytical modeling as well as testing should be undertaken. To this end, a number of geometries are systematically investigated leading to a set of parameters establishing the values required for bistable behavior. Within the class of laminated composites exhibiting bistable behavior an investigation is performed as to the implementation of actuation scheme for snap-through and snap-back using active materials. A nonlinear finite element methodology using the commercial code ABAQUS™ is developed and predictions are validated through comparisons with test data. Non-dimensional parameters controlling the behavior of bistable composites are confirmed through validation and comparisons. Application of selected geometries to wing configurations illustrates their potential aerodynamic benefits. A literature review of pertinent works follows to underline the relevance and contributions of the current research.

1.1 Literature Review

The following review highlights works pertinent to the main components of current research namely, prediction of cured shapes of cross-ply unsymmetric laminates, their stability characteristics, inducing snap-through behavior, and potential applications.

Predicting the cured shapes of cross-ply unsymmetric laminates

When cured in an autoclave out-of-plane deformations are developed in unsymmetric composite laminates at room temperature. These deformations are mainly caused by the mismatch in the coefficients of thermal expansion and elastic properties of laminae within the laminate. Hyer [20] reported the shapes of several families of cross-ply unsymmetric laminates and observed that the room-temperature shapes do not always conform to the predictions of classical lamination theory (CLT), which is a geometrically linear theory. CLT predicts the out-of-plane deformations to follow a saddle-like shape while actual observation of cured unsymmetric laminates, in most cases, shows a cylindrical shape, Figure 1-1. Furthermore this cylindrical shape could be triggered to snap-through into a second cylindrical shape with a different curvature. Given that the out-of-plane deformations are finite (an order of magnitude larger than the laminate thickness) geometric nonlinearities had to be incorporated. Hyer [19, 21] extended the CLT to account for geometric nonlinearities via a polynomial expansion of displacements and referred to as the Extended Classical Lamination Theory (ECLT). The same acronym is adopted in the current work to refer to Hyer's formulation.

The ECLT is based on the Principle of Minimum Total Potential Energy (PMTPE) and it predicts curvatures and agrees well with test data [19, 21] as shown in Figure 1-2. However, assuming polynomial expansion of displacements limits the generality of these solutions confining the applicability of the ECLT to square or rectangular plates only. A number of investigators followed the same approach suggested by Hyer to obtain more accurate predictions. Dang and Tang [8], Jun and Hong [22, 23] modified Hyer's approach to predict the room temperature shapes by modifying the assumed displacement field. These modifications were implemented either by accounting for more independent constants or by including more complete sets of polynomials for the displacement functions. In spite of the modifications presented in [8, 22, 23],

sometimes leading to more complex analysis; there were no significant enhancements to the results.

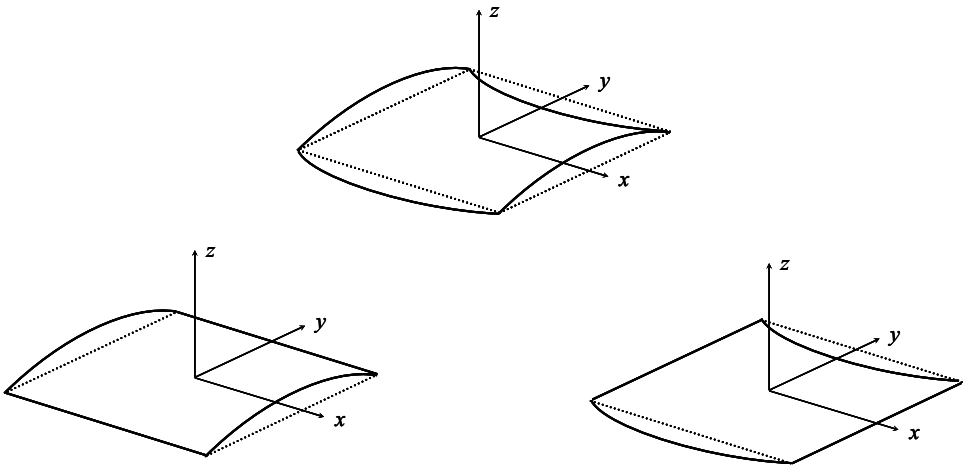

Figure 1-1. Observed cured shapes of unsymmetric cross-ply laminates at room temperature [20]

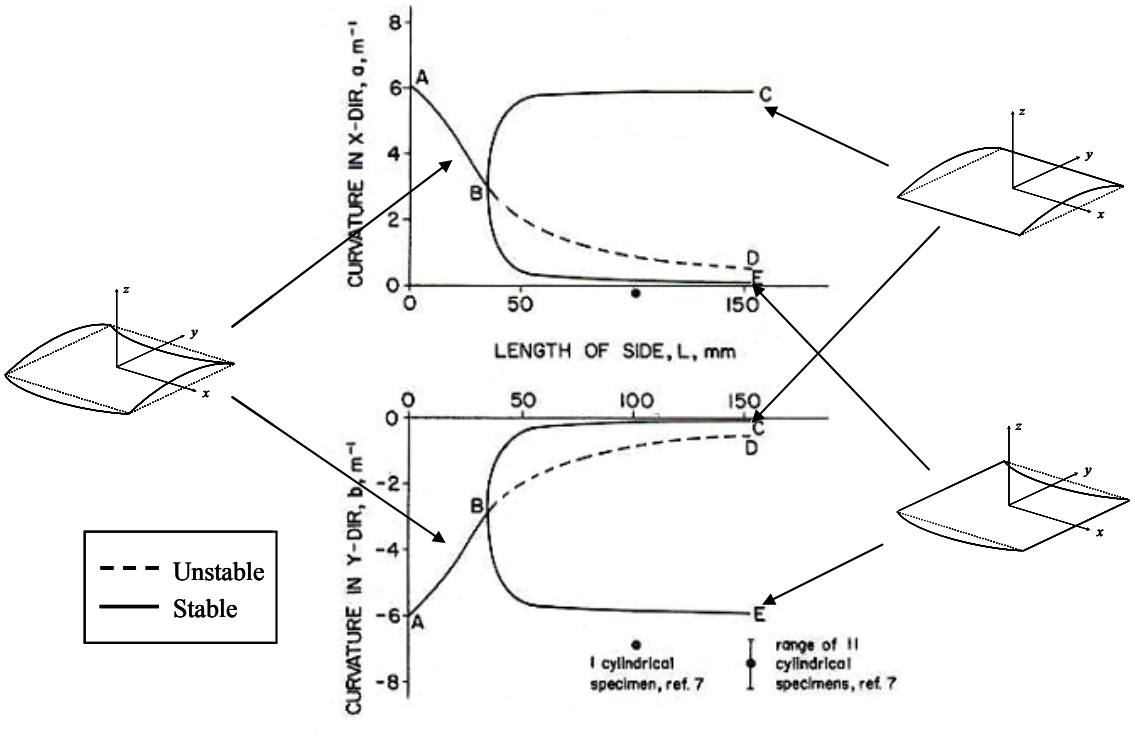

Figure 1-2. ECLT predictions of unsymmetric cross-ply laminates shapes at room temperature [19, 21]

The out-of-plane deformation mismatch between ECLT predictions and experimental measurements of a cured panel, mainly at the bifurcation point, motivated Hamamoto and Hyer [16] to account for geometric imperfections. Ochinero [34] also investigated the effect of different types of geometric imperfections. Results presented in [16, 34] proved the importance of including geometrical imperfections to obtain better correlation between theory and experiment.

Luo, and Daniel [28] presented a solution for angle-ply laminates by modifying the assumption that the mid-plane strains are independent of spatial location which was discussed in [19]. Their modification involved assuming the curvatures as well as strains to be independent of locations thus satisfying zero Gaussian curvature, i.e. a laminate will warp in such a way that one of the curvatures in the principal directions will be zero. The out-of-plane deformations were constrained to follow the same assumption, hence restricting the validity of the results to only large sidelength-to-thickness ratios. A major advantage of this approach is the elimination of the need to assume a displacement field.

Schlecht, Schulte and Hyer [41] and Schlecht and Schulte [42] provided the room temperature shapes of unsymmetric square cross-ply laminates using MARC Finite Element Analysis (FEA) software. A so-called backward method was used to model the snap-through behavior associated with cylindrical panels. Results of such FEA agreed with those of [41, 42] for determining the curved shapes of cured laminates, but no measure of the critical force required for the snap-through behavior was provided.

Despite the advantages of the FEA, particularly in tailoring this snap-through configuration in an efficient way, few published works dealt with the problem directly. The FEA model proposed by Schlecht *et al.* [41, 42] requires intensive computational effort and complex manual simulations for predicting snap-through. Other works proposed a separately written FEA code or sub-routines as add-ons [41, 42] to model the problem. While either approach is viable, they represent custom solutions to the same

problem making the FEA analysis less portable. Moreover, formulations that are based on PMTPE confines the problem to those with regular boundaries.

Tawfik *et al.* [50, 52] presented a finite element approach using ABAQUS™ in order to predict the unsymmetric cross-ply laminate shapes under thermal curing stresses. The cured shapes were in good agreement with Hyer's observations [20] and numerical results [19, 21].

Stability characteristics of unsymmetric laminates

Few previously published research papers provide the measure of force or moment required to trigger the snap-through behavior of bistable panels. The published work in [9-12] presented a treatise of this problem but did not provide accurate measure of the forces. Dano and Hyer [9] modeled the snap-through behavior using Rayleigh-Ritz approach of the ECLT and provided the force requirement by a Shape Memory Alloy (SMA) wire to trigger snap-through. They constructed a model to simulate snap-through and snap-back and compared the results obtained from experiment and analysis. A schematic of their experimental setup and ECLT model is shown in Figure 1-3. The snap-through behavior is triggered by a force F developed in the SMA wires and applied to the ends of two posts of height *e*, attached to the laminate to increase the actuating moment. The force *F* is oriented along line *l* and at an angle β from the x-axis. Dano and Hyer [9] concluded that an overall agreement between analysis and experiment existed. Dano [10] further explained that correlations between theory (ECLT) and experiment were good except for force levels just prior to snap-through.

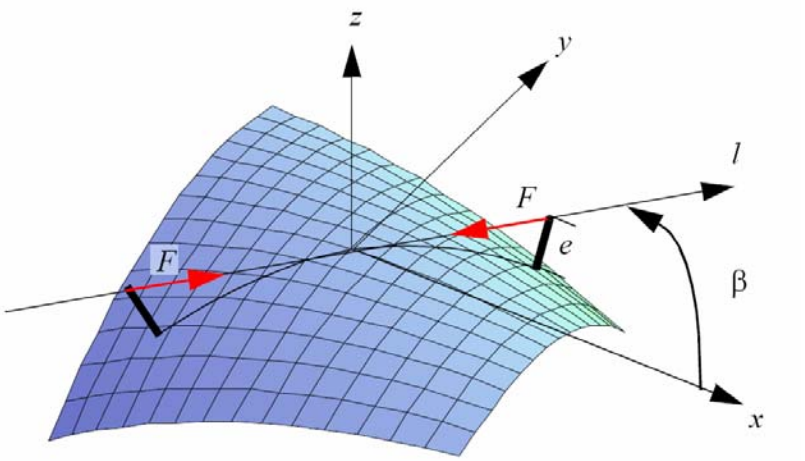

Figure 1-3. Experimental setup and ECLT model for thermally induced snap-through behavior [9-12]

Tawfik *et al.* [50, 52] addressed the snap-through problem of a cross-ply unsymmetric laminate using ABAQUS™ finite element code. A snap-through experiment was constructed applying a concentrated load, in the z direction, at the middle point of the panel as shown in Figure 1-4.

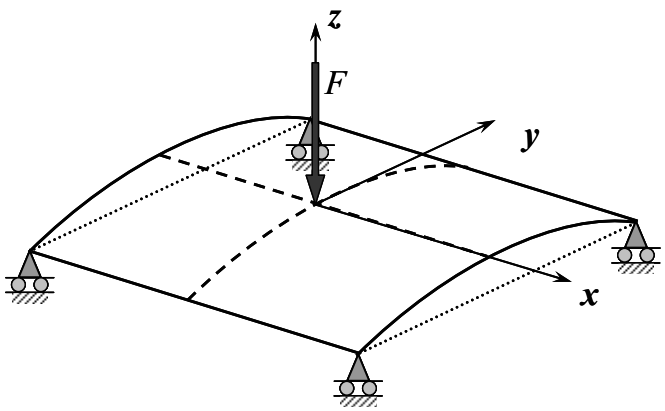

Figure 1-4. Applying a concentrated force to triggering snap-through behavior [50, 52]

Tawfik *et al.* [50, 52] also presented an aspect ratio study of stability characteristics of rectangular unsymmetric panels. In this study they proved a previously

observed trend i.e. the only stable configuration for rectangular laminates with high aspect ratios is associated with curvature of the large side and investigated the panel stability characteristics with increasing aspect ratio. They verified their analytical results by comparison with test data obtained for specimens manufactured from Hexcel IM7/8551-7 Graphite/Epoxy Prepreg with a stacking sequence of $[0_2/90_2]_T$. The specimens' geometries correspond to Aspect Ratio (AR) ranging from 1 to 8. The experiment was conducted using an Instron machine with a 25 mm wide plunger that pushed on the center point of the panels. The panels were to slide against a table till snap-through. The percent difference between analytical predictions and test data ranged from 3.78 to 46.20%. They explained the difference between analytical predictions and experimental measurements as due to the friction at the edges of the panel when sliding on the table and the contact surface associated with the wide plunger used to apply the load.

Inducing snap-through behavior

Two major techniques are adopted to induce snap-through behavior of bistable composites, Shape Memory Alloy wires and piezoelectric actuators. Shape Memory Alloy (SMA) wires were first used by Dano and Hyer in their published work [9-12]. Hufenbach *et al.* [17, 18] addressed the same concept but did not provide the details or requirements of test cases for affecting the snap-through behavior using SMA wires.

The second technique is by bonding piezoelectric actuators to the panel surface(s) to produce a force/displacement large enough to trigger the snap-through behavior. This technique was adopted first by Schultz [44] and Schultz and Hyer [43, 45] using Macro-Fiber Composite (MFC) Actuators. These actuators were developed by Wilkie *et al.* [55, 56] at the NASA Langley Research Center. Schultz [44] and Schultz and Hyer [43, 45] compared the numerical results obtained by a Rayleigh-Ritz formulation of the ECLT with experimental measurements. Their formulation of the Rayleigh-Ritz formulation

was based on three different displacement fields with 4, 10 and 16 terms. The comparison with experiments showed that the bistable shapes were closely predicted but the required electric potential was under predicted by all displacement fields.

Schultz [44] and Schultz and Hyer [43, 45] also discussed using an ABAQUS finite element model of the problem. They mentioned that finite element results agreed with experiment regarding the general trend but did not report the electric potential required for snap-through. They added that finite-element solutions were able to capture behavior not predicted by the Rayleigh-Ritz solutions such as significant shear strain near the corners. It is worth noting that in [43-45] a calibration was performed to measure the MFC piezoelectric constants which predicted values different from those specified by the manufacturer [55, 56]. No clear explanation was provided in [43-45] regarding the reason for the difference.

Using MFC actuators to trigger the snap-through behavior was also discussed by Gude and Hufenbach [15]. In [15] a 4-term displacement field Rayleigh-Ritz formulation of the ECLT was used. They also suggested using an ANSYS finite element model of the bonded panel/actuator structure. Gude and Hufenbach [15] provided experimental measurements for the electric potential values required for the MFC to induce snap-through. Although it was mentioned in [15] that the bistable panels were manufactured from $[0_n/90_n]$ CFRP-T300 no further information was provided regarding material properties, number of layers or actuator dimensions and/or properties.

Potential applications

Cured unsymmetric panels possess two major features; the first is related to their cured shape characterized by large out-of-plane deformation. The second feature is their unique bistable behavior. They can be used to manufacture curved structures without the need to use curved molds and hence reduce the manufacturing cost. While this application does not offer an optimal use of unsymmetric panels it remains a viable one.

An accurate prediction of the cured shape using the ECLT [19, 21] or the established finite element methodology [50, 52] facilitates the design of a curved panel and may eliminate the need for curved molds.

One application of the stability characteristics of unsymmetric panel was suggested by Dano [10] and Schultz [44] in connection with a fluid filled transformable cross section duct, thus providing a means to control fluid flow through adaptable local cross-section areas.

Mattioni *et al.* [30] proposed using bistable panels manufactured by combining symmetric and unsymmetric layups. These panels were used as spars of a variable sweep wing. As was pointed out in their work the suggested design requires accommodating constraints related to the assembly of wing parts including the wing box and ribs.

The concept of combining different stacking sequences within the same panel was also investigated by Tawfik and Armanios [51] as a means for achieving a planform wing with morphed elliptic cambered span capabilities.

1.2 Manuscript Outline

An analytical Finite Element (FE) methodology using ABAQUS commercial software is presented in Chapter 2 and applied to predict thermal stresses due to curing of unsymmetric of square unsymmetric cross-ply laminates presenting aspects of the methodology. The use of the methodology to identify the stability characteristics of square unsymmetric laminates is introduced and suggestions for experimental verifications are made.

Chapter 3 focuses on delineating the stability characteristics of cross-ply unsymmetric laminates and the influence of geometry. An experimental setup is designed to minimize at the boundary conditions of tested panels for an accurate determination of their stability characteristics. Different panel geometries are tested. Test results are

compared to the analytical predictions of the FE methodology inducing the geometric factors affecting stability characteristics.

The conclusions of Chapter 3 are used in Chapter 4 to design an unsymmetric morphing panel. Morphing of the unsymmetric panel is attained by using piezoelectric actuators. The FE methodology is extended to be used for the design of the morphing panel. This led to a new method of actuator bonding to an unsymmetric panel. A test is constructed to verify the design/bonding technique and analytical predictions of the FE methodology.

In Chapter 5, bistable panels are proposed for use as wings for Uninhabited Aerial Vehicles (UAV) and manufacturing method is presented. Preliminary aerodynamic analysis is carried out to verify their potential benefits.

Chapter 6 presents general conclusions and recommendations for future work.

CHAPTER 2

ROOM-TEMPERATURE SHAPES AND STABILITY CHARACTERISTICS OF SQUARE UNSYMMETRIC CROSS-PLY COMPOSITES

2.1 Introduction

When curing an unsymmetric composite laminate at a temperature different than the usage temperature it develops out-of-plane deformations. These deformations are due to the mismatch in the coefficients of thermal expansion and elastic properties of laminae within the laminate. The efforts of many investigators were recorded in the literature review part of Chapter 1. Most of the developed solutions to predict the cured shape of unsymmetric composites are based on the Principle of Minimum Total Potential Energy (PMTPE) and to some extent the works of Hyer and his colleagues or extensions to Hyer's Extended Classical Lamination Theory (ECLT). An attempt of using finite element analysis, as recorded in the literature review, was developed by Schlecht *et al.* [41, 42]. This attempt required manual adaptation and intensive computational effort. On the other hand, Finite Element Analysis (FEA) is being used efficiently in the majority of design problems as it offers great flexibility in handling complex geometries and irregular boundary conditions. Hence, the motivation of this study is to provide an FEA-based solution to predict the cured shapes of unsymmetric laminates and their stability characteristics.

The proposed FEA methodology was the subject of the work presented in Tawfik *et al.* [50, 52]. In this chapter, an in-depth investigation of this methodology is presented starting by providing its theoretical background and discussing its particulars.

Subsequently the methodology is used to identify the design parameters of square unsymmetric cross-ply laminates. Furthermore it is employed to predict their stability characteristics.

2.2 Analysis Background and FE Modeling

In this section the theoretical background of the FEA methodology is presented. ABAQUS finite element commercial software was selected for the current study. ABAQUS provides varying orders of elements formulation and hence offers more flexibility to handle intricate details suitable to a range of applications.

Solution of nonlinear system of equations

A nonlinear system of equations is required to be solved in large deformation analysis of structures. Common methods of solving these systems of equations are iterative techniques where small incremental changes in displacement are found by imposing small incremental changes in load on the structure. The arc length methods are most commonly used to overcome the problem of tracing the equilibrium path in the neighborhood of limit points. The applied load increment becomes an additional unknown in the arc length methods following a Newton-Raphson approach. Riks [39, 40] and Wempner [53] originally introduced the arc length methods which rendered the numerical solution inefficient due to the loss of symmetry of the finite element equations. Crisfield [7], Ramm [37] and Powell and Simons [36] later modified the Riks-Wempner method to retain the symmetry of the finite element equations.

Two procedures, namely `RIKS` and `STABILIZE`, are available in ABAQUS™ and both are capable of solving a nonlinear system of equations and hence suitable procedures for studying unstable post-buckling behavior. Each procedure is formulated differently and their respective input parameters are also different. The implementation of

the RIKS method is efficiently improved if the buckling load is known beforehand. This is due to the method's dependency on the load range and the load increments. When comparing the RIKS and the STABILIZE procedures, the former provides a measure of the severity of the snap-through by predicting the entire non-linear behavior in the case of load reversal. However it has the disadvantage of making the RIKS procedure less suitable for solving problems prone to local instabilities. In contrast, an artificial damping is introduced by the STABILIZE procedure rather than incrementing the load. Introducing an artificial damping into the solution makes the STABILIZE procedure more suitable in dealing with local instabilities. A demonstrative example using a typical load versus displacement curve can be used to explain the difference between these two procedures in capturing snap-through behavior, as illustrated in Figure 2-1 by the solid squares representing STABILIZE procedure and the non-filled squares representing RIKS procedures. The STABILIZE procedure is analogous to an experiment under load control, where the initial configuration snaps to another stable configuration when the critical load is reached, while the RIKS procedure is analogous to that under displacement control, where each unstable configuration and its corresponding load drop are tracked.

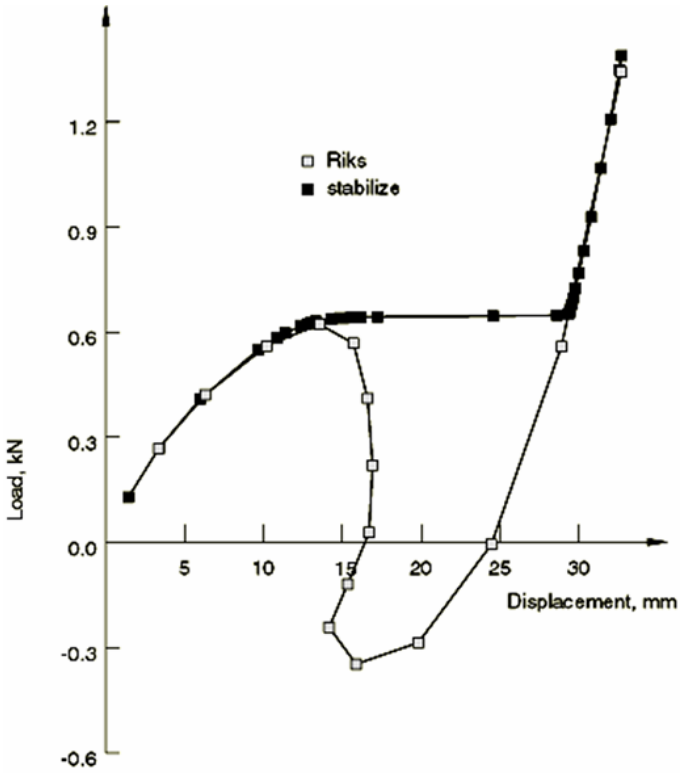

Figure 2-1. Difference in P-δ curve using `RIKS` and `STABILIZE` procedures (ABAQUS™ Benchmarks Manual V6.4)

Buckling with Initial Imperfections

Large discrepancies are found to exist between theoretical and experimental buckling loads. Koiter [25] showed that these large differences in theoretical and experimental results are caused by small imperfections in actual structures. Consequently, for investigating post-buckling behavior small imperfections should be used in perturbing the geometry of the structure under consideration. Imperfections are usually introduced by superimposing perturbations to the perfect geometry. One way to determine the level of imperfection needed is through accurate measurements of variables in actual structures. This method leads to accurate results, yet remains costly and time consuming. Attempts have been made to produce random imperfections that restricted the analysis to provide predictions only for the worst case imperfection.

ABAQUS™ offers three ways to define an imperfection: as a linear superposition of buckling eigenmodes, or from the displacements of a static analysis, or by specifying the location and magnitude of imperfection from direct measurements of a manufactured specimen. A straight forward approach involves two analysis runs with the same model definition:

– An eigenvalue buckling analysis is performed on the "perfect" structure to establish probable collapse modes and to verify that these modes are accurately discretized.
– In the second analysis run imperfections in the geometry are introduced through the addition of the buckling modes to the "perfect" geometry using the `*IMPERFECTION` option. The imperfection has the form

$$\Delta x_i = \sum_{i=1}^{N} \omega_i \varphi_i \tag{2.1}$$

  Where φ_i is the i^{th} eigenmode and ω_i is an associated scale factor. The magnitudes of the perturbations are typically a few percent of a relative structural dimension such as a beam cross-section, in-plane length or shell thickness.
– Finally, a geometrically nonlinear load-displacement analysis of the structure containing the imperfections is performed using the modified `RIKS` or `STABILIZE` methods.

Applying the same concept, the cured shapes of an unsymmetric laminate are obtained in ABAQUS. First, boundary conditions are selected to correspond to the laminate during the cure cycle, i.e. the mold condition. For this purpose the middle point of the panel is selected to be fixed in all degrees of freedom. Then a linear eigenvalue buckling problem is solved for the unsymmetric laminate under the thermal load associated with the curing cycle. Once the linear eigenmodes are obtained, the `IMPERFECTION` command is used to superimpose mode shapes to the perfect laminate

nodal coordinates to obtain the "imperfect" laminate geometry. Finally, a geometrically nonlinear `STATIC, RIKS` procedure is used to model the curing process of the imperfect laminate. Alternatively, a geometrically nonlinear `STATIC, STABILIZE` can be used instead and leads to identical results for the cured shapes.

2.3 Temperature-Curvature Relationship

Hamamoto and Hyer [16] used the ECLT to predict the nonlinear temperature-curvature relationship during the cooling part of the cure cycle. The cure cycle of Hexcel IM7/8551-7 Graphite/Epoxy Prepreg is shown in Figure 2-2. As the temperature drops from maximum curing temperature to room temperature residual stresses are developed resulting in out-of-plane deformations. The model assumed all the material properties are temperature independent. Using ABAQUS FEA methodology developed in Section 2.2 similar relationship can be obtained. A reference problem of a square unsymmetric $[0_2/90_2]_T$ laminate of sidelength 150 mm is used throughout this section. The laminate is manufactured from Hexcel IM7/8551-7 Graphite/Epoxy Prepreg with the material properties provided in Table 2-1. The maximum curing temperature is 177^oC and the room temperature is 21^oC. According to observations the cured laminate possesses a cylindrical shape that can be snapped into another with orthogonal and opposite curvature. The temperature-curvature relationship predicted using the current FEA methodology is compared to predictions from ECLT.

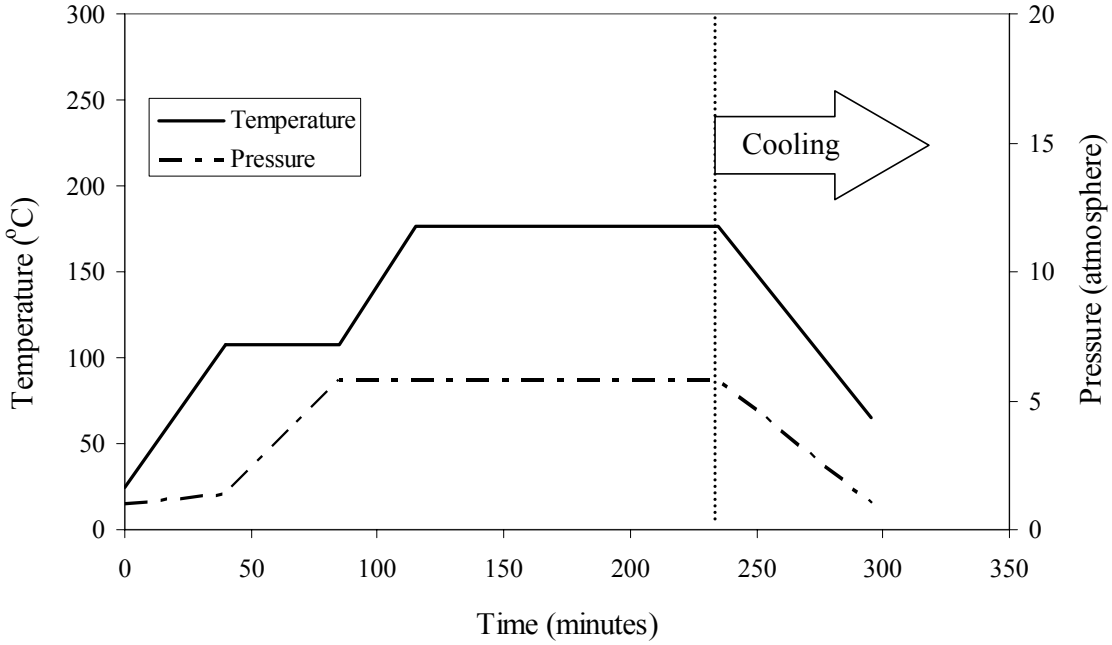

Figure 2-2. Cure cycle of Hexcel IM7/8551-7 Graphite/Epoxy prepreg

Table 2-1 Properties of Graphite/Epoxy prepreg

Material	E_{11} (GPa)	E_{22} (GPa)	G_{12} (GPa)	ν_{12}	α_1 (10^{-6}/°C)	α_2 (10^{-6}/°C)	t (μm)
IM7/8551-7 Graphite/Epoxy prepreg	141.18	7.20	4.45	0.30	0.14	30.98	138.75

The finite element analysis predicts the out-of-plane deformations and the curvature is calculated using the approximation

$$\kappa = \frac{1}{R} = \frac{8d}{C^2 + 4d^2} \tag{2.2}$$

for κ is the laminate curvature and R, C, and d are shown in Figure 2-3. This expression is used throughout the entire work to calculate the curvature from the out-of-plane deformations.

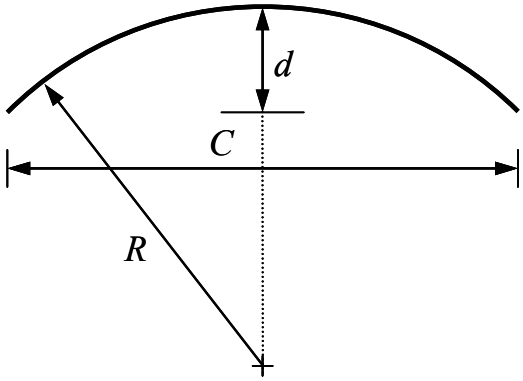

Figure 2-3. Calculation of curvature κ

The temperature-curvature relationship is predicted employing a moderate finite element mesh of 20×20 four-noded, reduced integration, doubly curved shell elements S4R. This element mesh is selected as it requires a computational time similar to ECLT to predict the same relationship using the same temperature increments. Figure 2-4 provides the temperature-curvature relationship obtained using both methods. Since the modeled laminate is of a square shape the curvature of only one side is shown. Imperfection scaling factor is one hundredth of the laminate thickness.

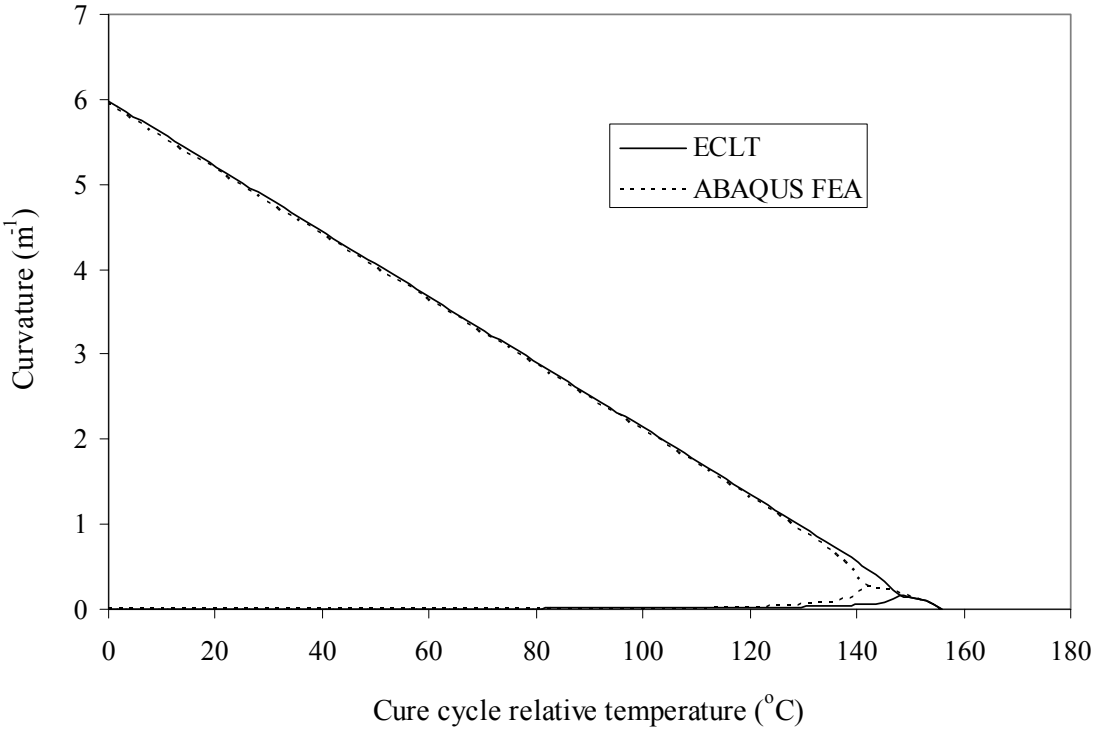

Figure 2-4. Temperature-curvature of a square $[0_2/90_2]_T$ Hexcel IM7/8551-7 Graphite/Epoxy prepreg laminate

Both methods feature identical trends of nearly linear increase of curvature as the cure cycle's temperature decreases. Also within the linear portion the numerical values are nearly identical. On the other hand, the predicted bifurcation point differs in both the temperature value and corresponding curvature. Figure 2-5 shows a close-up view of the bifurcation point.

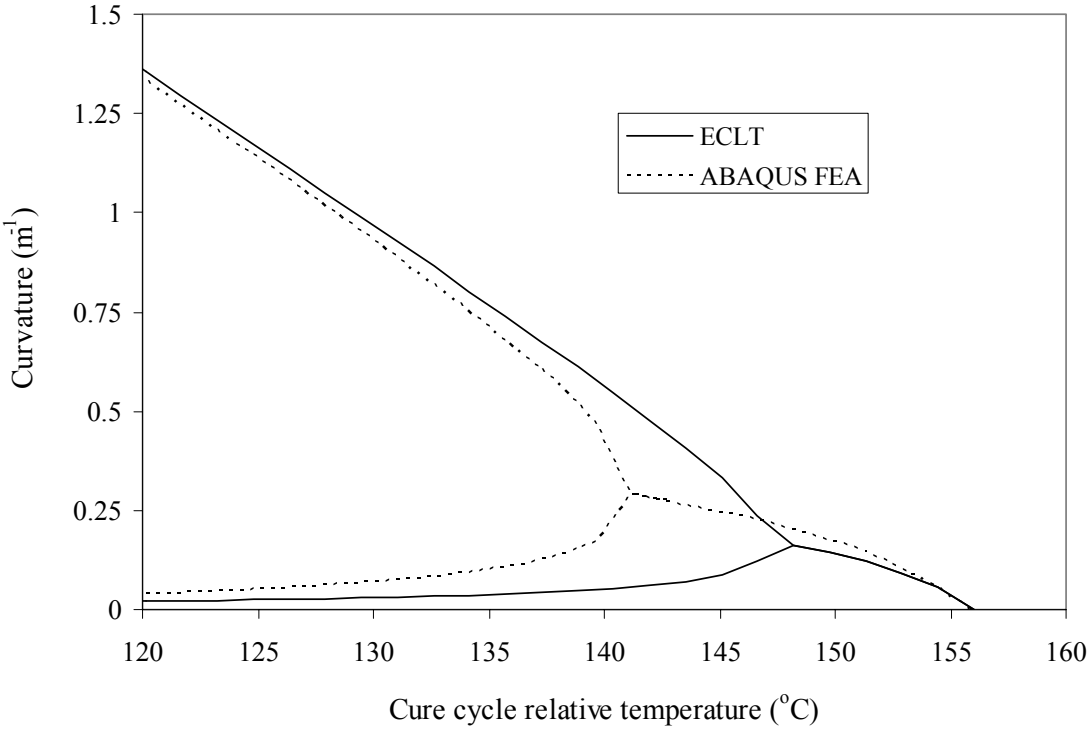

Figure 2-5. Bifurcation point of the square, Hexcel IM7/8551-7, $[0_2/90_2]_T$ laminate

ECLT predicts the bifurcation point to occur at temperature of 148.2 ^{o}C with laminate curvature of 0.159 m^{-1}, while the corresponding values predicted by the FEA are 140.6 ^{o}C and 0.290 m^{-1}, respectively. The trend from the maximum curing cycle temperature to the bifurcation point is similar in both methods.

FEA model accuracy

It is beneficial to discuss the FEA model specifics and study their effect on the accuracy of the provided solution. To this end, initial imperfections, mesh size, element type, and material properties.

Effect of imperfections

One of the major steps of the methodology is to account for geometric imperfections. In this step, mode shapes obtained from an eigenvalue buckling analysis of the laminate are superimposed to those associated with perfect geometry. The scale factors in Equation (2.1) are typically few percent of the laminate thickness. Using only the first eigenmode and varying the value of the scaling factor general trends related to the effect of imperfections on predictions is demonstrated. Values of scale factor equal to one tenth, one hundredth and one thousandth of the laminate thickness are used.

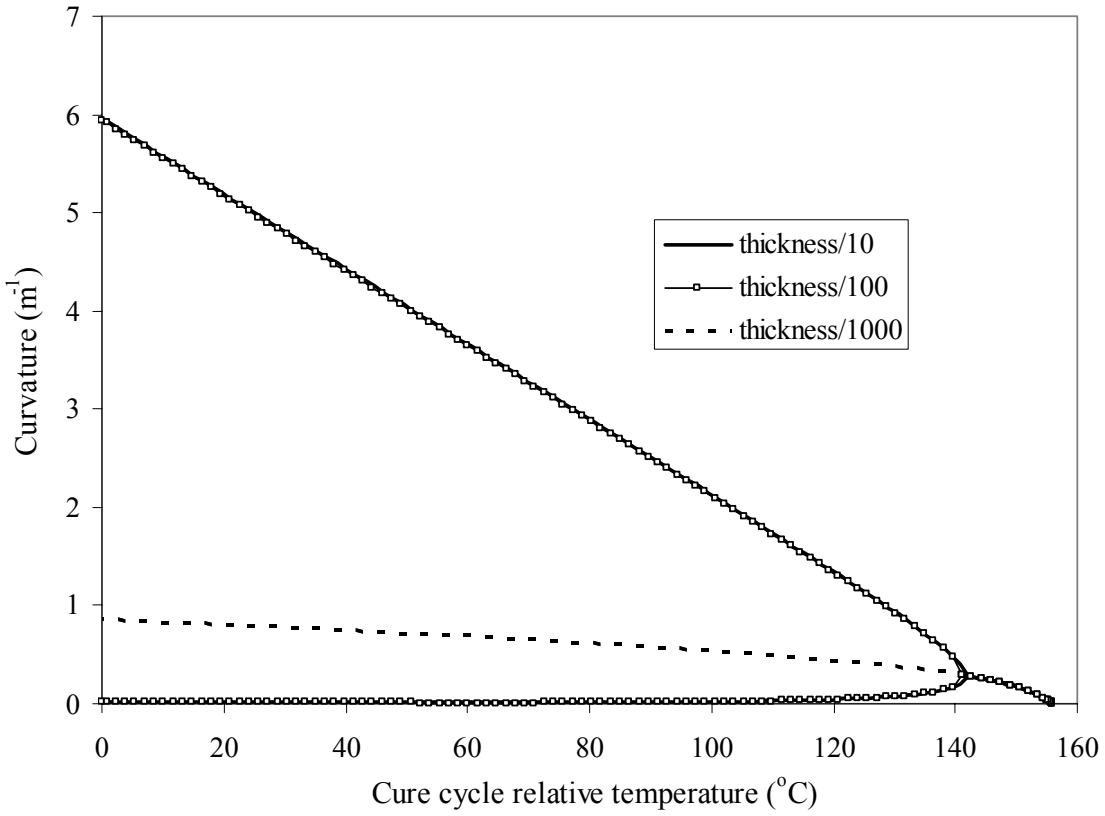

Figure 2-6. Influence of scale factor on predictions

Figure 2-6 provides the temperature-curvature relationship obtained using the aforementioned values of scaling factors. In the case of a scale factor equal to one thousandth of the laminate thickness the analysis predicted the laminate to conform to a

saddle shape at room temperature. Once the scaling factor is increased to one hundredth or one tenth of the thickness, results from the analysis agreed with observations predicting the laminate to exhibit cylindrical shapes. Identical curvatures are obtained for both cases at room-temperature. For further clarification Figure 2-7 provides a magnification at the bifurcation point in Figure 2-6.

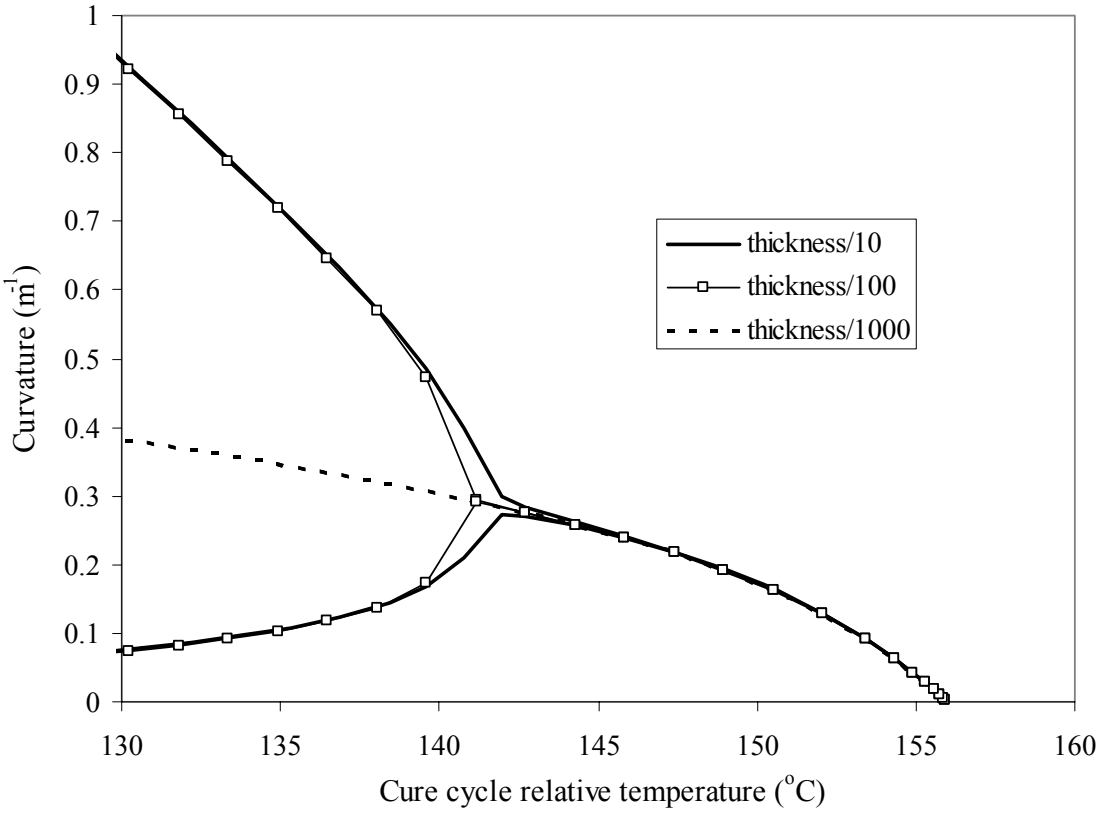

Figure 2-7. Influence of scale factor - magnification at the bifurcation point

From Figure 2-7 the scaling factor of one tenth of the thickness caused earlier prediction of the bifurcation point with no significant effect on the predicted room-temperature curvature. Further increase of the scaling factor beyond tenth of the thickness has the same effect on predicted values of the bifurcation point. Consequently, the default value

used for scaling factor throughout the current work is one hundredth of the thickness unless otherwise mentioned.

Convergence study

ABAQUS FEA software offers a library of shell elements. A set of elements are chosen for the purpose of the current study and subsequent results. Each element of this set possesses six degrees of freedom per node, three translations and three rotations. Therefore these elements form a compatible set that can be used individually or in combinations if needed. The elements of this set are

- *S3*: A three-node triangular general-purpose shell with finite membrane strains.
- *S4*: A four-node doubly curved general-purpose shell with finite membrane strains.
- *S4R*: A four-node doubly curved general-purpose shell with reduced integration, hourglass control and finite membrane strains
- *S8R*: An eight-node doubly curved thick shell, reduced integration. ABAQUS does not offer an eight node element with no reduced integration formulation.

Two parameters are considered for the convergence study, namely the curvature at room-temperature and the bifurcation point. Different mesh sizes were used for the current study corresponding to total number of unconstrained Degrees-of-Freedom (D.o.F) ranging from 96 to 9594. Mesh sizes used for *S3* element are 12×12, 20×20, 40×40 and 80×80 corresponding to total number of D.o.F. of 210, 594, 2394, and 9594, respectively. *S4* and *S4R* elements used mesh sizes are 6×6, 10×10, 20×20 and 40×40 corresponding to total number of D.o.F. of 210, 594, 2394, and 9594, respectively. While mesh sizes used for *S8R* element are 2×2, 4×4, 10×10 and 20×20 with corresponding total number of D.o.F. of 96, 288, 1440, and 5280, respectively The Convergence history plots for the bifurcation point temperature and the laminate curvature at room-temperature are

provided in Figures 2-8 and 2-9, respectively. In both Figures 2-8 and 2-9 the D.o.F. axis is logarithmic.

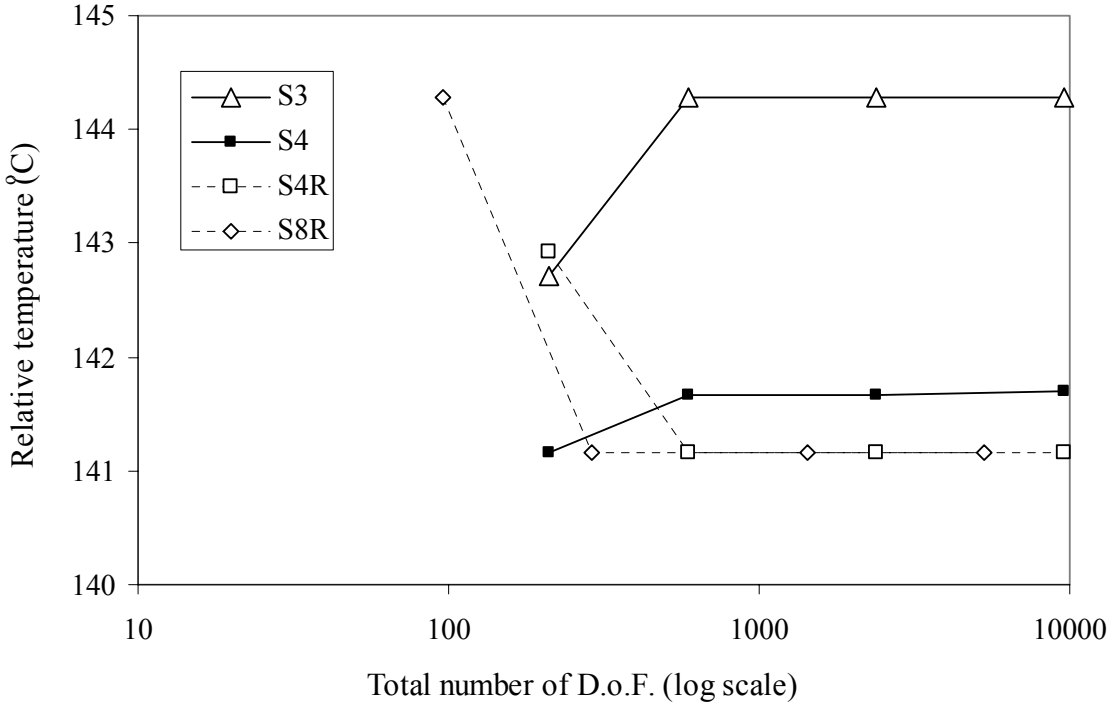

Figure 2-8. Convergence history in terms of bifurcation point relative temperature

Figure 2-8 provides predictions of bifurcation point temperature using elements *S3*, *S4*, *S4R* and *S8R* for different mesh sizes. Elements *S3*, *S4* and *S4R* attain convergence using 594 unconstrained D.o.F. corresponding to a 20×20 mesh for *S3* and 10×10 mesh for *S4* and *S4R* elements. Element *S8R* attain convergence at 288 D.o.F. corresponding to a 4×4 element mesh. Reduced integration elements converge from above while elements without reduced integration, *S3* and *S4*, convergence from below. Both *S4R* and *S8R* elements converge to the same values. Numerical values associated to mesh convergence in terms of bifurcation point relative temperature are provided in Table 2-2.

Table 2-2 Bifurcation point relative temperature (^{o}C) – convergence study

Element / # of D.o.F.	*S3*	*S4*	*S4R*	*S8R*
96				144.28
210	142.72	141.16	142.92	
288				141.16
594	144.28	141.67	141.16	
1440				141.16
2394	144.28	141.67	141.16	
5280				141.16
9594	144.28	141.70	141.16	

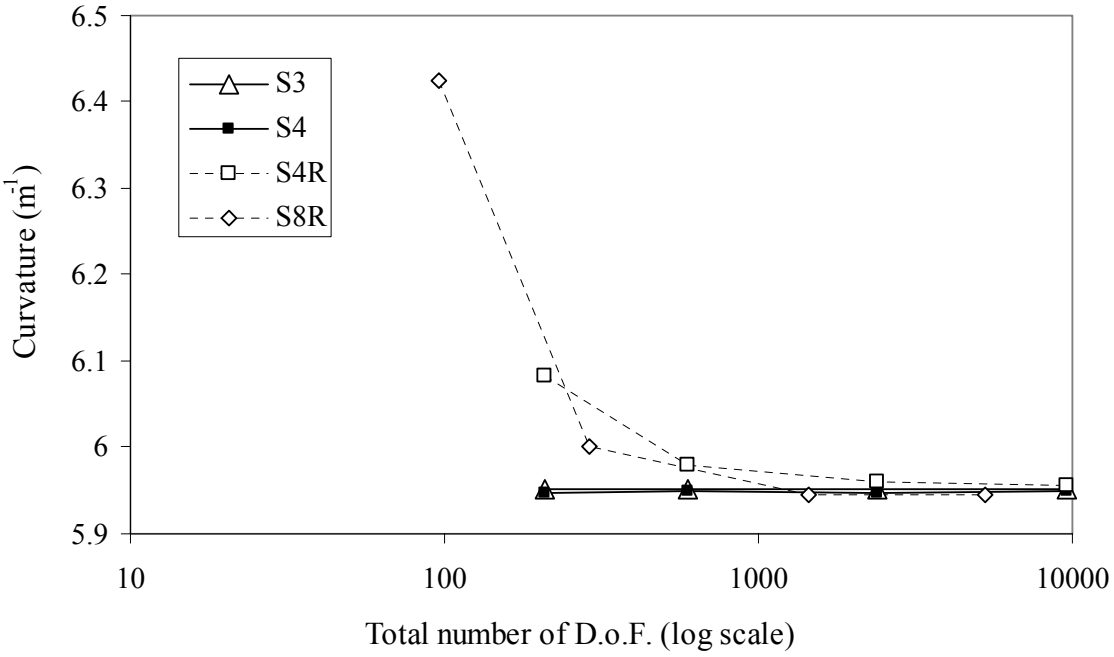

Figure 2-9. Convergence history in terms of room-temperature curvature

Figure 2-9 provides the convergence history in terms of room-temperature curvature. Reduced integration elements, *S4R* and *S8R*, follow the same trend by converging to the results from above. Despite the differences in bifurcation point temperatures predicted by different elements, all elements converge to nearly the same curvature at room temperature. Also convergence is attained at 12×12 mesh for *S3*, 6×6 mesh for *S4*, 10×10 mesh for *S4R* and 4×4 mesh for *S8R*. All these mesh sizes correspond to either coarse or moderate mesh categories. Consequently, a 20×20 refined mesh of *S4R* elements is selected to be used through subsequent sections of this chapter. Numerical values associated to mesh convergence in terms of room-temperature curvature are provided in Table 2-3.

Table 2-3 Room-temperature curvature (m^{-1}) – convergence study

Element / # of DoF	*S3*	*S4*	*S4R*	*S8R*
96				6.64
210	5.95	5.95	6.08	
288				6.00
594	5.95	5.95	5.98	
1440				5.95
2394	5.95	5.95	5.96	
5280				5.95
9594	5.95	5.95	5.96	

Material aging

The Hexcel IM7/8551-7 Graphite/Epoxy Prepreg has been the main source material used in several research topics by the Advanced Composites Group in the

School of Aerospace Engineering at Georgia Institute of Technology. Kim [24] conducted material characterization of the Hexcel IM7/8551-7 prepreg according to the ASTM standards [1, 2]. The material properties reported by Kim [24] are provided in Table 2-4. It was found essential to repeat the material characterization to account for any change of properties due to material aging. Following the ASTM standards [1, 2] Hexcel IM7/8551-7 prepreg material properties were determined and provided earlier in Table 2-1. In the following comparison it is found convenient to refer to Kim's characterization results as "03 properties" and to the recent characterization as "08 properties". Temperature-curvature relationships are obtained for both cases and provided in Figure 2-10.

Table 2-4 Elastic properties of Graphite/Epoxy prepreg reported by Kim [24]

Material	E_{11} (GPa)	E_{22} (GPa)	G_{12} (GPa)	ν_{12}
IM7/8551-7 Graphite/Epoxy Prepreg	146.14	8.472	3.879	0.341

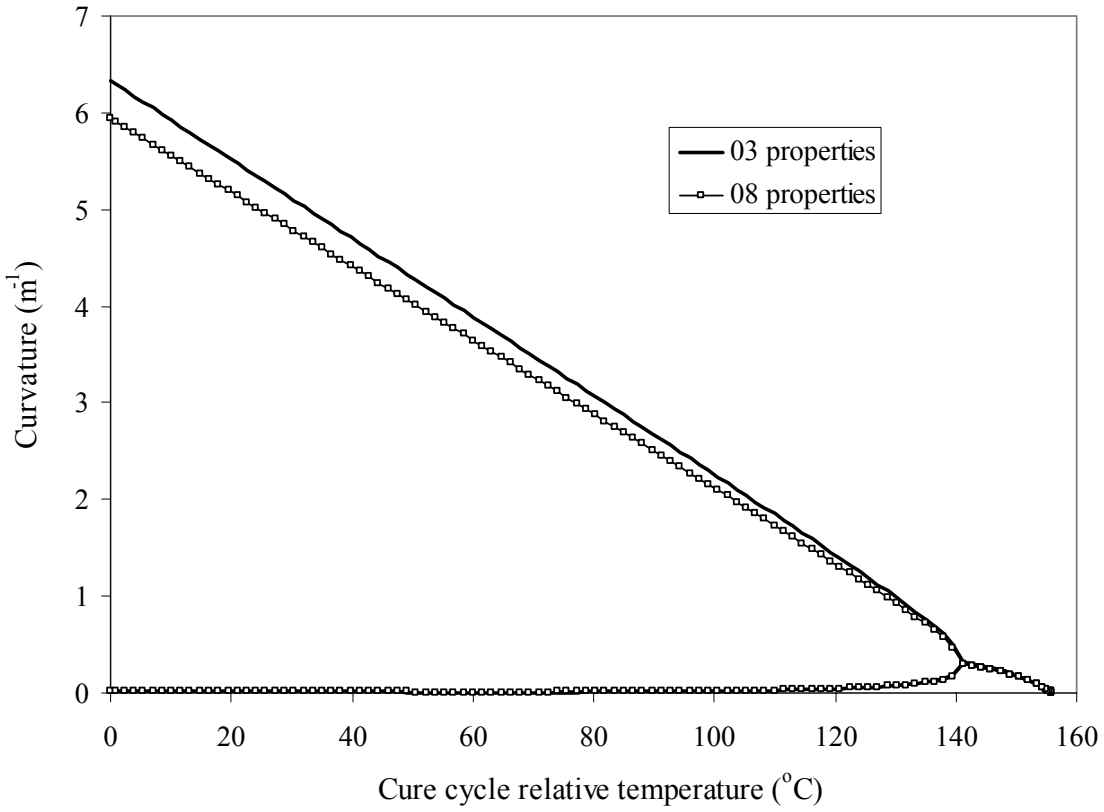

Figure 2-10. Material aging, effect on temperature-curvature relationship

As shown in Figure 2-10 room-temperature curvature predicted using the recent properties is lower. The effect on the bifurcation point temperature is provided in Figure 2-11. The bifurcation point temperature is not affected by material properties change. On the other hand the corresponding curvatures at the common bifurcation point are not equal. Numerical values of room-temperature curvature, bifurcation point temperature (measured difference above room temperature) and corresponding curvatures are provided in Table 2-5.

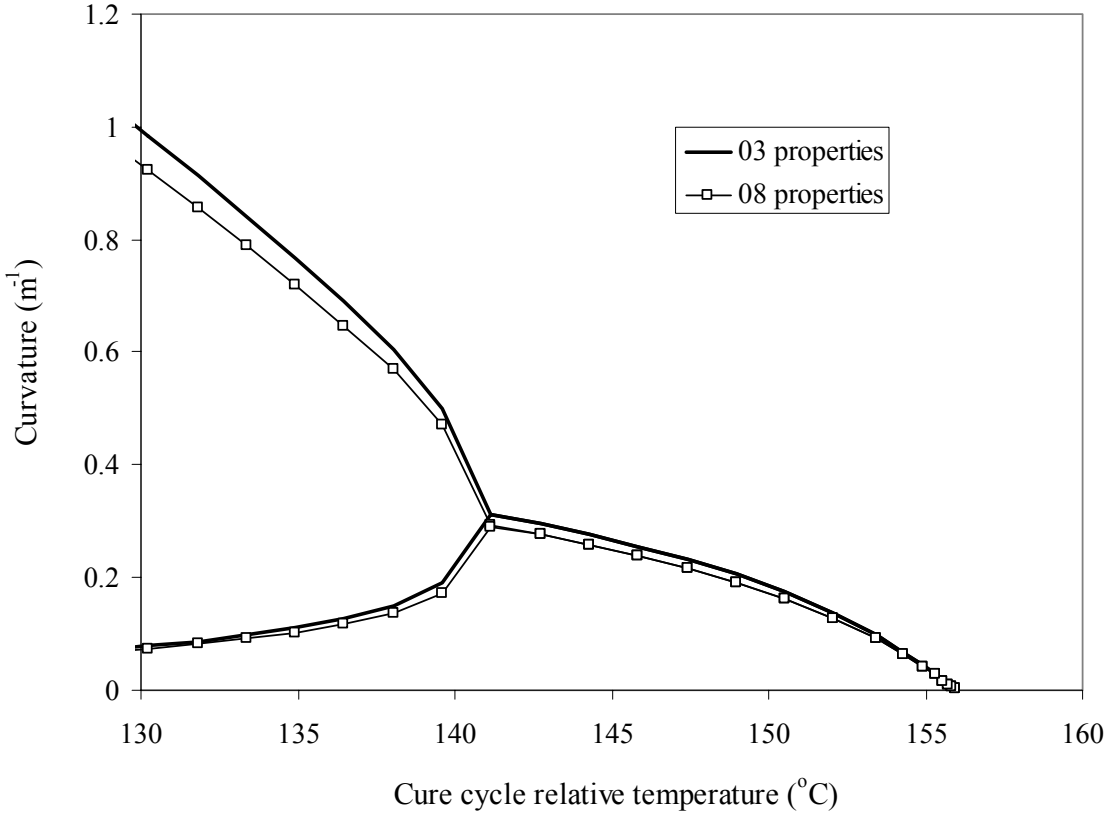

Figure 2-11. Material aging - magnification at the bifurcation point

Table 2-5 Effect of material aging

	03 properties	08 properties
1st equilibrium shape, κ_x (m^{-1})	6.33	5.94
2nd equilibrium shape, κ_x (m^{-1})	0.08	0.015
Bifurcation point temperature (°C)	141.16	141.16
Associated κ_x at bifurcation point (m^{-1})	0.31	0.29

To this point and according to the results of the sensitivity analysis educated selection of imperfections and mesh size are made. Material properties according to the recent characterization, Table 2-1, will be used throughout.

2.4 The Design Curve

The temperature-curvature relationship allows the prediction of the laminate curvatures at room temperature. All the results obtained in previous sections correspond to a square cross-ply $[0_2/90_2]_T$ laminate of sidelength 150 mm. The out-of-plane deformation, and hence curvatures, can be obtained for square laminate as a function of the sidelength. Curvature as a function of the sidelength was obtained using ECLT for a different material system by Hyer in [19]. The ABAQUS FEA methodology is a suitable tool to obtain such a relationship. Therefore the curvatures of a square cross-ply $[0_2/90_2]_T$ laminate with varying sidelength are obtained. The material properties of Hexcel IM7/8551-7 Graphite/Epoxy Prepreg, Table 2-1, are used. The laminate sidelength is increased from 10 mm to 150 mm and the corresponding room-temperature curvature was calculated using Equation 2.2 for each case.

According to the sidelength value, given that the thickness is held constant, a laminate will either possess a saddle or cylindrical shape at room temperature. It is found more convenient to present the results according to the predicted room-temperature shape of the laminate. Therefore according to the FEA predictions a sample of the temperature-curvature relationship for laminates of saddle shapes, is provided in Figure 2-12. Meanwhile Figure 2-14 provide the same relationship predicted for laminates with cylindrical shapes. All predictions are obtained using a 20×20 mesh of S4R elements and imperfection scale factor of one hundredth of the laminate thickness.

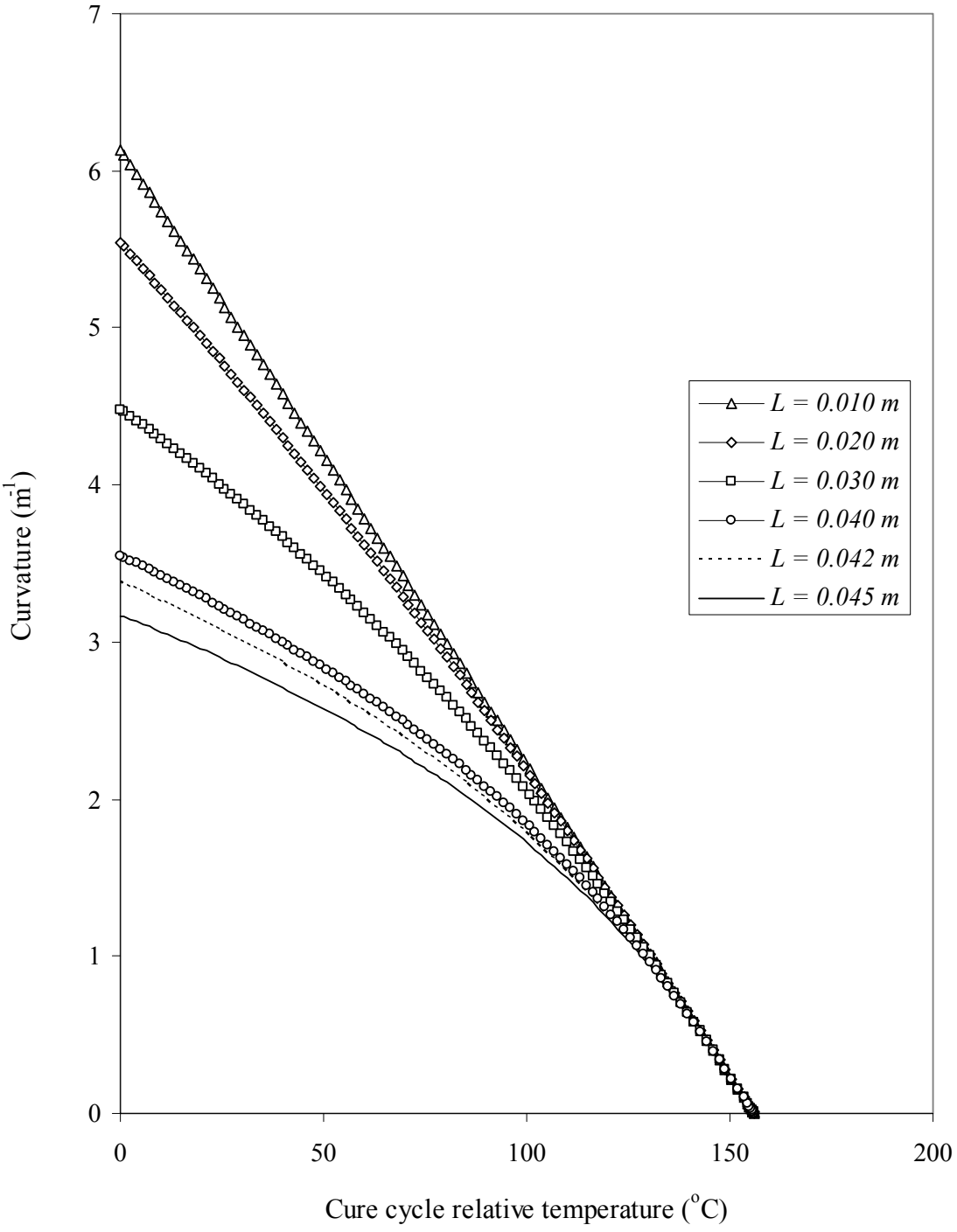

Figure 2-12. Temperature-curvature relationship for saddle shape $[0_2/90_2]_T$ square laminates

First by inspecting Figure 2-12 the temperature-curvature relationship starts out linear for sidelength L = 10 mm. As the sidelength increases to L = 45 mm the nonlinear behavior becomes more pronounced. This figure provides an insight on the problem and agrees with the published information regarding the restrictions on the Classical Lamination Theory that prevent it from predicting the correct room-temperature shape for thin unsymmetric laminates. The saddle shape laminate, shown in Figure 2-13, room-temperature curvature for sidelength varying from L = 10 to L = 45 mm is reported in Table 2-6.

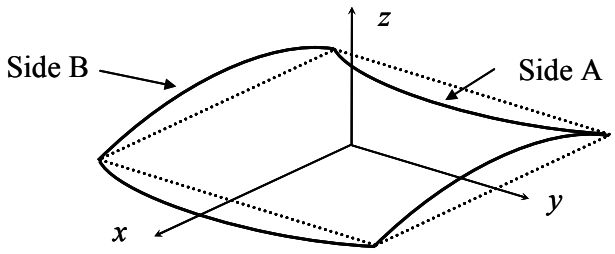

Figure 2-13. Saddle shape of a square unsymmetric cross-ply laminate

Table 2-6 Predicted curvatures of a saddle shape square laminate at room temperature

Sidelength (mm)	Side A, κ_x (m^{-1})	Side B, κ_y (m^{-1})
10	6.13	-6.13
15	5.93	-5.93
20	5.54	-5.54
25	5.02	-5.02
30	4.48	-4.48
35	3.98	-3.98
40	3.55	-3.55
42	3.39	-3.39
44	3.24	-3.24
45	3.16	-3.16

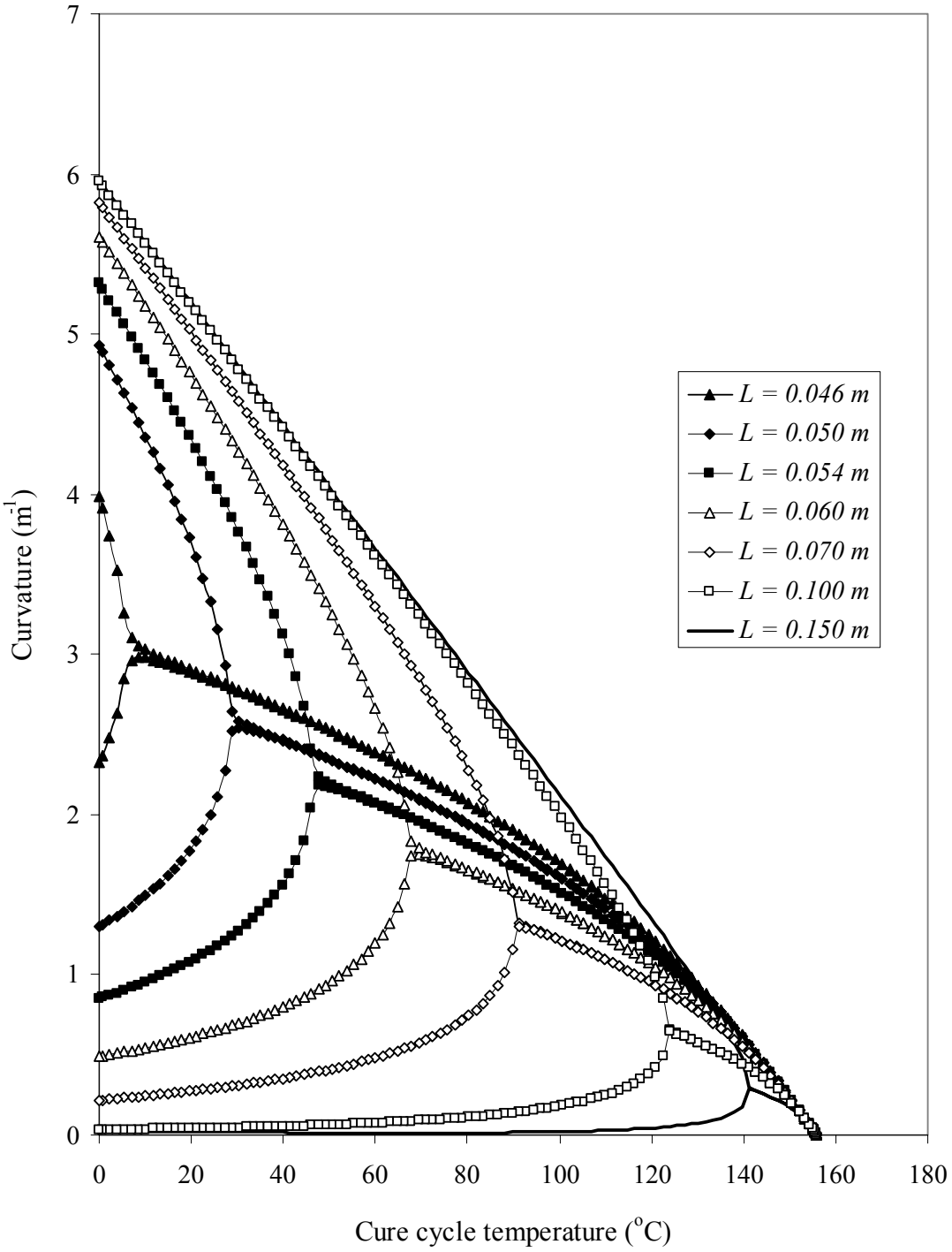

Figure 2-14. Temperature-curvature relationship for cylindrical-like shape $[0_2/90_2]_T$ square laminates

Inspecting Figure 2-14 at sidelength of L = 46 mm the temperature-curvature relationship starts to become doubly valued above a certain temperature. A bifurcation point exists for a laminate with L = 46 mm at temperature ~3 ºC above room temperature. As the sidelength increases till L = 150 mm the bifurcation point travels towards the beginning of the cooling segment of the curing cycle. As predicted earlier the bifurcation point temperature for L = 150 mm is 141.16 ºC. As shown in Figure 2-15 the cylindrical-like shape laminate will have two equilibrium shapes with equal and opposite orthogonal curvatures. Table 2-6 provides the numerically predicted values of bifurcation point temperatures as well as the curvature of Side A in each equilibrium shape for cylindrical-like shape laminates with sidelength varying from L = 45 mm to 150 mm. It is worthy to notice that laminate shape departs from being nearly saddle towards being nearly cylindrical as the sidelength increases.

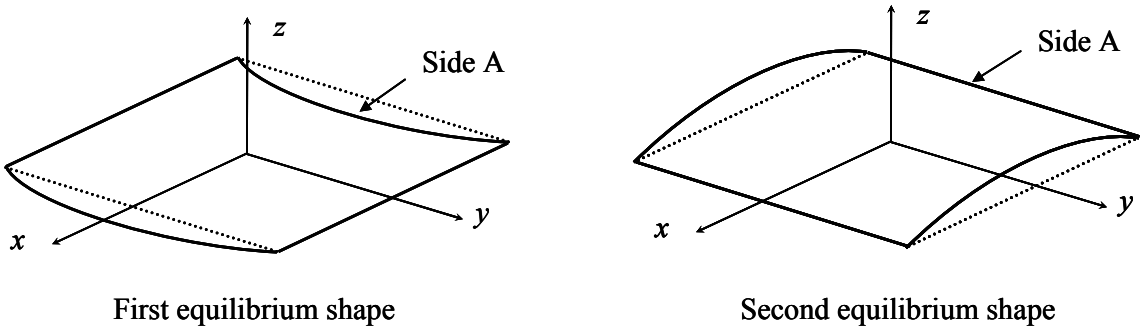

First equilibrium shape

Second equilibrium shape

Figure 2-15 Cylindrical-like shapes of a square unsymmetric cross-ply laminate

Table 2-7 Predicted curvatures of a cylindrical-like shape square laminate at room temperature

Sidelength (mm)	Bifurcation point temperature (ºC)	First equilibrium shape, κ_x (m^{-1})	Second equilibrium shape, κ_x (m^{-1})
46	3.0	3.99	2.32
48	19.5	4.59	1.67
50	28.8	4.93	1.30
52	38.2	5.11	1.05
54	48.6	5.32	0.85
56	53.8	5.44	0.70
58	60.04	5.53	0.58
60	67.84	5.61	0.49
70	91.24	5.82	0.22
80	105.28	5.90	0.10
100	124.00	5.95	0.03
125	134.92	5.96	0.02
150	141.16	5.96	0.02

It is also interesting to inspect the effect of cure cycle temperature on the curvature-sidelength relationship. Figure 2-16 is provided to demonstrate this behavior at different curing cycle temperatures. It assumes that all laminates at the beginning, of the cooling part of the curing cycle are flat. As the temperature starts decreasing out-of-plane-deformations starts to develop due to the mismatch in thermal expansion coefficients and elastic properties in each lamina based on its layup angle. Close to 145ºC above room-temperature all unsymmetric cross-ply laminates possess saddle shape of very low curvature. As the cure cycle temperature decreases laminates of large sidelength starts to attain a cylindrical-like shape. With further decrease in temperature the sidelength of the laminate tends to acquire a cylindrical-like shape and decreases. The critical sidelength at

which a $[0_2/90_2]_T$ square laminate possesses two equilibrium shapes is at L = 46 mm as provided in Table 2-7.

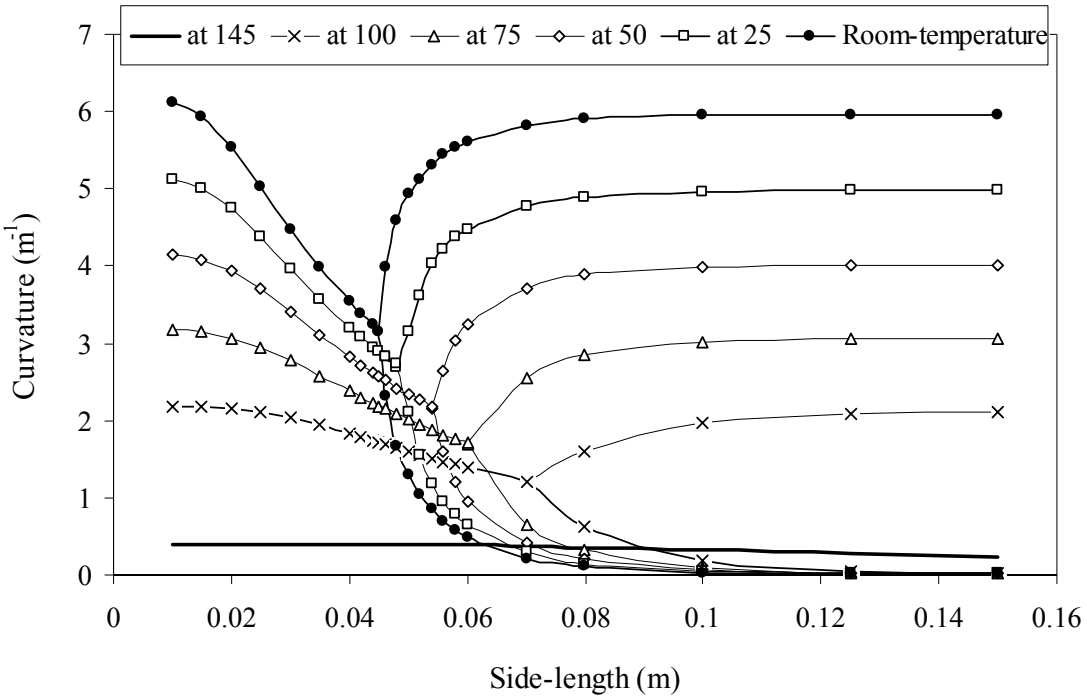

Figure 2-16. Effect of cure cycle relative temperature on curvature-sidelength relationship, $[0_2/90_2]_T$ square laminates

All the results presented up to this point include unsymmetric laminates with four plies, i.e. $[0_2/90_2]_T$ square laminates. It is desirable to investigate the room-temperature curvatures of square unsymmetric cross-ply with different number of plies. For this purpose the curvatures at room-temperature of square cross-ply $[0/90]_T$ laminate with varying sidelength is obtained. A comparison between cases of n=1 and n=2 of square cross-ply $[0_n/90_n]_T$ laminates is presented in Figure 2-17.

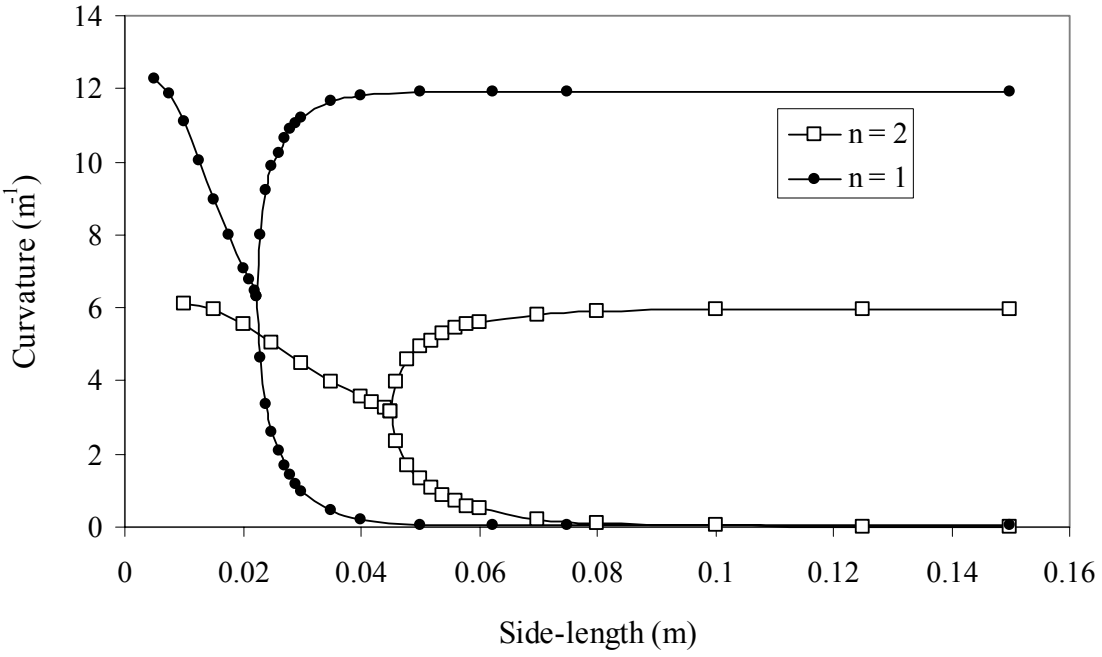

Figure 2-17. Curvatures of square $[0_n/90_n]_T$ laminates with varying sidelength

According to Figure 2-17 The critical sidelength at which a $[0/90]_T$ square laminate possesses two equilibrium shapes is at L = 23 mm. The critical sidelength in the case of n=1 is half of its counterpart in the case of n=2. This presented a motivation to identify non-dimensional parameters for both the curvature and the sidelength for square $[0_n/90_n]_T$ laminates. The suggested non-dimensional values are

$$L^* = \frac{L}{t}$$
$$\kappa^* = \kappa \times L \times \frac{180}{\pi} \tag{2.3}$$

For L^* and κ^* are the non-dimensional sidelength and curvature respectively, and L, t and κ are the square cross-ply laminate sidelength, thickness and curvature, respectively. These non-dimensional parameters provide physical meaning to the results as the sidelength is expressed in units of the laminate thickness and the curvature becomes the angle at the center of the arc defined by the curved shell.

Predictions obtained in Figure 2-17 for square $[0_n/90_n]_T$ laminates are repeated in terms of the non-dimensional parameters and presented in Figure 2-18.

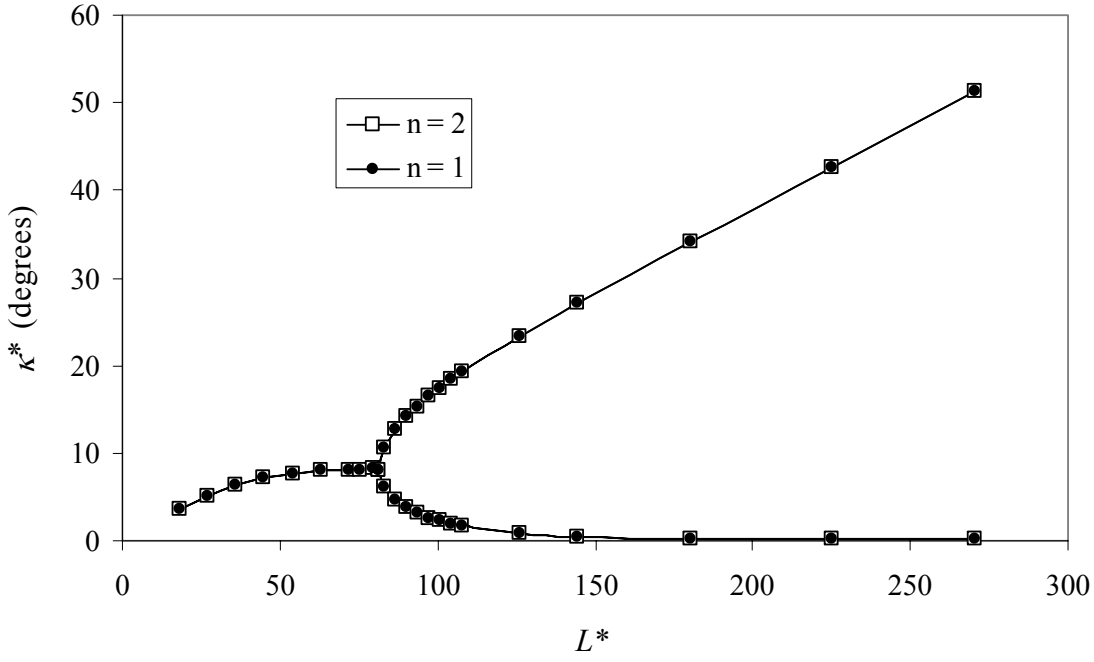

Figure 2-18. Non-dimensional curvatures of square $[0_n/90_n]_T$ laminates with varying non-dimensional sidelength

Figure 2-18 reflects the advantage of employing non-dimensional terms as it caused both curves for n=1 and 2 to coincide. The results from Figure 2-18 provided an incentive for further investigation of the temperature-curvature relationship in these cases. Figure 2-19 provides the temperature-curvature relationship for square $[0_n/90_n]_T$ laminates of n=1 with sidelength = 75 mm and n=2 with sidelength = 150 mm. A magnification at the bifurcation point is provided in Figure 2-20.

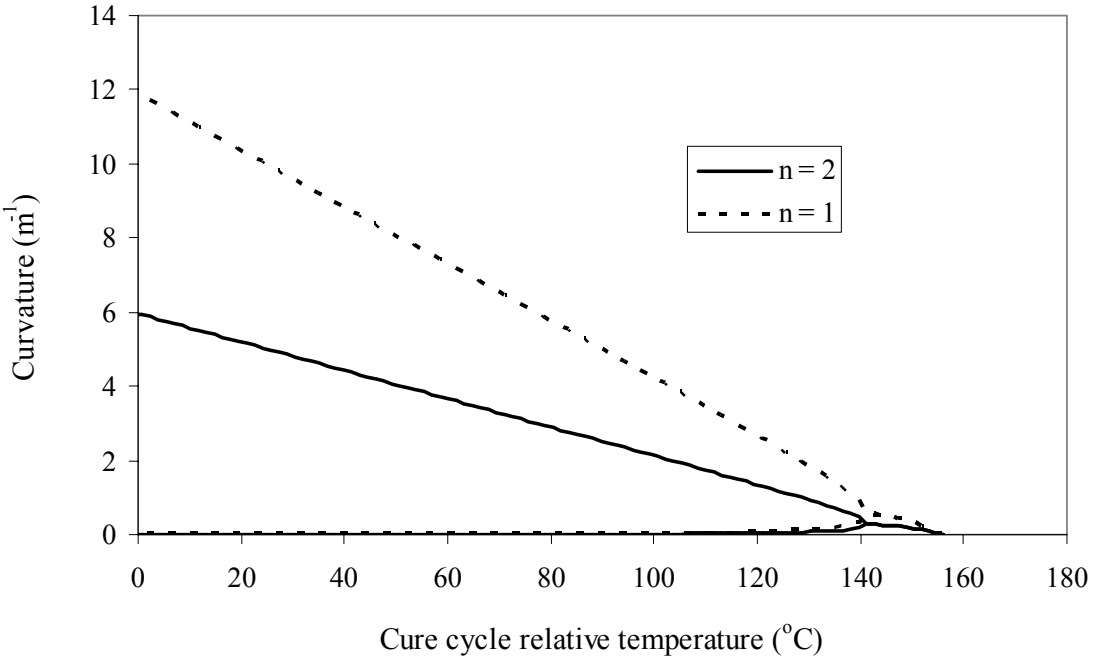

Figure 2-19. Temperature-curvature relationship, two square $[0_n/90_n]_T$ laminates, n = 1 with sidelength = 75 mm and n = 2 with sidelength = 150 mm

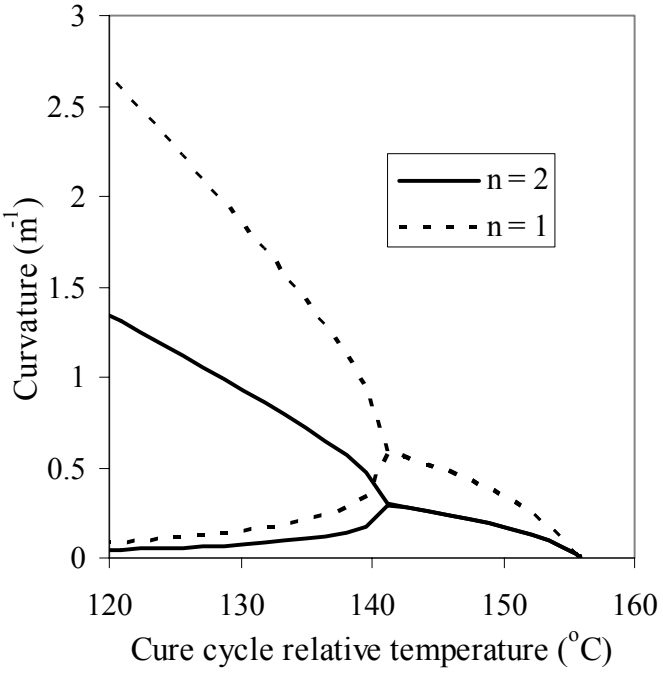

Figure 2-20. Temperature-curvature relationship, magnification at bifurcation point

Interestingly enough the two unsymmetric laminates happen to have the same temperature bifurcation point at 141.16 ºC. Therefore, a third non-dimensional parameter is introduced in terms of the normalized temperature

$$T^* = \frac{\Delta T}{\Delta T_C} \tag{2.4}$$

For T^* is the normalized temperature, ΔT is the curing cycle relative temperature and ΔT_C is the difference between the maximum curing cycle temperature and room-temperature, i.e. 156 ºC for Hexcel IM7/8551-7 Graphite/Epoxy Prepreg. Predictions provided Figures 2-19 and 2-20 are reproduced in terms of κ^* and T^* in Figures 21 and 22, respectively.

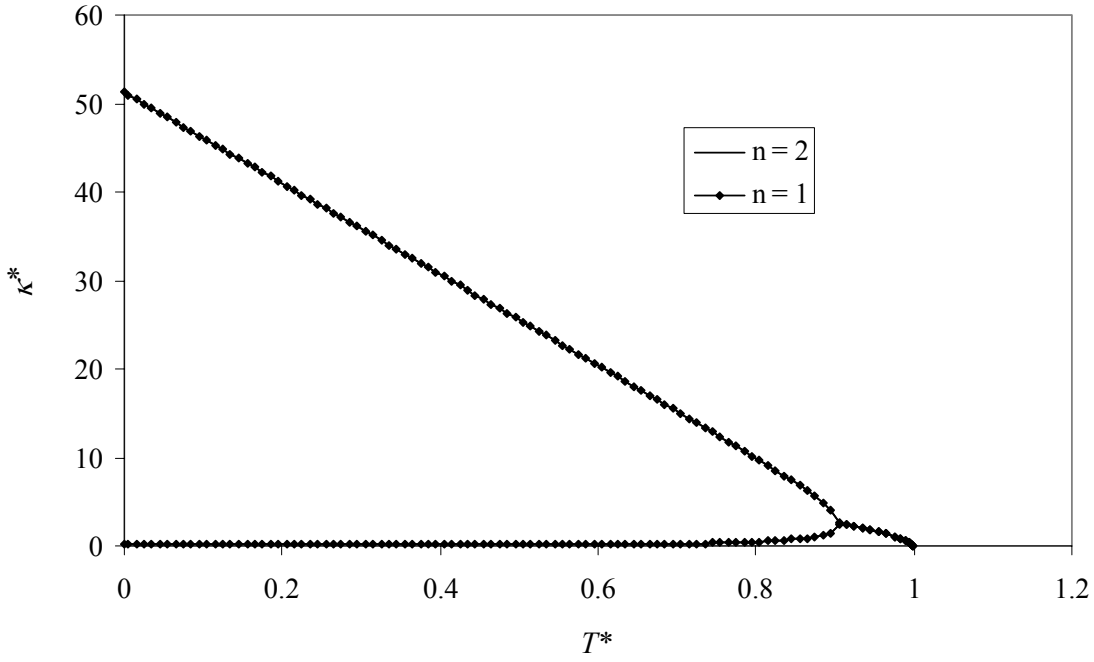

Figure 2-21. Non-dimensional temperature-curvature relationship, two square $[0_n/90_n]_T$ laminates, n = 1 with sidelength = 75 mm and n = 2 with sidelength = 150 mm

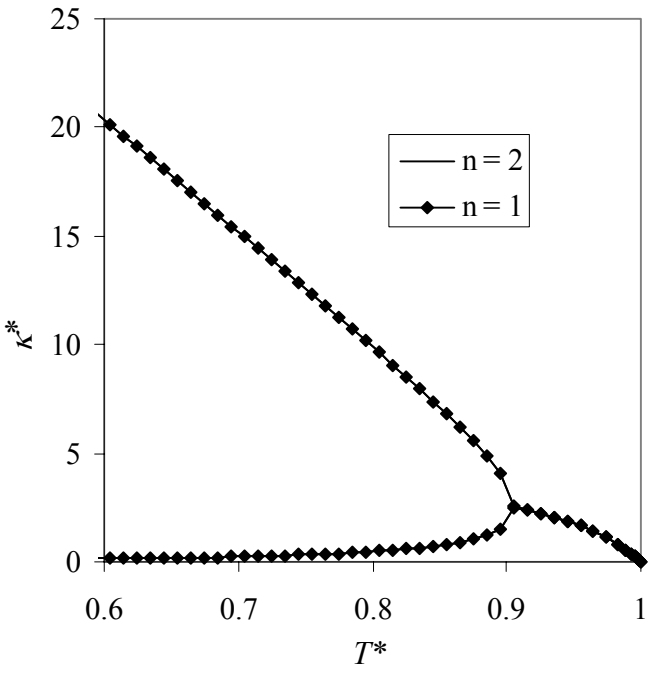

Figure 2-22. Non-dimensional temperature-curvature relationship, square $[0_n/90_n]_T$ laminates, magnification at bifurcation point

The non-dimensional parameterization is performed at different sidelength values and for n = 1 to 5 of square $[0_n/90_n]_T$ laminates. The non-dimensional sidelength, L^*, and its corresponding non-dimensional curvatures, κ_x^* (curvature of the same side in two equilibrium shapes) and bifurcation temperature, T_b^*, are obtained in each case and presented in Table 2-8.

Table 2-8 Non-dimensional parameterization applied to square $[0_n/90_n]_T$ laminates

n	t (m)	L (m)	$\kappa_x\|_I$ (m^{-1})	$\kappa_x\|_{II}$ (m^{-1})	T_b (ºC)	L^*	$\kappa_x^*\|_I$	$\kappa_x^*\|_{II}$	T_b^*
1	0.0002775	0.03	11.220	0.979	67.84	108.108	19.286	1.68	0.435
2	0.0005550	0.06	5.610	0.489	67.84	108.108	19.284	1.68	0.435
3	0.0008325	0.09	3.739	0.326	67.84	108.108	19.282	1.68	0.435
4	0.0011100	0.12	2.804	0.245	67.84	108.108	19.280	1.68	0.435
5	0.0013875	0.15	2.243	0.196	67.84	108.108	19.280	1.68	0.435

The numerical values presented in Table 2-8 show the effectiveness of the non-dimensional parameterization in terms of the three dimensional space of the problem (sidelength, curvature and temperature) and illustrated by the single design curve for square $[0_n/90_n]_T$ laminates manufactured from Hexcel IM7/8551-7 Graphite/Epoxy Prepreg in Figure 2-23.

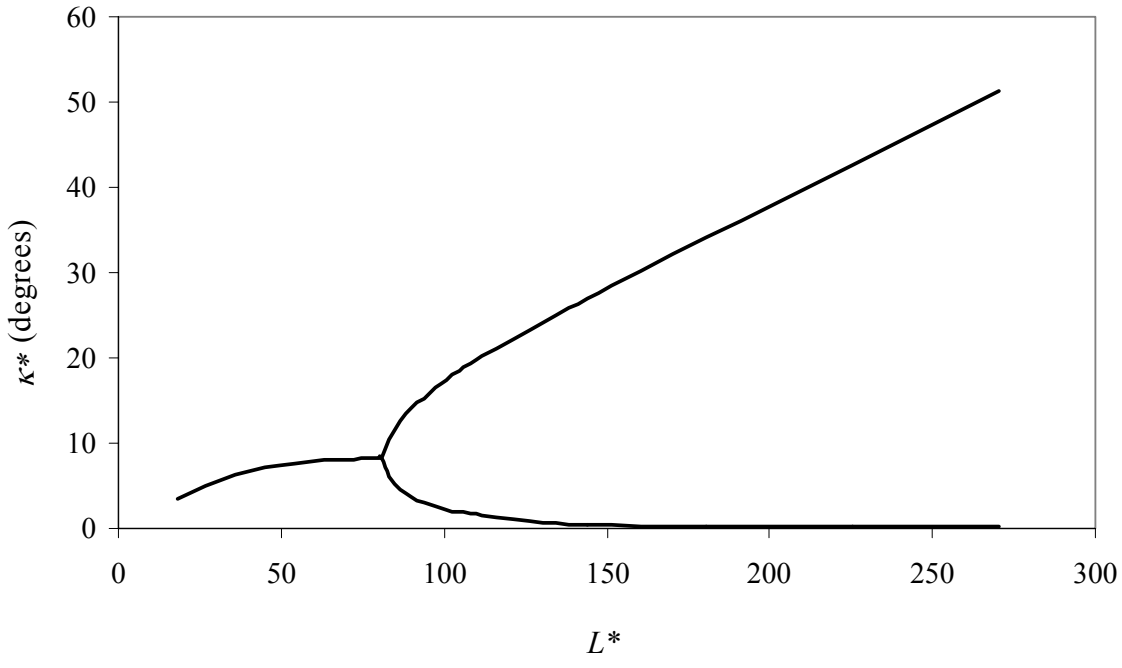

Figure 2-23. The design curve of square $[0_n/90_n]_T$ laminates

This curve presents a concise yet effective description of square unsymmetric balanced cross-ply laminate behavior for any number of plies. It provides the critical sidelength responsible for causing the laminate to acquire cylindrical-like shape in units of thickness. This non-dimensional critical sidelength value is $L_C^* = 82.88$. Therefore the design curve can be used backwards to determined the required sidelength for a laminate with predetermined unsymmetric stacking sequence to have certain curvature. Further advantage of this curve lies in formulating the relationships in terms of physically meaningful parameters and hence leading to better understanding.

2.5 Stability Characteristics

The ABAQUS FEA methodology is also used to investigate the stability characteristics of square unsymmetric laminate with cylindrical-like shape. This can be attained by utilizing nonlinear analysis step(s) similar to the methodology for obtaining the room-temperature shape of the laminate. Consider the case of triggering snap-through behavior via a concentrated load as shown in Figure 2-24.

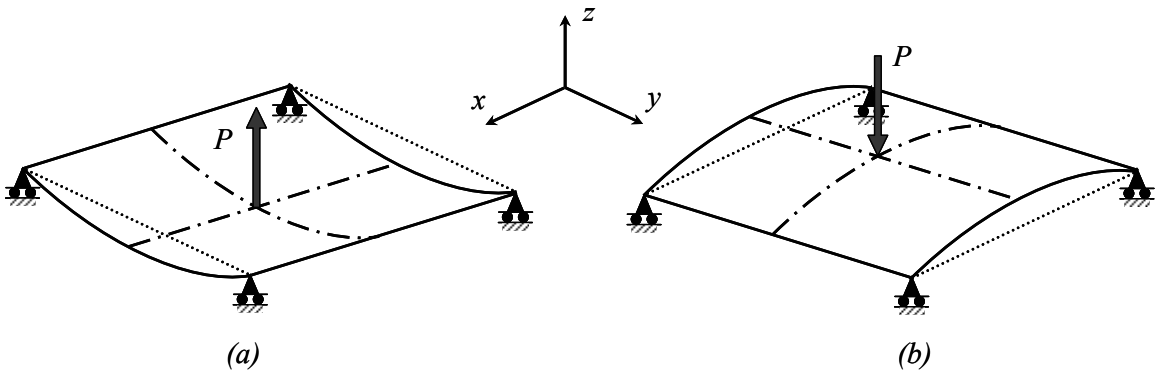

Figure 2-24. Triggering snap-through in cylindrical panel via concentrated force

As mentioned earlier that ABAQUS offers two nonlinear procedures, `RIKS` and `STABILIZE`, which can be used interchangeably to predict the room-temperature shape

of the laminate. When applying a concentrated load to trigger snap-through behavior the laminate may run into local instabilities. The thinner the laminate the higher the possibility of local instabilities to occur. Consequently, the `STABILIZE` procedure is a more appropriate choice from a practical standpoint. However, when the `STABILIZE` procedure is used, only the stable branches of the load-deflection curve can be predicted as illustrated in Figure 2-1. In this case the response of the cylindrical laminate, shown in Figure 2-24, subject to a concentrated force, is tracked by performing the following

- Reset the boundary conditions of the obtained cured shape such that the corner points are restrained from movement in the z direction while the middle point is restricted from movement in both x and y directions.
- A concentrated load, P, is applied at the middle point of the panel in the z direction, (Figure 2-23 a). The applied load is normally higher than the one that cause the panel to snap through. This will cause the panel to deform past the other equilibrium position. A nonlinear analysis step is used to predict the load-deflection curve
- In order to make sure that the laminate will retain a stable equilibrium position that is different from the one obtained at the end of the curing cycle the applied load is removed. A nonlinear analysis step is used to deactivate the applied load.
- Once the second equilibrium shape is realized, a concentrated load is applied at the middle point of the plate in the negative z direction, (Figure 2-23 b). All boundary conditions at corners and middle point are kept the same. For an applied load higher than the critical value, the panel will deform past the original cured shape. Load deflection curve can be predicted in a nonlinear analysis step.
- The applied load is removed, and the resulting curved shape of the plate is verified against to the one obtained at the end of the curing cycle simulation.

The load deflection curve of a square unsymmetric $[0_2/90_2]_T$ laminate with a sidelength of 150 mm is predicted following these steps and provided in Figure 2-25. The laminate is manufactured from Hexcel IM7/8551-7 Graphite/Epoxy Prepreg.

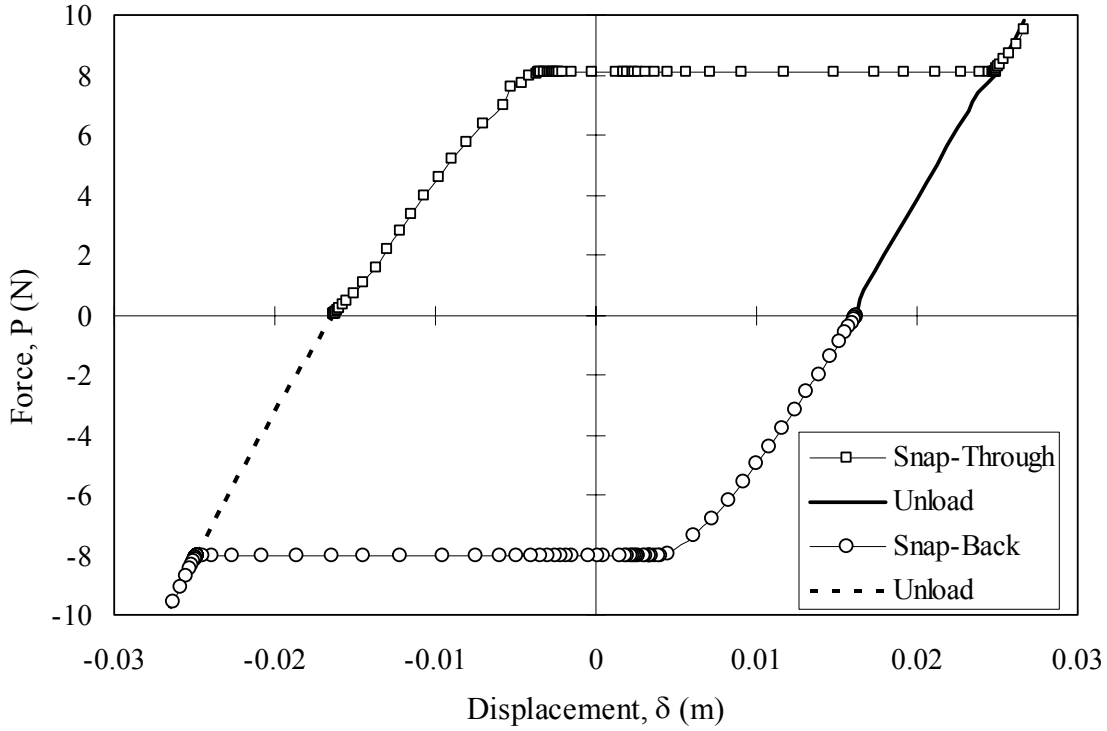

Figure 2-25. P-δ curve of a square unsymmetric $[0_2/90_2]_T$ laminate

As can be seen in Figure 2-25 the load is applied first to trigger snap-through then deactivated to realize the other equilibrium shape. In following steps, the load is reversed to trigger snap-back behavior then unloaded or deactivated to realize the first equilibrium shape. The two starting points of the loading curves (snap-through and snap-back) correspond to the middle point out-of-plane deformation in both equilibrium shapes. As the applied loads are higher than the critical value, the laminate deforms beyond its equilibrium shapes. Hence the function of load deactivation or unloading is to verify that another equilibrium shape exists. It also verifies the accuracy of the solution as the load deactivation branches ends exactly at one of the equilibrium shapes.

For demonstration purposes the critical snap-through and snap-back loads are predicted for a number of $[0_2/90_2]_T$ laminates with various sidelengths. The numerical values of these predictions are provided in Table 2-9. The difference between the predictions of snap-through and snap-back load is due to accounting for geometric imperfections. It will be shown in Chapter 3 that accounting for geometric imperfections provides realistic predictions when compared to actual specimens.

Table 2-9 Predictions of snap-through and snap-back loads of $[0_2/90_2]_T$ square laminates

Side Length (mm)	Snap-through load (N)	Snap-back load (N)
60	1.604	1.601
62	1.854	1.852
64	2.095	2.105
70	2.796	2.810
80	3.880	3.887
90	4.776	4.760
100	5.570	5.552
150	8.180	8.110

Because of the versatility that FEA offers in dealing with complex geometry and irregular boundary conditions, the stability characteristics can be predicted for an unsymmetric laminate of any shape. Therefore, providing the tool and motivation to the shape influence study presented in Chapter 3.

2.6 Conclusions

A finite element methodology is presented using ABAQUS commercial software. The methodology is established and its specifics are discussed. Temperature-curvature relationship is predicted using this methodology and compared to results from existing analytical method, ECLT. Element choice and mesh convergence are addressed in terms of the predicted temperature-curvature relationship.

The curvature-curvature relationship is used to develop the relation between curvature and sidelength of square unsymmetric laminates. The sidelength critical value is obtained for certain stacking sequences. Further application of the demonstrated methodology leads to the development of a single "design curve" relating non-dimensional curvature of an unsymmetric laminate and its non dimensional-sidelength. The non-dimensional parameterization is introduced and proved unique in the three dimensional parameters, namely, temperature, curvature and sidelength. The design curve is simple to reproduce for different composite materials.

Finally, the methodology is used to predict the stability characteristics of bistable panel. Predictions using the same methodology are in agreement with observations and test data as shown by the extensive experimental effort presented in Chapter 3. This effort is entailed to provide both the advantages and disadvantages of the presented methodology.

CHAPTER 3

INFLUENCE OF GEOMETRY ON THE STABILITY CHARACTERISTICS OF BISTABLE CROSS-PLY LAMINATES

3.1 Introduction

In comparison to analytical modeling few research addresses the experimental aspect of the snap-through behavior of bistable panels. As mentioned in literature review Dano and Hyer [9] performed a snap-through experiment. Its objective was to provide the force required by a shape memory alloy wire to trigger snap-through behavior in an unsymmetric laminate. Tawfik *et al.* [50, 52] presented a snap-through experiment of an unsymmetric rectangular cross-ply panel. In this experiment the panel was placed on a table and a force was applied using a 25 mm plunger at its middle point and normal to the plane of the table to trigger snap-through. The edges of the rectangular specimen were allowed to slide against the table. It was noticed that only a portion of the edges slides against the table during the course of motion and its length varied with increase in applied load. Tawfik *et al.* [50, 52] also provided analytical predictions for the required force to cause snap-through in the panel. In their study analytical predictions and experimental measurements were in good correlation but the entire trend was not fully captured.

The influence of boundary conditions on stability characteristics of various structures is discussed by Simitses and Hodges [47]. Also Marshall *et al.* [29] provided experimental results for spherical panels of rectangular planform manufactured from unidirectional E-type Tyglas impregnated with Crystic 272 ployester resin. They obtained test results in both cases of simply supported or clamped edges. When Marshall *et al.*

reported the results of their experiments they provided a fruitful discussion regarding two aspects, namely the panel aspect ratio and the boundary conditions. Based on one or both of these aspects the panel undergoes bifurcation buckling rather than snap-through buckling. In this chapter a new experimental setup is presented to accurately identify the stability characteristics of bistable panels. A modification to the previous experiment [50, 52] is targeting two objectives. The first objective is to minimize friction at the boundary conditions, while the second is related to load application.

3.2 Experimental Setup

In order to eliminate the effect of friction at the edges of the bistable panel two steps are followed. First, the edges need to be supported at one point, i.e. pin support. Second the pin supports are mounted on air bearing to minimize friction due to in-plane motion. In order to clearly demonstrate these steps a brief introduction is dedicated for aspects of frictionless motion.

Frictionless motion

Frictionless motion is achieved through the use of an air cushion. In order to provide an air cushion at the supports either one of two strategies can be followed. The first strategy is based on supplying the air through the table surface on top of which the pin supports can float. In this strategy the air is delivered by means of a plenum or hoses to the bottom side of a porous medium, Figure 3-1, or a series of nozzles arranged in a particular geometric pattern, Figure 3-2. While in the second strategy the air is supplied into the pin supports themselves, Figure 3-3 and air bearings can be used as the pin supports. As shown in Figure 3-3 the air source is connected directly to the pin support via air hose. In order to avoid the stiffening and uncoiling effects that may occur in this type of setup, the first strategy is adopted.

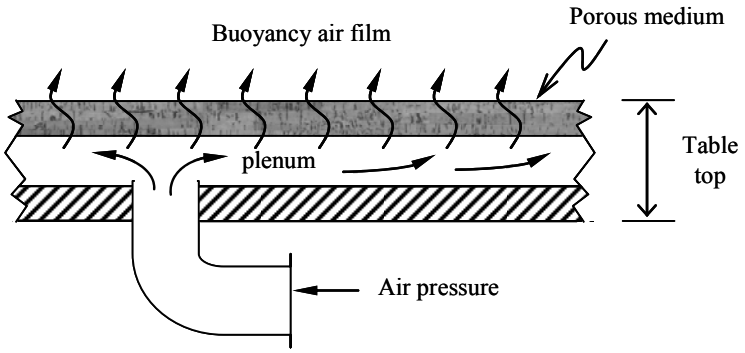

Figure 3-1. Porous media air table

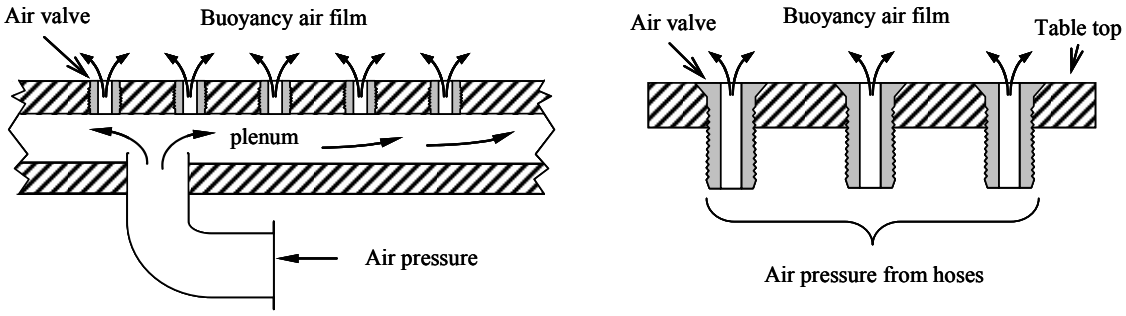

Figure 3-2. Air table with valves or nozzles

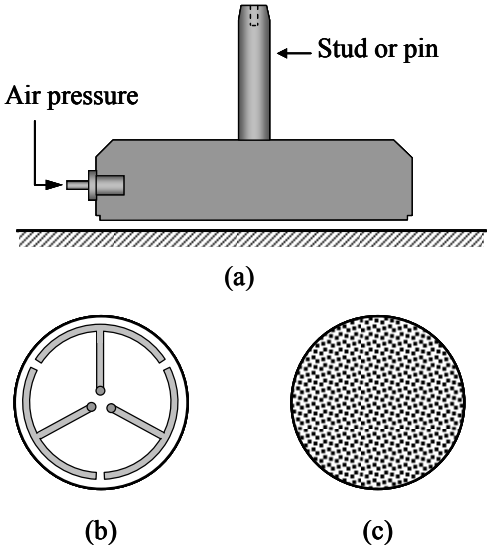

Figure 3-3. (*a*) Air bearing (side view), (*b*) Orifice air bearing (bottom view), and (*c*) Porous material air bearing (bottom view)

The options in first strategy for providing the air cushion, as shown Figure 3-1 and 3-2 should be investigated. In order to make an educated selection among these options, aspects such as surface roughness as well as stability and pitching stiffness are addressed.

Stability and pitching stiffness

Utilization of porous media to provide the air cushion provides high stiffness to pitching moments. This property distinguishes porous media from their orifice/nozzle based counterparts. As depicted in Figure 3-4 when a pitching moment is applied on a pin support floating on orifice/nozzle air table, the height of the air gap will become larger at one side of the pin support. This de-stabilizing condition allows the air flow pumped through the orifices, where the air gap is smaller, to escape through the side with the larger air gap. Therefore, rapid loss of air pressure is created in the path of least resistance. On the other hand, the porous media air table will maintain an air pressure on the side with smaller air gap that will resist the de-stabilizing pitching motion of the pin support or puck.

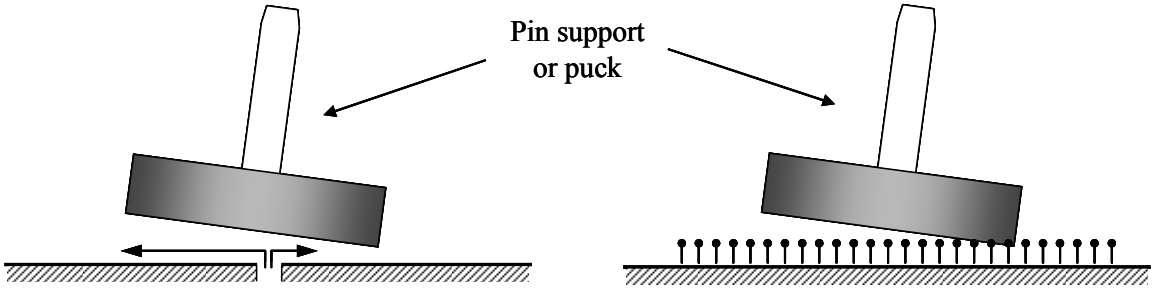

Figure 3-4. Pitching moment stiffness, orifice and porous media air table

Moreover, manufacturing an air table with orifices, valves or nozzles and maintaining the table surface at high degree of smoothness is challenging. Consequently, the option of using porous material for the table surface is adopted. Also using a table top made of porous material will provide the advantage of high pitching stiffness. A helpful

discussion regarding the selection and design of porous air bearing is provided in Reference [5].

The quality of the produced air cushion is dependent on the porosity of the air table. Flatness of the table top should also be guaranteed. Air bearings manufactured from porous carbon material by New Way®, Figure 3-5, withstand higher pressure values than regular porous media and therefore are selected.

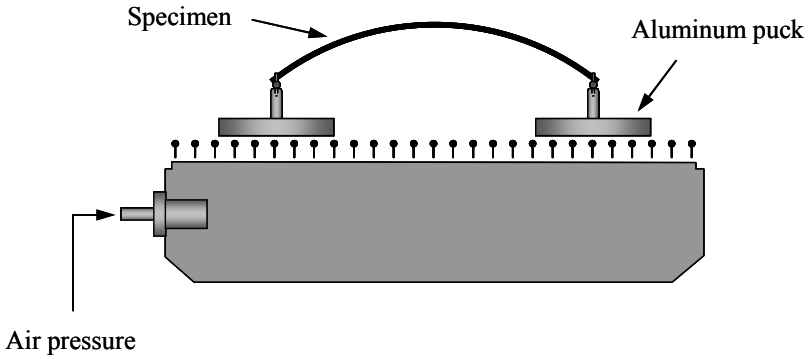

Figure 3-5. New Way® Flat air bearing used as an air table

In this setup two major issues are to be considered. The first issue is the size of the flat air bearing used as this size will add limitations on specimen size. Also the size of the pucks is determined by the applied load which is dictated by the specimen size and number of plies. According to the lift-load curves provided by the manufacturer of the porous air bearings, a polished puck of 25 mm diameter can carry load up to 80 N at input pressure of 60 psi. This leads to the second issue which is attaining the required surface finish of the pucks to provide the required carrying capacity. The manufacturer recommends a surface roughness of 16 RMS. Accordingly a set of Aluminum polished pucks are manufactured, each puck weighs 14 grams and has a diameter of 25 mm. A schematic of the manufactured pucks is provided in Figure 3-6.

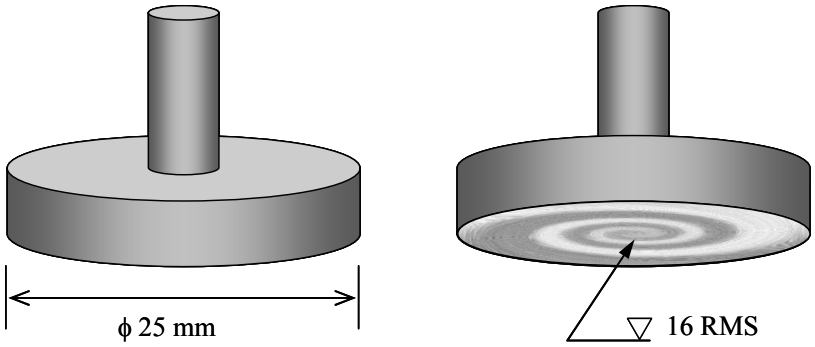

Figure 3-6. Schematic of the manufactured Aluminum pucks

It is also recommended to allow a distance from the edge of the air bearing to avoid edge effects. Therefore the air table is selected to be 250 mm long by 125 mm wide. A schematic of the air bearings and the pucks with a specimen undergoing snap-through is provided in Figure 3-7. Accordingly, a specimen size is limited to 150 mm in length and its width can be 150 mm or less.

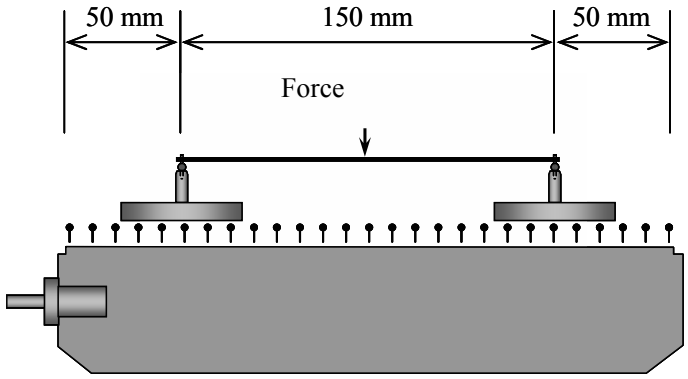

Figure 3-7. Schematic of air table and pucks with a specimen undergoing snap-through

Experimental setup

The experimental setup includes a number of components such as the air compressor, air filter stage, and the load cell. The selection of these components is made based on the air quality and load measurement requirements.

Air Compressor

A SPEEDAIRE industrial duty portable air compressor is used. It is a one phase, one stage air compressor that uses an AC induction motor and has power of 1½ H.P. The air compressor can provide air pressure up to 150 psi.

Clean air requirements

In order to achieve adequate quality in terms of moisture and oil content a three-stage filter arrangement with air pressure gauge as shown in Figure 3-8 is used. First, a general-purpose filter is used to remove any dust particles from the air to protect the Coalescing filter. Then a Coalescing filter is used to remove oil and water particles. In the final stage a desiccant dryer is used to remove water vapor before it condenses. The clean air goes subsequently through a pressure gauge to control the pressure entering the flat air bearing.

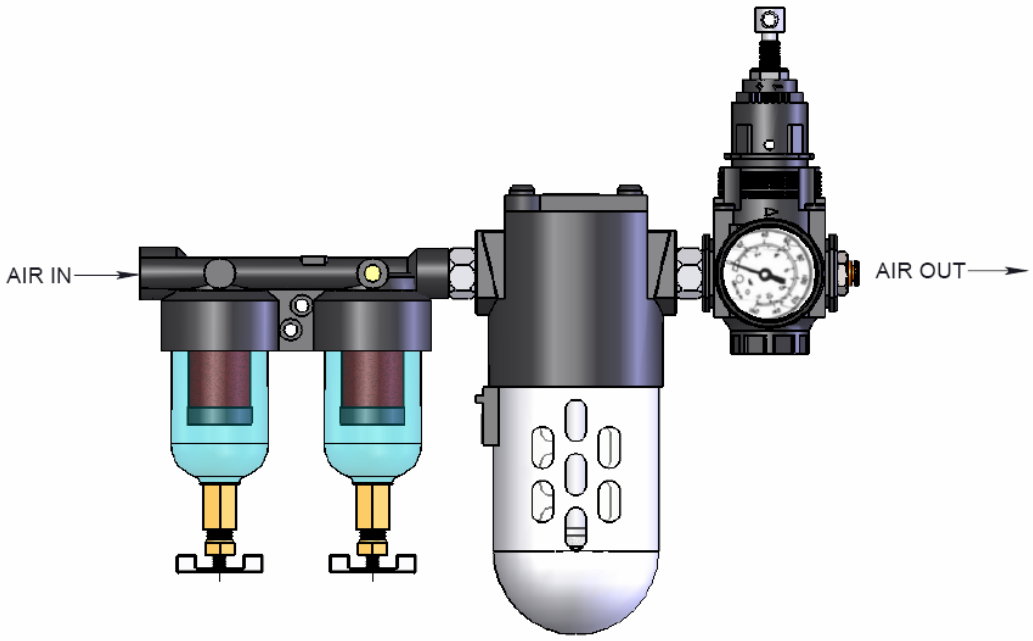

Figure 3-8. Three-stage filter and pressure gauge assembled

(Courtesy of New Way® air bearing)

Load cell

There are two different options in terms of selecting a load cell, a traditional load cell or Digital USB load cell. A traditional load cell requires signal conditioning and a data acquisition system. The data acquisition system includes the computer interface hardware and the associated software such as MATLAB or LabVIEW. On the other hand, a Digital load cell such as Loadstar's USB iLoad load cell offers simplified, robust performance and requires no load conditioning. A USB load cell is selected for this experiment with 10 lb (44.45 N) capacity and 0.05% accuracy. The computer interface of the USB load cell is shown schematically in Figure 3-9. The data is transferred from the load cell into a computer and collected using the LoadVUE software. LoadVUE permits the user to perform nine-point calibration on attached sensors, curve-fit data from the sensors, display individual loads plus the sum of all loads, and log data on screen and to a file.

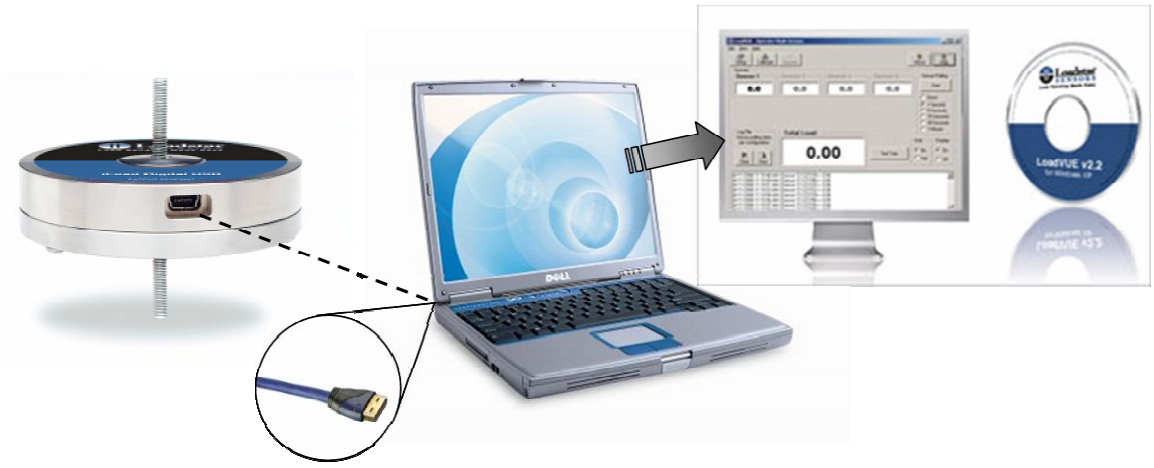

Figure 3-9. USB Load cell computer interface

A schematic of the load measurement apparatus is provided in Figure 3-10. Its components include a load application and load measurement frames, a linear air bearing, two Thomson bars and a supporting table. A threaded load application rod with 40

threads per inch guarantees finer control. The load application rod passes through a threaded hole in the load application frame and is attached to the load measurement frame via a load application attachment. The load application attachment connects the load application rod to the load measurement frame but allows free rotation at the connection. The load application frame is clamped in place to the Thomson bars using four shaft clamps. In contrast, the load measurement frame slides on the Thomson bars using two linear bearing to ensure vertical alignment. The load cell is attached to the load measurement frame via a load cell mount and is in contact with the specimen through a load application pin of 0.04" diameter. The pin diameter of the each puck is 0.04".

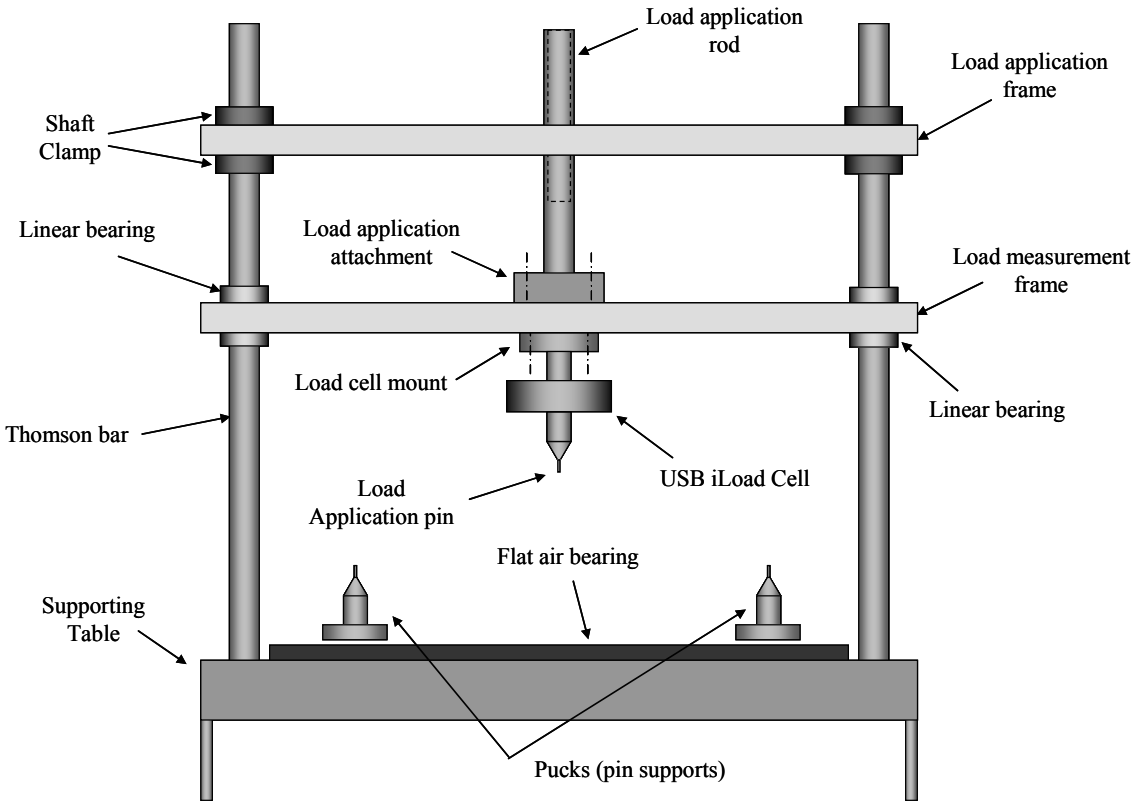

Figure 3-10. Load measurement apparatus

The load measurement apparatus works by rotating the load application threaded rod which in turn cause the load measurement frame to move vertically. When the load measurement frame moves downward it pushes on the specimen through the load application pin. Consequently the two supporting pucks of the specimen will slide horizontally on the air table. As the load value is increased to force the specimen to snap-through the pucks move away from each other. The applied load is recorded at all times by the load cell software and the maximum value corresponds to the snap-through load.

The assembled load measurement apparatus is shown in Figure 3-11. Also the specimen attachment to the pucks and load cell pins are shown in Figures 3-12 and 3-13.

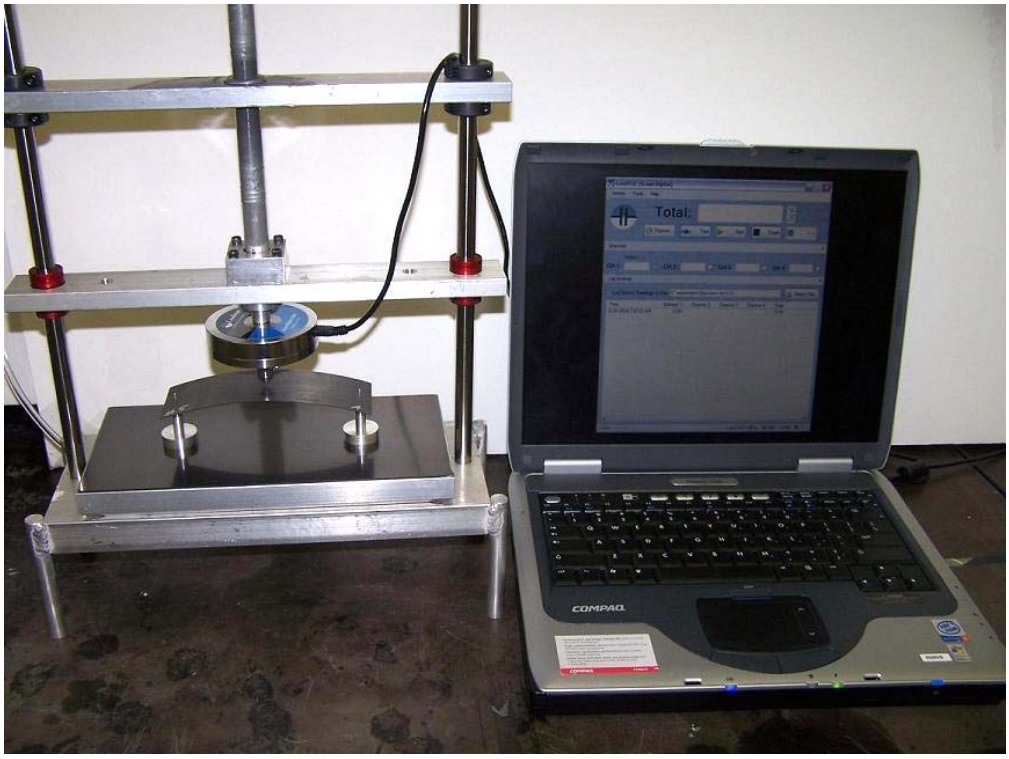

Figure 3-11. Load measurement apparatus and setup

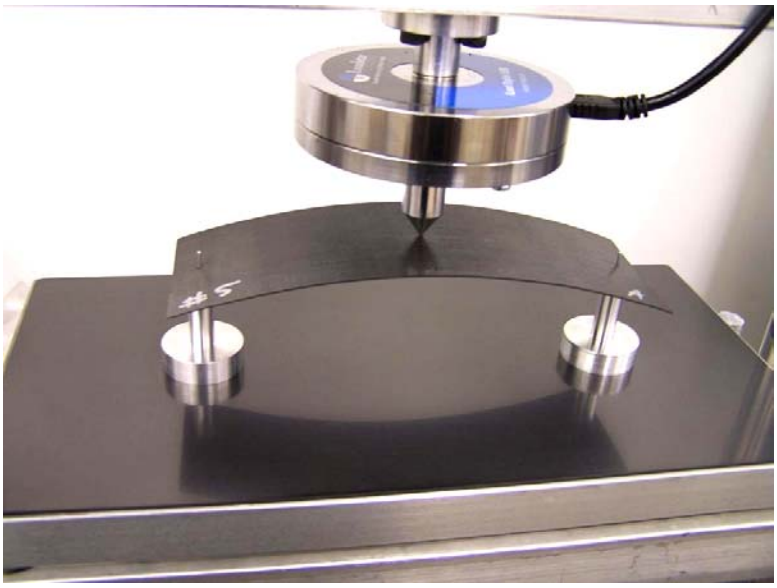

Figure 3-12. Specimen attachment (top view)

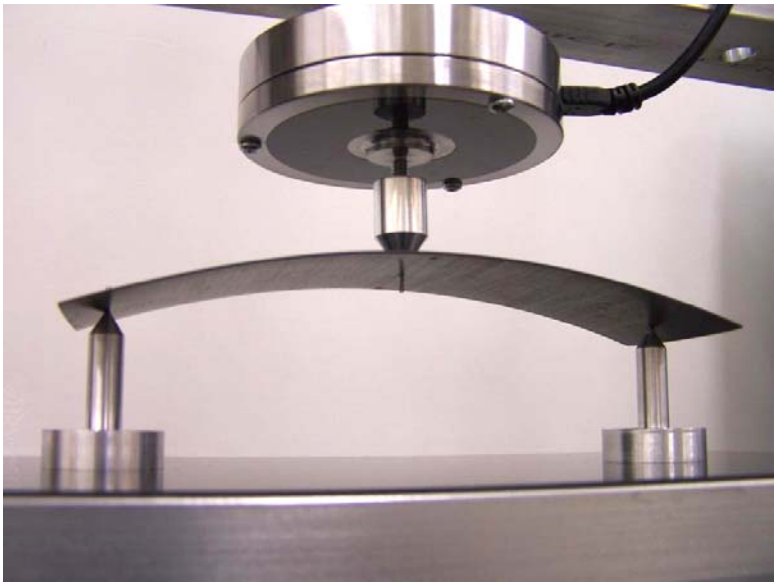

Figure 3-13. Specimen attachment (bottom view)

Specimens manufacturing

All specimens are manufactured from Hexcel IM7/8551-7 Graphite/Epoxy prepreg with unsymmetric $[0_2/90_2]_T$ stacking sequence. The length of any specimen is limited to a maximum value of 150 mm. Specimens are manufactured in a flat mold of

size 450 mm by 350 mm. A number of restrictions on the manufacturing were posed by the mold size and the available Graphite/Epoxy Prepreg material.

Detailed manufacturing practices

- Four plies of predetermined size are cut from the composite prepreg, two at zero orientation and another two at ninty degrees orientation. The total nominal thickness of a 4-plies laminate is 555 μm.
- The desired unsymmetric stacking sequence is attained using manual layup technique. An area heater was used during layup to increase the stickiness (tack) of the composite prepreg, as shown Figure 3-14.
- Once the laminate stacking is finalized, the shape of the selected set of specimens is drawn on the flat laminate using permanent ink marker. This step is performed in a pre-curing stage to guarantee more accurate measurement of shape while the laminate is still flat. All the specimens associated with certain geometry are cut from the same panel. This ensured that any deviation or bias due to stacking sequence can be isolated in the results. An example of a triangular set of specimens is shown in Figure 3-14.
- The laminate is laid in the mold, the mold is closed and the breather cloth and vacuum bag are prepared
- The laminate is then cured in the composites laboratory horizontal autoclave which has a workspace of size 0.5 m × 0.75 m and is manufactured and maintained by the American Autoclave Co.
- The curing cycle recommended by the prepreg manufacturer is applied. The cure cycle for Hexcel IM7/8551-7 Graphite/Epoxy prepreg, shown earlier in Figure 2-2, is repeated in Figure 3-15 for convenience.
- As the cured laminate is removed from the mold it had a curved shape with two cylindrical shapes. The specimen's dimensions drawn earlier on the panel are

verified.

- All straight edges specimens are cut from their respective panels using a diamond cutter. Specimens' edges were finished using sandpaper for better straightness. On the other hand, all the round edge specimens are cut from their respective panels using a computerized waterjet machine.
- A paper stamp with the identical size of each specimen with marked holes' location is attached to the specimen surface, as shown in Figure 3-16. Holes locations were predetermined according to the selected finite element mesh. Holes were then drilled using a 3/64" drill bit to allow clearance fit with the load cell pin and the pucks' pins.

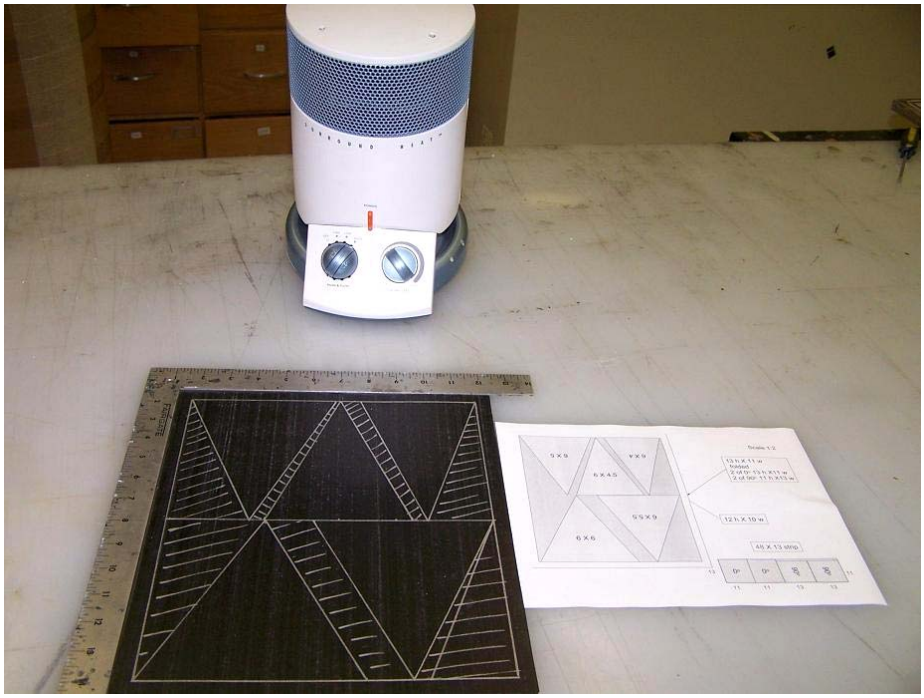

Figure 3-14. Manual layup of the composite prepreg and area heater

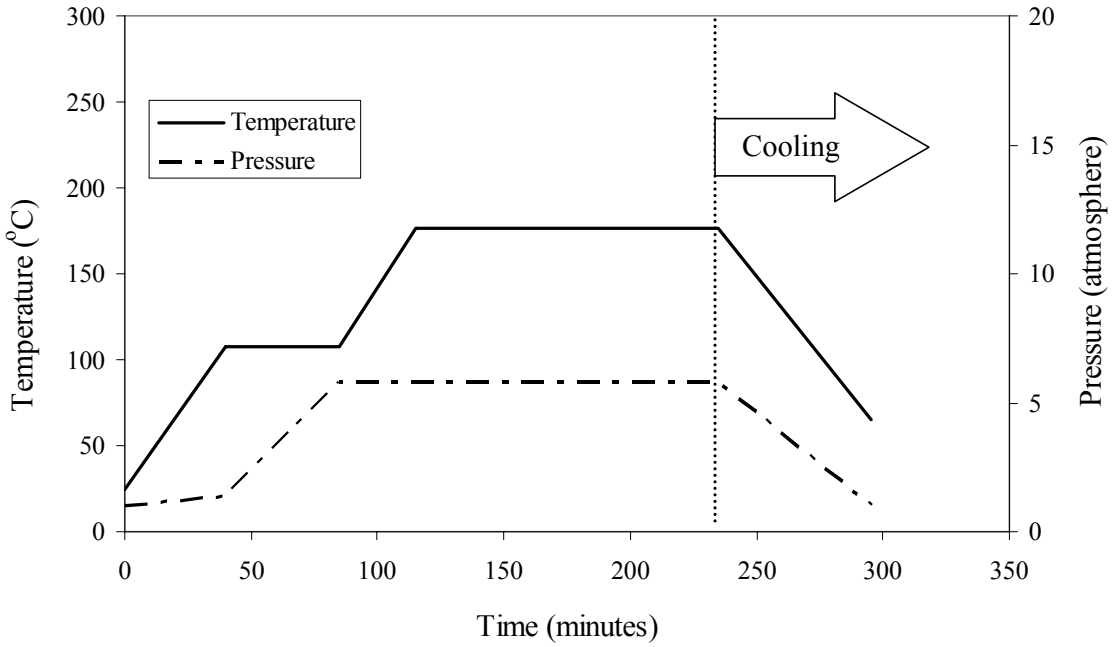

Figure 3-15. Cure cycle of Hexcel IM7/8551-7 Graphite/Epoxy prepreg

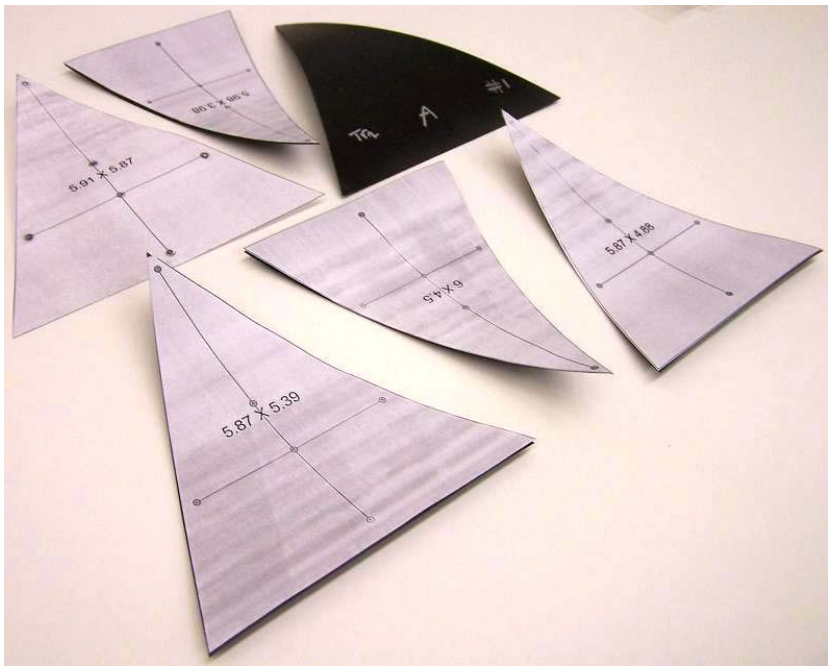

Figure 3-16. Drilling holes in triangular specimens

3.3 Experimental Measurements and Analytical Predictions

To investigate the influence of geometry on the stability characteristics a number of specimens with various geometries were tested. Manufactured specimens belong to two categories, namely straight edges and round edges geometry. Each category is subdivided into a number of common geometric groups. Within each group one dimension is held constant and the other is varied.

The following notation is used to document the test/analysis results.

- *First equilibrium shape*: Specimen's shape characterized by being mainly curved in a direction associated with the *x*-axis.
- *Second equilibrium shape*: Specimen's shape characterized by being mainly curved in a direction associated with the *y*-axis.
- *Snap-through*: Forcing a specimen to snap from the "first equilibrium shape" to the "second equilibrium shape".
- *Snap-back*: Forcing a specimen to snap from the "second equilibrium shape" to the "first equilibrium shape".

During the experiment each specimen was forced to snap-through and snap-back three times in order to assess the repeatability of the test. The mathematical mean is reported together with the standard deviation for the three readings.

According to the sensitivity study of scale factors used for geometric imperfection, Chapter 2, one hundredth of the thickness provides good correlation with observations. Meanwhile, manual manufacturing and preparation of the specimens used for the current study results in larger deviation, i.e. imperfections, in terms of specimens' dimensions.

Therefore, the scale factors of imperfections used to obtain the analytical predictions are within tenth the thickness throughout.

Geometries with straight edges

Geometries belonging to the straight edge category are divided into seven geometric groups. The six geometric groups are Square, Rectangular, Trapezoidal A and B and Triangular A and B as shown in Figure 3-17.

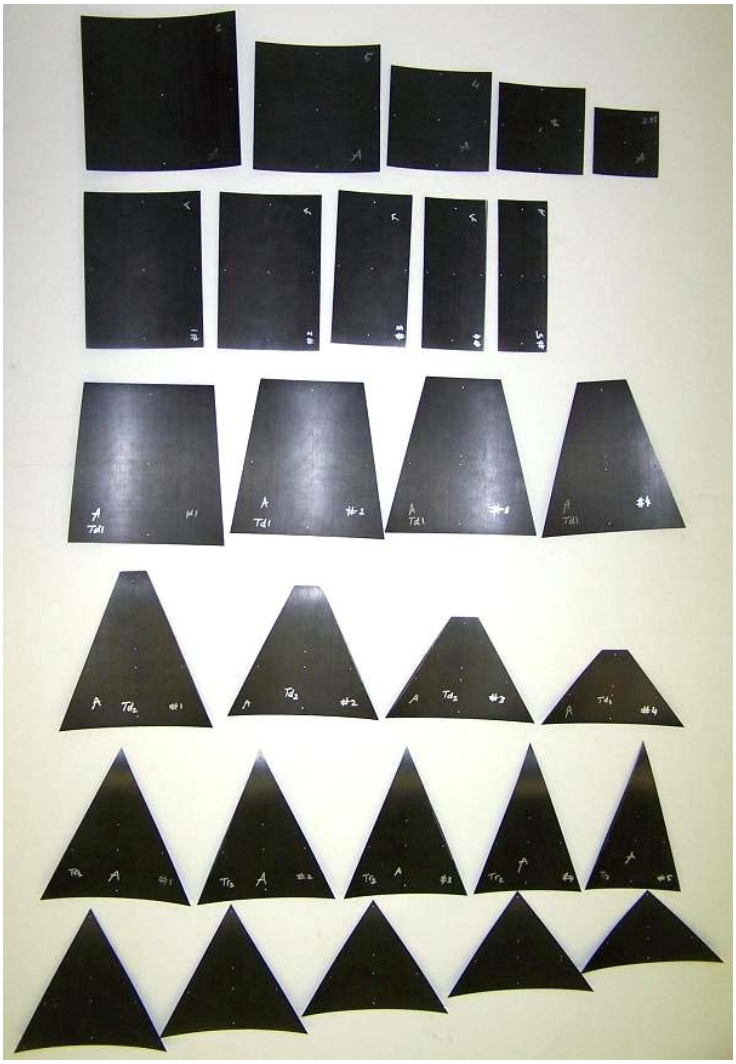

Figure 3-17. Straight edges category

Square specimens

Within this group the sidelength of the square is varied from 150 to 67 mm. Figure 3-18 shows the set of specimens in the Square group and Table 3-1 provides the dimensions of each specimen. The snap-through and snap-back load determined from the experiment are provided in Table 3-2. As all specimens are doubly symmetric the loads are applied at their center point to cause them to snap-through or snap-back.

Figure 3-18. Square specimens

Table 3-1 Geometry of square specimens

Specimen	*a* (mm)	*b* (mm)	Remarks
1	151	150	
2	123	125.5	
3	100	101	
4	87	88	misaligned holes
5	67	67	holes axis not orthogonal

Table 3-2 Experimental snap-through and snap-back loads of square specimens

Specimen	Snap-through		Snap-back	
	P (N)	Standard deviation	P (N)	Standard deviation
1	9.61*	0.06	10.39	0.06
2	8.90*	0.04	10.06	0.05
3	8.09	0.04	8.27	0.04
4	5.11	0.13	6.12	0.12
5	2.75	0.02	4.45	0.04

* Local instability

Both snap-through and snap-back load are decreasing as the sidelength decreases. This trend was predicted in Chapter 2. Standard deviation in all test data reflects adequate repeatability. The specimens marked with a star experienced a local buckling around the load application point before undergoing a complete snap-through.

A mesh of 20×20 shell S4R elements is used to model each specimen. The analytical predictions of the snap-through and snap-back are obtained by applying the boundary conditions described in Figure 3-19. A sample of the equilibrium shapes of the manufactured panels are included in Figure 3-20 together with the ones predicted from the analysis.

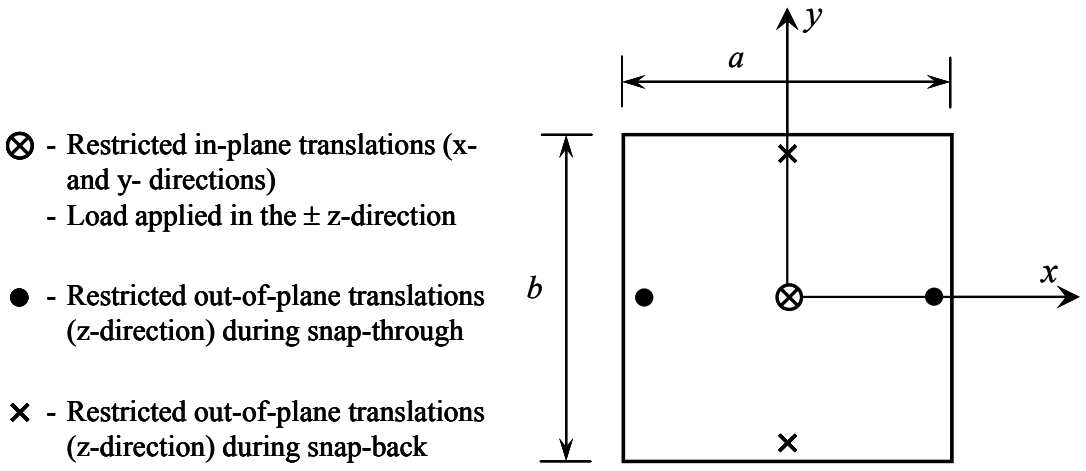

Figure 3-19. Boundary conditions of a square specimen

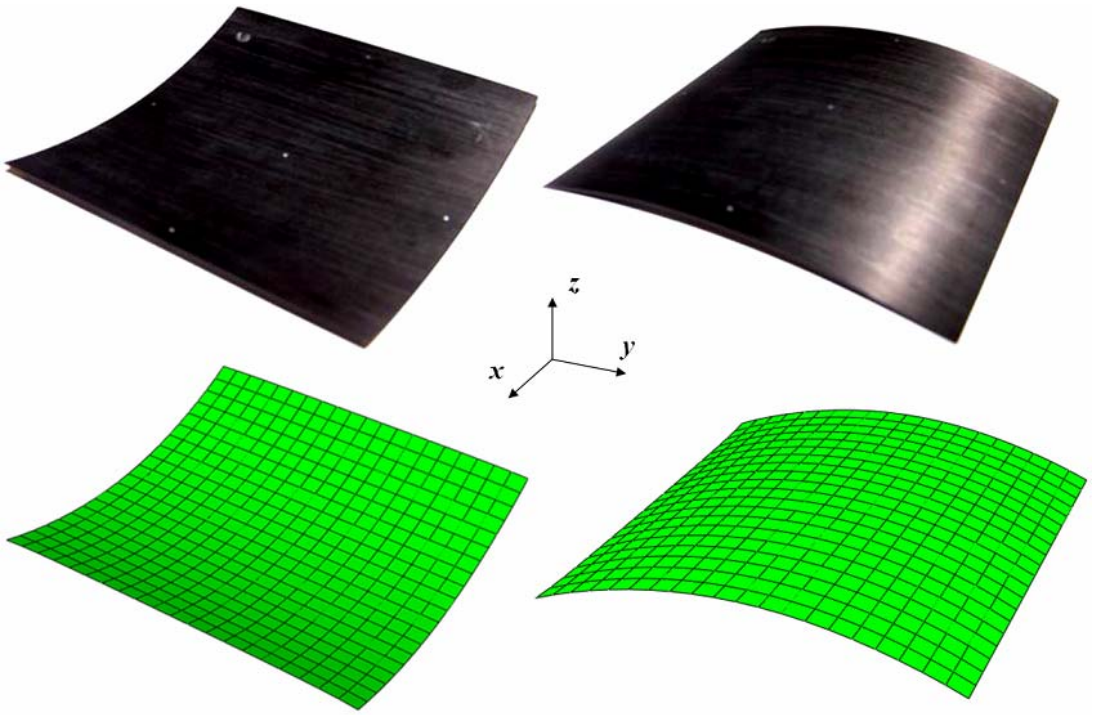

Figure 3-20. Equilibrium shapes of a square specimen, manufactured versus predicted

Analytical predictions of snap-through and snap-back load of square panels are provided in Table 3-3 together with the percentage difference compared to the test results. The curvatures along the x-and y-directions of the panels in each equilibrium configuration are provided in Table 3-4.

Table 3-3 FE snap-through and snap-back loads of square specimens

Specimen	Snap-through		Snap-back	
	P (N)	% Difference	P (N)	% Difference
1	8.72	-9.29	9.42	-9.36
2	8.15	-8.46	9.25	-8.02
3	7.54	-6.76	7.75	-6.35
4	4.93	-3.46	5.37	-12.27
5	2.70	-1.81	2.97	-33.26

As indicated in the remarks of Table 3-1, errors associated with specimens #4 and #5 have incorrect holes location, whether misaligned or non-orthogonal set of holes. These errors have a significant effect on their predicted stability characteristics. Numerical predictions were not able to capture the effect of displaced loads of these specimens. Numerical predictions follow the decreasing trend of load required for snap-through and snap-back with decrease in the sidelength.

Table 3-4 FE predicted curvatures of equilibrium shapes of square specimens

Specimen	First equilibrium shape		Second equilibrium shape	
	κ_x (m^{-1})	κ_y (m^{-1})	κ_x (m^{-1})	κ_y (m^{-1})
1	5.989	-0.024	0.020	-5.967
2	5.981	-0.021	0.020	-5.950
3	5.977	-0.019	0.023	-5.940
4	5.966	-0.060	0.068	-5.918
5	5.823	-0.266	0.301	-5.649

The predicted curvatures provided in Table 3-4 follow an expected trend migrating from cylindrical-like shape to a saddle-like shape as the sidelength decrease. These results are consistent with the results provided in Chapter 2.

The values of snap-through and snap-back loads obtained from the experiment and FE analysis are provided in Figures 3-21 and 3-22 respectively.

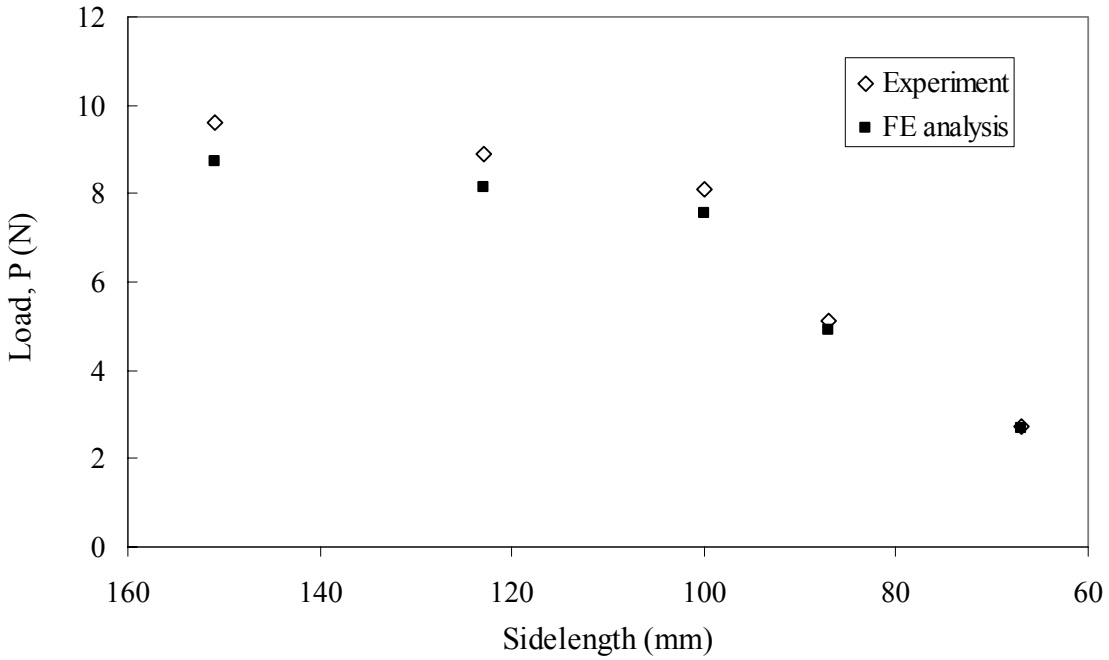

Figure 3-21. Snap-through load of square specimens, Experiment vs. FE analysis

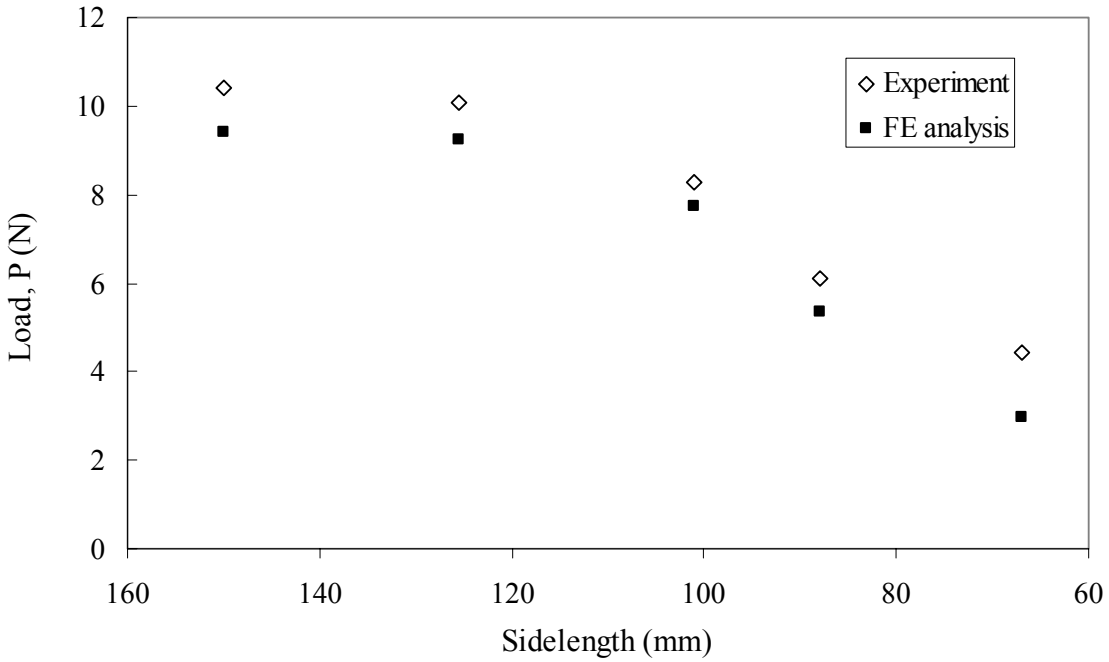

Figure 3-22. Snap-back load of square specimens, Experiment vs. FE analysis

Rectangular specimens

Within this group one sidelength is held constant at 150 mm and the other is decreased from 113 mm to 50 mm. Figure 3-23 shows the set of specimens in the rectangular group and Table 3-5 provides the dimensions of each specimen. The snap-through and snap-back load determined from the experiment are provided in Table 3-6. The loads are applied at the center point of the panel to force the specimen to snap-through or snap-back.

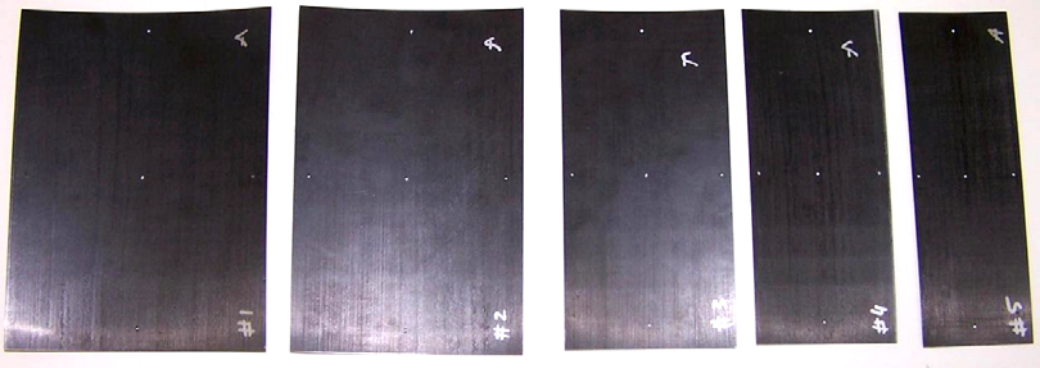

Figure 3-23- Rectangular specimens

Table 3-5 Geometry of rectangular specimens

Specimen	*a* (mm)	*b* (mm)
1	151	113
2	151	99
3	148.5	73
4	148	62
5	150	50

Table 3-6 Experimental snap-through and snap-back loads of rectangular specimens

Specimen	Snap-through		Snap-back	
	P (N)	Standard deviation	P (N)	Standard deviation
1	6.11*	0.08	13.54	0.04
2	5.46*	0.05	15.71	0.06
3	3.78*	0.06	9.14	0.08
4	2.72*	0.21	8.51	0.11
5	2.13	0.17	2.48	0.12

* Local instability

Standard deviation in the results is within the acceptable range of a repeatable experiment. The snap-through load decreases as the width, *b* decreases. Whereas the snap-back load increase at first from specimen #1 to #2 then decreases rapidly. The same phenomenon was recorded by Tawfik *et al.* [50, 52] and will be hereafter termed the "transverse-side stiffening effect".

A mesh of 20×20 shell S4R elements is used to model each specimen. The analytical predictions of the snap-through and snap-back are obtained by applying the boundary conditions described in Figure 3-24. A sample of the equilibrium shapes of the manufactured panels are included in Figure 3-25 together with the ones predicted from the analysis.

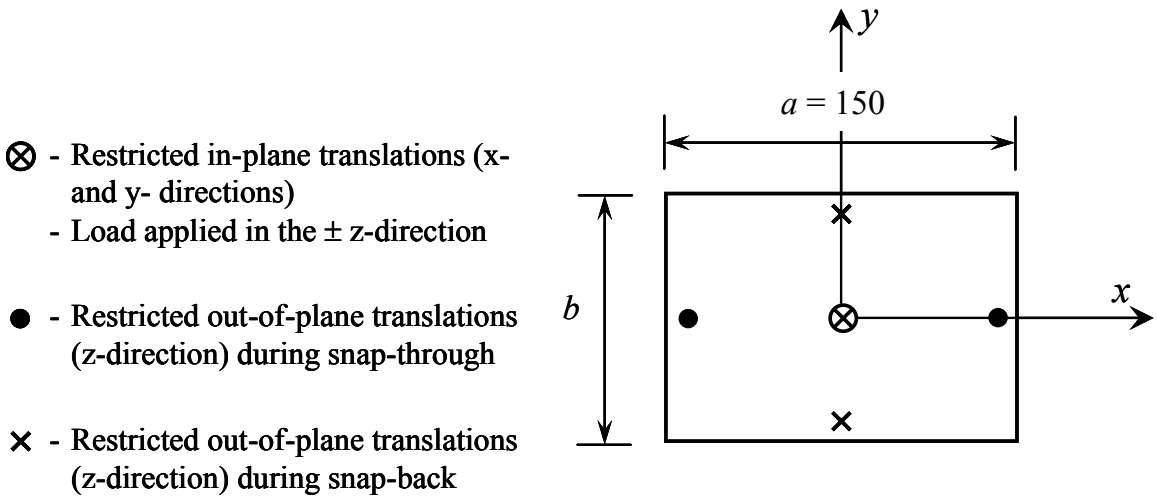

Figure 3-24. Boundary conditions of a rectangular specimen

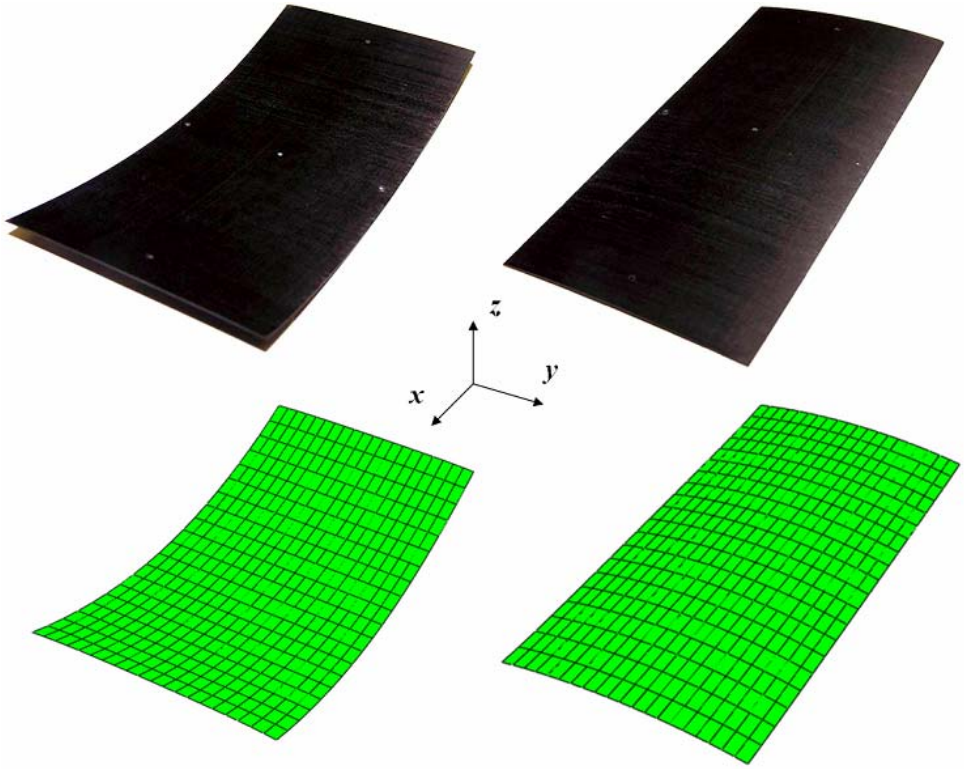

Figure 3-25. Equilibrium shapes of a rectangular specimen, manufactured versus predicted

Analytical predictions of snap-through and snap-back load of rectangular specimens are provided in Table 3-7 together with the percentage difference compared with the test data. The curvatures along the x-and y-directions of the panels in each equilibrium configuration are provided in Table 3-8.

Table 3-7 FE snap-through and snap-back loads of rectangular specimens

Specimen	Snap-through		Snap-back	
	P (N)	% Difference	P (N)	% Difference
1	5.87	-3.91	11.81	-12.79
2	5.21	-4.54	12.98	-17.40
3	3.61	-4.58	8.65	-5.32
4	2.67	-1.88	8.09	-4.99
5	1.95	-8.31	3.98	60.70

In the snap-through loads the percentage difference between the analytical predictions and the experiment ranges from -1.88% to -8.31%. The corresponding values in snap-back range between -12.79% and 60.7%. The percentage difference in snap-back results is significantly higher than in the case of snap-through.

Table 3-8 FE predicted curvatures of equilibrium shapes of rectangular specimens

Specimen	First equilibrium shape		Second equilibrium shape	
	κ_x (m^{-1})	κ_y (m^{-1})	κ_x (m^{-1})	κ_y (m^{-1})
1	5.909	-0.057	0.005	-6.042
2	5.882	-0.081	0.012	-6.062
3	5.806	-0.158	0.073	-6.002
4	5.752	-0.221	0.142	-5.907
5	5.674	-0.343	0.328	-5.670

In the predicted curvatures provided in Table 3-8, it can be noticed that the curvature in the x-direction decreases in the first equilibrium shape and increases in the second equilibrium shape as the specimen width is decreased. Similar trends can be noticed in the y-direction curvature. The effect of changing one dimension of the panel is equivalent to the results of square panels. Decreasing the width, *b*, of the manufactured panel to a value less that 50 mm results in eliminating its second equilibrium shape. The analytically predicted critical width is 46 mm.

The values of snap-through and snap-back loads obtained from the experiment and FE analysis are provided in Figures 3-26 and 3-27, respectively. Predictions from FE analysis are in agreement with the experimentally obtained values.

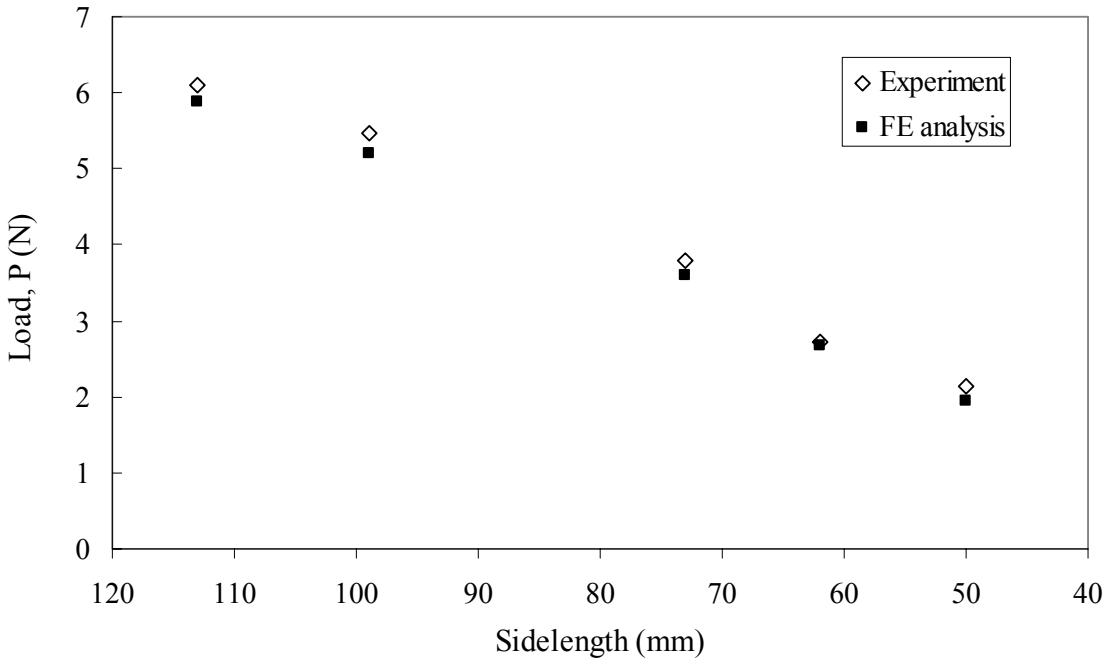

Figure 3-26. Snap-through load of rectangular specimens, Experiment vs. FE analysis

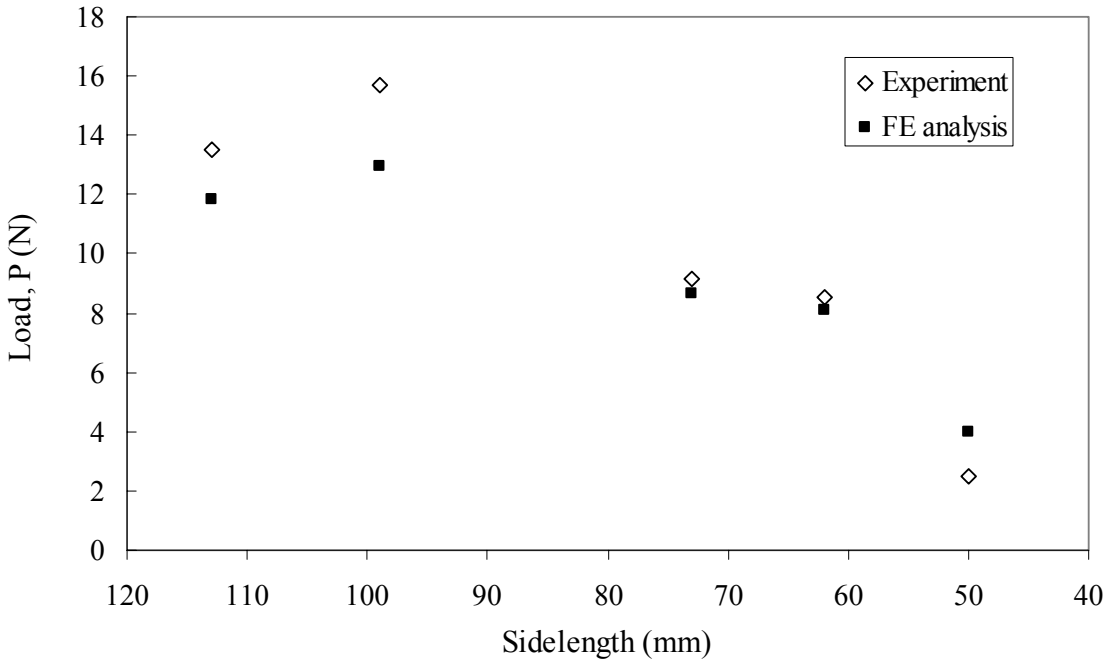

Figure 3-27. Snap-back load of rectangular specimens, Experiment vs. FE analysis

Trapezoidal-A specimens

Within this group the lower side and the height of the trapezoid is held constant at 150 mm and the top side is decreased from 125 mm to 50 mm. Figure 3-28 shows the set of specimens in the trapezoidal-A group and Table 3-9 provides the dimensions of each specimen. The snap-through and snap-back load determined from the experiment are provided in Table 3-10. As the trapezoid is not a doubly symmetric shape its center point is not always the optimum selection for load application. Therefore for snap-through the load is applied at the center point while for the snap-back the load is applied at the center of gravity to prevent the specimen from tilting.

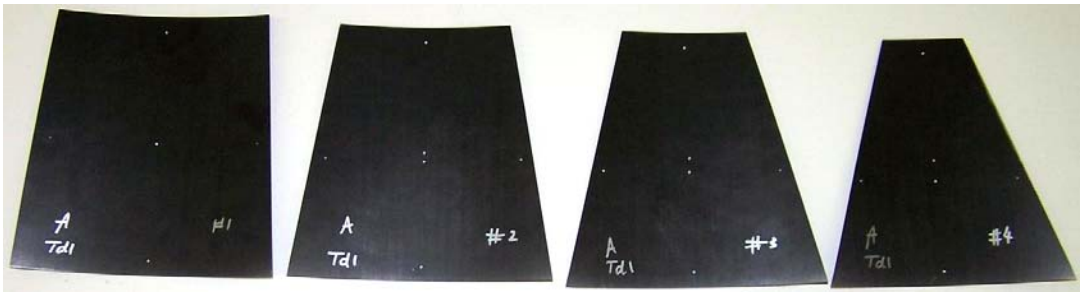

Figure 3-28. Trapezoidal-A specimens

Table 3-9 Dimensions of trapezoidal-A specimens

Specimen	*h* (mm)	*a* (mm)	*b* (mm)	Remarks
1	152	125	152	holes misaligned in y-direction
2	149	100	150	
3	151	74	150	
4	149	50	150	

Table 3-10 Experimental snap-through and snap-back loads of trapezoidal-A specimens

Specimen	Snap-through		Snap-back	
	P (N)	Standard deviation	P (N)	Standard deviation
1	9.11*	0.04	12.63	0.91
2	7.89*	0.03	12.19	0.02
3	6.90	0.04	11.23	0.22
4	5.97	0.01	7.30*	0.11

* Local instability

From the results in Table 3-10 it can be noticed that changing the size of the top side of trapezoidal-A specimens lead to a "transverse-side stiffening effect" similar to that caused by decreasing the width of a rectangular panel.

A mesh of 20×20 shell S4R elements is used to model each specimen. The analytical predictions of the snap-through and snap-back are obtained by applying the boundary conditions described in Figure 3-29. As can be seen in Figure 3-29 for snap-through case the load is applied at the center point of the specimen, while in the case of snap-back the load is applied at the center of gravity to exactly replicate the experiment. A sample of the equilibrium shapes of a manufactured panel is included in Figure 3-30 together with the ones predicted from the analysis.

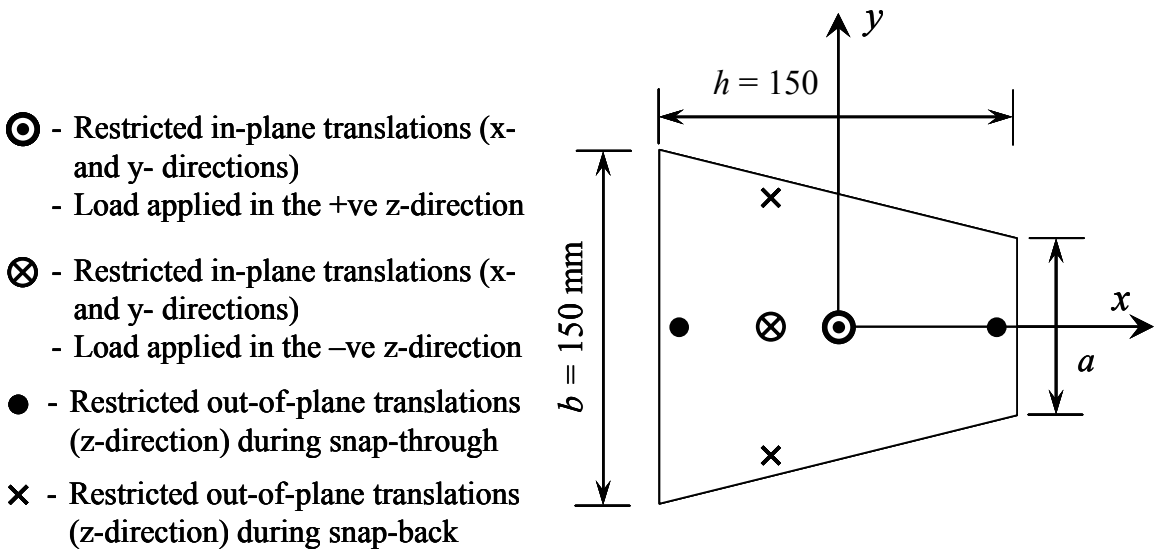

Figure 3-29. Boundary conditions of a trapezoidal-A specimen

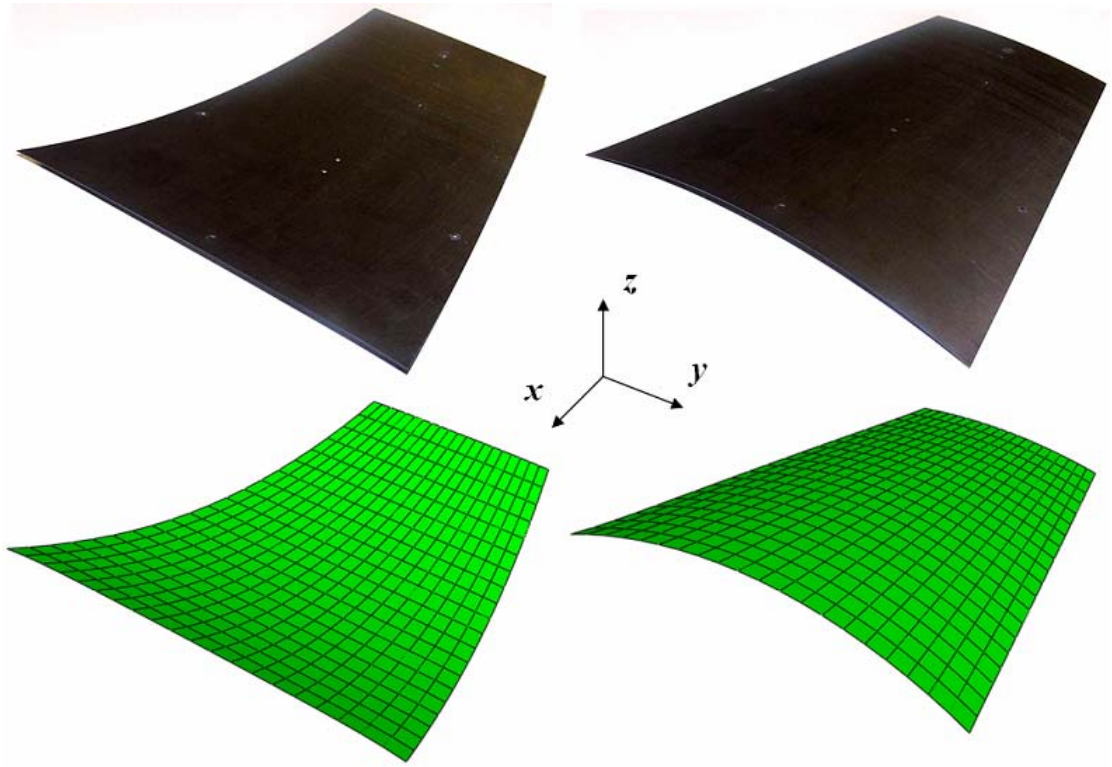

Figure 3-30. Equilibrium shapes of a trapezoidal-A specimen, manufactured versus predicted

Analytical predictions of snap-through and snap-back load of trapezoidal-A specimens are provided in Table 3-11 together with the percentage difference compared to the test data. The curvatures along the x-and y-directions of the panels in each equilibrium configuration are provided in Table 3-12.

Table 3-11 FE snap-through and snap-back loads of trapezoidal-A specimens

Specimen	Snap-through		Snap-back	
	P (N)	% Difference	P (N)	% Difference
1	8.49	-6.88	11.12	-11.95
2	7.38	-6.42	10.78	-11.55
3	6.34	-8.23	10.38	-7.57
4	5.77	-3.35	6.88	-5.77

In the snap-through loads the percentage difference between the analytical predictions and the experiment ranges from -3.35% to -8.23%. For the case of snap-back load the percentage difference started high at -11.95% and ended at -5.77%. The percentage difference in snap-back results is slightly higher than in the case of snap-through. The "transverse-side stiffening effect" is captured by the numerical predictions.

Table 3-12 FE predicted curvatures of equilibrium shapes of trapezoidal-A specimens

Specimen	First equilibrium shape		Second equilibrium shape	
	κ_x (m^{-1})	κ_y (m^{-1})	κ_x (m^{-1})	κ_y (m^{-1})
1	5.948	-0.034	0.013	-5.999
2	5.993	-0.051	0.001	-6.032
3	5.987	-0.084	0.002	-6.088
4	6.196	-0.124	0.036	-6.111

In the predicted curvatures provided in Table 3-12, it can be noticed that the curvature of the first equilibrium shape in the x-direction increases as the top side of the specimen decreases. In the second equilibrium shape the specimen's curvature in the x-direction is decreasing till reaching a minimum then increasing again. Similar trends can be noticed in the y-direction curvature of the second equilibrium shape. Therefore, changing the size of the top side of the panel does not have an effect identical to changing the width of a rectangular panel.

The values of snap-through and snap-back loads obtained from the experiment and FE analysis are provided in Figures 3-31 and 3-32, respectively. Predictions from FE analysis are in agreement with the experimental values.

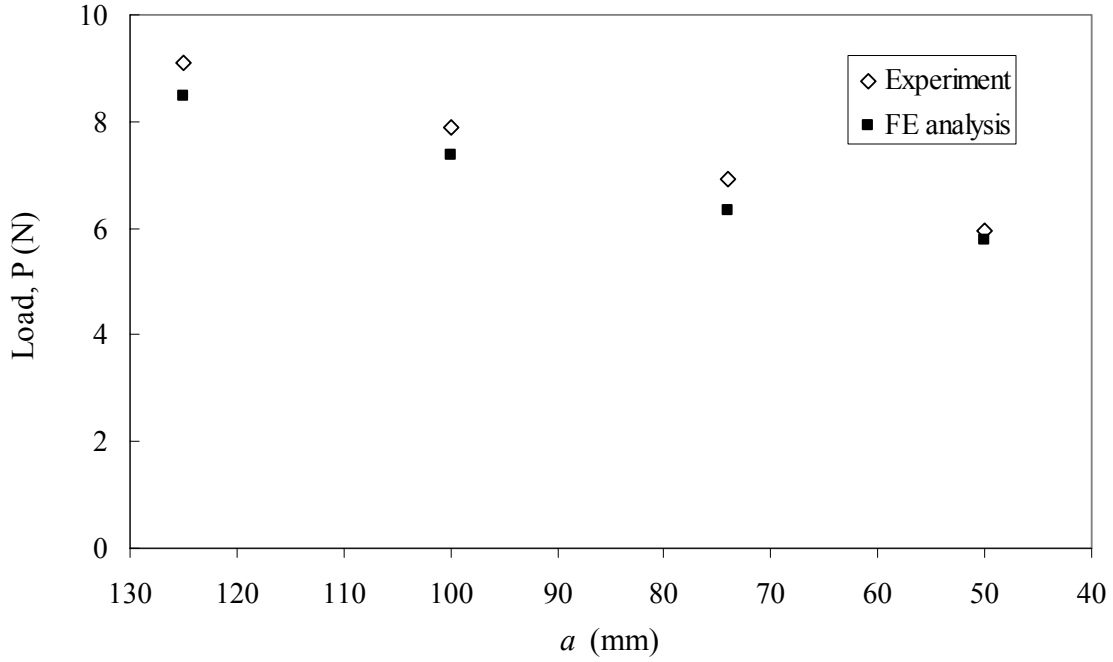

Figure 3-31. Snap-through load of trapezoidal-A specimens, Experiment vs. FE analysis

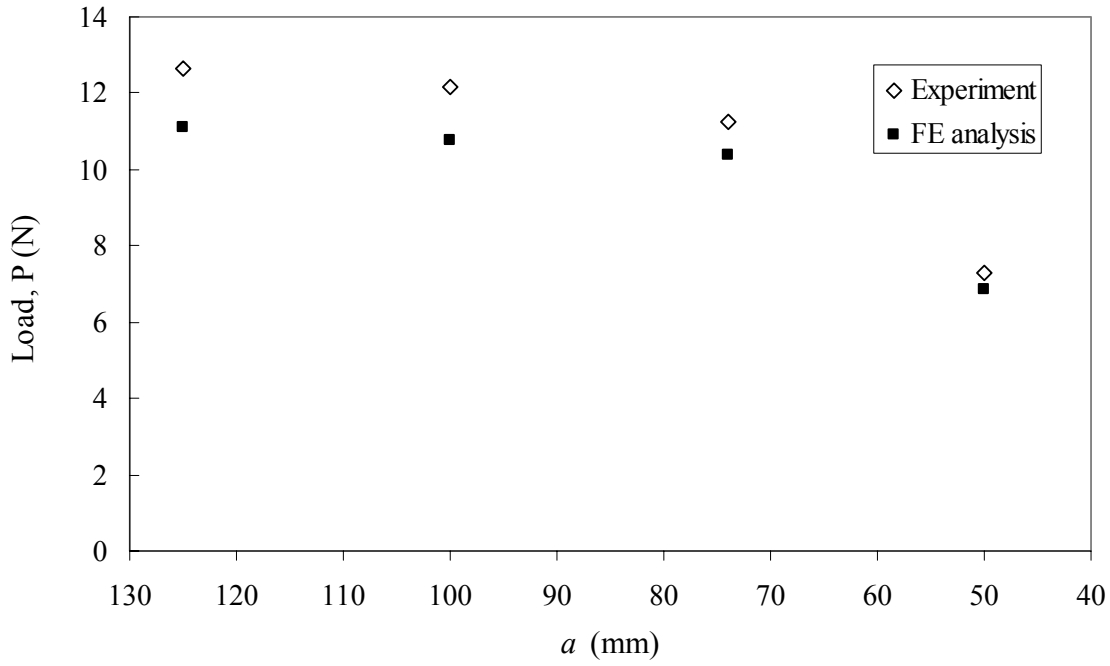

Figure 3-32. Snap-back load of trapezoidal-A specimens, Experiment vs. FE analysis

Trapezoidal-B specimens

Within this group the lower side is held constant at 150 mm, the top side is held constant at 25 mm and the height is decreased from 150 mm to 74 mm. Figure 3-33 shows the set of specimens in the trapezoidal-B group and Table 3-13 provides the dimensions of each specimen. The snap-through and snap-back load determined from the experiment are provided in Table 3-14. Similar to trapezoidal-A specimens the snap-through load is applied at the center point while for the snap-back the load is applied at the center of gravity to prevent the specimen from tilting.

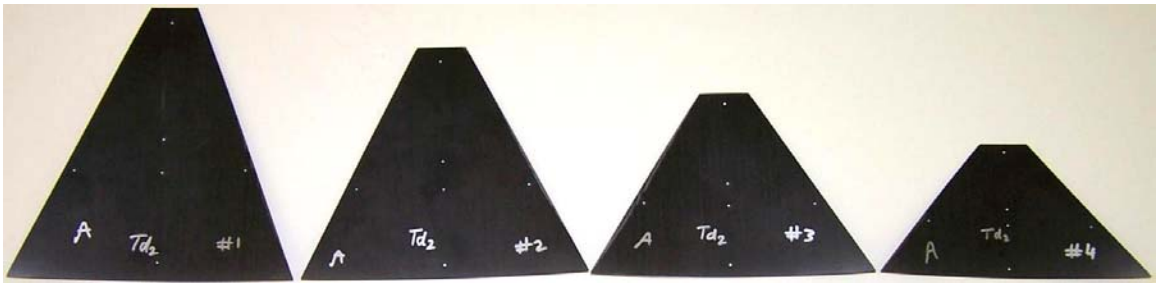

Figure 3-33. Trapezoidal-B specimens

Table 3-13 Dimensions of trapezoidal-B specimens

Specimen	*h* (mm)	*a* (mm)	*b* (mm)
1	150	25	150
2	126	26	149
3	100	26	150
4	74	26	149

Table 3-14 Experimental snap-through and snap-back loads of trapezoidal-B specimens

Specimen	Snap-through		Snap-back	
	P (N)	Standard deviation	P (N)	Standard deviation
1	5.89	0.07	2.87	0.03
2	6.38	0.01	3.87	0.07
3	4.48	0.11	3.50	0.10
4	2.32	0.05	2.42	0.05

As the trapezoid height is decreased the "transverse-side stiffening effect" is reflected in both snap-through and snap-back loads. Decreasing the height does not cause a drastic increase in these loads before they start decreasing again.

A mesh of 20×20 shell S4R elements is used to model each specimen. The analytical predictions of the snap-through and snap-back are obtained by applying the boundary conditions described in Figure 3-34. Similar to the trapezoidal-A specimens the load application points used are in agreement with those used in the experiment. A sample of the equilibrium shapes of a manufactured panel are included in Figure 3-35 together with the ones predicted from the analysis.

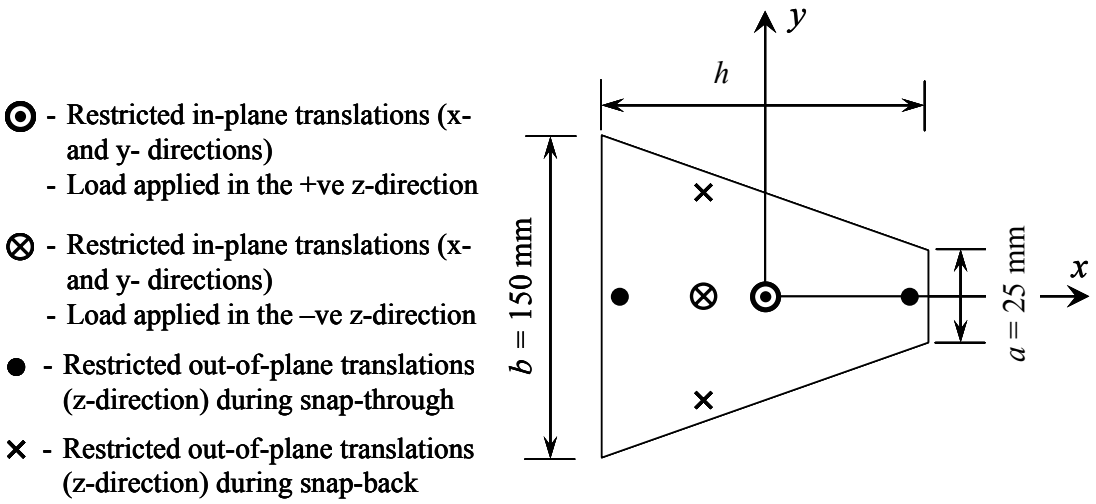

Figure 3-34. Boundary conditions of a trapezoidal-B specimen

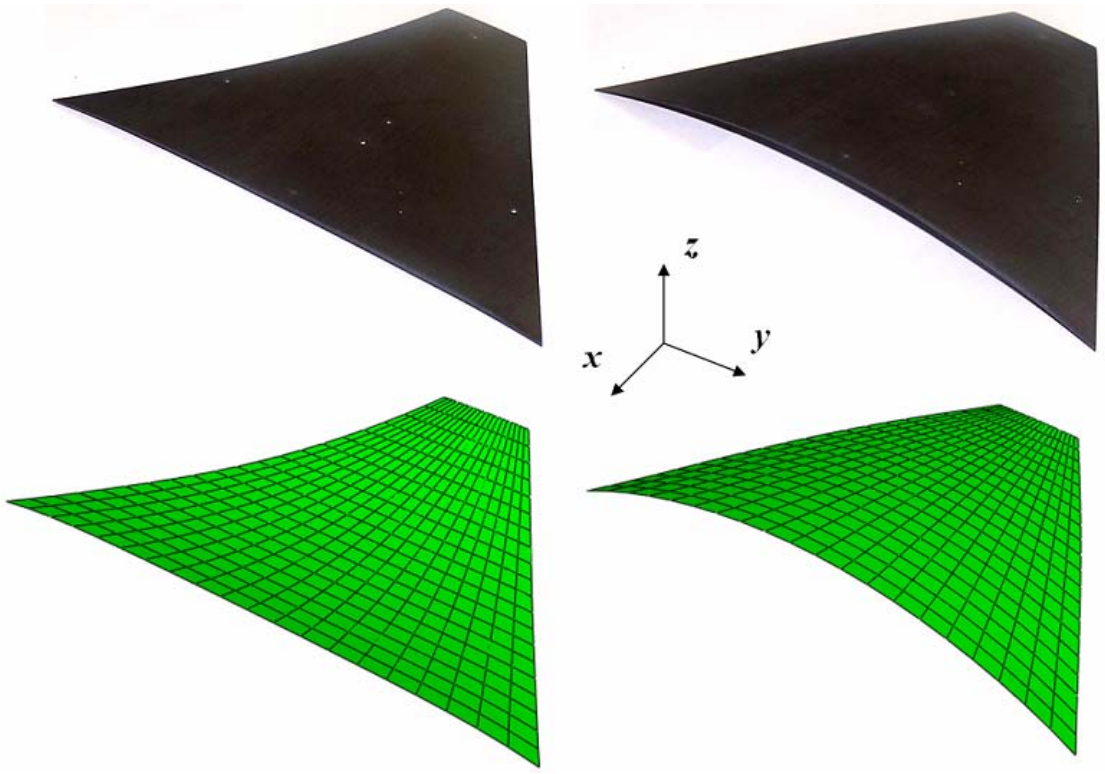

Figure 3-35. Equilibrium shapes of a trapezoidal-B specimen, manufactured versus predicted

Analytical predictions of snap-through and snap-back load of trapezoidal-B specimens are provided in Table 3-15 together with the percentage difference with compared to experiment. The curvatures along the x-and y-directions of the panels in each equilibrium configuration are provided in Table 3-16.

Table 3-15 FE snap-through and snap-back loads of trapezoidal-B specimens

Specimen	Snap-through		Snap-back	
	P (N)	% Difference	P (N)	% Difference
1	5.67	-3.77	2.77	-3.34
2	5.85	-8.29	3.70	-4.34
3	4.26	-4.96	3.28	-6.25
4	2.14	-8.02	2.17	-10.58

In the snap-through loads the percentage difference between the analytical predictions and the experiment ranges from -3.77% to -8.29%. For the case of snap-back load the percentage difference started at –3.34% reaching -10.58% as the height is decreased. The percentage difference in snap-back results is slightly higher than in the case of snap-through. The effect of changing the height predicted by the analysis is in agreement with the experiment.

Table 3-16 FE predicted curvatures of equilibrium shapes of trapezoidal-B specimens

Specimen	First equilibrium shape		Second equilibrium shape	
	κ_x (m^{-1})	κ_y (m^{-1})	κ_x (m^{-1})	κ_y (m^{-1})
1	6.209	-0.187	0.101	-6.031
2	6.286	-0.187	0.099	-6.025
3	6.393	-0.211	0.091	-5.998
4	7.144	-0.103	0.183	-5.877

It can be noticed in the predicted curvatures, provided in Table 3-16, that the x-direction curvature in the first equilibrium shape increases as the specimen height decreases. The

opposite trend is associated with the curvature in the y-direction of the second equilibrium shape. While for the y-curvature of first equilibrium shape and x-curvature of second equilibrium shape, the curvatures are slightly changing with the change in height except for specimen #4.

The values of snap-through and snap-back loads obtained from the experiment and FE analysis are provided in Figures 3-36 and 3-37 respectively. Predictions from FE analysis are in agreement with the experimental values

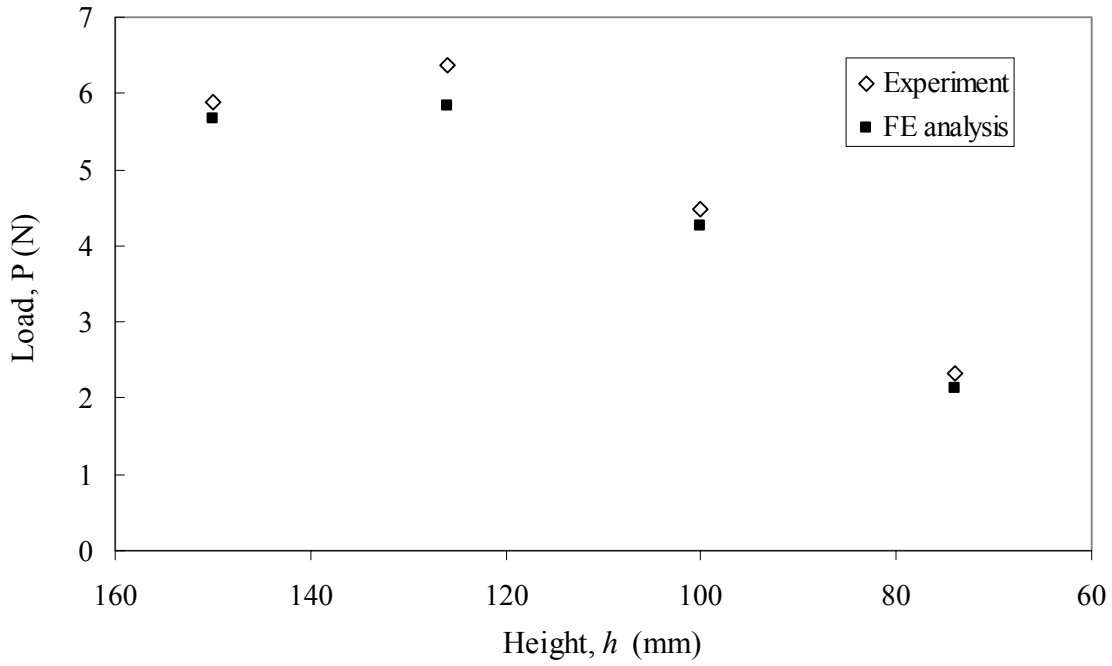

Figure 3-36. Snap-through load of trapezoidal-B specimens, Experiment vs. FE analysis

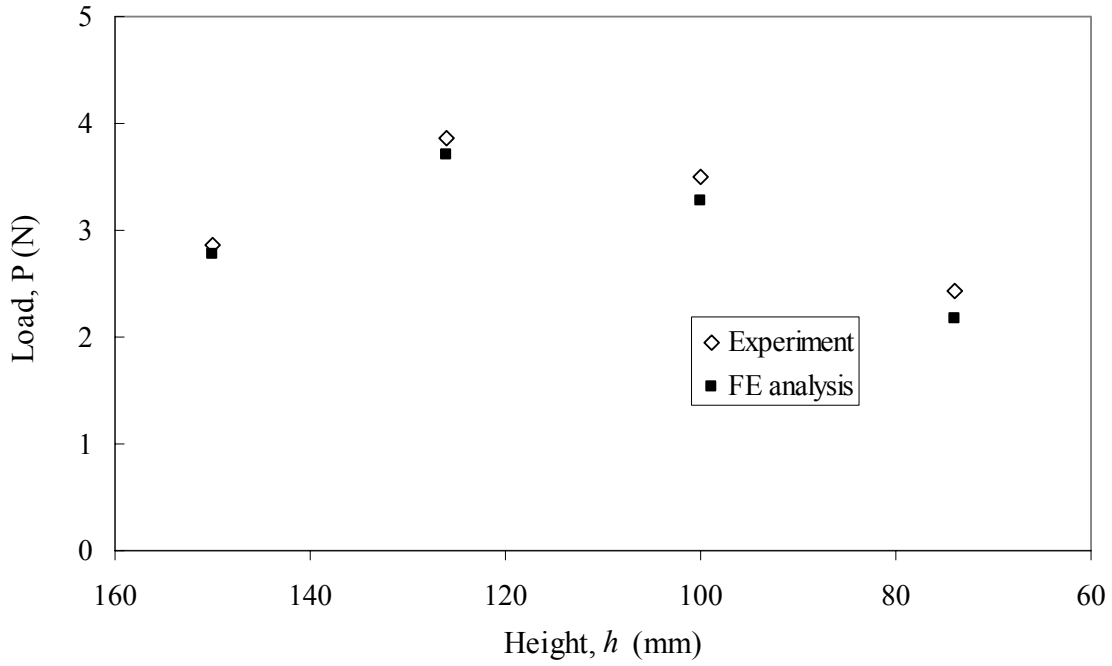

Figure 3-37. Snap-back load of trapezoidal-B specimens, Experiment vs. FE analysis

Triangular-A specimens

Within this group the height of the triangle is held constant at 150 mm and the base is decreased from 149 mm to 101 mm. Figure 3-38 shows the set of specimens in the triangular-A group and Table 3-17 provides the dimensions of each specimen. The snap-through and snap-back load determined from the experiment are provided in Table 3-18. Similar to the trapezoidal-A and –B specimens, the snap-through load is applied at the center point while for the snap-back the load is applied at the center of gravity of the triangle to prevent the specimen from tilting.

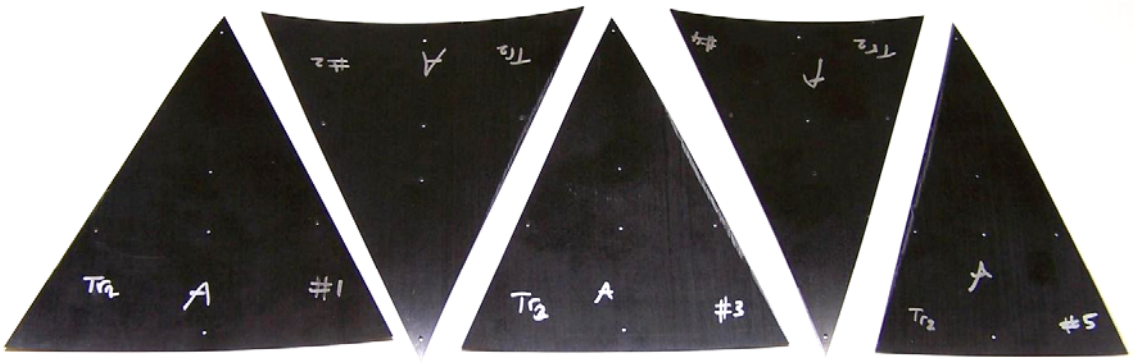

Figure 3-38. Triangular-A specimens

Table 3-17 Dimensions of triangular-A specimens

Specimen	*h* (mm)	*b* (mm)
1	150	149
2	149	137
3	149	124
4	152	110
5	152	101

Table 3-18 Experimental snap-through and snap-back loads of triangular-A specimens

Specimen	Snap-through		Snap-back	
	P (N)	Standard deviation	P (N)	Standard deviation
1	5.43	0.13	2.89	0.10
2	4.89	0.08	2.77	0.06
3	6.08	0.03	2.32	0.07
4	3.95	0.05	1.25	0.11
5	3.39	0.04	1.07	0.13

An observation can be made regarding specimen #3 requiring much higher load to snap-through than specimens of larger size #1 and #2. The test data for this specimen was verified by carrying out the experiment for six times instead of three. Except for this case, changing the base size of a triangle generally has similar effect to that of changing the sidelength of a square on the critical loads.

A mesh of 485 shell S4R and three shell S3 elements is used to model each specimen. The analytical predictions of the snap-through and snap-back are obtained by applying the boundary conditions described in Figure 3-39. Similar to the trapezoidal specimens the load application points are identical to those of the experiment. A sample of the equilibrium shapes of a manufactured panel are included in Figure 3-40 together with the ones predicted from the analysis.

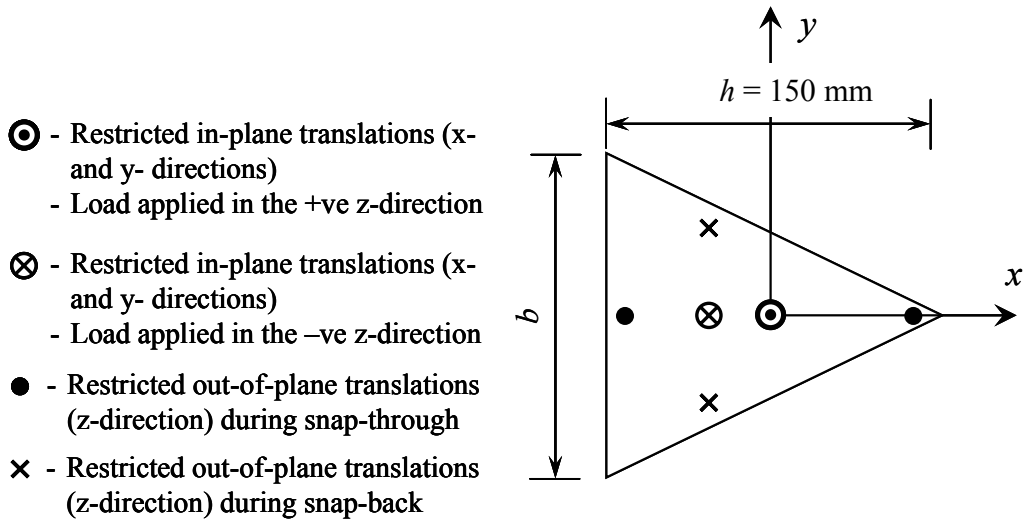

Figure 3-39. Boundary conditions of a triangular-A specimen

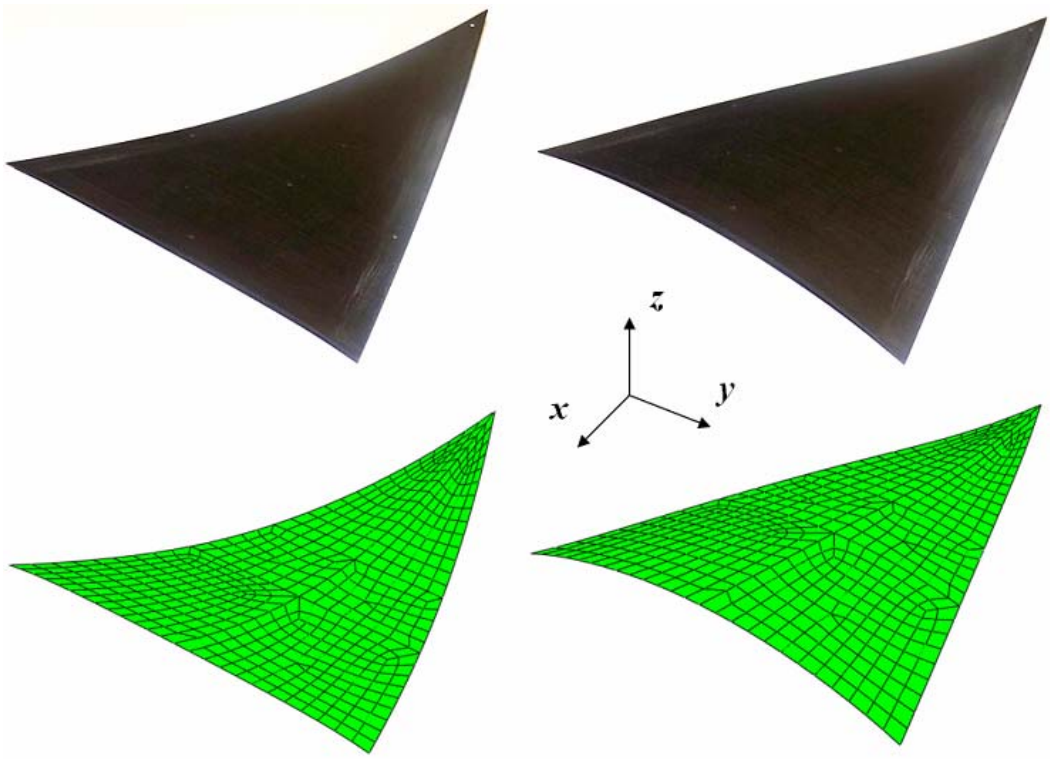

Figure 3-40. Equilibrium shapes of a triangular-A specimen, manufactured versus predicted

Analytical predictions of snap-through and snap-back load of triangular-A specimens are provided in Table 3-19 together with the percentage difference compared to the experiment. The curvatures along the x- and y-directions of the panels in each equilibrium configuration are provided in Table 3-20

Table 3-19 FE snap-through and snap-back loads of triangular-A specimens

Specimen	Snap-through		Snap-back	
	P (N)	% Difference	P (N)	% Difference
1	5.08	-6.47	2.64	-8.72
2	4.57	-6.56	2.57	-7.40
3	5.66	-6.94	2.13	-7.93
4	3.66	-7.39	1.32	5.36
5	3.14	-7.37	1.21	12.73

The percentage difference between the analytical predictions and the experiment are around the 7.0% throughout except for specimens #1 and #4 in the snap-back load. It is worth noting that the snap-through load of specimen #3 represents a peak, interrupting a consistent decrease of critical load as the base decreases. Analytical predictions capture the same trend observed in the test data.

Table 3-20 FE predicted curvatures of equilibrium shapes of triangular-A specimens

Specimen	First equilibrium shape		Second equilibrium shape	
	κ_x (m^{-1})	κ_y (m^{-1})	κ_x (m^{-1})	κ_y (m^{-1})
1	6.040	-0.143	0.524	-6.088
2	5.936	-0.159	0.666	-6.014
3	5.912	-0.185	0.817	-5.994
4	5.805	-0.224	0.976	-5.936
5	5.765	-0.234	1.126	-5.822

In the predicted curvatures provided in Table 3-20 the x-curvature of the first equilibrium shape is decreasing with the base dimension. While in the second equilibrium shape the

x-curvature is increasing. This is the regular trend of narrower specimens but the specimen is approaching a saddle shape much faster. That is the base size of the triangular-A specimen has a more pronounced effect on its stability characteristics. On the other hand decreasing the base size is of lower effect on the y-curvature.

The values of snap-through and snap-back loads obtained from the experiment and FE analysis are provided in Figures 3-41 and 3-42, respectively. It can be noticed that predictions from FE analysis are in agreement with the experimental values. The peak of critical load associated to specimen #3 is clearly identified in Figure 3-41. Numerical FE predictions are providing the same trend in the measured critical load.

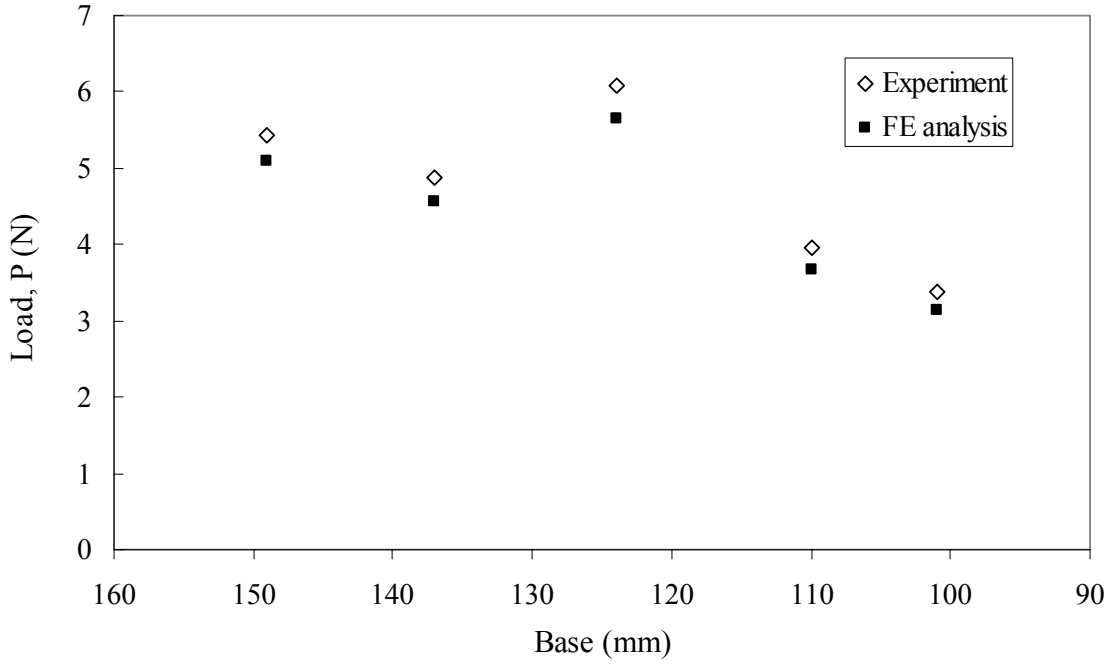

Figure 3-41. Snap-through load of triangular-A specimens, Experiment vs. FE analysis

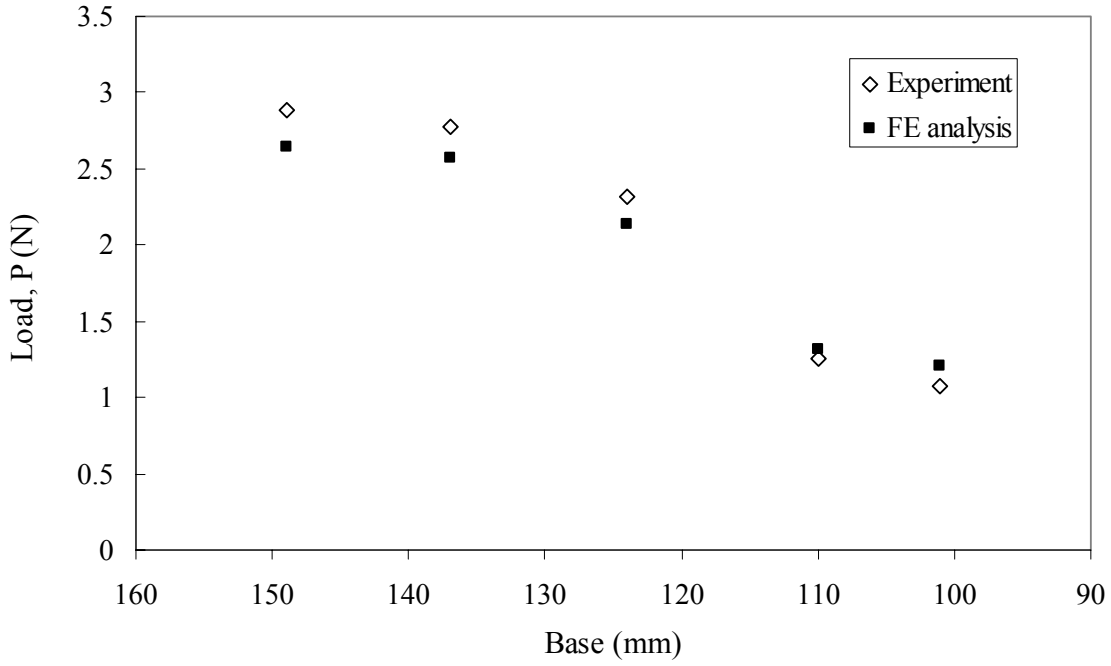

Figure 3-42. Snap-back load of triangular-A specimens, Experiment vs. FE analysis

Triangular-B specimens

Within this group the base is held constant at 150 mm and the height of the triangle is decreased from 138 mm to 75 mm. Figure 3-43 shows the set of specimens in the triangular-B group and Table 3-21 provides the dimensions of each specimen. The snap-through and snap-back load determined from the experiment are provided in Table 3-18. The snap-back load is applying at the center of gravity similar to the trapezoidal-A and –B and the triangular-A specimens to prevent the specimen from tilting.

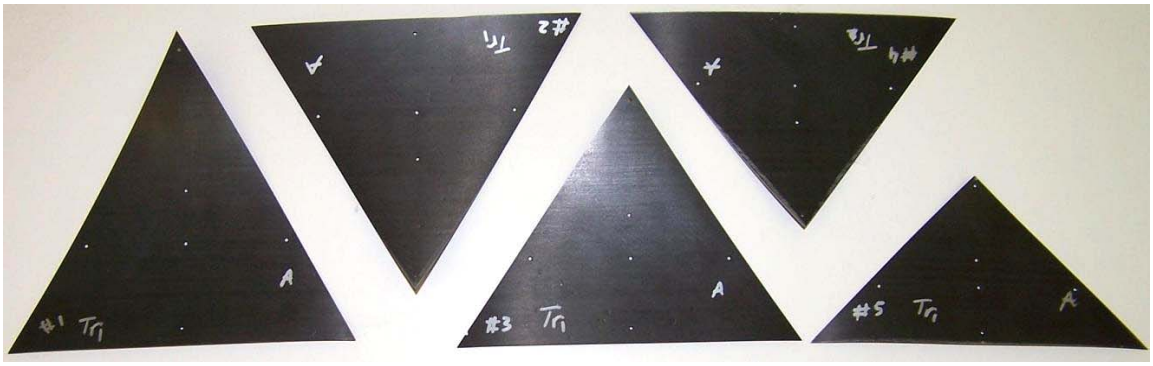

Figure 3-43. Triangular-B specimens

Table 3-21 Dimensions of triangular-B specimens

Specimen	*h* (mm)	*b* (mm)
1	138	151
2	128	148
3	112	148
4	101	150
5	75	152

Table 3-22 Experimental snap-through and snap-back loads of triangular-B specimens

Specimen	Snap-through		Snap-back	
	P (N)	Standard deviation	P (N)	Standard deviation
1	6.42	0.03	3.84	0.11
2	5.07	0.02	2.86	0.04
3	5.19	0.01	3.25	0.02
4	3.85	0.03	1.63	0.02
5	3.36	0.04	1.58	0.01

Peaks in the snap-through and snap-back loads are observed for specimen #3. Whereas changing the height of the triangle has generally similar effect on the stability characteristics as changing the sidelength of the square.

A mesh of 485 shell S4R and 3 shell S3 elements is used to model each specimen. The analytical predictions of the snap-through and snap-back are obtained by applying the boundary conditions described in Figure 3-44. Similar to all specimens with no double symmetry the load application points are selected at the center point and the center of gravity. A sample of the equilibrium shapes of a manufactured panel are included in Figure 3-45 together with the ones predicted from the analysis.

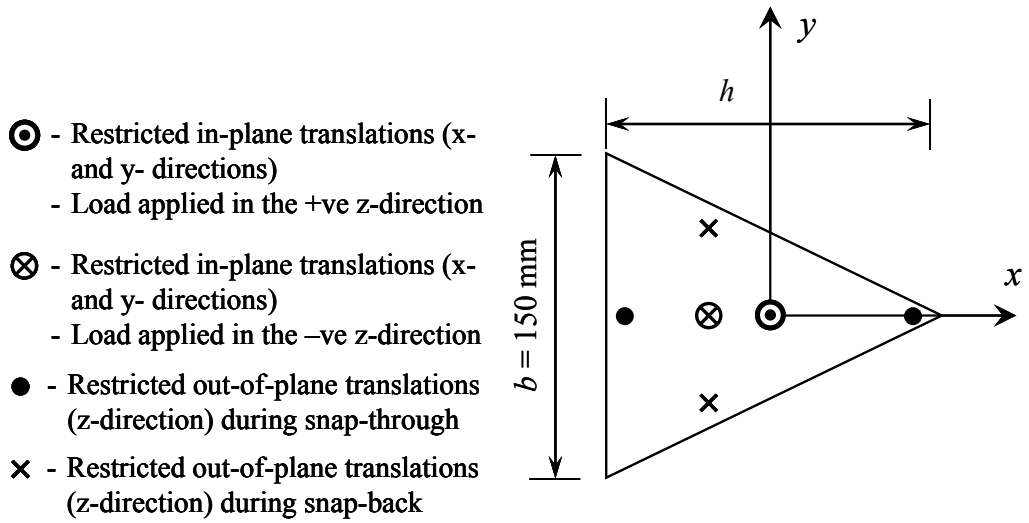

Figure 3-44. Boundary conditions of a triangular-B specimen

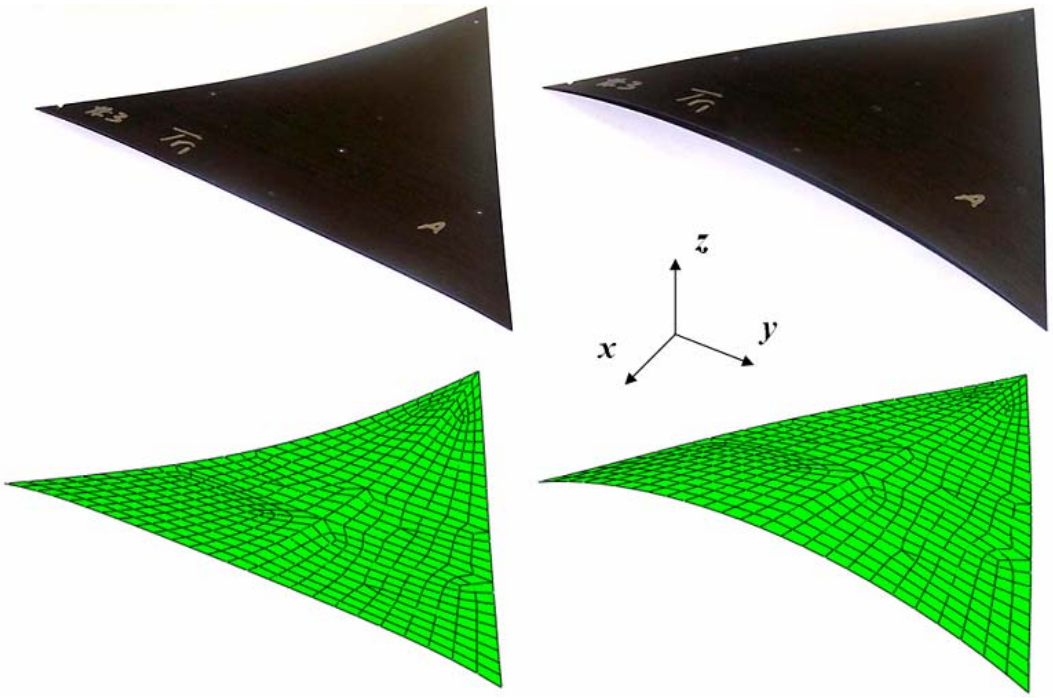

Figure 3-45. Equilibrium shapes of a triangular-B panel, manufactured versus predicted

Analytical predictions of snap-through and snap-back load of triangular-B specimens are provided in Table 3-23 together with the percentage difference compared to the experiment. The curvatures along the x- and y-directions of the panels in each equilibrium configuration are provided in Table 3-24

Table 3-23 FE snap-through and snap-back loads of triangular-B specimens

Specimen	Snap-through		Snap-back	
	P (N)	% Difference	P (N)	% Difference
1	5.93	-7.66	3.54	-7.86
2	4.77	-6.08	2.80	-2.16
3	4.86	-6.44	2.94	-9.69
4	3.84	-0.48	1.77	8.50
5	2.54	-24.35	1.71	7.97

The percentage difference between the analytical predictions and the test results ranges from -0.48% to -24.35% in the snap-through case. While the percentage differences in the case of snap-back load range from -9.69% to 8.5%. Both snap-through and Snap-back loads predicted for specimen #3 represent a peak that interrupts a continuous decrease of required load. The predictions are in agreement with test results.

Table 3-24 FE predicted curvatures of equilibrium shapes of triangular-B specimens

Specimen	First equilibrium shape		Second equilibrium shape	
	κ_x (m^{-1})	κ_y (m^{-1})	κ_x (m^{-1})	κ_y (m^{-1})
1	6.057	-0.158	0.426	-6.058
2	6.118	-0.184	0.473	-6.049
3	6.180	-0.249	0.493	-6.021
4	6.252	-0.320	0.528	-5.956
5	6.107	-0.821	0.582	-5.863

As can be noticed in the predicted curvatures, provided in Table 3-24, the x-curvature of the second equilibrium shape is increasing as the height decreases. The x-curvature in the

first equilibrium shape does not follow a certain trend. As for the y-curvatures in both equilibrium shapes they indicate that the triangles are approaching a saddle shape. This conclusion can be verified against Figure 3-45.

The values of snap-through and snap-back loads obtained from the experiment and FE analysis are provided in Figures 3-46 and 3-47, respectively. Similar observation can be made about the consistent agreement between both.

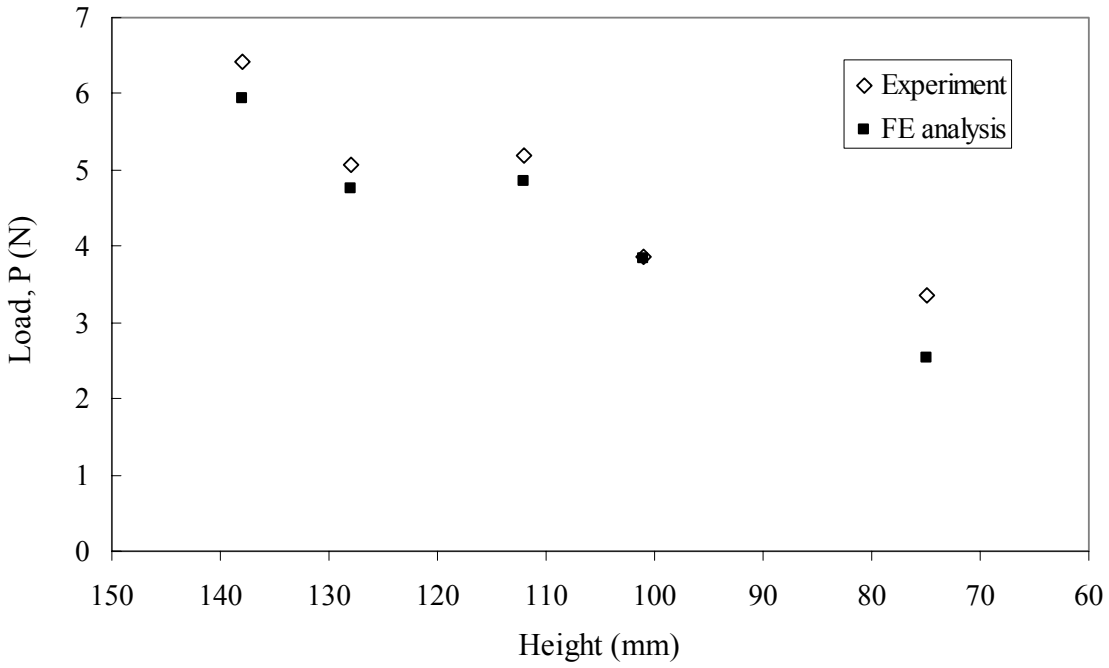

Figure 3-46. Snap-through load of triangular-B specimens, Experiment vs. FE analysis

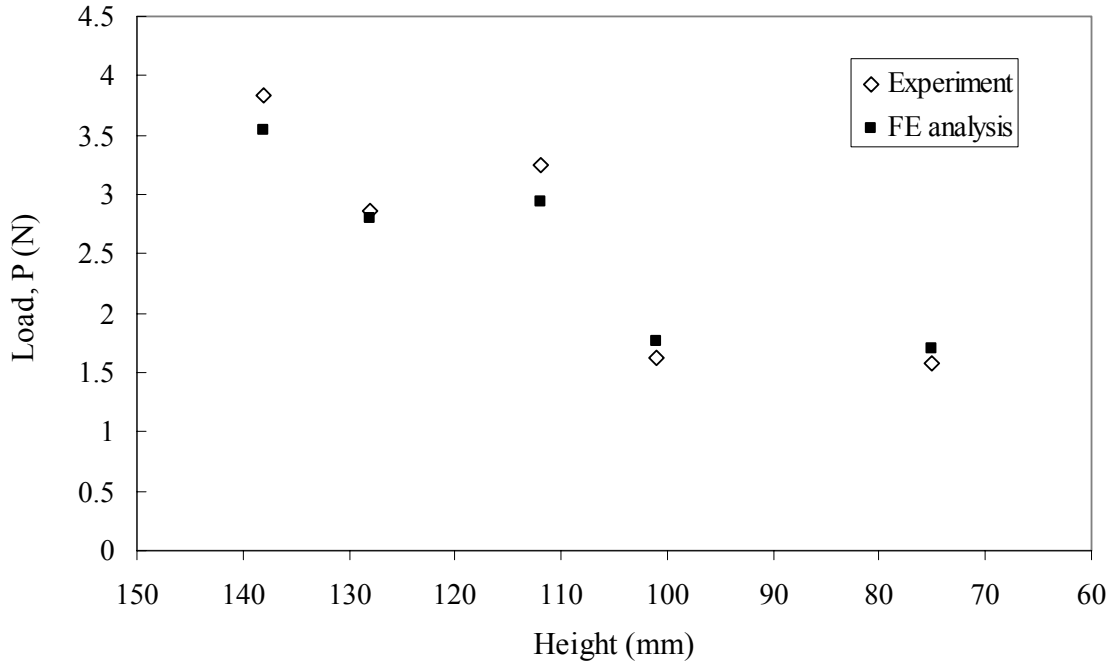

Figure 3-47. Snap-back load of triangular-B specimens, Experiment vs. FE analysis

Discussion

Non-dimensional parameters are used to study the influence of geometry on stability characteristics in the straight edges group. In this context, the effect of varying a non-dimensional length on the non-dimensional critical force values presents the influence trend. The non-dimensional critical snap-through/snap-back loads are obtained using the ones associated to the first specimen of the square group as

$$P^* = \frac{P_i}{P_{Square\#1}} \tag{3.1}$$

The nominal thickness of the panel, t = 555 μm, is used to obtain the non-dimensional length parameter as

$$L^* = \frac{L}{t} \tag{3.2}$$

for L is a characteristic length of the investigated geometry. These non-dimensional parameters will be used throughout the study of straight edge geometries.

The non-dimensional values of both force and sidelength of square specimens are obtained and provided in Figure 3-48. The averaged non-dimensional force, P^*, as a function of the sidelength, L^*, of a square can be described by a monotonically decreasing quadratic expression as illustrated in Figure 3-48. This monotonically decreasing quadratic trend will be referred to as the "shape scaling effect".

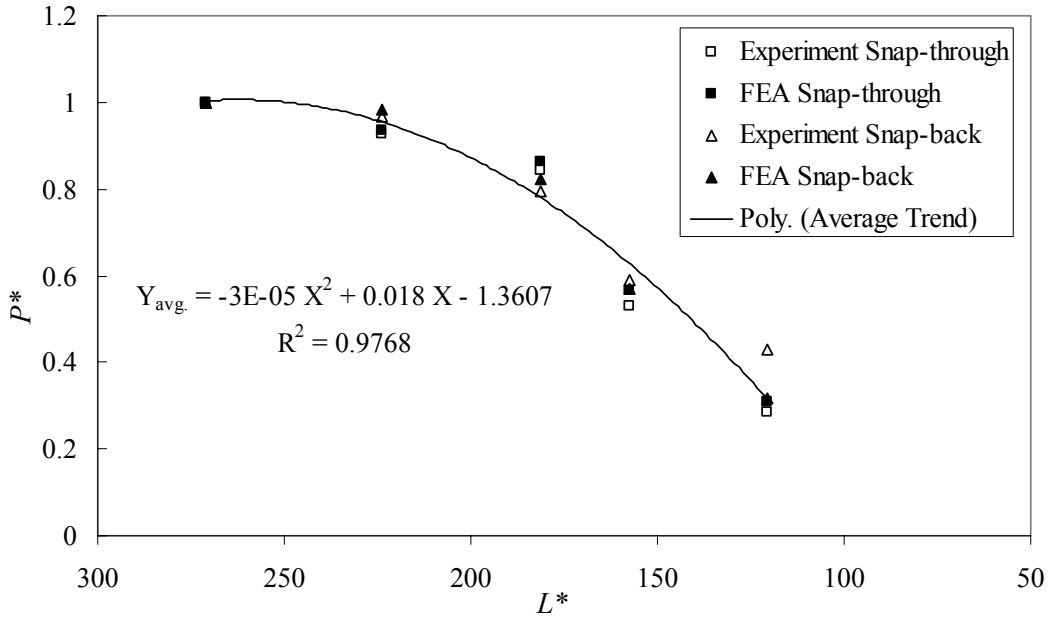

Figure 3-48. Non-dimensional snap-through and snap-back results for square specimens

It is beneficial to allow specimens from a certain group to join a different group as a special case. For example specimen #1 in the square group can join the rectangular group as the base state. This represents a more general rectangular array of specimens. Therefore the general rectangular set is included in Table 3-25 while the numerical predictions and test data are provided in Figures 3-49 and 3-50.

Table 3-25 Geometry of the general rectangular specimens

Specimen	*a* (mm)	*b* (mm)	Source
1	151	150	Square # 1
2	151	113	Rectangular # 1
3	151	99	Rectangular # 2
4	148.5	73	Rectangular # 3
5	148	62	Rectangular # 4
6	150	50	Rectangular # 5

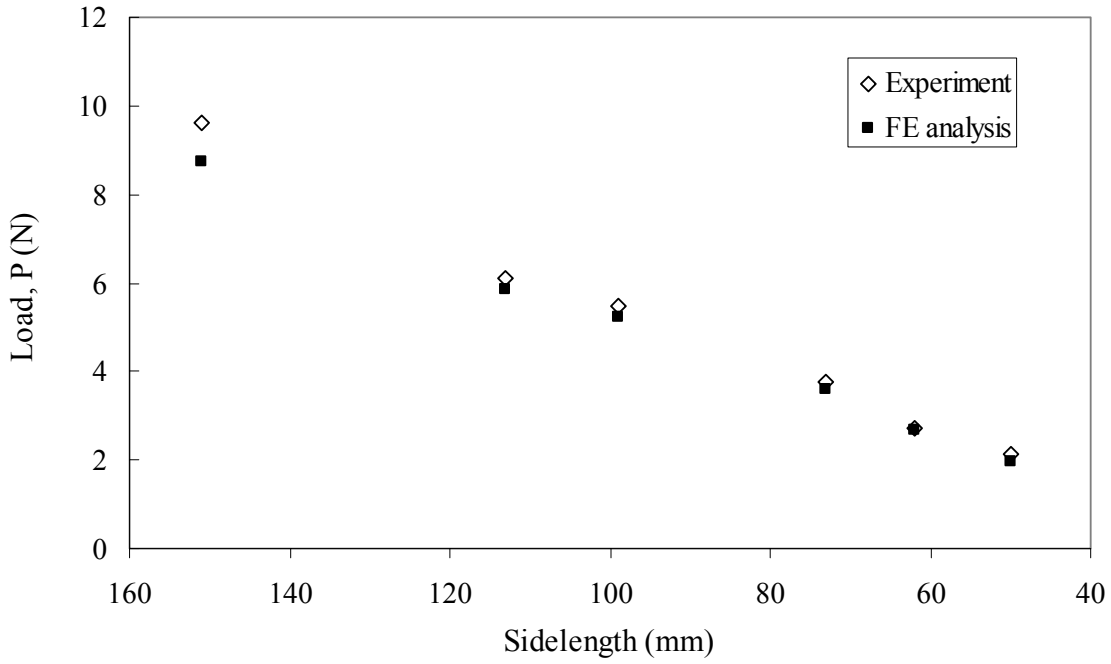

Figure 3-49. Snap-through load of the general rectangular set, Experiment vs. FE analysis

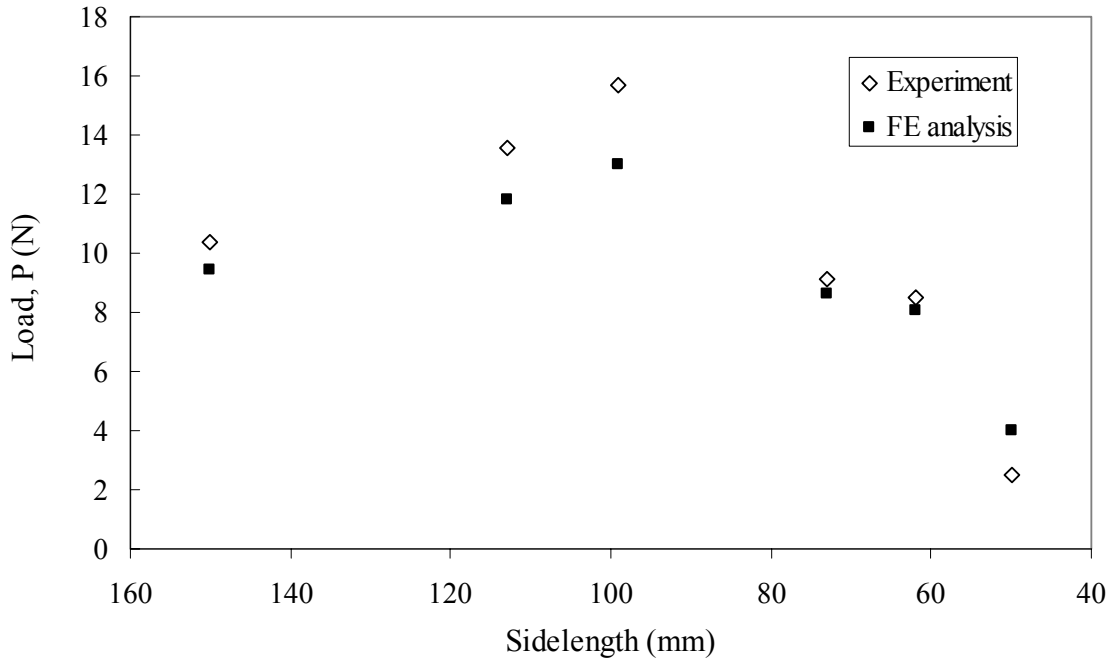

Figure 3-50. Snap-back load of the general rectangular set, Experiment vs. FE analysis

In Figure 3-50, the critical load required for snap-back can increase by 50% as the panel width decreases. This effect is similar to moving the support symmetrically towards each other in a square panel. In doing this the required concentrated load to trigger snap-back will be higher. To verify this observation, an experiment is carried out by supporting the square specimen #1 at points corresponding to the rectangular #1 specimen. The required load to snap-back the square panel is recorded to be 17.89 N. Whereas, rectangular specimen #1 required only 13.54 N. The closer the supports in a square panel, the higher the measured critical load when compared with the corresponding rectangular panel. Accordingly, moving the support inward is not identical to trimming the panel into a rectangular shape, however it has similar effect.

The critical snap-through/snap-back loads are used as a non-dimensional parameter in the general rectangular specimens set as

The analytically and experimentally obtained values are non-dimensionalized by their corresponding values of the square panel. Non-dimensional width, b^*, is obtained using Equations (3.2) for specimens' nominal thickness, t, of 0.555 mm. Figures 3-49 and 3-50 are reproduced in Figures 3-51 and 3-52 using these non-dimensional parameters.

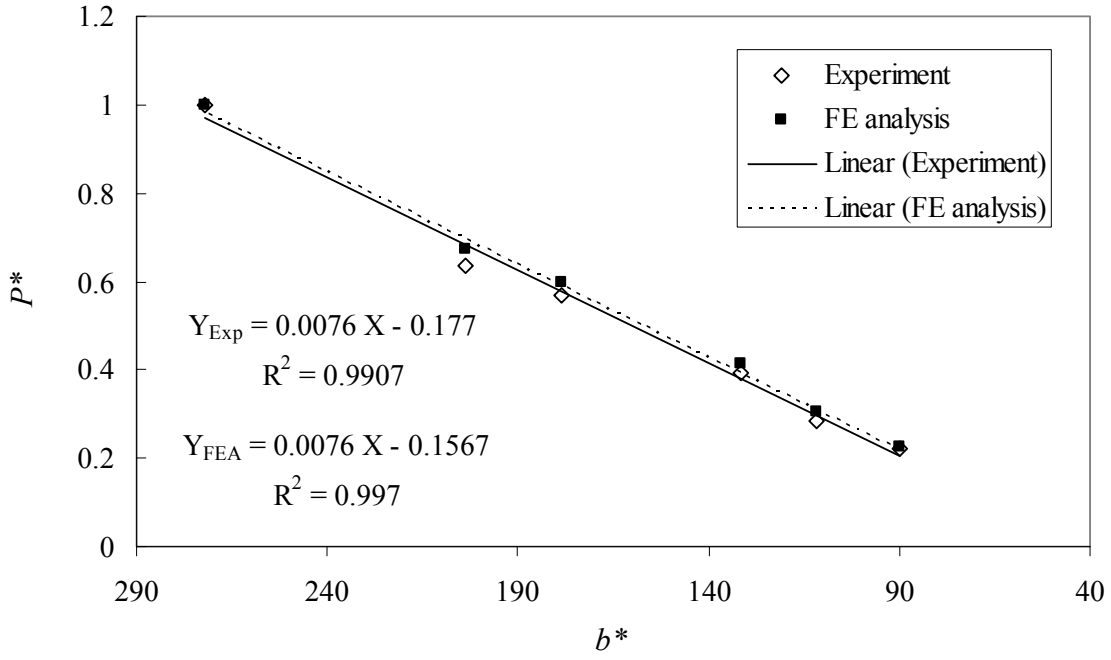

Figure 3-51. Non dimensional snap-through results of the general rectangular set, Experiment vs. FE analysis

Figure 3-51 shows that the snap-through load can be expressed in terms of a linear relationship with the sidelength of the rectangle. The least square expressions for both analytical and experimental values have the same slope. The analytical predictions capture the experimentally obtained trends.

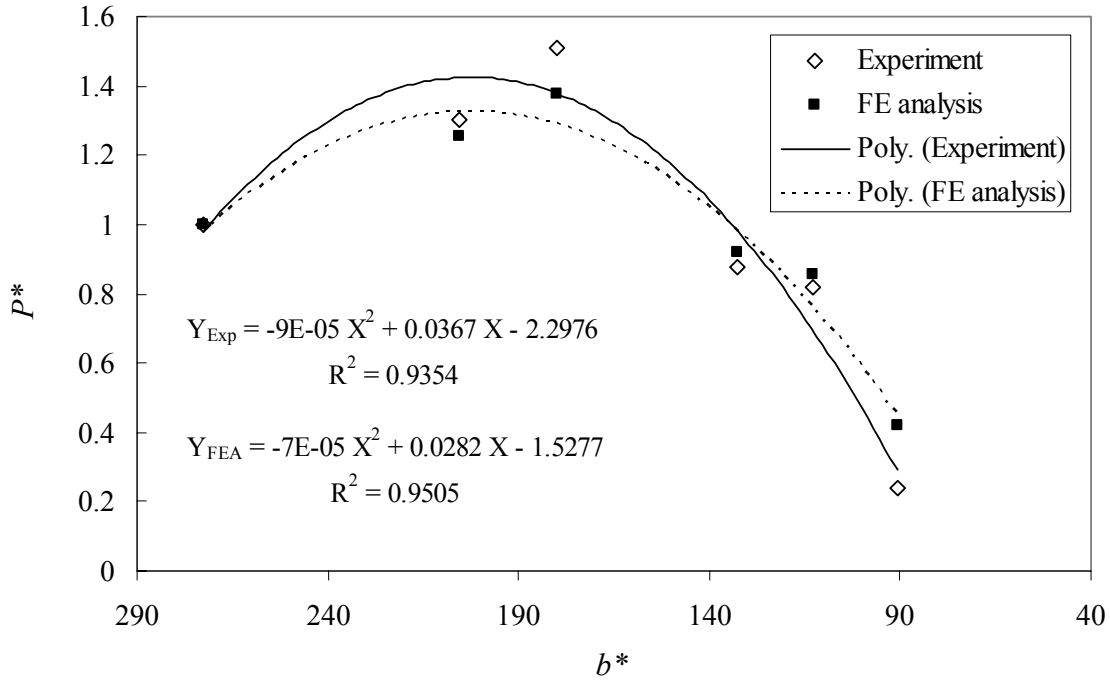

Figure 3-52. Non dimensional snap-back results of the general rectangular set, Experiment vs. FE analysis

Figure 3-52 shows that a quadratic expression could be used to express the relationship between the non-dimensional values of snap-back load and width of the rectangle. The coefficients of the least square expressions for both analytical and experimental are of the same sign although slightly different. The analytical results are in general agreement with the test data. Meanwhile, both test results and predictions are slightly scattered around the trend lines. Specimens' deviation from their nominal dimensions are claimed to be responsible for such a scatter. This deviation of dimensions is caused by the manual preparation process of specimens. In order to verify this statement, a finite element study is obtained for rectangular panels with the nominal dimensions provided in Table 3-26. Their predicted snap-through and snap-back loads are also provided in the Table 3-26.

Table 3-26 Rectangular panels of nominal dimensions, FE study of stability trends

a (mm)	*b* (mm)	Snap-through load (N)	Snap-back load (N)
150	150	9.347	9.536
150	140	8.477	10.425
150	130	7.594	11.370
150	120	6.755	12.106
150	110	5.959	12.787
150	100	5.196	13.000
150	90	4.432	12.497
150	80	3.717	11.512
150	70	3.020	9.980
150	60	2.514	7.520
150	50	1.950	3.980

Obtaining non-dimensional loads using Equation (3.1) and non-dimensional width using Equation (3.2) non-dimensional stability trends are obtained. Figures 3-53 and 3-54 include the predictions from the finite study together with non-dimensional predictions and test data obtained for the general rectangular specimen set.

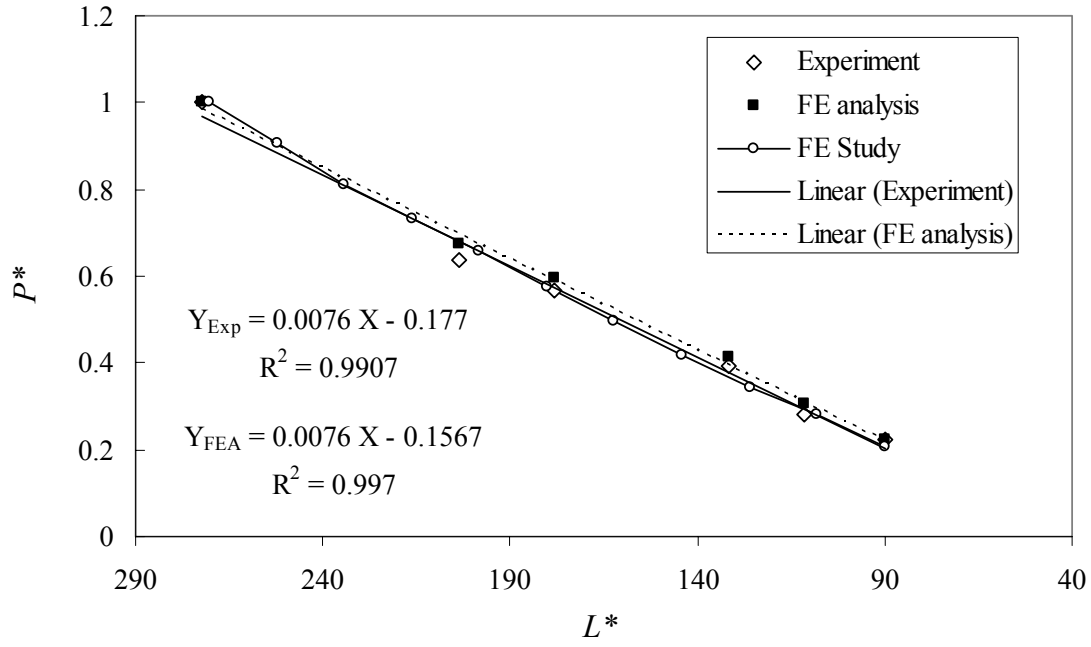

Figure 3-53. Non dimensional snap-through trends of a general rectangular set and FE study

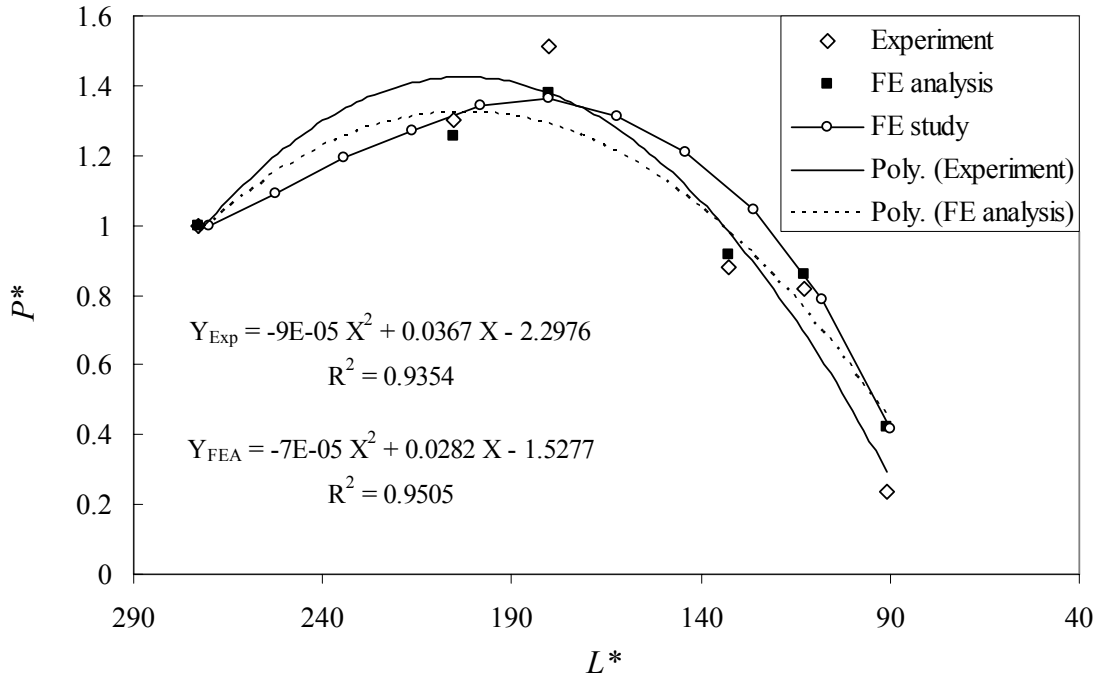

Figure 3-54. Non dimensional snap-back trends of a general rectangular set and FE study

The linear trend of snap-through load provided earlier in Figure 3-51 and repeated in Figure 3-53 is in perfect agreement with the one obtained from the F.E. Study. The quadratic trend associated to the snap-back load, provided in Figure 3-52 and reproduced in Figure 3-54, are slightly different from the one obtained from the F.E. Study. The reason for this difference is entailed by deviations in specimens' dimensions from the nominal dimensions used for the F.E. Study. Meanwhile, the analytically predicted "transverse-side stiffening effect" is in general agreement with test results.

Another general geometric set is formed as provided in Table 3-27. In this comparison a trapezoid of height 150 mm and bottom side 150 mm, has a top side, *a*, ranging from 151 mm (case of a square) to zero mm (case of a triangle). This set will be referred to as generalized trapezoidal set.

Table 3-27 Geometry of the general trapezoidal-A specimens

Specimen	*h* (mm)	*a* (mm)	*b* (mm)	Source
1	150	151	151	Square # 1
2	152	125	152	Trapezoidal-A # 1
3	149	100	150	Trapezoidal-A # 2
4	151	74	150	Trapezoidal-A # 3
5	149	50	150	Trapezoidal-A # 4
6	150	25	150	Trapezoidal-B # 1
7	150	0	149	Triangular-A # 1

The snap-through/snap/back loads of the first square specimen are used to obtain non-dimensional critical loads following Equation (3.1). Non-dimensional top side, a^*, is

obtained by dividing by the nominal thickness of specimens. Figures 3-55 and 3-56 provide the non-dimensional results obtained for the general trapezoidal-A set.

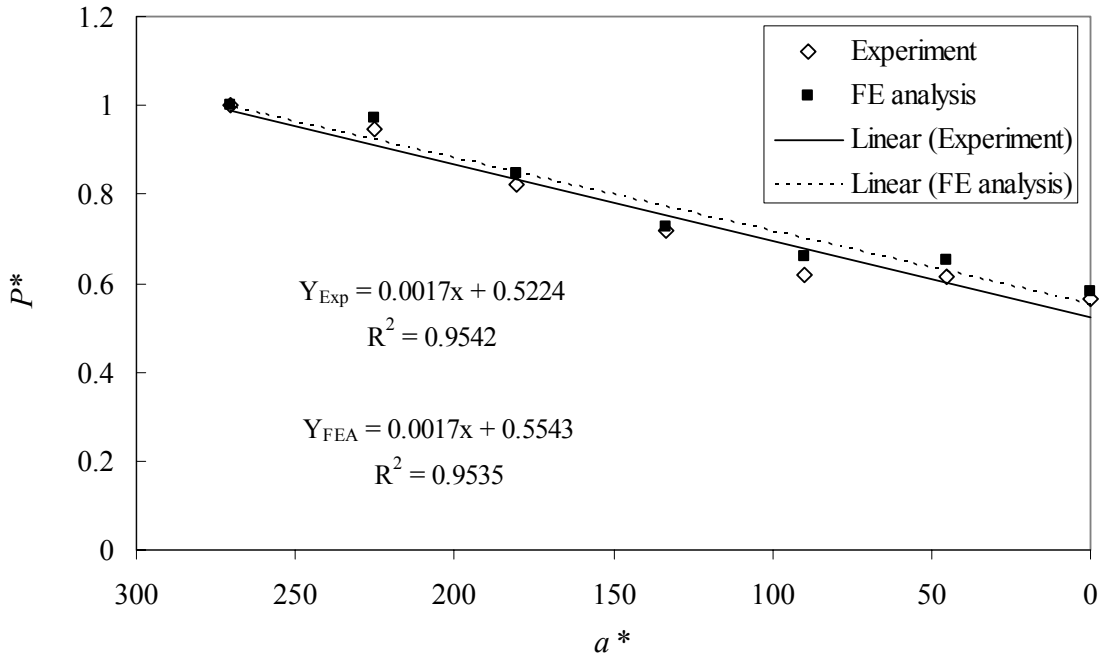

Figure 3-55. Non-dimensional snap-through behavior of the general trapezoidal-A set, Experiment vs. FE analysis

Similar snap-through trend to that of the general rectangular set is adopted by the general trapezoidal-A set as shown in Figure 3-55. Linear trend of non-dimensional snap-through load as a function of the non-dimensional top side length is captured by the analysis.

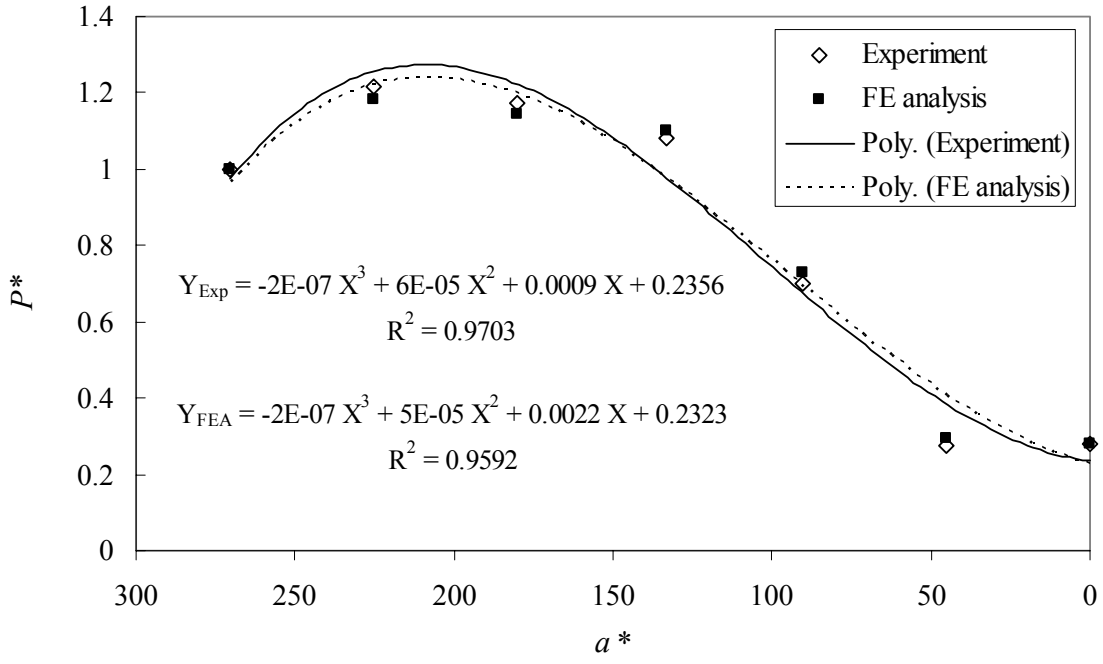

Figure 3-56. Non-dimensional snap-back behavior of the general trapezoidal set, Experiment vs. FE analysis

Figure 3-56 shows that better least square fit of snap-back behavior can be obtained by adopting cubic expression. Decreasing the length of the top side of the trapezoidal-A results in the "transverse-side stiffening effect" similar to changing the width of the rectangular shape although less pronounced. The analytical predictions are in agreement with the trends obtained from the test data.

The same non-dimensional parameterization is employed to the results of the trapezoidal-B specimens to obtain the effect of changing the height of the trapezoid on the critical loads. Non-dimensional loads, P^*, at corresponding non-dimensional height, h^*, of a trapezoidal-B are provided in Figures 3-57 and 3-58 for snap-through and snap-back, respectively. The "transverse-side stiffening effect" is adopted in both cases and demonstrated by the slight increase in the non-dimensional critical loads. The analytical

predictions capture the experimentally obtained trends in both cases of snap-through and snap-back.

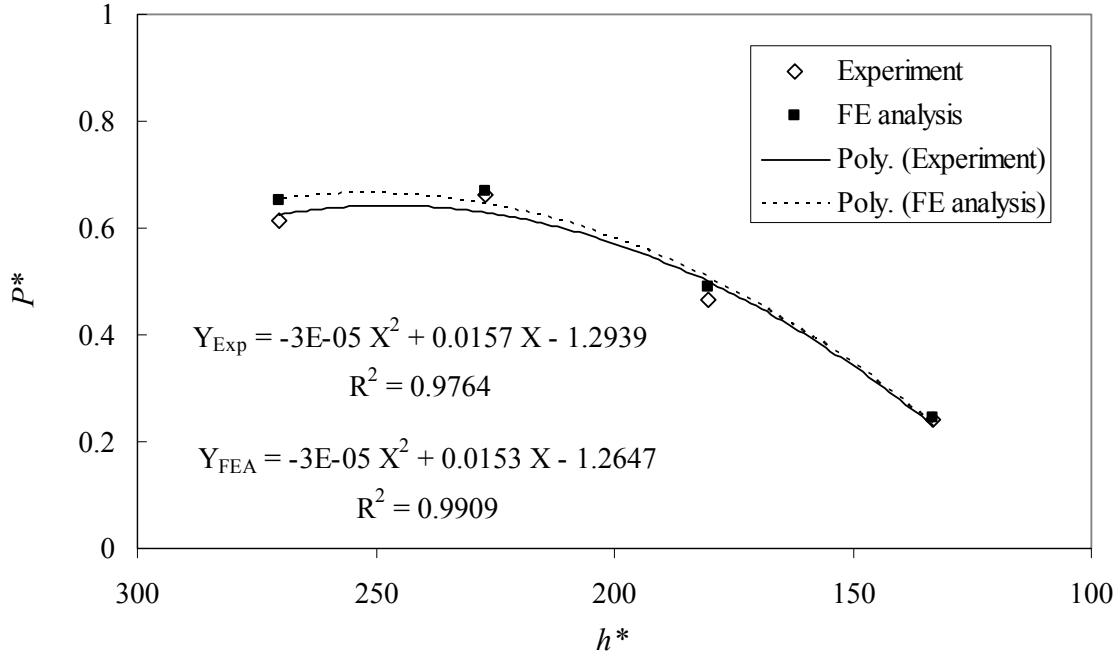

Figure 3-57. Non dimensional snap-through results of the trapezoidal-B group

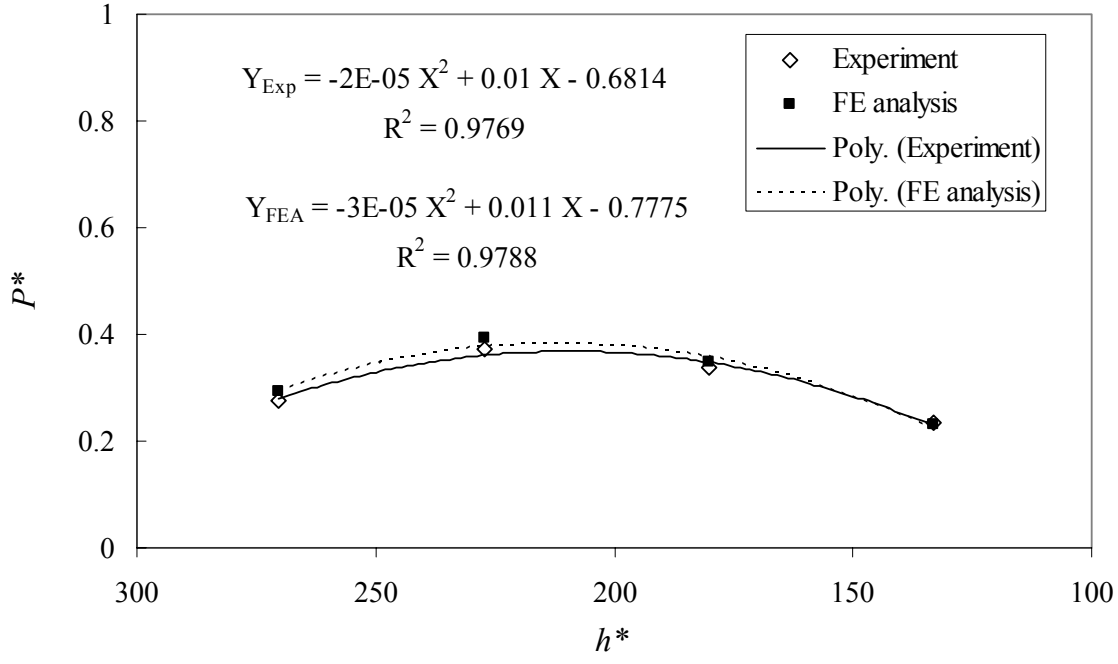

Figure 3-58. Non dimensional snap-back results of the trapezoidal-B group

Non-dimensional loads, *P**, at corresponding non-dimensional base, *b**, of the triangular-A specimens are provided in Figures 3-59 and 3-60 for snap-through and snap-back, respectively. Considering specimen # 3 an outlier, linear trends are adopted in both snap-through and snap-back cases. The analytical predictions capture the experimentally obtained trends in both cases.

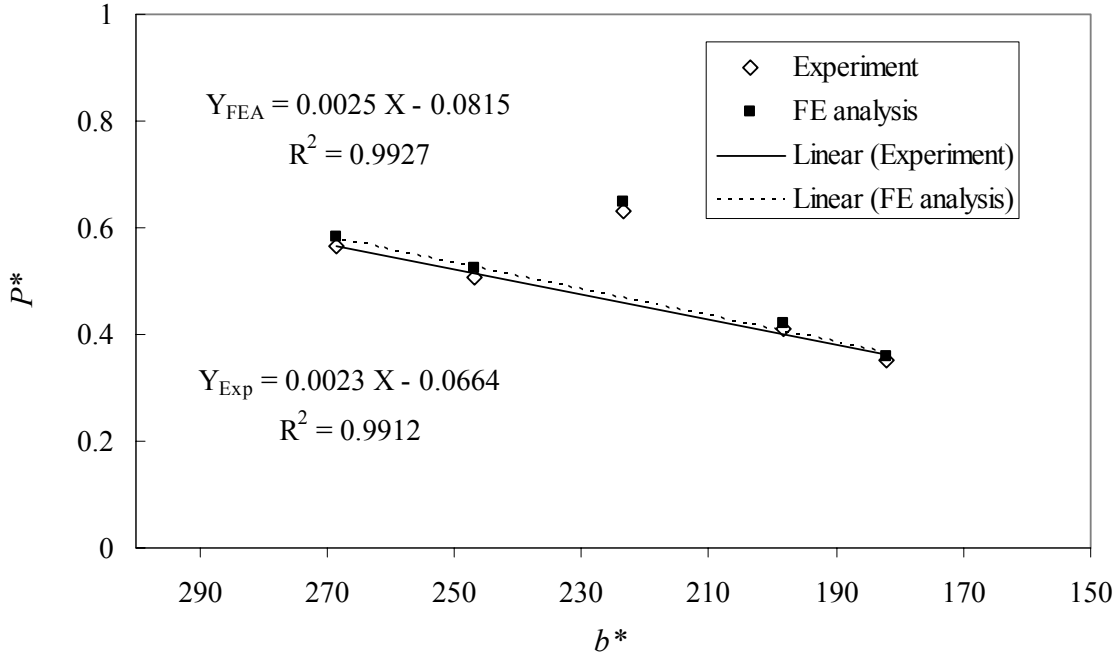

Figure 3-59. Non dimensional snap-through results of the triangular-A group

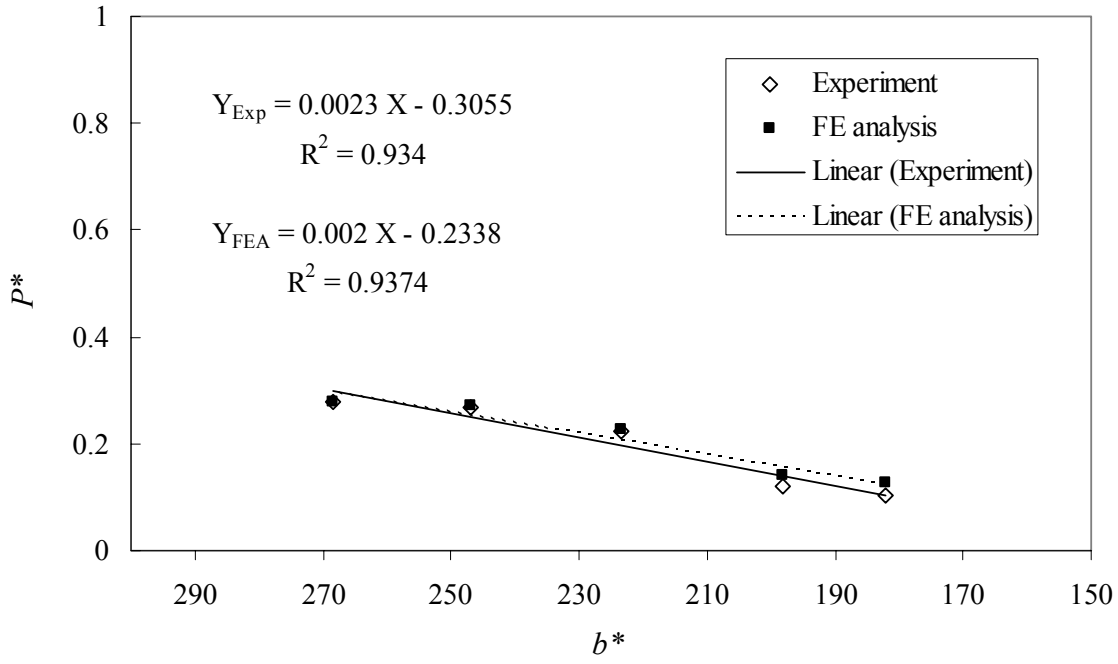

Figure 3-60. Non dimensional snap-back results of the triangular-A group

Similarly, non-dimensional loads, P^*, at corresponding non-dimensional height, h^*, of the triangular-B specimens are provided in Figures 3-61 and 3-62 for snap-through and snap-back, respectively. Linear trends are adopted in both snap-through and snap-back cases. The analytical predictions capture the experimentally obtained trends in both cases.

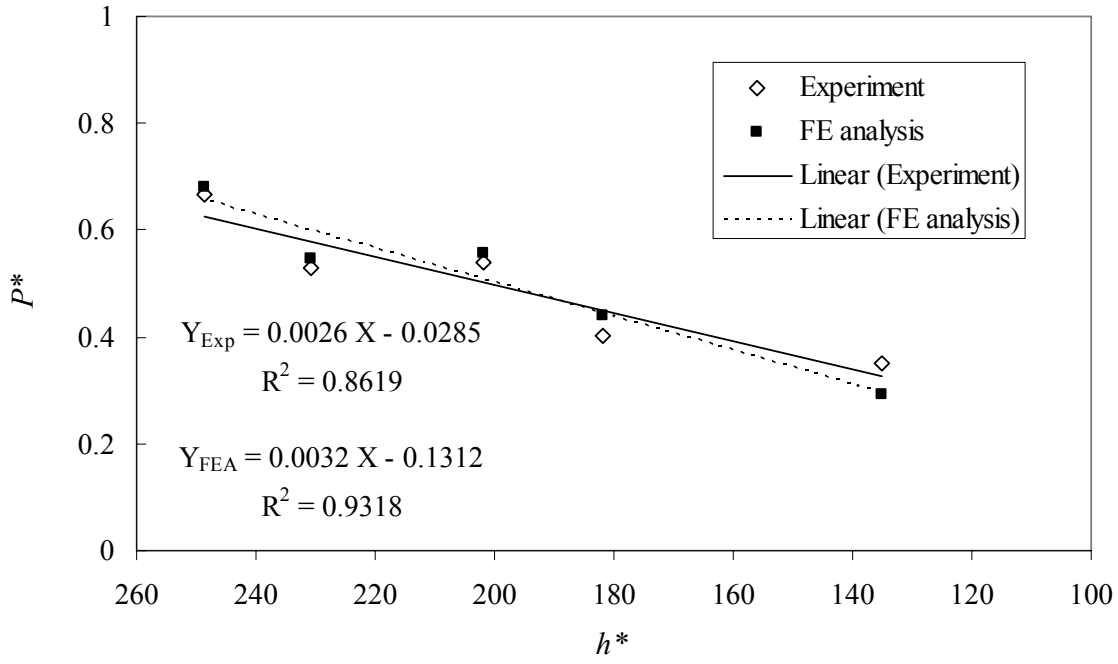

Figure 3-61. Non dimensional snap-through results of the triangular-B group

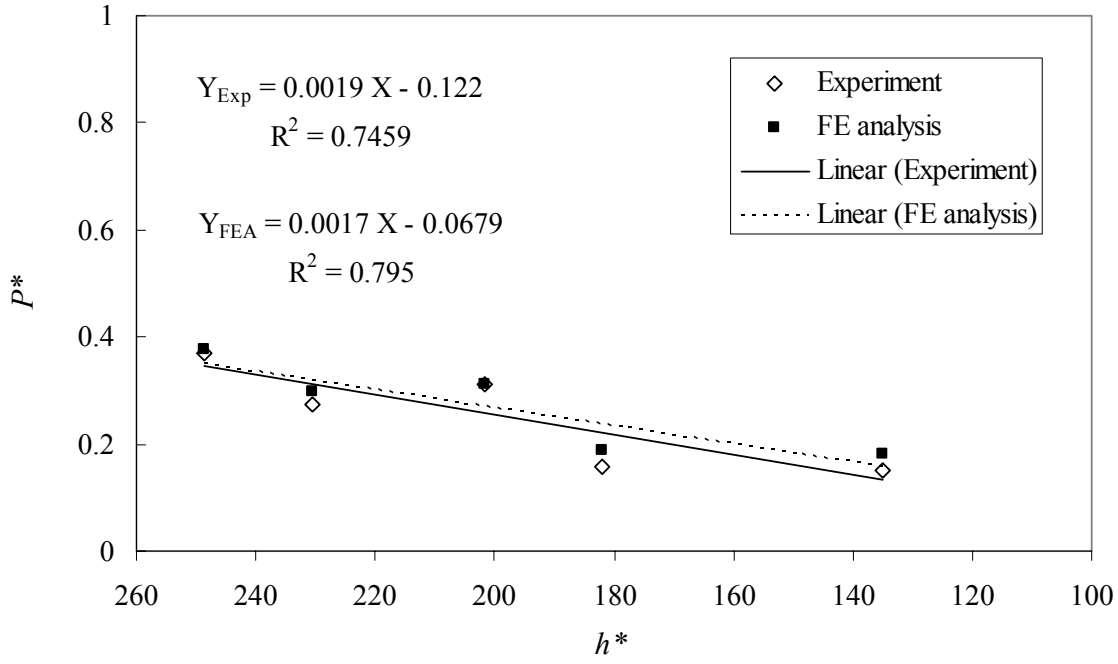

Figure 3-62. Non dimensional snap-back results of the triangular-B group

Through this non-dimensional study the influence of geometry on stability characteristics of geometries with straight edge three trends are observed, namely linear, monotonically decreasing quadratic and quadratic or cubic non-monotonic one. The linear behavior dominates the snap-through trend in most cases, while the "transverse-side stiffening effect" dominates snap-through behavior in all cases but triangular geometries which follow a linear trend with change of base or height. The "shape scaling effect" dominates both snap-through and snap-back behaviors when changing a characteristic length results in considerable change of the total area of the shape.

Geometries with round edges

Geometries from the round edges category are divided into three geometric groups, namely circular, elliptical, and bi-elliptical and shown in Figure 3-63.

Figure 3-63. Round edges category

Circular specimens

Within this group the diameter of the circle varies from 151 to 70 mm. Figure 3-64 shows the set of specimens in the circular group and Table 3-28 provides the dimensions of each specimen. As noted in Table 3-28 these specimens had visual surface defects. When their parent panel was removed out of the autoclave it had a dull looking surface. The specimens were cut out of the parent panel using a waterjet machine that did not affect their surface quality. When the time came to test them, they have gained a dry looking surface. The snap-through and snap-back load determined from the experiment are provided in Table 3-29. The loads are applied at the center point of the panel to force the specimen to snap-through or snap-back.

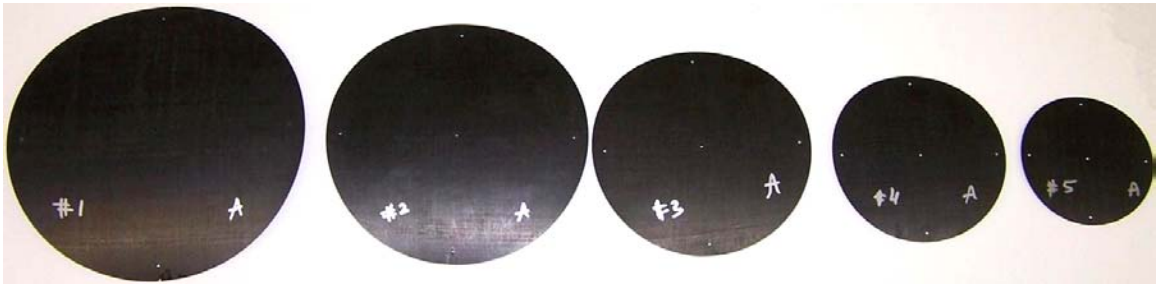

Figure 3-64. Circular specimens

Table 3-28 Geometry of circular specimens

Specimen	*D* (mm)	Remarks
1	151	dry surface appearance
2	131	dry surface appearance
3	111	dry surface appearance
4	91	dry surface appearance
5	70	dry surface appearance

Table 3-29 Experimental snap-through and snap-back loads of circular specimens

Specimen	Snap-through		Snap-back	
	P (N)	Standard deviation	P (N)	Standard deviation
1	6.42	0.06	5.71	0.05
2	5.61	0.15	5.41	0.09
3	5.28	0.01	3.96	0.01
4	3.59	0.03	2.88	0.06
5	1.98	0.09	1.02	0.04

Test data for each specimen are providing different snap-through and snap-back loads following a trend similar to changing the sidelength of the square panels.

A mesh of 640 shell S4R elements is used to model each specimen. The analytical predictions of the snap-through and snap-back are obtained by applying the boundary conditions described in Figure 3-65. A sample of the equilibrium shapes of the manufactured panels are included in Figure 3-66 together with the ones predicted from the analysis.

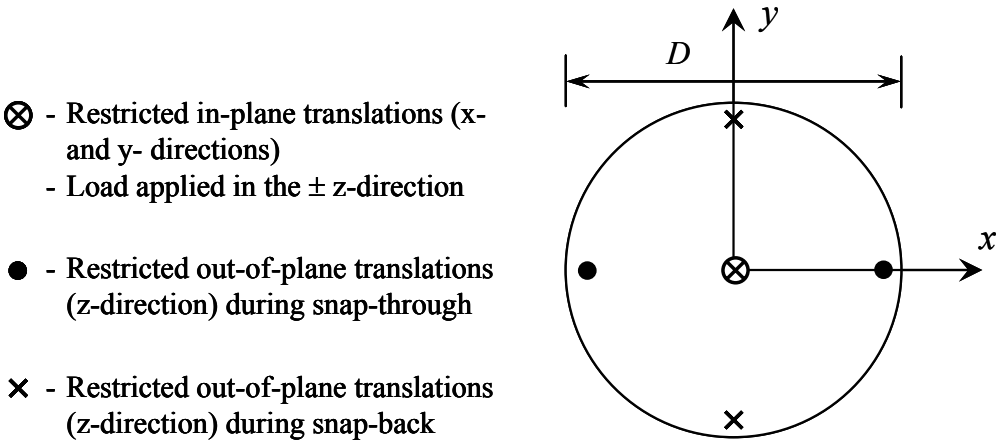

Figure 3-65. Boundary conditions of a circular panel

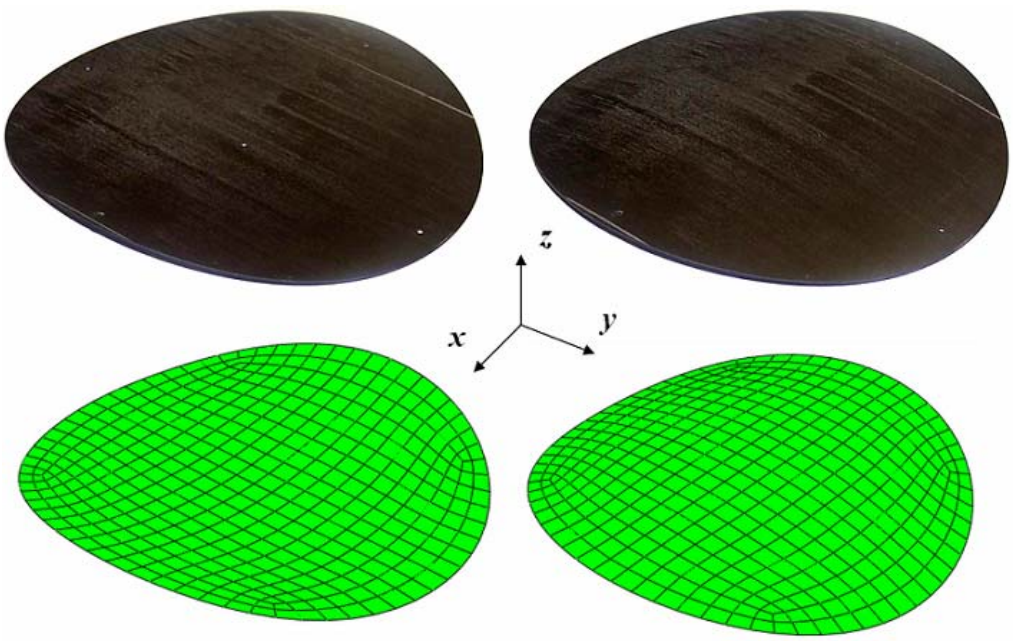

Figure 3-66. Equilibrium shapes of a circular specimen, manufactured versus predicted

Due to the surface appearance of these specimens the analytical predictions were obtained using the default value of the scale factors, i.e. tenth of the thickness. Predictions obtained using tenth of the thickness scale factor are provided in Table 3-30 together with the percentage difference compared to the test data. Similar results are provided in Table 3-31 using imperfections of the order of the thickness.

Table 3-30 FE snap-through and snap-back loads of circular specimens (scale factors in the order of tenth of the thickness)

Specimen	Snap-through		Snap-back	
	P (N)	% Difference	P (N)	% Difference
1	6.29	-2.02	6.04	5.82
2	5.53	-1.40	5.51	1.77
3	5.32	0.71	5.16	30.36
4	3.93	9.23	3.73	29.56
5	2.31	16.47	2.09	105.00

Table 3-31 FE snap-through and snap-back loads of circular specimens (scale factors in the order of the thickness)

Specimen	Snap-through		Snap-back	
	P (N)	% Difference	P (N)	% Difference
1	6.04	-5.92	5.88	2.98
2	5.51	-1.81	5.28	-2.48
3	5.16	-2.43	4.50	13.61
4	3.72	3.61	3.49	21.25
5	2.10	5.88	1.86	81.96

Using scale factors of higher values resulted in decreasing the percentage difference between the analysis and test results. This agrees with the recommendations made in Chapter 2 regarding the choice of their values.

The curvatures along the *x*-and *y*-directions of the panels in each equilibrium configuration are provided in Table 3-32.

Table 3-32 FE predicted curvatures of equilibrium shapes of circular specimens

Specimen	First equilibrium shape		Second equilibrium shape	
	κ_x (m^{-1})	κ_y (m^{-1})	κ_x (m^{-1})	κ_y (m^{-1})
1	6.150	-0.021	0.022	-6.095
2	6.197	-0.024	0.034	-6.114
3	6.374	-0.051	0.057	-6.164
4	6.251	-0.156	0.160	-6.202
5	6.066	-0.519	0.560	-5.943

The predicted curvatures provided in Table 3-32 do not present a specific trend in terms of x-curvature in the first equilibrium shape or y-curvature in the second equilibrium shape. On the other hand a trend is exhibited by the x-curvature in the second equilibrium shape as it increases with decreasing the diameter. Similar observation can be made regarding the magnitude of the y-curvature in the first equilibrium shape. This trend is in agreement with the analytical predictions indication that a laminate approaches a saddle shape with a decrease in its diameter.

The values of snap-through and snap-back loads corresponding to the test data and analytical predictions (for the case of scale factors in the order of thickness) are provided in Figures 3-67 and 3-68, respectively. The predicted trend from the FE analysis is in agreement with experiment.

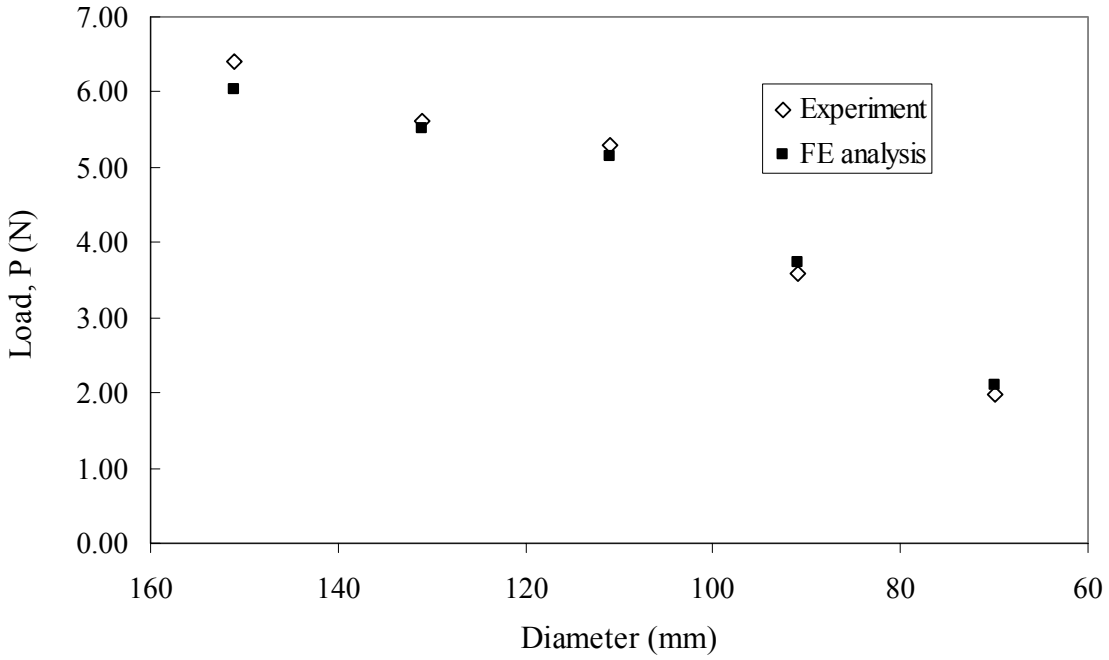

Figure 3-67. Snap-through load of circular specimens, Experiment vs. FE analysis

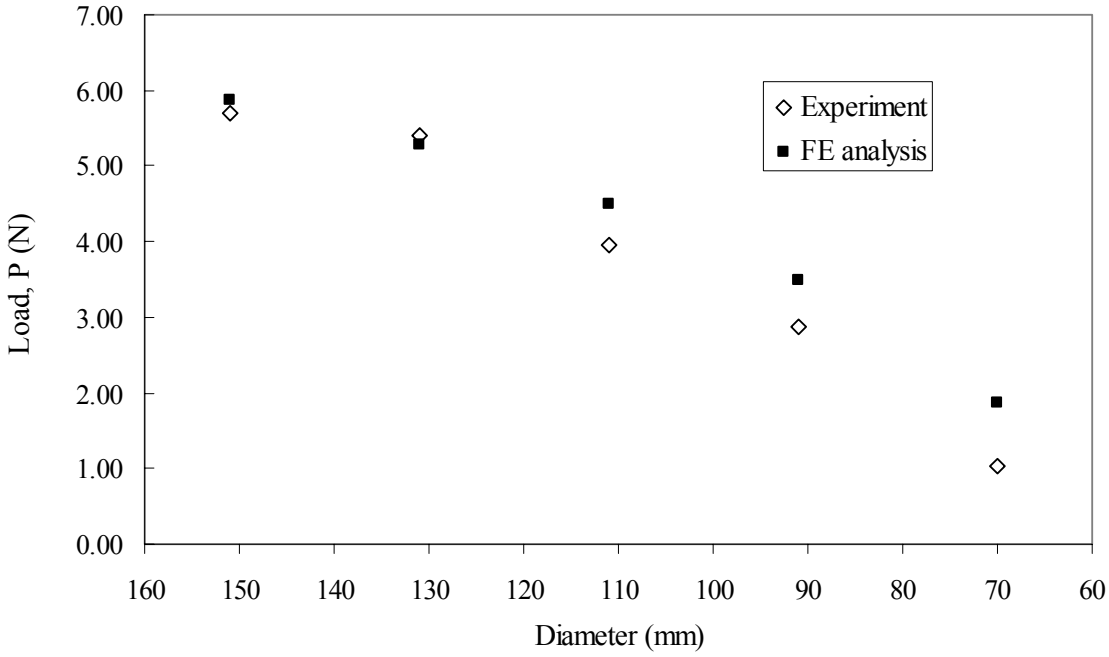

Figure 3-68. Snap-back load of circular specimens, Experiment vs. FE analysis

Elliptical specimens

Within this group the major diameter of the ellipse is held constant at 151 mm and the minor diameter varies from 131 to 70 mm. Figure 3-69 shows the set of specimens in the elliptical group and Table 3-33 provides the dimensions of each specimen. The snap-through and snap-back load determined from the experiment are provided in Table 3-34. The loads are applied at the center point to force the specimen to snap-through or snap-back.

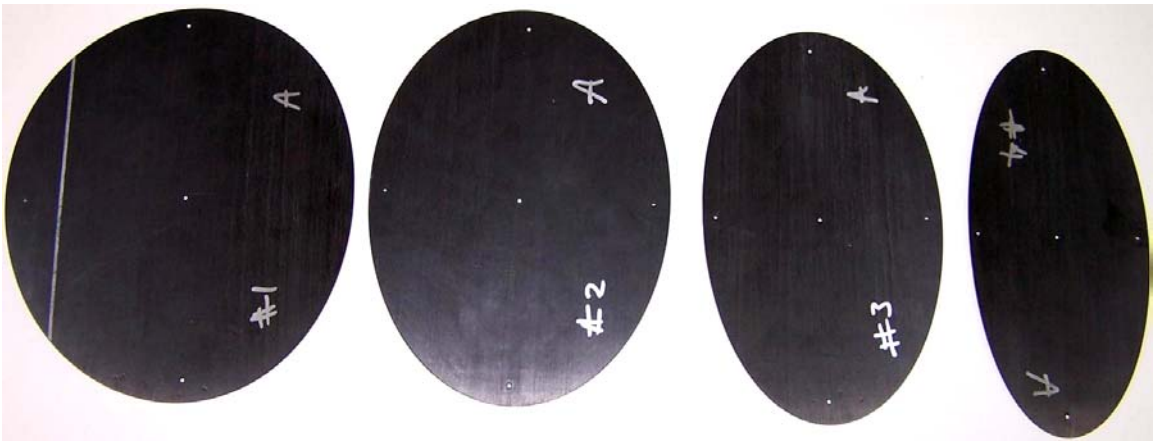

Figure 3-69. Elliptical specimens

Table 3-33 Geometry of elliptical specimens

Specimen	*D* (mm)	*d* (mm)	Remarks
1	151	131	holes' axis in not aligned with specimen's axis
2	151	111	
3	151	90	
4	151	70	

Table 3-34 Experimental snap-through and snap-back loads of elliptical specimens

Specimen	Snap-through		Snap-back	
	P (N)	Standard deviation	P (N)	Standard deviation
1	5.98	0.06	9.18	0.04
2	5.04	0.02	9.32	0.02
3	3.74	0.006	10.40	0.04
4	2.61	0.02	7.32	0.006

The snap-through loads show a consistent decrease while the snap-back loads increase till reaching a peak then decrease as the minor diameter is decreased. The "transverse-side stiffening effect" exhibited by the elliptical specimens reflects the trend observed in the rectangular ones.

A Python script is used to automatically generate the finite element mesh of each elliptic specimen. The number of S4R elements used in each mesh is 680, 620, 478 and 416 for specimens 1 to 4, respectively. The analytical predictions of the snap-through and snap-back are obtained applying the boundary conditions described in Figure 3-70. A sample of the equilibrium shapes of the manufactured panels are included in Figure 3-71 together with the ones predicted from the analysis.

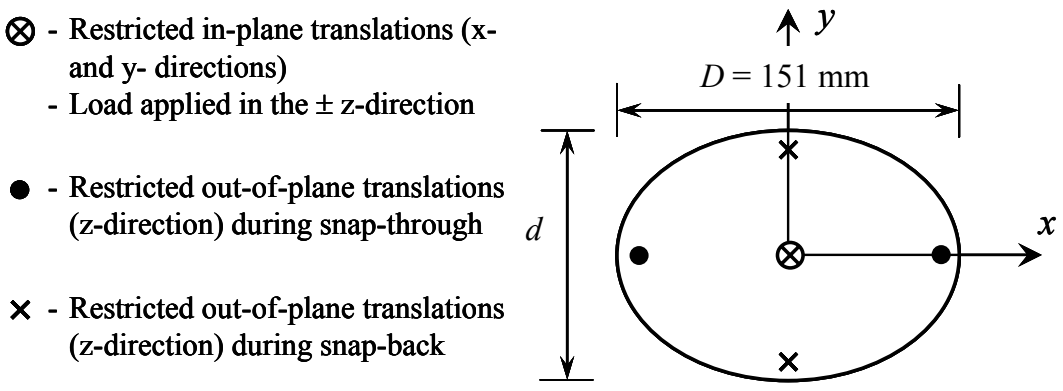

Figure 3-70. Boundary conditions of an elliptical specimen

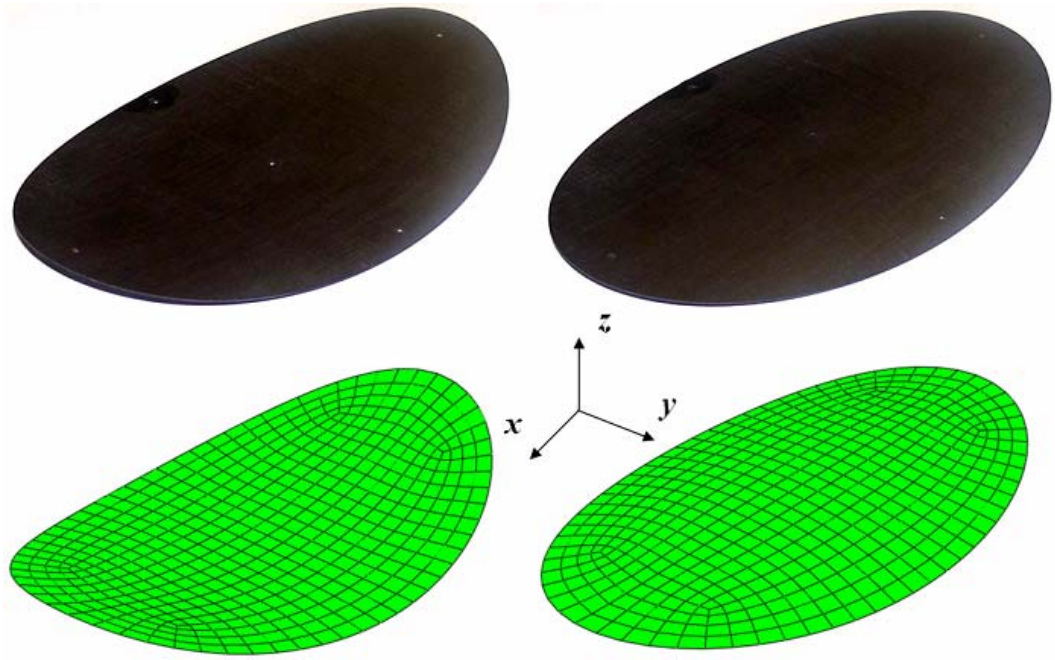

Figure 3-71. Equilibrium shapes of an elliptic panel, manufactured versus predicted

Analytical predictions obtained are provided in Table 3-35 together with the percentage difference compared to the test data.

Table 3-35 FE snap-through and snap-back loads of elliptical specimens

Specimen	Snap-through		Snap-back	
	P (N)	% Difference	P (N)	% Difference
1	5.33	-10.95	6.79	-26.04
2	4.88	-3.32	8.09	-13.23
3	3.58	-4.11	7.76	-25.39
4	2.67	2.15	6.63	-9.33

The large percentage difference in specimen #1 is due to the holes axis misalignment noted in Table 3-32. Further investigation of analytical predictions showed little

sensitivity towards holes misalignment. The analytical predictions show the "transverse-side stiffening effect" similar to the test data.

The curvatures along the x-and y-directions of the panels in each equilibrium configuration are provided in Table 3-36.

Table 3-36 FE predicted curvatures of equilibrium shapes of elliptical specimens

Specimen	First equilibrium shape		Second equilibrium shape	
	κ_x (m^{-1})	κ_y (m^{-1})	κ_x (m^{-1})	κ_y (m^{-1})
1	6.079	-0.060	0.036	-5.945
2	6.262	-0.050	0.059	-6.193
3	6.274	-0.063	0.156	-6.144
4	6.104	-0.056	0.350	-6.121

The influence of changing the minor axis is mainly noticed in x-curvature of the second equilibrium shape. The same trend can be observed in rectangular specimens and result in the second equilibrium shape being replaced by a saddle shape.

The values of snap-through and snap-back loads obtained from the experiment and FE analysis are provided in Figure 3-72 and 3-73, respectively. Predictions from FE analysis are in agreement with the experimental values. The relative increase in measured critical load for specimen # 3 is not reflected by the FE predictions.

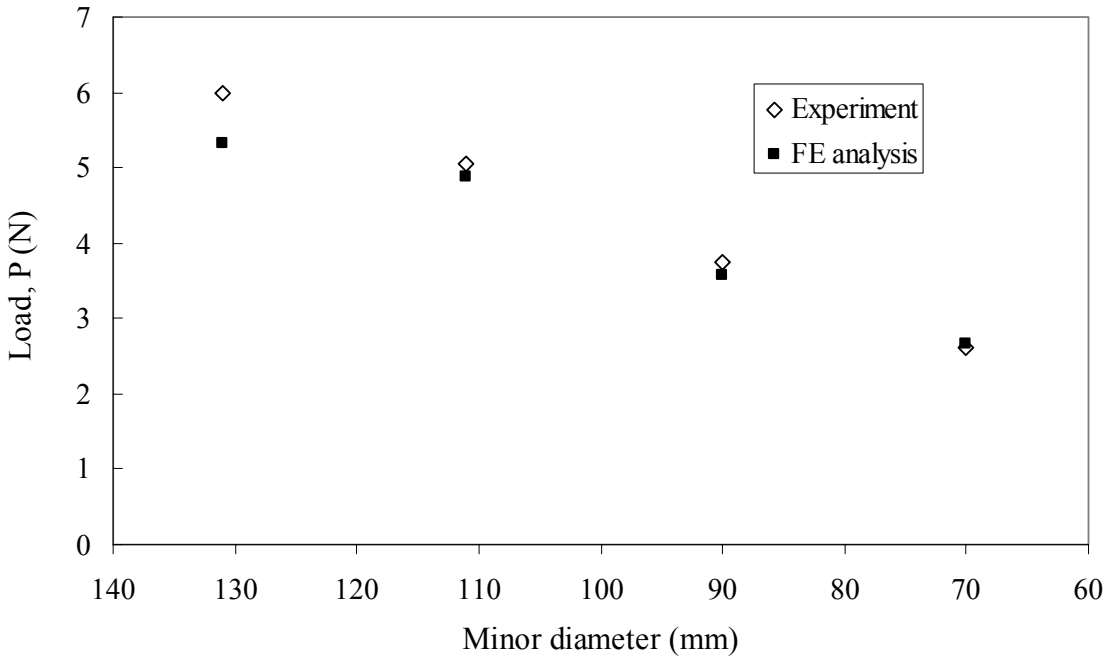

Figure 3-72. Snap-through load of elliptical specimens, Experiment vs. FE analysis

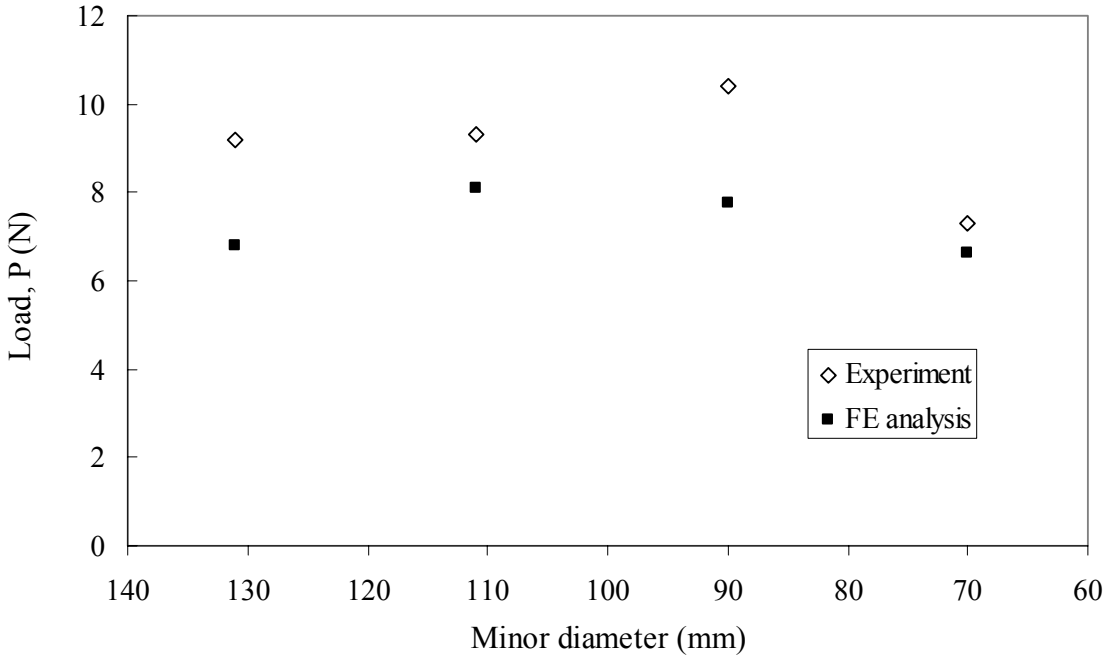

Figure 3-73. Snap-back load of elliptical specimens, Experiment vs. FE analysis

Bi-elliptical specimens

Specimens in this group are shaped after an elliptic wing planform with a straigh quarter chord line. The chord or minor dimension at any point on the major axis of each bi-elliptical specimen is identical to its corresponding specimen from the elliptical group. Studying the stability characteristics of a bi-ellipse shed further light into understanding the influence of geometry. Similar to the case of the elliptical specimens the major diameter of bi-elliptical specimens is held constant at 151 mm and the minor varies from 131 to 70 mm. Figure 3-74 shows the set of specimens in the bi-elliptical group and Table 3-37 provides the dimensions of each specimen. The definitions of the half minors R_{21} and R_{22} are shown in Figure 3-75.

The snap-through and snap-back loads determined from the experiment are provided in Table 3-38. The loads are applied at different points of the panel to force the specimen to snap-through or snap-back as shown in Figure 3-75. These points were selected to enable correlation of results with those obtained for the elliptical specimens. Rubber cement was used at the load cell pin to decrease the specimens' tendency to tilt during load application.

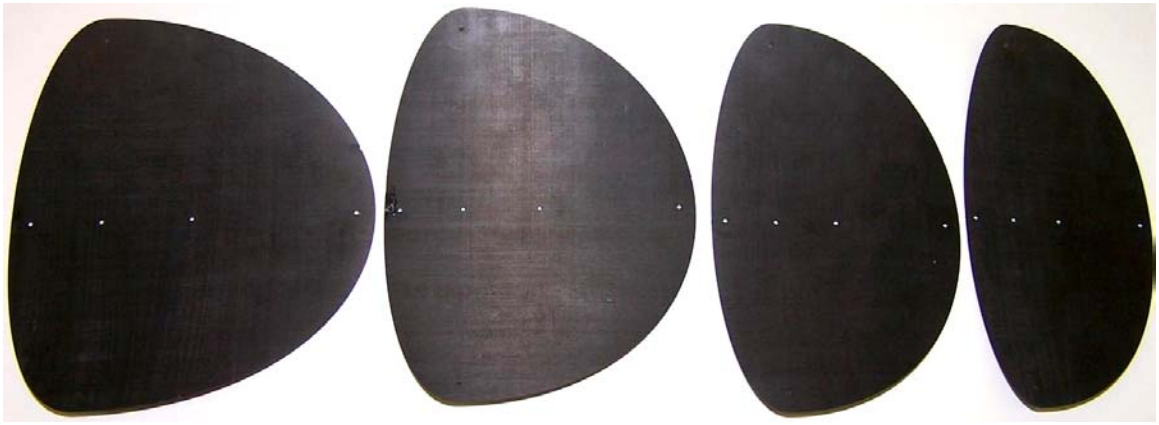

Figure 3-74. Bi-elliptical specimens

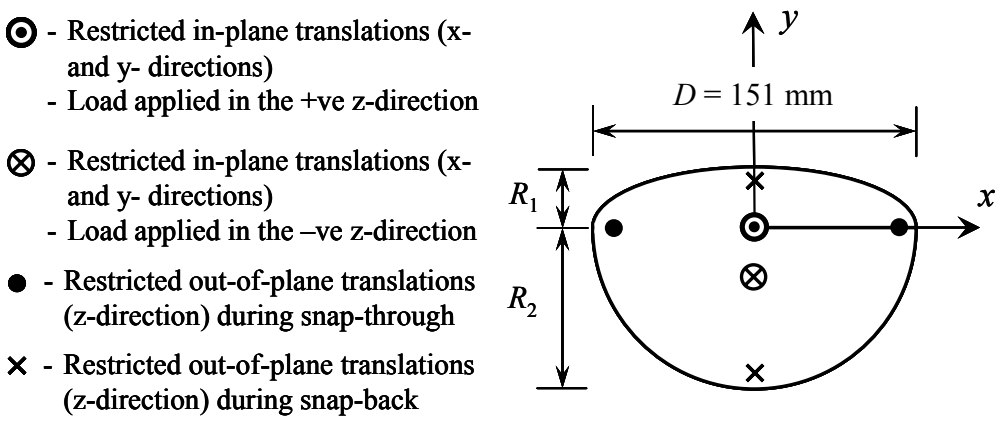

Figure 3-75. Boundary conditions of a bi-elliptical specimen

Table 3-37 Geometry of bi-elliptical specimens

Specimen	D (mm)	R_{21} (mm)	R_{22} (mm)
1	151	32.75	98.25
2	151	27.75	83.25
3	151	22.5	67.5
4	151	17.5	52.5

Table 3-38 Experimental snap-through and snap-back loads of bi-elliptical specimens

Specimen	Snap-through		Snap-back	
	P (N)	Standard deviation	P (N)	Standard deviation
1	5.78	0.01	8.62	0.04
2	4.44	0.04	8.99	0.08
3	3.44	0.02	11.21	0.08
4	2.40*	0.08	8.74	0.08

* Local instability

Similar to the elliptical specimens the critical load data reflect the "transverse-side stiffening effect" in the bi-elliptical specimens, as well. Decreasing the major axis has a more pronounced effect on the stability characteristics than changing the geometry from elliptical to bi-elliptical.

A sample the equilibrium shapes of the manufactured panels are included in Figure 3-69 together with the ones predicted from the analysis.

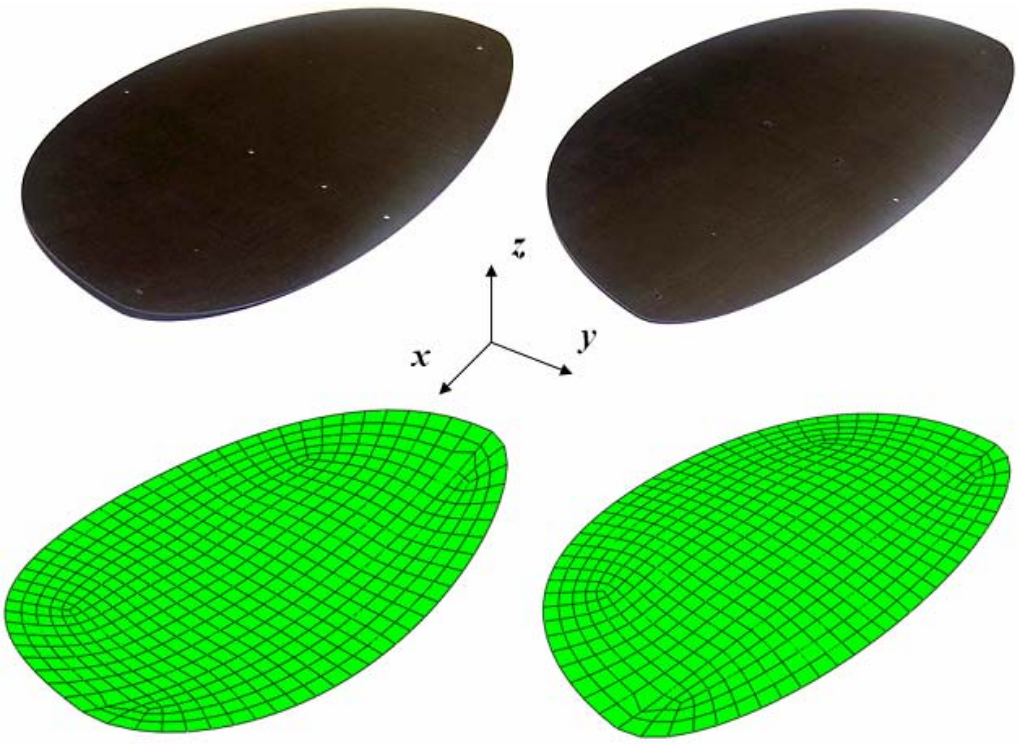

Figure 3-76. Equilibrium shapes of a bi-elliptical specimen, manufactured vs. predicted

A Python script is used to automatically generate the finite element mesh of each elliptic specimen. The number of S4R elements used in each mesh is 690, 640, 502 and 350 for specimens 1 to 4, respectively. The analytical predictions of the snap-through and snap-back are obtained applying the boundary conditions described in Figure 3-75. Analytical

predictions are provided in Table 3-39 together with the percentage difference compared to test data.

Table 3-39 FE snap-through and snap-back loads of bi-elliptical specimens

Specimen	Snap-through		Snap-back	
	P (N)	% Difference	P (N)	% Difference
1	5.49	-5.03	7.21	-16.39
2	4.30	-3.09	7.53	-16.25
3	3.40	-1.10	7.77	-30.74
4	2.60	8.48	6.79	-22.29

Although the analytical predictions show similar trends to the test data, the percentage differences are large in the snap-back loads.

The curvatures along the x-and y-directions of the panels in each equilibrium configuration are provided in Table 3-40.

Table 3-40 FE predicted curvatures of equilibrium shapes of bi-elliptical specimens

Specimen	First equilibrium shape		Second equilibrium shape	
	κ_x (m^{-1})	κ_y (m^{-1})	κ_x (m^{-1})	κ_y (m^{-1})
1	6.161	0.004	0.148	-6.562
2	6.030	-0.028	0.193	-6.563
3	6.170	-0.060	0.246	-6.650
4	6.010	-0.072	0.402	-6.203

Changing the minor diameter size has a more pronounced effect on the x-curvature of the second equilibrium shape. Similar to the rectangular and elliptical specimens the second equilibrium shape is migrating towards a saddle-like shape.

The values of snap-through and snap-back loads obtained from experiment and FE analysis are provided in Figures 3-77 and 3-78, respectively. Predictions from FE analysis are in agreement with the test results in the snap-through case, while the snap-back case does not show similar consistency.

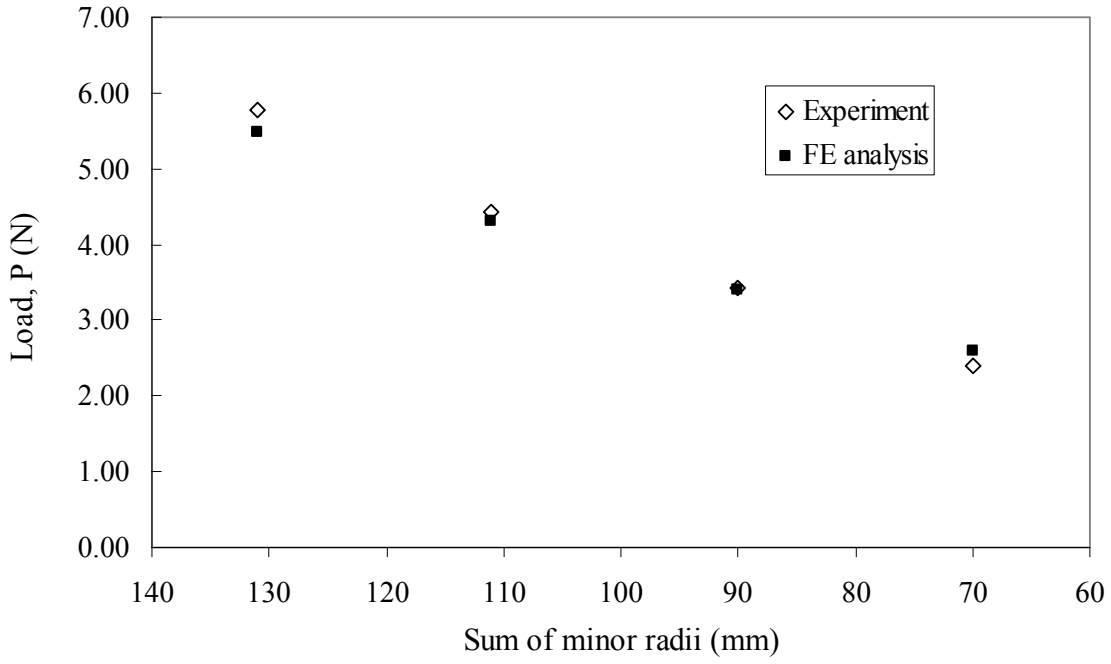

Figure 3-77. Snap-through load of bi-elliptical specimens, Experiment vs. FE analysis

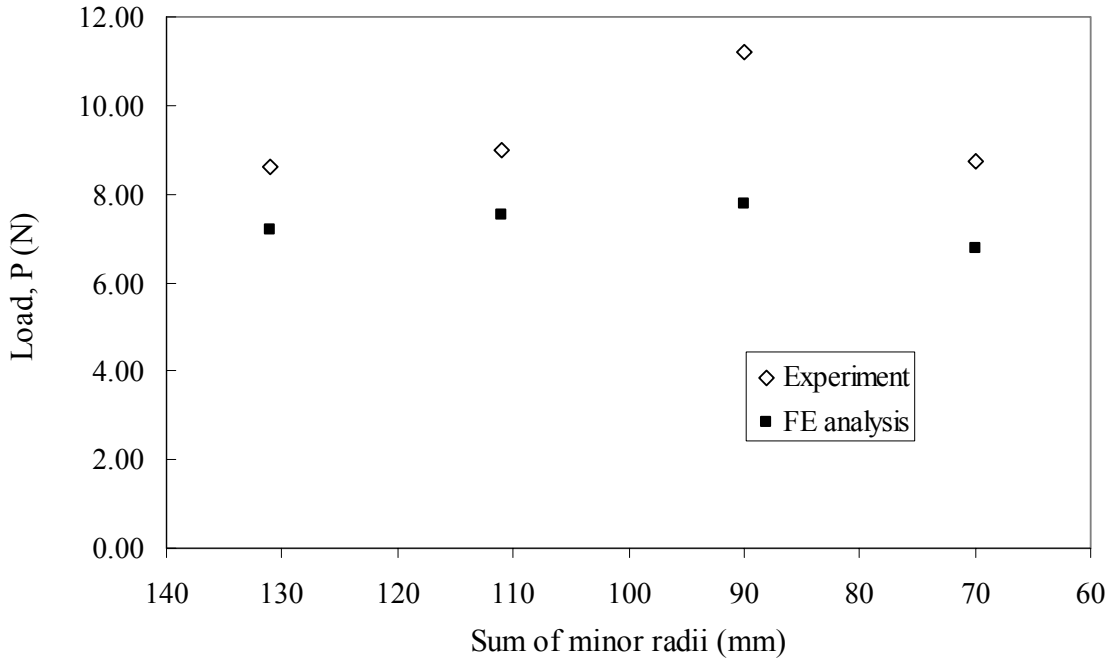

Figure 3-78. Snap-back load of bi-elliptical specimens, Experiment vs. FE analysis

Discussion

Non-dimensional parameters are again used to study the influence of geometry on stability characteristics in the round edges group. The non-dimensional critical snap-through/snap-back loads are obtained using the ones associated to the first specimen of the circular group, as

$$P^* = \frac{P_i}{P_{Circular\ \#1}} \tag{3.3}$$

Non-dimensional parameterization of length is obtained using the nominal thickness of the panel, t = 555 μm, as in Equation (3.2).

Non-dimensional values of both force and sidelength of circular specimens are obtained and provided in Figure 3-79. The average trend of the non-dimensional force, P^*, as a function of the non-dimensional diameter, D^*, follows the "shape scaling effect" similar to square specimens.

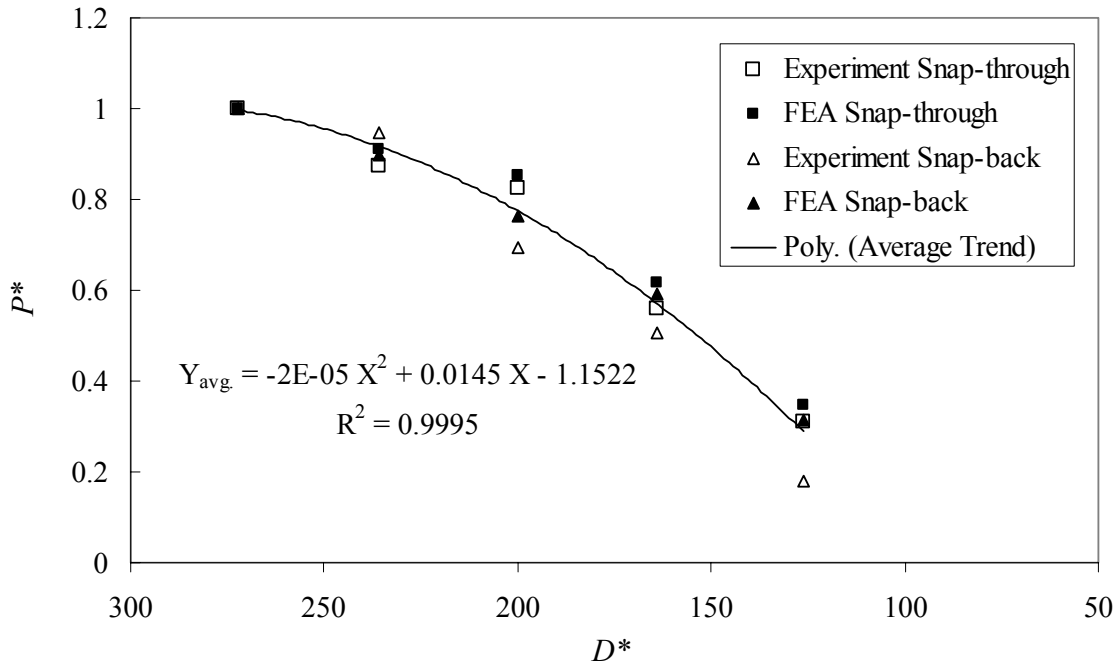

Figure 3-79. Non-dimensional snap-through and snap-back results for circular specimens

A general elliptical set is formed by allowing the first circular specimen to join the elliptical group. Non-dimensional loads, *P**, at corresponding non-dimensional minor diameters, *d**, of an elliptical specimen are provided in Figures 3-80 and 3-81 for snap-through and snap-back, respectively. The general elliptical set is included in Table 3-41.

Table 3-41 Geometry of the general elliptical specimens

Specimen	*D* (mm)	*d* (mm)	Source
1	151	151	Circular # 1
2	151	131	Elliptical # 1
3	151	111	Elliptical # 2
4	151	90	Elliptical # 3
5	151	70	Elliptical # 4

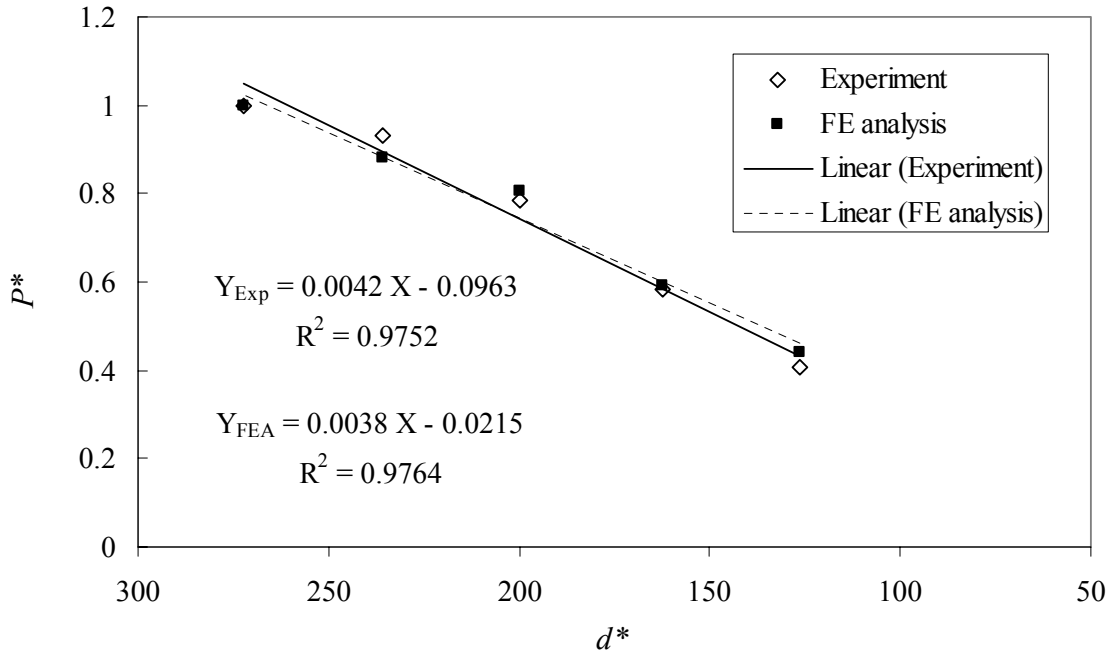

Figure 3-80. Non dimensional snap-through results of the general elliptical set

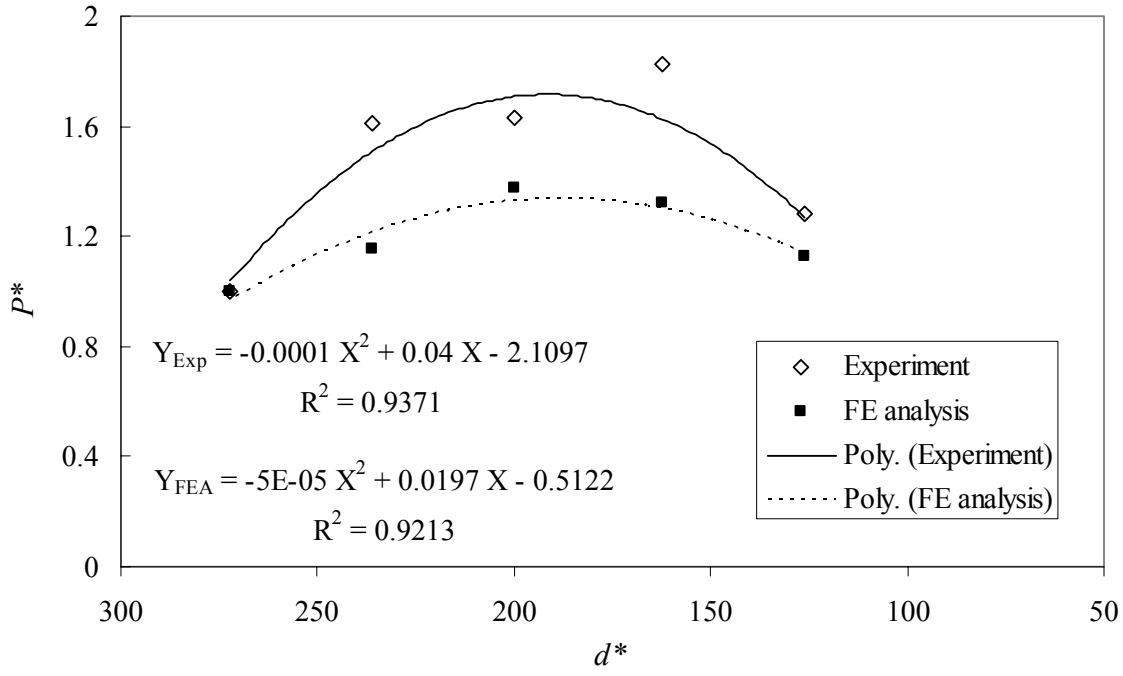

Figure 3-81. Non dimensional snap-back results of the general elliptical set

In the case of snap-through, Figure 3-80, analytical predictions capture the linear observed trend associated to the test results. While in the case of snap-back, Figure 3-81, the "transverse-side stiffening effect" predicted by the analysis does not capture the exact behavior demonstrated in the test results. Meanwhile, it is noticed that reducing the minor axis of the ellipse provides similar influence on stability characteristics to that of reducing the width of the rectangular

Similar conclusions can be made when comparing analytical predictions with test results in the case of bi-elliptical group. Meanwhile, it is interesting to investigate the influence of shape migration from elliptical to bi-elliptical. Therefore, the snap-through and snap-back test data are used to construct Figures 3-82 and 3-83, respectively. Both geometry follow similar trends in case of snap-through and snap-back. The effect of the geometric migration is more pronounced in the case of snap-back as the critical load of specimen #4 is nearly 20% larger than the corresponding specimen from the elliptical group. Finally, the "transverse-side stiffening effect" is more pronounced in both geometries than in the rectangular case.

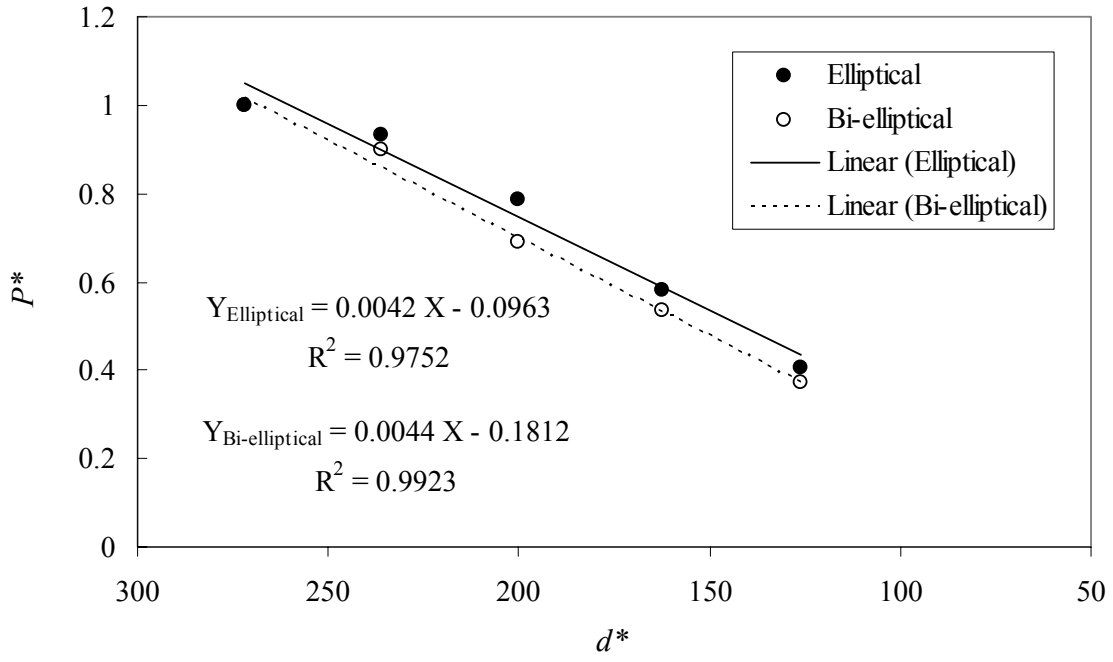

Figure 3-82. Non dimensional snap-through results, elliptical vs. bi-elliptical

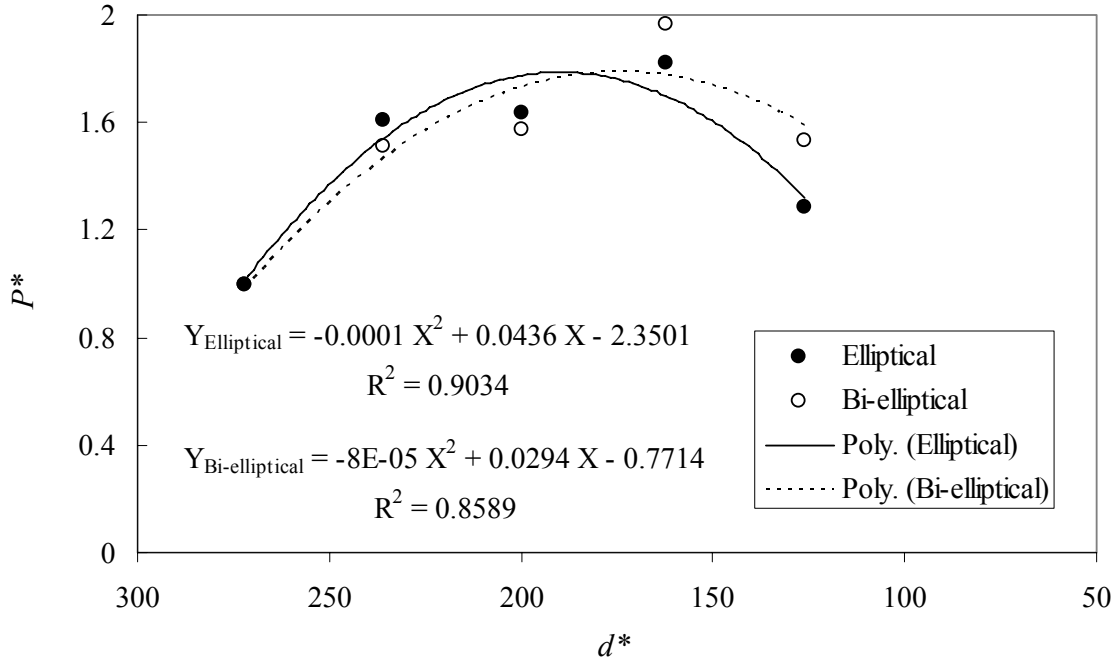

Figure 3-83. Non dimensional snap-through results, elliptical vs. bi-elliptical

When comparing the results of straight edge and round edge categories it is observed that numerical predictions in the case of straight edge category is closer to their test results. This difference can be explained in terms of specimens manufacturing process. Recalling that round edge specimens were cut from their respective panels using a computerized waterjet machine while straight straight edges specimens are cut from their respective panels using a diamond cutter. Waterjet cutting involves submerging the panels in water resulting in unavoidable effects due to moisture absorption. This effect is more pronounced in snap-back results than snap-through.

3.4 Conclusions

An apparatus and test method has been designed and applied to the measurement of critical loads for snap-through and snap-back to set of laminates with straight and curved edges. The apparatus and test minimize friction effects via an air cushion design.

The developed finite element analysis methodology and its predictions provided similar trend effects as test data. Quantitative agreement for snap-through loads is consistently closer than their snap-through counterparts.

Correlation of straight edges specimen and curved edges specimen sets into single curves provides a generalized means for predicting critical loads associated with snap-through and snap-back behavior across geometries.

CHAPTER 4

INDUCING SNAP-THROUGH BEHAVIOR THROUGH ACTUATION

4.1 Introduction

A bistable composite laminate requires an external source, in the form of forces or moments, to trigger its snap-through behavior. One way to trigger snap-through action and hence provide morphing capabilities to a bistable panel is by attaching piezoelectric actuators to its surface. In such a design an electric potential is applied to the piezoelectric actuators to trigger snap-through behavior of the panel/actuator assembly. However bonding an actuator to a bistable panel may significantly affect its shape, i.e. curvature. This change in shape will consequently affect the panel's stability characteristics and may cause it to cease to snap-through. Therefore, in this context, the main challenge in providing actuation of bistable panels is to optimize the actuator performance while conserving their stability characteristics. The ABAQUS finite element methodology, presented in Chapter 2 and 3, is extended and employed as a tool to design a morphing unsymmetric panel/actuator(s) assembly. As an outcome of this design tool a new method is suggested for bonding the actuator(s) to the bistable panel. This method seeks to preserve the bistable behavior of the panel while optimizing actuator's performance. Accordingly a morphing panel is manufactured and tested in order to evaluate both the analysis and the manufacturing techniques.

Schultz and Hyer [45] used Macro-fiber Composite (MFC) actuators to trigger snap-through in an unsymmetric panel. MFC actuators are stiff and found to greatly decrease the panel curvature when bonded to its surface. The current study investigates the use of

two actuator types, namely MFC and Polyvinylidene Fluoride (PVDF) piezoelectric actuators. PVDF is commercially available in various film thicknesses; hence suitable for fabrication into complex shapes. Typical properties of a piezoelectric PVDF film are provided in Table 4-1. The properties for MFC actuators are provided in Table 4-2.

Table 4-1 Piezoelectric (PVDF) film properties, [4]

		Property	Units
Thickness		9, 28, 52, or 110	μm
Piezo Strain Constants	d_{31}	23×10^{-12}	m/V
	d_{33}	-33×10^{-12}	m/V
Young's Modulus	Y^E	2-4	GPa
Max Operating Voltage	V_{max}	30	V/μm
Breakdown Voltage		80	V/μm

Table 4-2 Macro-Fiber Composite (MFC) piezoelectric actuators properties, [3]

		Property	Units
Thickness		300	μm
<u>High-field (|E| > 1kV/mm)</u>			
Piezo Strain Constants	d_{33}	460×10^{-12}	m/V
	d_{31}	-210×10^{-12}	m/V
<u>Low-field (|E| < 1kV/mm)</u>			
Piezo Strain Constants	d_{33}	400×10^{-12}	m/V
	d_{31}	-170×10^{-12}	m/V
Young's Moduli	Y_1^E	30.336	GPa
	Y_2^E	15.857	GPa
Shear Modulus	G_{12}^E	5.515	GPa
Poisson's ratio	ν_{12}	0.31	
Max Operating Voltage	V_{max}	1500	V
		-500	V

4.2 Analysis and Modeling

A simple model is developed to assess actuator performance. In this model piezoelectric actuator(s) are used to control the tip displacement of an unsymmetric composite cantilever beam. This allows identifying the controlling parameters that govern the morphing panel design. Guidelines in terms of actuator parameters are extracted and used to form a basis to design a morphing panel.

Piezoelectric actuators are used to provide extension/contraction as shown in Figure 4-1. An actuator will shrink or expand depending on the polarity of the applied electric potential through the thickness. PVDF actuators are transversely isotropic in terms of material properties, and their electrodes are aligned parallel to one direction only, referred

to as actuation direction. On the other hand MFC actuators possess orthotropic mechanical and piezoelectric properties.

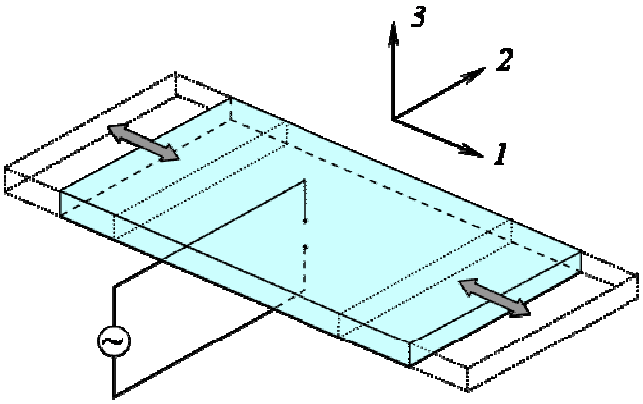

Figure 4-1. PVDF actuator in an extension actuation mechanism

A thermal analogy approach [13, 48] is used to model piezoelectric behavior. In this analogy an applied electric field is modeled as a thermal load while equivalent piezoelectric constants are used to replace the thermal expansion coefficients. Equivalent piezoelectric constants can be easily derived in the case of extension actuation mechanism, i.e. where the electric field and poling is through the thickness. The three-dimensional thermo-elastic strain-stress relations are given by

$$\{\varepsilon\} = [S]\{\sigma\} + \{\alpha\}\Delta T \tag{4.1}$$

where $\{\varepsilon\}$ are the total strains, [S] is the compliance matrix, $\{\sigma\}$ the mechanical stresses, $\{\alpha\}$ the thermal expansion coefficients and ΔT the temperature difference.

A similar equation can be written in the case of extension actuation mechanism, i.e. only the electric potential ψ_3 across the thickness is nonzero

$$\{\varepsilon\} = [S]\{\sigma\} + \{d\}\frac{\psi_3}{t} \tag{4.2}$$

where $\{d\}$ is the piezoelectric strain coefficient vector and t is the piezoelectric actuator thickness.

Relationships establishing a thermal analogy of piezoelectric actuator response are achieved by comparing Equations (4.1) and (4.22). For a given actuator, the piezoelectric strain coefficient vector can be used to provide the equivalent thermal expansion coefficients

$$\alpha_1 = \frac{d_{31}}{t},\ \alpha_2 = \frac{d_{32}}{t},\ \alpha_{12} = 0,\ \Delta T = \psi_3 \tag{4.3}$$

This approach is well suited for finite element formulation. Modeling electric actuation of an orthotropic piezoelectric actuator based on the thermal analogy approach can be performed easily in ABAQUS.

Cantilever beam configuration

The stability characteristics of unsymmetric cross-ply rectangular panel, shown in Figure 4-2, were investigated in [50, 52] and Chapter 3. Analytical results reported a sidelength-to-thickness ratio below which the rectangular laminate ceases to possess two equilibrium configurations, i.e. become mono-stable. The laminate will cease to maintain the equilibrium configuration identified by being curved along the shorter side, and retain only the equilibrium configuration associated with being curved along the longer side. This characteristic is basis for determining the dimensions of an unsymmetric panel with small width-to-thickness ratio. This panel is used in a cantilever beam setup curved along its length. The curvature can be controlled by attaching two layers of actuators to both the top and bottom surfaces of the laminate.

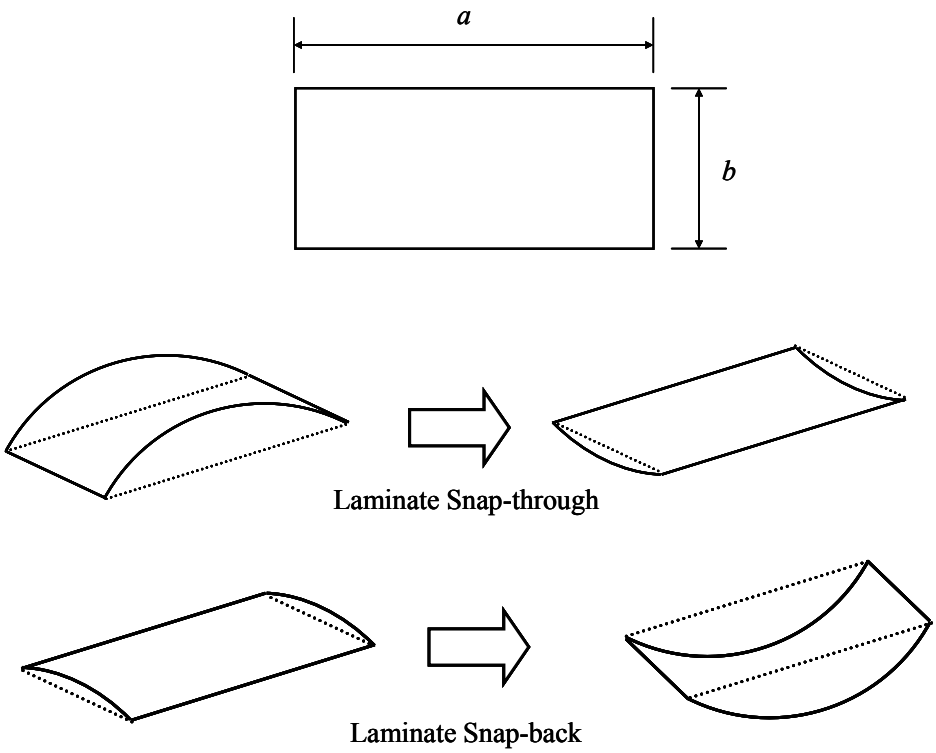

Figure 4-2. Cured shapes of a rectangular laminate with unsymmetric stacking

A schematic of a bonded cantilever laminate with actuators bonded to its top and bottom surfaces is shown in Figure 4-3. The laminate/actuator beam has length L = 200 mm, width w = 10 mm and total thickness t. The unsymmetric cross-ply laminate has two plies each of thickness t_{layer} while each piezoelectric actuator has a thickness t_{piez} as shown in the cross section detail of Figure 4-4.

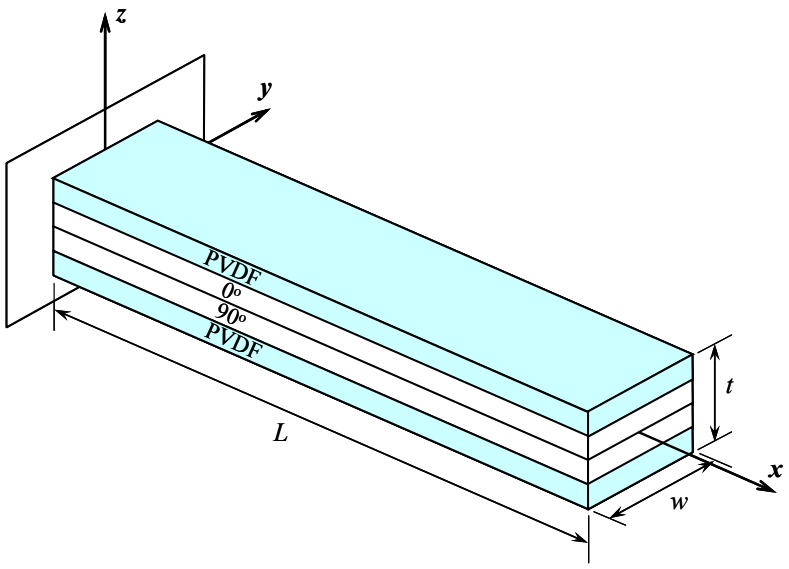

Figure 4-3. Laminate/actuator assembly as cantilever beam

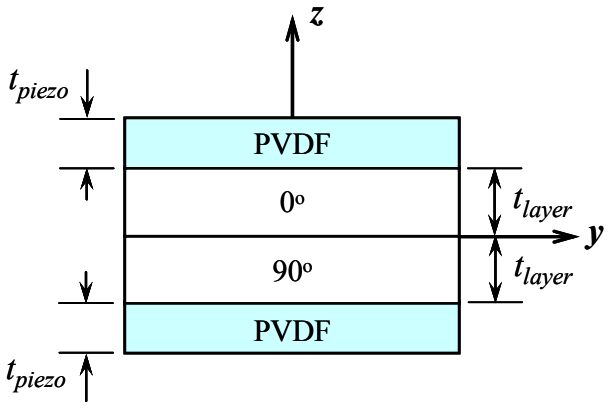

Figure 4-4. Cantilever beam cross-section detail

The curvature κ of the cured laminate before attaching the actuators corresponds to a tip deflection d_i. Assuming actuators are perfectly bonded to the laminate in its straight configuration, i.e. before curing. Upon bonding the actuators to the laminate its initial curvature will decrease and consequently the tip deflection will be reduced from d_i to d_o,

as shown in Figure 4-5. The deformed shape of the laminate/actuator assembly is assumed to conform to a cylindrical surface and its curvature κ can be controlled by the actuators and used to evaluate their performance.

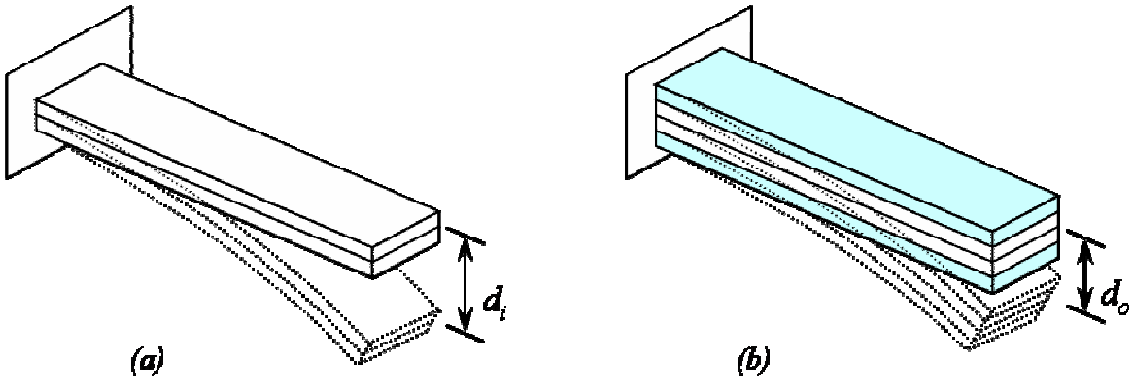

Figure 4-5. (*a*) Cured cantilever laminate with unsymmetric stacking (*b*) Bonded laminate/actuator assembly (no actuation)

Figure 4-6 shows a laminate/actuators assembly with the electric potential being applied through the thickness of each actuator to cause the top actuator to contract and the bottom one to extend. Actuation in this sense, termed direct actuation, results in reducing the beam curvature and minimizes the tip deflection or even cause the beam to acquire an opposite curvature. Two factors control the beam curvature namely the actuator thickness and the level of actuation, i.e. applied electric potential. Causing the assembly to curve in the opposite direction is of no significance and successful actuation will be based on reducing its curvature to zero. This problem is studied initially utilizing PVDF actuators. They will be subsequently replaced by MFC actuators for performance comparison.

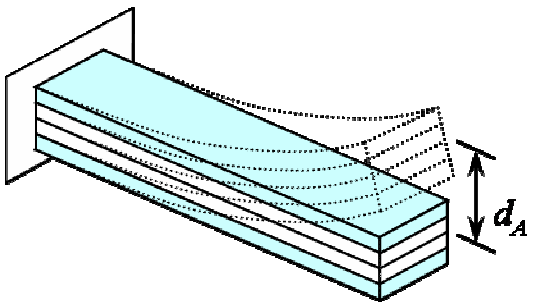

Figure 4-6. Laminate/actuator assembly in direct actuation

Beam Theory (BT) Model

The engineering beam theory is used to calculate the beam curvature due to thermal loads representing the curing cycle and actuation potential, respectively.

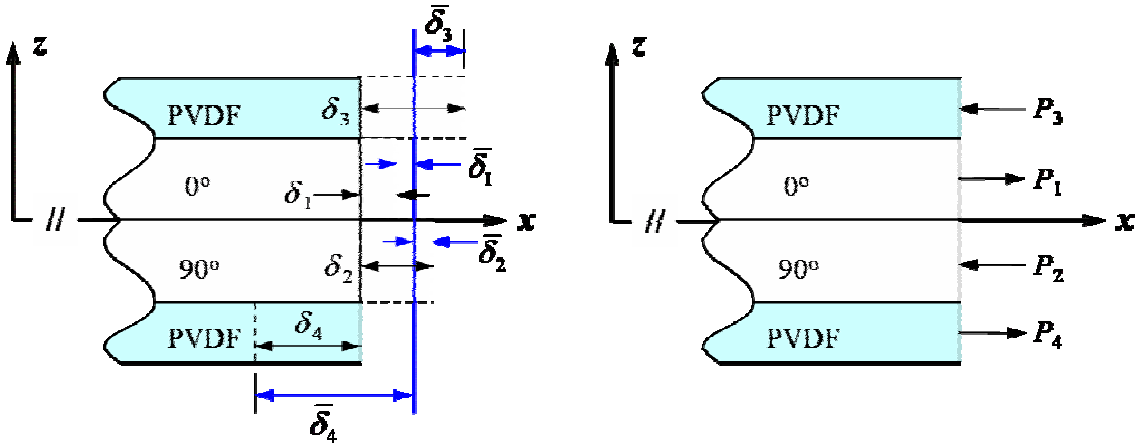

Figure 4-7. Forces and displacements in the beam due to thermal and electric loads

From equilibrium of forces acting on the composite laminate layers and piezoelectric actuator layers, as shown in Figure 4-7

$$P_1 - P_2 - P_3 + P_4 = 0 \tag{4.4}$$

Using thermal analogy and assuming perfect bonding the tip extension δ can be written as

$$\begin{aligned}\delta &= \delta_3 - \bar{\delta}_3 = \alpha_p \, \Delta V \, L - \frac{P_3 \, L}{E_p \, A_p} \\ &= \delta_1 + \bar{\delta}_1 = \alpha_1 \, \Delta T \, L + \frac{P_1 \, L}{E_{11} \, A_c} \\ &= \delta_2 - \bar{\delta}_2 = \alpha_2 \, \Delta T \, L - \frac{P_2 \, L}{E_{22} \, A_c} \\ &= -\delta_4 + \bar{\delta}_4 = -\alpha_p \, \Delta V \, L + \frac{P_4 \, L}{E_p \, A_p}\end{aligned} \tag{4.5}$$

where E_{11} and E_{22} denote Young's moduli of the composite ply in the principal material directions respectively, α_1, α_2 the corresponding thermal expansion coefficients, E_p the Young's modulus of the PVDF actuators, α_p the equivalent thermal expansion coefficient, A_c the cross-sectional area of a single composite lamina, and A_p the cross-sectional area of a single PVDF layer.

For effective actuation, the moments in the unsymmetric laminate due to the thermal loads associated with the cure cycle, should be balanced by the moment introduced by the piezoelectric layers upon actuation.

$$\kappa = \frac{M^T + M^E}{EI} \tag{4.6}$$

where M^T denote the bending moment due to curing, M^E the bending moment due to actuation and EI the total equivalent flexural stiffness of the bonded laminate/actuators assembly.

The mechanical properties of Hexcel IM7/8551-7 graphite/epoxy prepreg are used throughout the analysis, provided earlier in Table 2-1 and repeated in Table 4-3 for convenience. The maximum curing temperature is 177^{o}C and the room temperature is 21^{o}C.

Table 4-3 Elastic properties for Graphite/Epoxy prepreg

Material	E_{11} (GPa)	E_{22} (GPa)	G_{12} (GPa)	ν_{12}	α_1 (10^{-6}/°C)	α_2 (10^{-6}/°C)	t (μm)
IM7/8551-7 Graphite/Epoxy Prepreg	141.18	7.20	4.45	0.30	0.14	30.98	138.75

The curvature is obtained using beam theory at values of curing cycle temperature and applied electric potential. Two limiting cases provide physical understanding of actuator response, namely no actuation and full actuation. The case at no actuation represents the stiffening effect associated with bonding the actuators to the unsymmetric laminate with no applied electric potential. While in the full actuation case the maximum operating voltage is applied. Figures 4-8 and 4-9 provide surface plots representing the curvature, κ_x, as a function of ply thickness t_{layer} and the PVDF layer thickness t_{piezo} for no and full actuation, respectively.

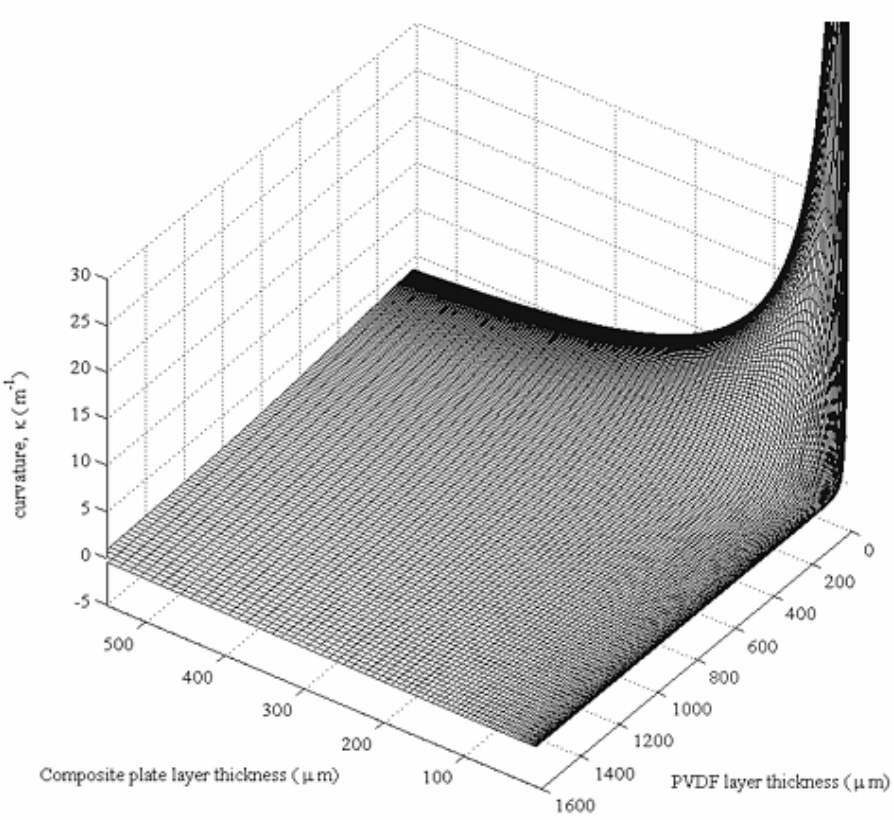

Figure 4-8. Beam curvature, κ_x, obtained from BT as a function of t_{layer} and t_{piezo} (case of no actuation)

The stiffening effect due to bonding the actuators to the panel can be seen in Figure 4-8 as the curvature decreases with the increase in actuator's thickness. While the actuation effect can be seen in Figure 4-9, as the curvature decreases beyond zero and reaches negative values.

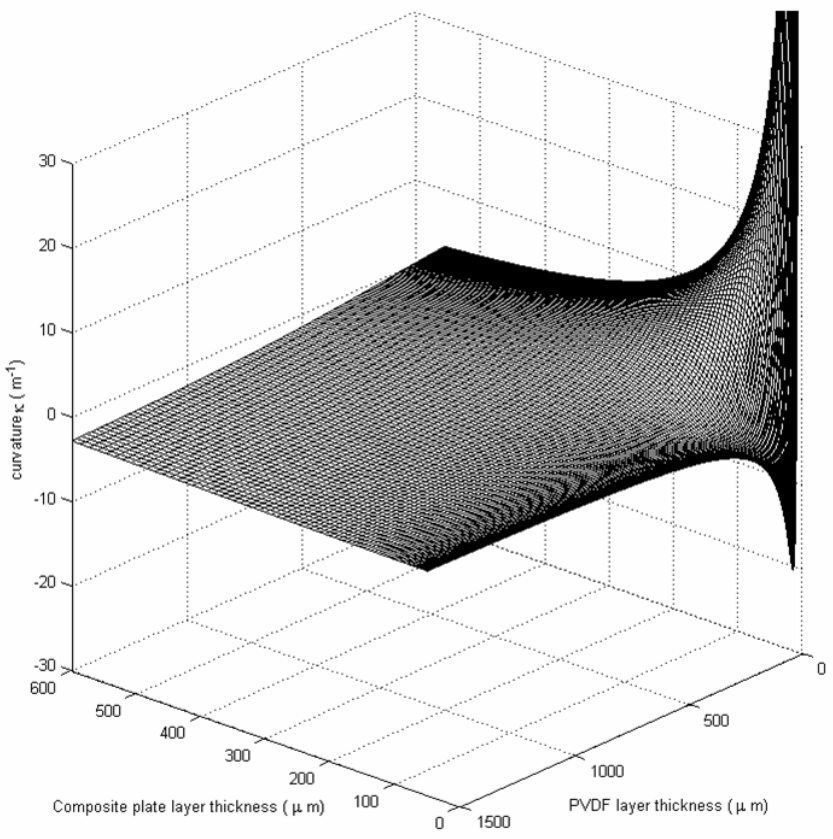

Figure 4-9. Beam structure curvature, κ_x, obtained from BT as a function of t_{layer} and t_{piezo}, (case of full actuation)

Extended Classical Lamination Theory (ECLT)

The Rayleigh-Ritz energy based extension to the Classical Lamination Theory accounting for geometrically nonlinear strain-displacement model is adopted. This analysis is developed by Schultz and Hyer in [45] and its details can be found in their work.

Similar curvature plots to those obtained using Beam Theory are obtained employing the ECLT and shown in Figure 4-10 for no actuation and Figure 4-11 for full actuation. Similar trends regarding stiffening and actuations effects can be observed in the ECLT results.

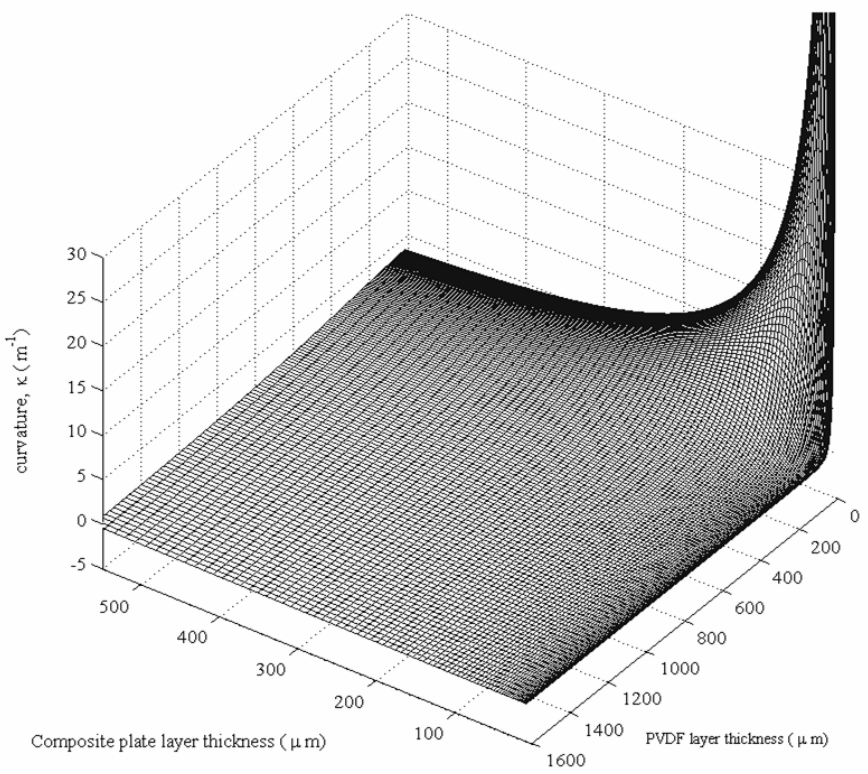

Figure 4-10. Beam curvature, κ_x, obtained from ECLT as a function of t_{layer} and t_{piezo} (case of no actuation)

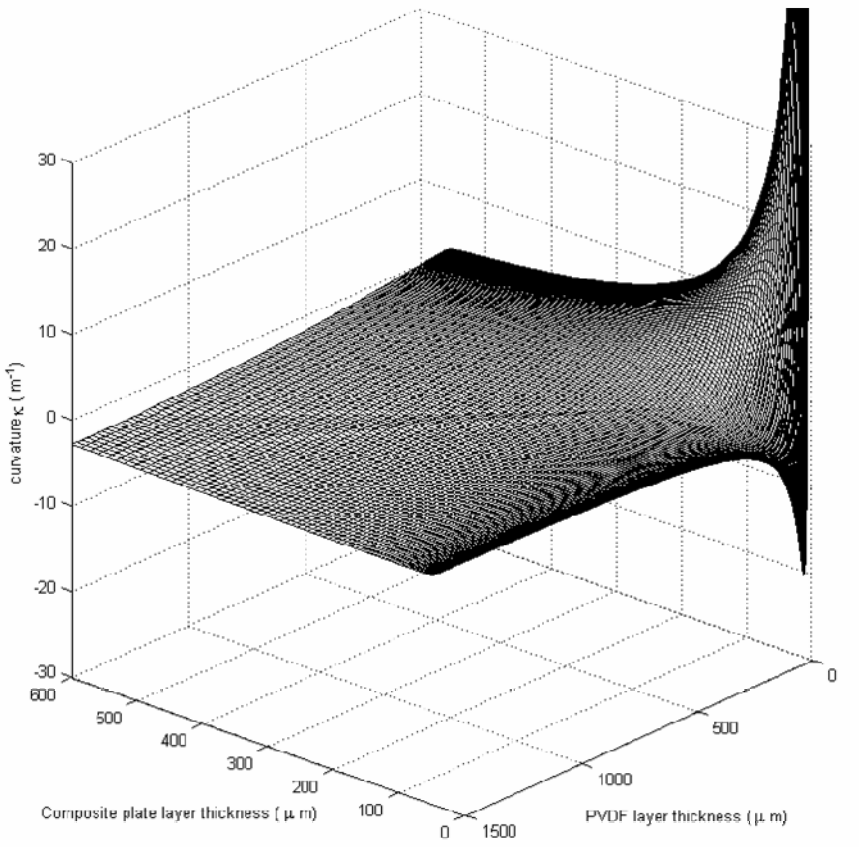

Figure 4-11. Beam curvature, κ_x, obtained from ECLT as a function of t_{layer} and t_{piezo}, (case of full actuation)

ABAQUS Finite Element Analysis

The beam/actuator assembly is modeled in ABAQUS finite element software for two cases. In the first case the nominal thickness of a composite ply is approximated as 100 μm and in the second case the thickness is chosen to be 300 μm. The cases of 100 and 300 μm of single ply thickness correspond to sidelength-to-thickness ratios of 50 and 16.67, respectively. Therefore neither one of those cases represents a bistable panel as the critical sidelength-to-thickness ratio is 82.88 as provided in Chapter 2. The finite element model used a total of 240 shell elements S4R to represent the three layers, i.e. the unsymmetric panel and the top and bottom actuators. A comparison of the actuator stiffening effect predicted using BT, ECLT and ABAQUS models at t_{layer} = 100 μm is

provided in Figure 4-12. The results obtained from all three methods are in good agreement.

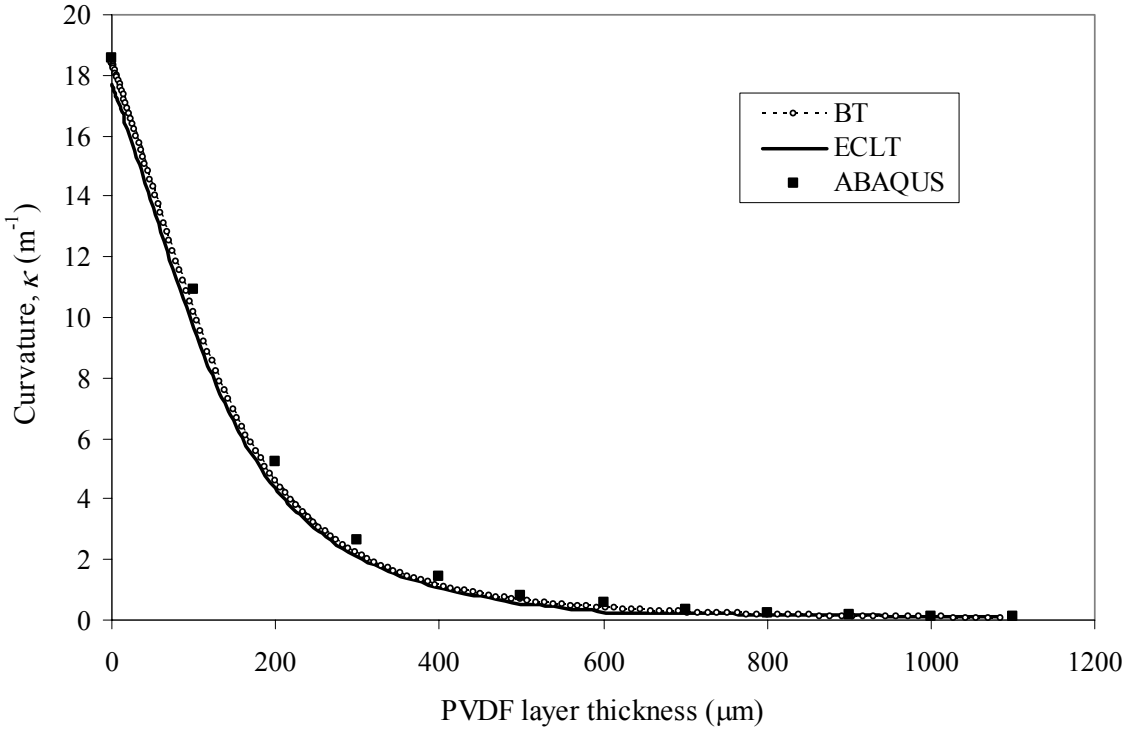

Figure 4-12. Curvature, κ_x, obtained from BT, ECLT and ABAQUS for t_{layer} = 100 μm, (case of no actuation)

Similar trends among all three models for the case of, t_{layer} = 300 μm are observed as shown in Figure 4-13.

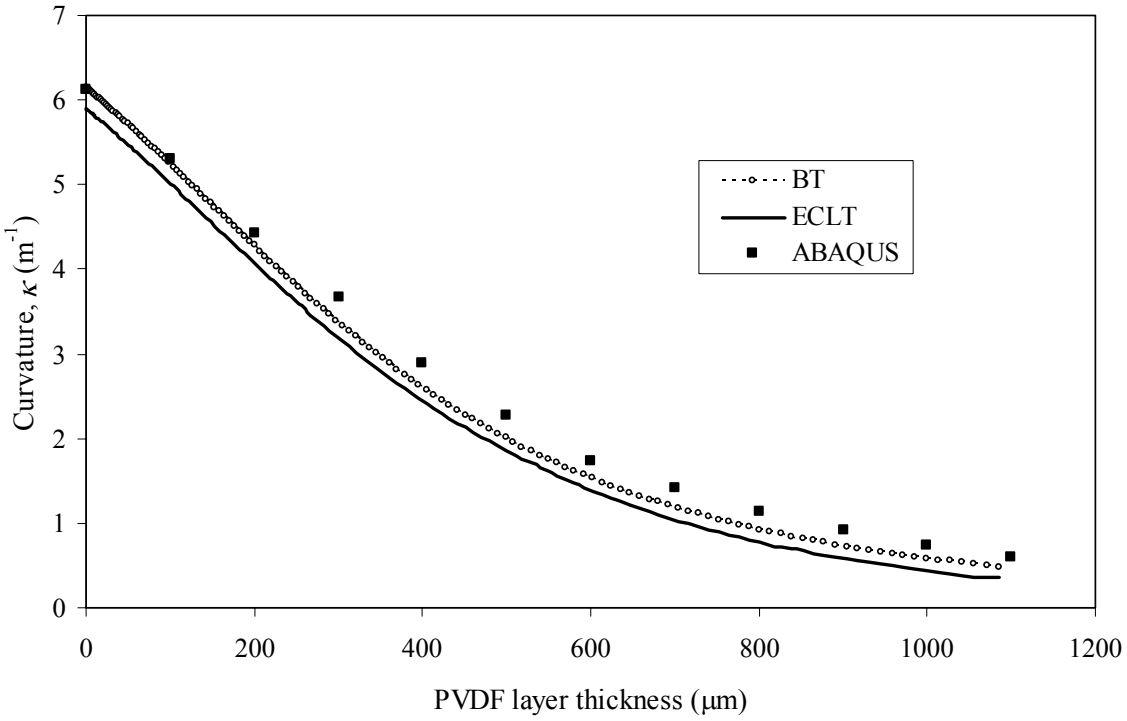

Figure 4-13. Curvature, κ_x, obtained from BT, ECLT and ABAQUS for t_{layer} = 300 μm, (case of no actuation)

An electric potential at V_{max} is applied in both cases, t_{layer} = 100 and 300 μm, in order to investigate the effect of actuation and the results are shown in Figures 4-14 and 4-15, respectively. In both cases BT and ABAQUS results are in good agreement. While values of curvature obtained from the ECLT are in good agreement except in the vicinity of zero curvature. Two steps in curvature are observed at both the beginning and the end of a zero curvature plateau.

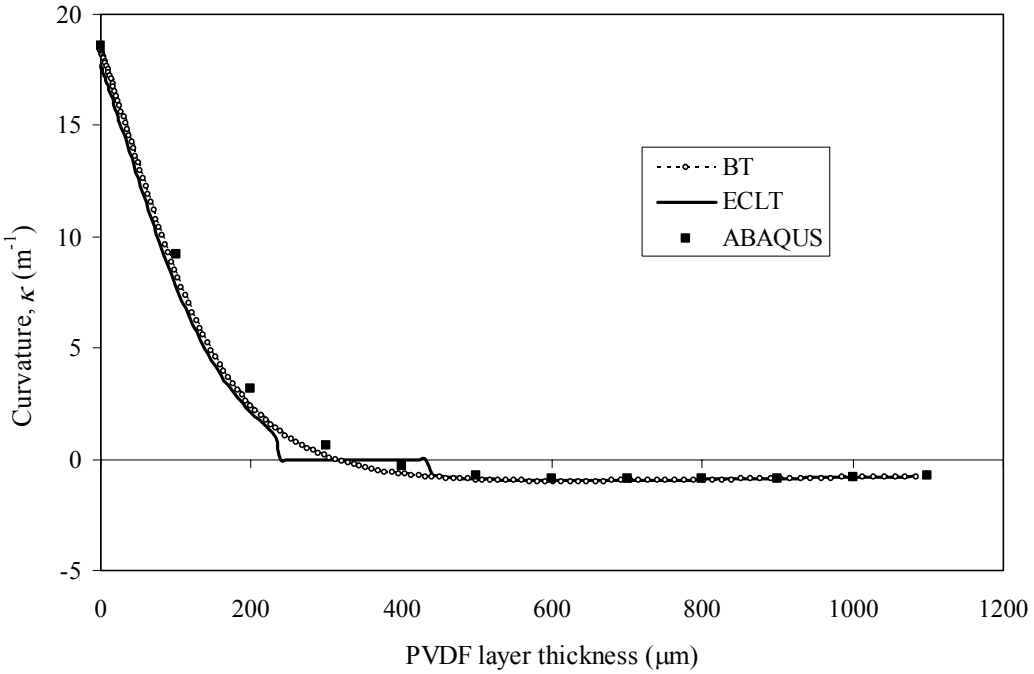

Figure 4-14. Curvature, κ_x, obtained from BT, ECLT and ABAQUS for t_{layer} = 100 μm, (case of full actuation)

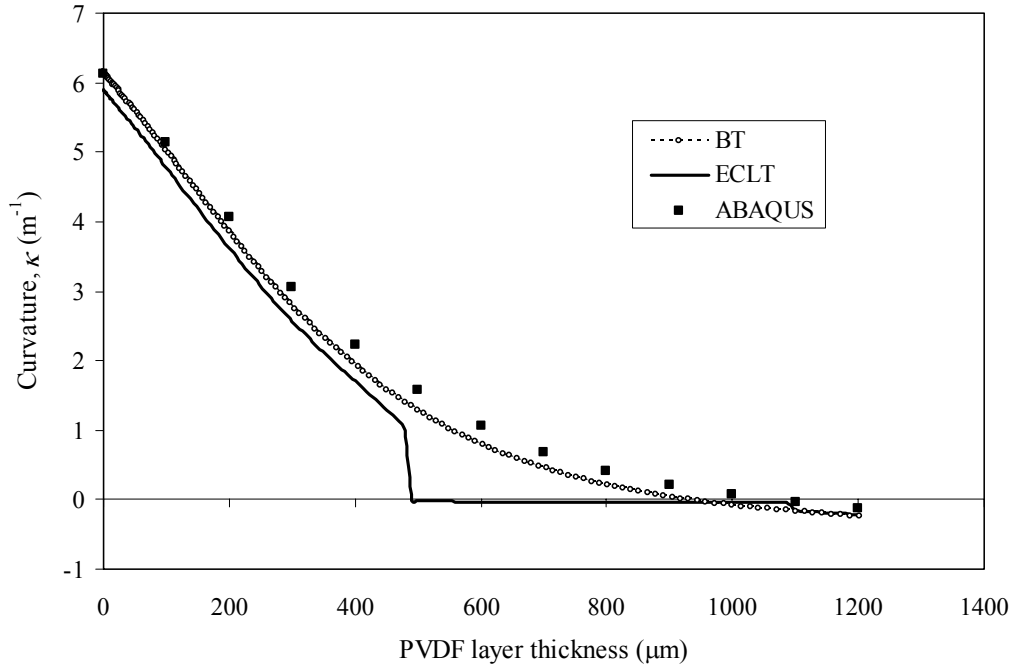

Figure 4-15. Curvature, κ_x, obtained from BT, ECLT and ABAQUS for t_{layer} = 300 μm, (case of full actuation)

Inspecting the numerical values of curvatures predicted by the ECLT in both cases it is found that at the first step, the curvature along the length of the beam, κ_x, changes from ~1 m^{-1} to nearly zero. The associated curvature in the width direction, κ_y, changes from being nearly zero to ~ -1 m^{-1} indicating snap-through from one equilibrium shape to the other.

In an effort to shed insight into this behavior, the curvatures, κ_x and κ_y, predicted by the ECLT using a 4-term displacement field for a thin [0/90] rectangular panel was considered. The panel is manufactured from Hexcel IM7/8551-7 graphite/epoxy prepreg. The length of one side was maintained constant while the other was varied. The sidelength-to-thickness ratio was intentionally decreased to values less than the critical. Analytical results obtained from the ECLT show no dependency on the sidelength-to-thickness ratio and the cured laminate maintained two equilibrium shapes for all vlaues. These results are in disagreement with the test observations and finite element predictions provided in Chapters 2 and 3.

Using a 4 term displacement field in the ECLT does not enable a prediction of the critical sidelength-to-thickness ratio at which a rectangular panel will cease to possess two equilibrium configurations. Also, according to the ECLT the beam is in its second equilibrium configuration (flat along the length and curved in the width direction) throughout a plateau of zero curvature. Further increase of the moments developed by the actuators forces the beam to go through same sense bending similar to a retractable tape or tape springs as shown in Figure 4-16. Therefore the zero curvature plateau predicted by the ECLT starts with beam assembly snap-through and ends with a same sense bending. Same sense bending of tape springs is extensively studied in [35, 46]. For illustration purpose the curvature as a function of PVDF thickness obtained using ECLT in Figure 4-14 is regenerated in Figure 4-17 and divided into three zones showing the corresponding schematic beam assembly shapes.

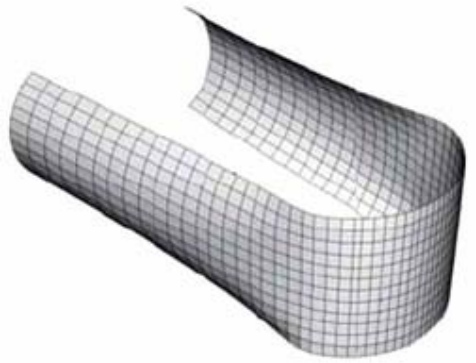

Figure 4-16. Same sense bending in tape springs [35, 46]

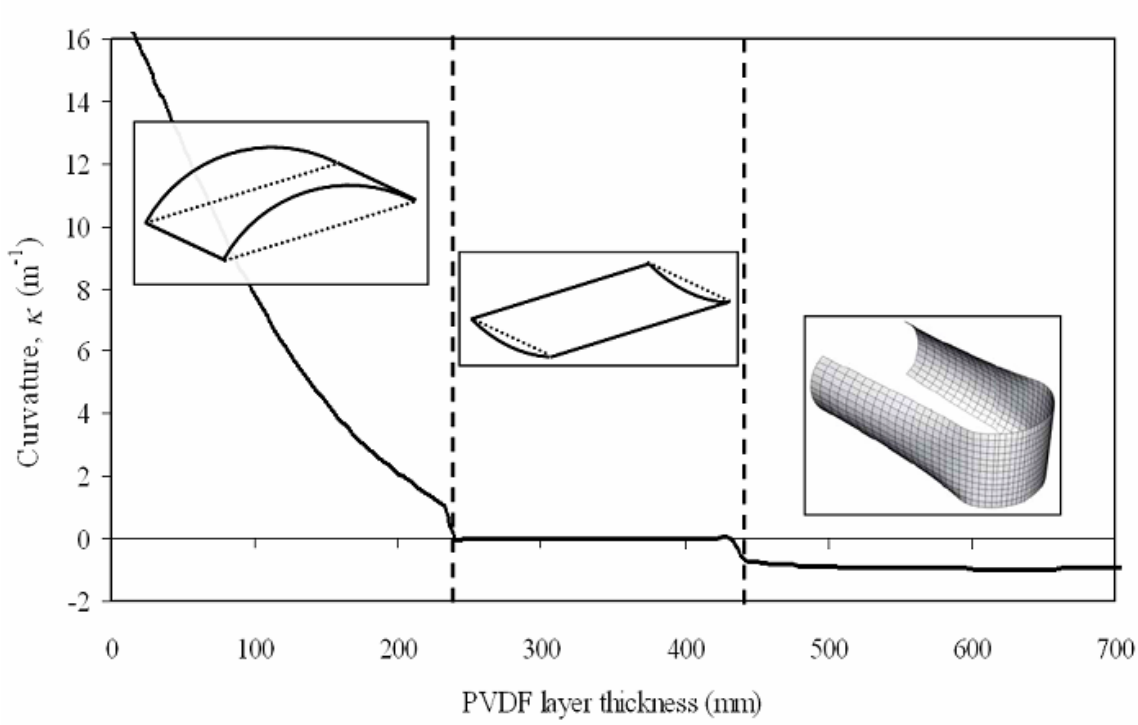

Figure 4-17. Curvature, κ_x, obtained from BT, ECLT and ABAQUS for t_{layer} = 100 μm, (case of full actuation). Corresponding beam assembly shapes illustrated

Table 4-4 provides the thickness of the PVDF layers required for actuation, i.e. for bringing the curvature of the beam/actuators assembly to zero. Also the table includes the initial curvature of the unsymmetric laminate, before bonding PVDF layers to its surfaces, and the curvature of the beam/actuators assembly at no actuation, i.e. V=0.

Table 4-4 PVDF actuator requirements for a composite beam with [90/0] layup

	Ply thickness 100 μm			Ply thickness 300 μm		
	BT	ECLT	ABAQUS	BT	ECLT	ABAQUS
PVDF thickness (μm)	306	239	360	931	788	1060
Initial Curvature (m^{-1})	18.44	17.69	18.56	6.15	5.89	6.13
Curvature upon bonding (m^{-1})	2.1	3.1	1.9	0.681	1.91	0.65

It can be concluded that successful actuation of an unsymmetric laminate with thickness *2t* requires two PVDF actuator layers each of thickness approximately *3t*. Bonding such thick actuators to the unsymmetric laminate leads to nearly 90% loss of curvature. Using thicker actuator layers may lead to causing the laminate to lose curvature entirely. Consequently actuation using PVDF actuator for this problem requires the electric potential to be always at V_{max} in order to keep the actuator thickness to a minimum and consequently decrease the stiffening effect.

A comparison between actuator types is subsequently conducted using the FE analysis in which it was taken into consideration that the MFC actuators are available commercially only in 300 μm thickness. Stiffening and actuation effects are studied for the case of bonding MFC actuators to cantilever beams of ply thicknesses 100 and 300 μm and presented in Table 4-5.

Table 4-5. Actuator comparison for a composite beam with [90/0] layup

	Ply thickness 100 μm		Ply thickness 300 μm	
	PVDF	MFC	PVDF	MFC
Actuator thickness (μm)	360	300	1060	300
Initial Curvature (m^{-1})	18.56		6.13	
Curvature upon bonding (m^{-1})	1.9	0.23	0.65	0.96
Curvature upon actuation (m^{-1})	~0	-4.56	~0	-0.94

Actuator stiffening effect is more pronounced when using MFC actuators. This can be clearly noticed for the case of the 100 μm ply thickness, as the curvature is reduced by 98.7% when using MFC actuators although both actuator types are nearly of the same thickness. Also, in the case of 300 μm ply thickness the curvature is 5% higher for an MFC than PVDF actuator whereas the MFC actuator thickness is approximately one third of its PVDF counterpart. Stiffening effect can be explained in terms of actuator stiffness as the Young's modulus of MFC actuators is one order of magnitude higher than PVDF ones. On the other hand for both 100 and 300 mm thicknesses, MFC actuators have higher actuation authority or effectiveness than PVDF actuators. This is reflected in the resulting curvature using MFC actuators can bring the bistable beam to an opposite curvature.

One can conclude therefore that MFC actuators are more suitable to induce snap-through behavior provided their high stiffening effect is reduced. Due to their high actuation effectiveness they are not required to be of the same size of the actuated panel. Therefore an actuator with a fractional surface area of the actuated panel is adequate, leading to decrease in its stiffening effect. Further reduction could be achieved through the means of bonding the actuator to the bistable panel. Two options were evaluated. The first is to force the curved panel into a flat configuration then bond the actuator to its surface.

While the other option is to bend the actuator causing it to conform to the panel's curvature then bond them together. All the numerical results presented in the present work are associated with the first option. The second option can be simulated in the current FE methodology by applying moments at the edges of the actuators to conform to the panel curvature. Considering only MFC actuators a comparison between both bonding options is presented in Table 4-6 for cantilever beams with thickness of 100 and 300 μm.

Table 4-6. MFC Actuator bonding options comparison

	Ply thickness 100 μm		Ply thickness 300 μm	
	$M = 0$	$M \neq 0$	$M = 0$	$M \neq 0$
Actuator thickness (μm)	300		300	
Initial Curvature (m^{-1})	18.56		6.13	
Curvature upon bonding (m^{-1})	0.23	2.17	0.96	1.24
Curvature upon actuation (m^{-1})	-4.56	-2.62	-0.94	-0.396

Predictions corresponding to the second option of bonding show 10.45% and 4.56% gain of curvature for 100 and 300 μm ply thickness, respectively. These gains decrease with the use of a thicker composite panel. Considering the levels of gain the second option can be adopted when bonding PVDF actuators but this may render them ineffective in terms of actuation.

4.3 Experimental and Analytical Results

In this section the design of an unsymmetric rectangular laminate/actuator assembly is considered based on the actuator assessment obtained from Section 2. A rectangular unsymmetric panel of width 65 mm and length 85 mm is manufactured from

Hexcel IM7/8551-7 Graphite/Epoxy prepreg with a stacking sequence of $[0/90]_T$. The description of its stability behavior follows the schematic of Figure 4-2. Two MFC actuators of dimensions 40 mm × 10 mm are centrally bonded to the top and bottom surfaces of the unsymmetric panel using Loctite's E120 HP Epoxy. The major axis of both actuators was aligned along the shorter dimension of the composite panel. The actuators were bent to conform to the curved surface of the cured panel and the adhesive applied. The panel/actuators assembly is placed in a vacuum bag to maintain its curvature and placed in an autoclave for three hours at 60ºC with the vacuum on to ensure better bonding.

Figures 4-18 and 4-19 show two side-by-side panels with and without assembled actuators for a qualitative comparison of the bonding method.

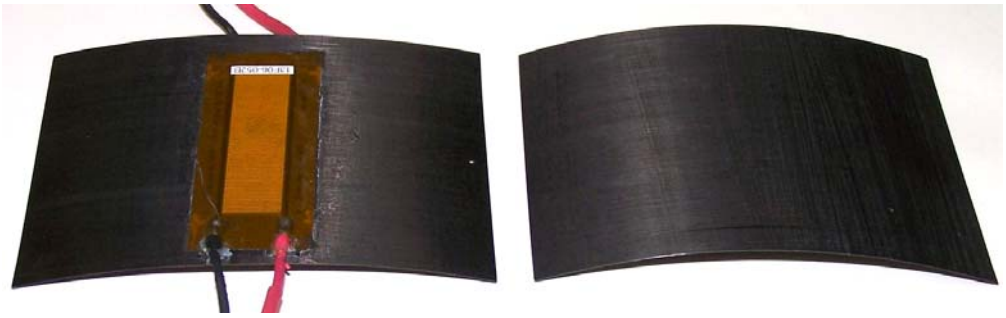

Figure 4-18. Bonded panel assembly vs. same dimension bistable panel (first equilibrium shape)

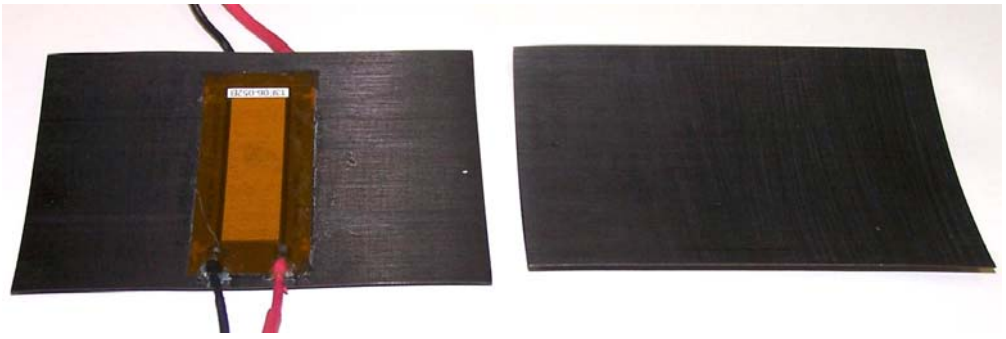

Figure 4-19. Bonded panel assembly vs. same dimension bistable panel (second equilibrium shape)

The experimental setup, shown in Figure 4-20, is used to measure the required voltage to trigger snap-through behavior. It includes three posts, one is used to suspend the panel/actuator assembly by a thread and the other two are used to support the actuators wiring. The setup consists of a variable voltage DC power supply, two miniature DC to High Voltage (HV) converters, a voltmeter and the manufactured panel/actuator assembly. A variable voltage DC power supply, Agilent E3648A, is used to generate a ramp signal. This ramp signal is fed into each of the miniature HV-DC converters, G05 and G15 obtained from AMCO. The isolated output of these HV-DC converters is linearly proportional to the input. The G05 amplifies a 12 V signal to 500 V while the G15 amplifies the 12 V signal to 1500 V, according to the G Series datasheet [6]. Each of these converters weighs 43 grams and has the dimensions of 38.1 mm × 38.1 mm × 16.0 mm. The voltmeter is used to check the amplified voltage applied to the actuators.

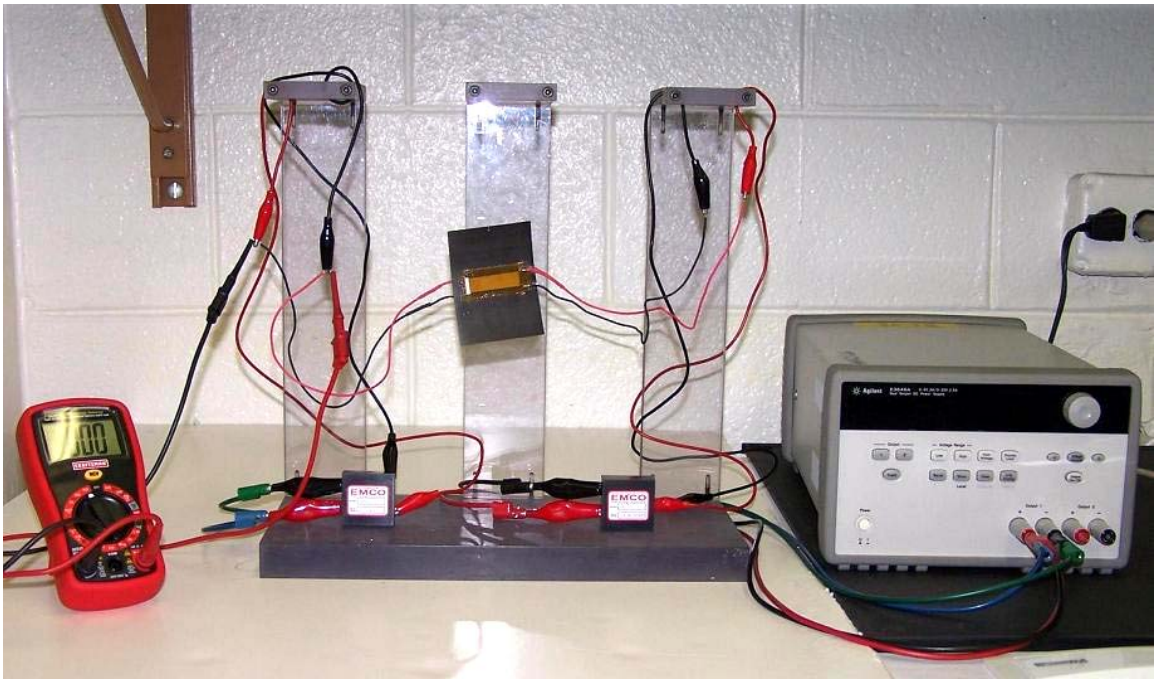

Figure 4-20. Experimental setup for piezoelectric actuation

According to observations in [10, 44] it is noted that an unsymmetric panel undergoes a loss of curvature during the post-cure stage. However this loss of curvature ceases after a limited period of time. On the other hand an unsymmetric panel/actuators assembly is not stress free in either equilibrium configuration due to actuator bonding. Therefore, the loss of curvature phenomenon should not be confused with the effect of bonding the actuators to the panel surface. In the current research, the panel/actuators assembly was snapped back-and-forth several times before performing the experiment. These pre-tests were carried out to eliminate any bias resulting from maintaining the assembly for some period of time in one equilibrium shape rather than the other. The experiment was repeated four times, for both snap-through and snap-back, and the required voltages were averaged and are provided in Table 4-7. Percentage deviations from the averaged values are shown in the same table.

Table 4-7 Voltage requirements obtained from experiment

	Required voltage (V)		Maximum percentage deviation
	Top actuator	Bottom actuator	
Snap-through	–460	1380	± 3.2 %
Snap-back	2217	–739	± 2.6 %

ABAQUS finite element simulation was used to predict the equilibrium shapes of the panel/actuator assembly and the voltage required to trigger snap-through behavior. Four-noded, reduced integration, doubly curved shell elements (S4R) are used to model both the unsymmetric laminate and the actuators. The unsymmetric panel is modeled using 884 elements. While for each actuator 64 elements are used to model its active portion and 156 elements to model its casing. The thermal analogy approach is used to model piezoelectric performance. Moreover, the nonlinear piezoelectric properties of the MFC actuator are incorporated in the thermal analogy model accounting for different ranges of

piezoelectric constants as provided in Table 4-2. Moments are calculated and applied at the actuator edges to simulate bonding in the panel's curved configuration. The three layers of elements representing the unsymmetric panel and the two actuators are tied together making sure to offset their respective neutral axis based on their position in the assembly. The panel/actuators assembly is held fixed in space at the midpoint of the panel by constraining all its degrees of freedom. The displacements of the four corner points are monitored throughout the analysis.

The FE simulation is carried out in several linear/nonlinear analysis steps. A linear eigenvalue buckling problem corresponding to the curing of the unsymmetric panel is solved to obtain the geometric imperfections corresponding to the temperature loads of the cure cycle. Subsequent analysis steps account for nonlinear geometric behavior with artificial damping subroutine. The geometric imperfections are implemented in the model together with moments applied at the actuators' edges to obtain the cured/bonded shape of the panel/actuators assembly. The thermal analogy approach is used by applying temperature loads to the actuators to trigger snap-through or snap-back. The model deforms into a different shape then the applied temperature load is deactivated to realize the second equilibrium shape. The last two steps of temperature application and deactivation are repeated for snap-back by reversing the applied temperature.

The equilibrium shapes of the panel/actuators assembly predicted by ABAQUS FE analysis are shown in Figure 4-21. The equilibrium shapes of the manufactured panel/actuators assembly are shown in Figure 4-22 for qualitative comparison.

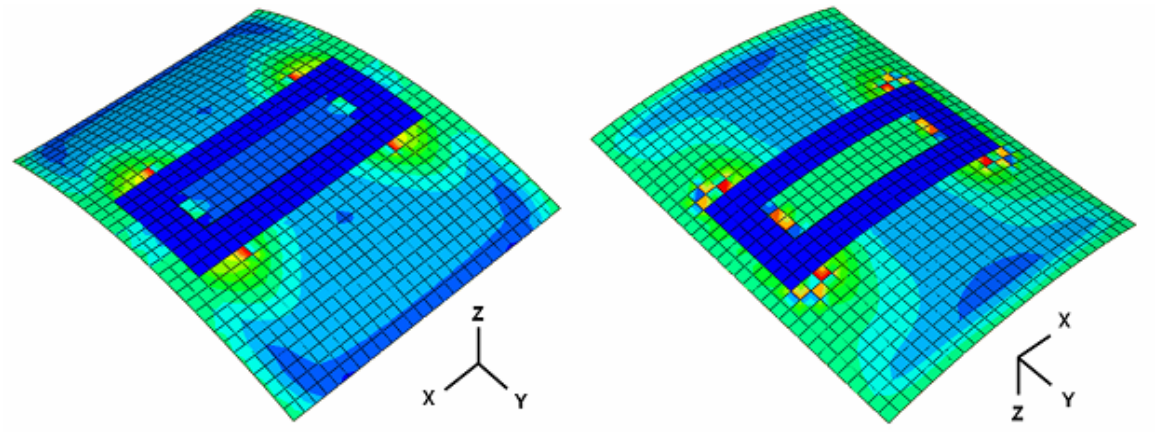

Figure 4-21. Predicted equilibrium shapes of the panel/actuators assembly

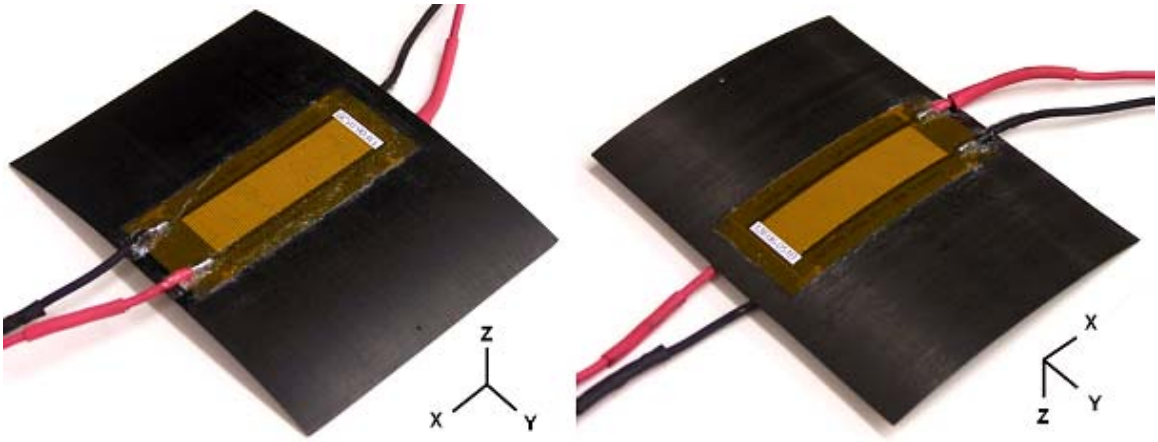

Figure 4-22. Equilibrium shapes of the manufactured panel/actuators assembly

FE predictions of the cured shapes and stability characteristics of an unsymmetric panel and a panel/actuator assembly are obtained as one qualitative measure for the manufacturing method. As shown in Figures 4-21 and 4-22 the actuators are aligned with the x-axis. The κ_y curvature is the curvature of panel/actuator assembly in the first equilibrium shape and κ_x is its curvature in the second shape. Accordingly, these curvatures are predicted for the panel/actuators assembly. A reference case is chosen to be an identical unsymmetric cross-ply panel with no actuators attached to it. Comparisons

of center curvatures between the actuated and the reference panels are provided in Table 4-8.

Table 4-8 Curvature comparison between actuated and reference panels

	Reference panel	Actuated panel
κ_x (m^{-1})	11.20	7.78 (-30.56%)
κ_y (m^{-1})	-11.995	-8.18 (-25.56%)

The loss of curvature due to bonding the actuators, as a percentage of the reference panel curvature, is provided in parenthesis in Table 4-8. The efficiency of the bonding method is indicated by the percentage loss in curvature. Normal to the actuators, the loss of curvature is 25.56% due to the stiffening effect of the narrow side of the actuators. While along the actuators, where the stiffening effect is expected to be a maximum, the loss of curvature is only 30.56%. Therefore bonding the actuators in the curved configuration contributes to minimizing the effect of stiffening on curvature. Although this comparison is useful, it is not accurate in the case of the actuated panel as the panel/actuator assembly is not perfectly cylindrical in either of its equilibrium configurations. Consequently, the out-of-plane deformations of actuated and reference panels are compared in Figures 4-23 and 4-24 for the first and second equilibrium shapes, respectively.

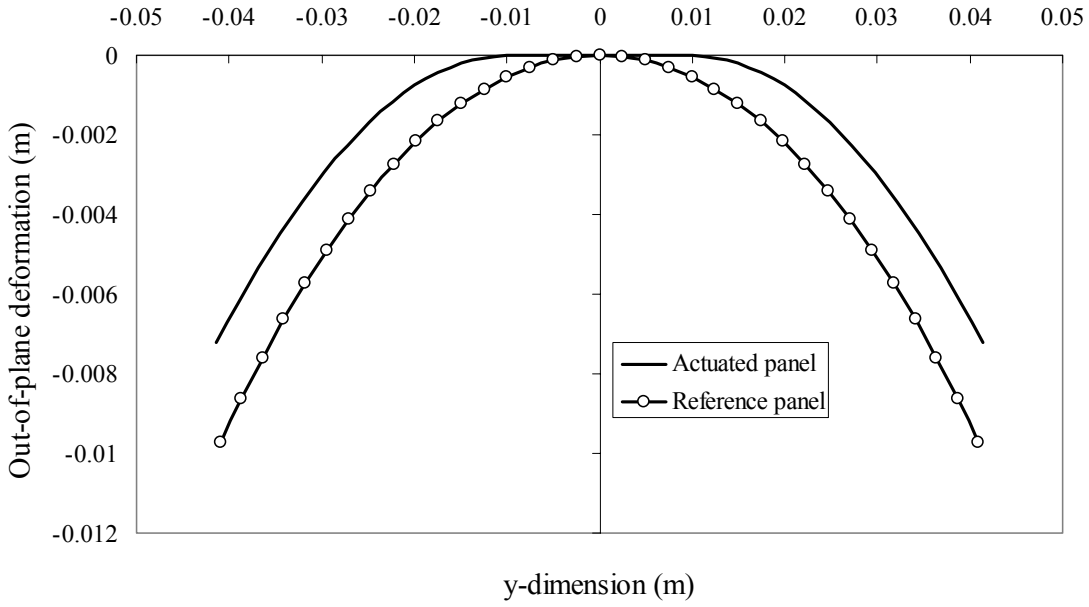

Figure 4-23. Out-of-plane deformation of the first equilibrium shape along y-axis

Figure 4-23 provides the out-of-plane deformation of both panels normal to the actuator at the panel center. The actuated panel flattens at the center where the actuators are bonded. This is indicative of the actuator stiffening effect; the actuators suppressed the curvature along their narrow side. The curved surface of the actuated panel is no longer cylindrical when compared to the reference panel case.

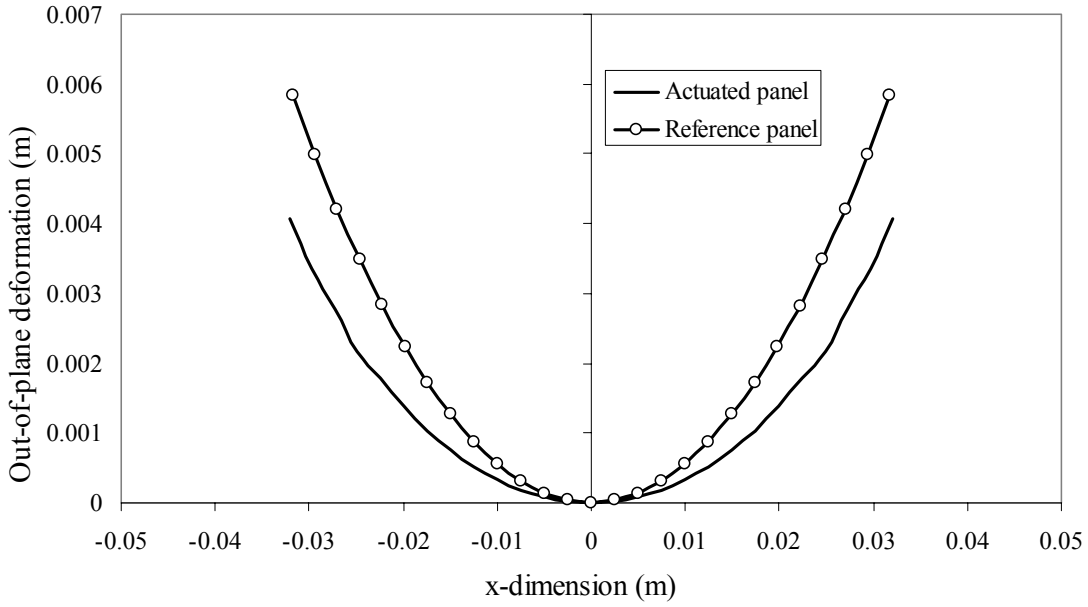

Figure 4-24. Out-of-plane deformation of the second equilibrium shape along x-axis

Figure 4-24 provides the out-of-plane deformation of both panels along the actuator at the panel center. As the actuators are bonded to the panel in the curved configuration the curvature is preserved in this equilibrium shape. If actuators were bonded to the panel in a straight configuration this equilibrium shape would have been eliminated. The stiffening effect is minimized in terms of out-of-plane deformation by utilizing this bonding method.

Another qualitative measure of the suggested bonding technique is to investigate the effect of bonding on the stability characteristics. To this end, the developed FE model is used to predict the response of each panel, actuated and reference, due to a concentrated force applied at the panel's center in the z-direction. The corner points were allowed to move only in the x-y plane but not in the z-direction. Snap-through and snap-back loads are predicted for both panels and provided in Table 4-9.

Table 4-9 Stability characteristics comparison between actuated and reference panels

	Reference panel	Actuated panel
Snap-through load (N)	1.238	0.596 (-51.85%)
Snap-back load (N)	1.783	2.272 (27.43%)

The snap-through load was reduced by 51.85% due to the stiffening effect of the actuators in the y-direction. The stiffening effect is indicated by the flattened portion due to the actuators bonding, Figure 4-23, which amounts to 23.5% of the panel's width. On the other hand the 27.43% increase of the predicted snap-back load is due to the actuator's contribution in stiffening the panel. These quantitative measures in terms of curvature and stability characteristics provide confidence in the used bonding technique.

Finally, the predicted response due to voltage application of the actuated panel is predicted by the developed FE model. The actuator cycle phases starting with voltage application the deactivation followed by reversed polarity application and deactivation, are shown in Figure 4-25. The function of voltage application in direct and reversed polarity is to simulate triggering from snap-through to snap-back. While each voltage deactivation is performed to realize one of the equilibrium shapes of the panel/actuator assembly.

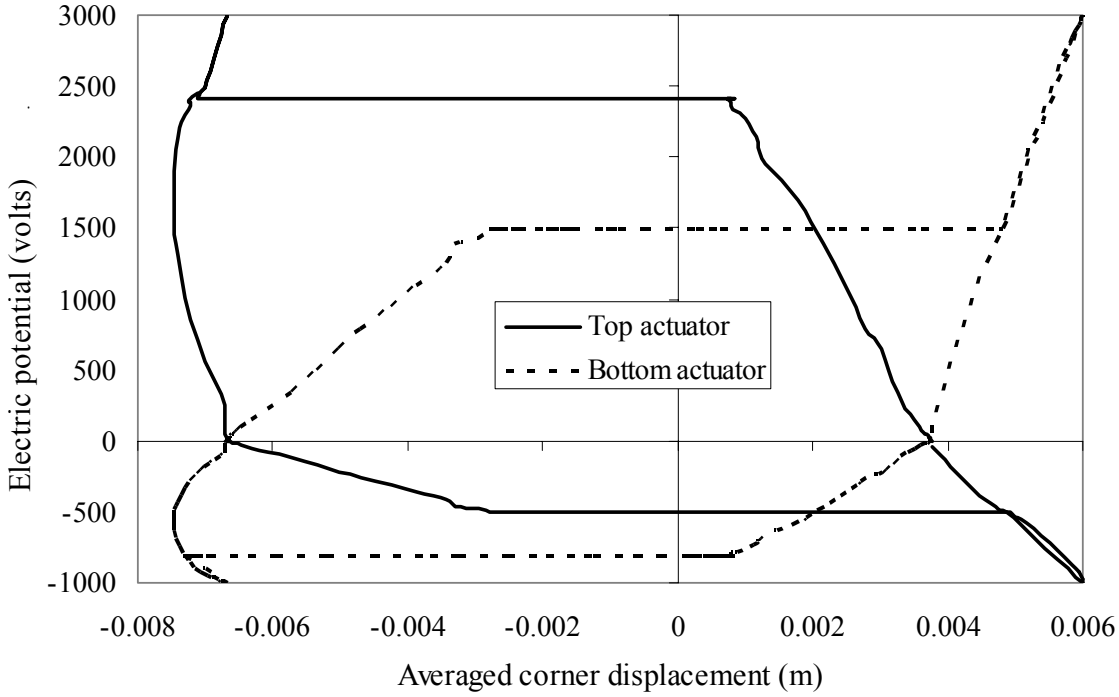

Figure 4-25. The actuators' cycle

The required voltage by each actuator to trigger snap-through and snap-back are delineated from Figure 4-25. The snap-through actuation curve is shown in Figure 4-26, while Figure 4-27 provides the snap-back actuation curve.

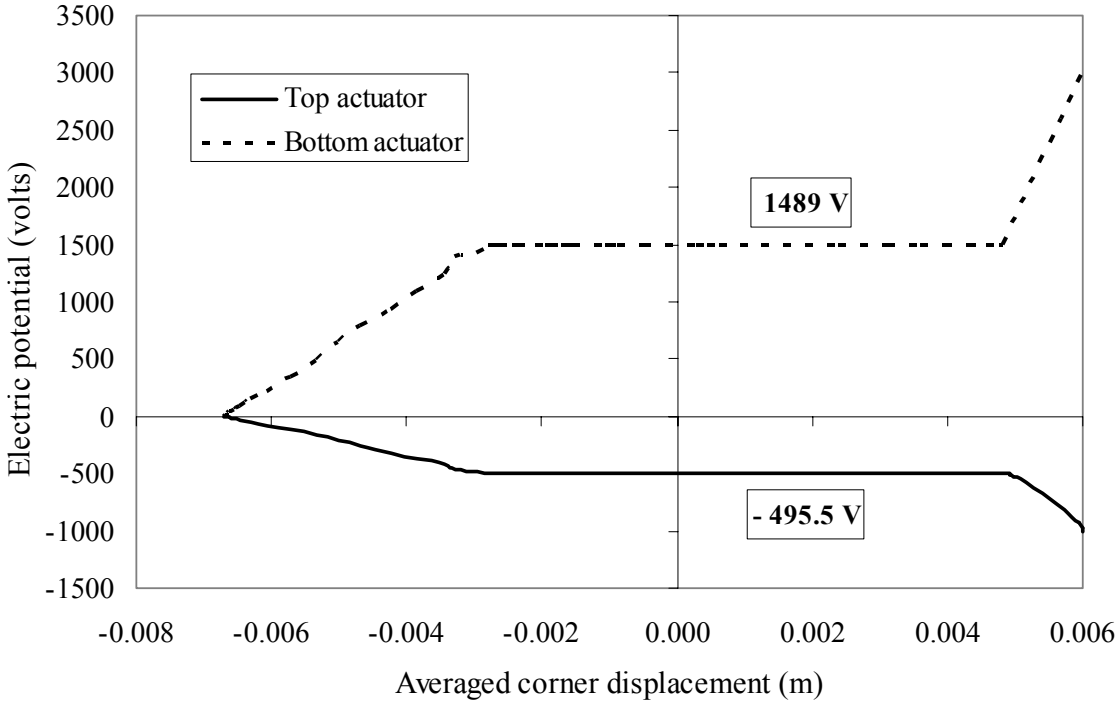

Figure 4-26. Snap-through actuation curve

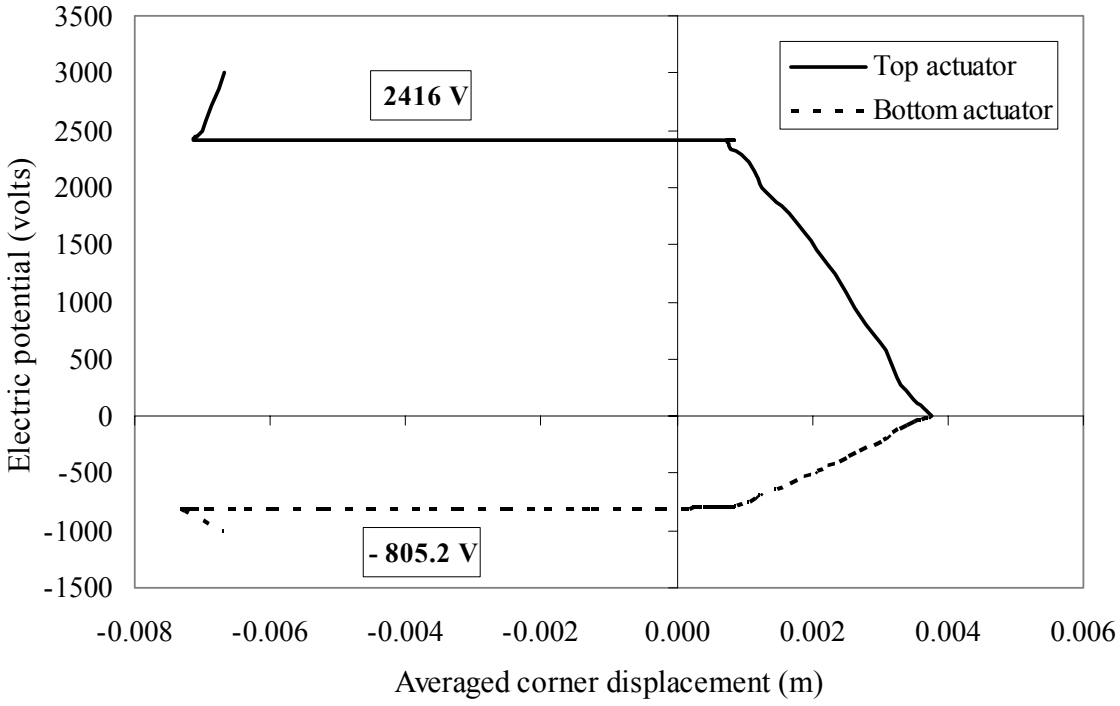

Figure 4-27. Snap-back actuation curve

Table 4-10 provides the predicted values of voltage together with the percentage difference with respect to the averaged experimental values. The electric potential in the FE simulation follows the same linear increase used in the experiment. Furthermore, the ratio of 3:1 of applied voltage, due to using the G05 and G15 amplifiers, is maintained in the simulation. This matching resulted in identical percentage difference in the predicted voltage in both top and bottom actuators in the case of snap-through. Similar observation can be made regarding the percentage difference of predicted values for snap-back.

Table 4-10. Required voltage to trigger snap-through behavior

	Required voltage (V)				Percentage difference
	Top actuator		Bottom actuator		
	Experiment	FEA	Experiment	FEA	
Snap-through	–460	– 495.5	1380	1489	7.89 %
Snap-back	2217	2416	–739	– 805.2	8.97 %

It can be seen from the results in Table 4-10 that trends in predicting the required voltage to trigger snap-through/snap-back behavior are captured by the numerical predictions. Another observation is that the predicted values using the finite element analysis represent an upper bound to the experimentally obtained ones. The differences between the finite elements results and the experiment could be due to the post-cure loss of curvature in unsymmetric panels, the assumption of perfect bonding between the panel and the actuators, the exact alignment of the actuators along the x-direction of the laminate, and/or uncoupled electrical, mechanical and thermal effects during bonding and actuation. Moreover, the presented FE simulation considers all material properties

independent of the cure cycle temperature and does not include any chemical reaction or conservation of heat during the cure simulation part.

4.4 Conclusions

A comprehensive study for design, analysis and manufacturing of morphing composites via piezoelectric actuators has been presented. The developed simplified beam theory model was validated by comparison of results with ABAQUS finite element and the Extended Classical Lamination Theory. The analogy associated with the Extended Lamination Theory for zero curvature was isolated. A comparison between PVDF and MFC actuators is performed leading to pertinent design, manufacturing and analysis guidelines for a rectangular unsymmetric panel/actuators assembly.

In terms of manufacturing it is recommended to bond the actuators with their axis along the shorter side of the rectangular panel in the curved configuration. This allows bonding of actuators to an unsymmetric bistable panel minimizing the loss of its bistable characteristics and better sensitivities snap-through/snap-back response.

In terms of analysis, the previously developed finite element methodology [50, 52] was extended to include actuation via a thermal analogy approach using the same commercial ABAQUS code. The developed provides a suitable tool for both design and analysis of morphing unsymmetric structures. It accurately models actuator bonding to a flat or curved panel, accounting for the actuator nonlinear properties as well as the requirements for inducing snap-through.

In terms of experimental effort, a morphing panel is manufactured and its predicted stability characteristics verified. The panel successfully snapped back-and-forth utilizing two MFC actuators that represented, collectively, only 14% of the panel surface

area. Hence the curvature loss of the unsymmetric panel due to bonding the actuators is kept to a minimum.

The successful actuation of the manufactured panels points to their viability for morphing wing applications to Unmanned Aerial Vehicles (UAV).

CHAPTER 5

POTENTIAL APPLICATION (UAV WING)

5.1 Introduction

Early attempts of flight were inspired by observing birds and/or flying insects forming the early start of the field of biomimetics leading to the attempts to build the first flying vehicle. The continuous progress in this field reflects better understanding of the concept of morphing. Biologically inspired morphing wings are not to be understood as straight forward mimicking of birds and/or flying insects as underscored by McGowan *et al.* [31]. Rather they should be the outcome of learning from nature's time tested designs in order to foster more robust and versatile enhanced configurations. For example a morphing wing from the structural perspective should not entail additional complexity due to the actuation process, while providing adequate stiffness for lifting surface of an adaptable or optimal shape over a broader range of flight missions.

NASA's morphing initiative [31, 32] resulted in the Gull Wing, the Shark wing and the Hyper-Elliptic Cambered Span (HECS) wing. Lazos and Vesser [26] conducted wind tunnel tests to ascertain the efficiency of HECS wings as well as Racked tip and Winglet configurations wings compared with a Baseline elliptical planform wing. Some of the models tested in this study appear in Figure 5-1 for the reader's convenience. In order to study the aerodynamic performance and wake characteristics of the tested models, comparisons were based on their lift-to-drag ratios. It was determined that all but one of the HECS configurations outperformed the baseline, i.e. the elliptical wing. In the case of the two conventional winglet configurations, Winglet2 (Figure 5-1c) performed the best, maintaining a lift-to-drag ratio improvement over a broad range of lift coefficients.

McGowan *et al.* [32] implemented the HECS wing in an experimental centerbody tailless Uninhabited Aerial Vehicle (UAV). The wing morphing concept encompassed a planar straight configuration and a curved-down non-planar one as shown in Figure 5-2. According to the flight mission of the UAV, the HECS morphed wing will eliminate the use of control surfaces such as flaps and ailerons. To this end, several mechanisms [38, 49, 54] of linkage systems were proposed for morphing actuation. Such mechanical systems provide several challenges, in addition to the weight penalty, due to the complexity of their design, actuation, maintenance and reliability.

(a) Baseline (b) HECSI (c) Winglet2

Figure 5-1. Tested wing models, Lazos and Vesser [26]

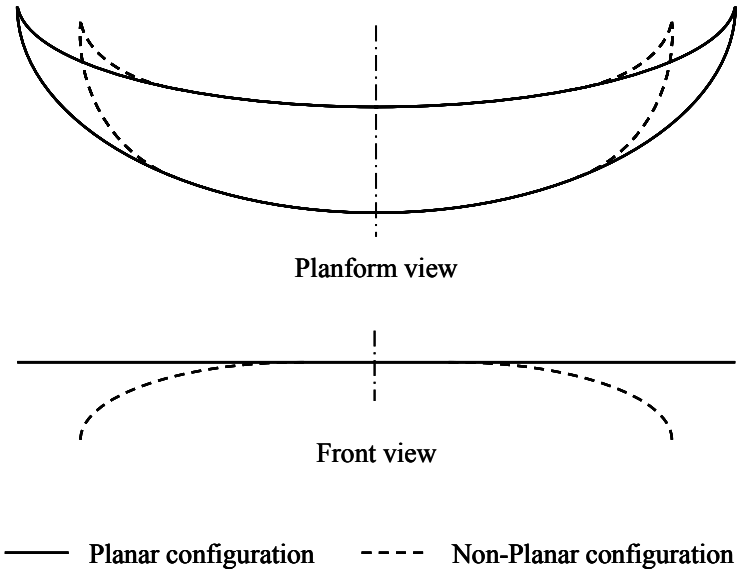

Figure 5-2. HECS wing configurations

The bistable equilibrium configurations developed and investigated in the present research could be used as an efficient structure for morphing wings. Demonstrating their viability for such applications is the main objective of this chapter. As illustrated in Chapter 4, MFC piezoelectric actuators can be used to actively control the snap-through behavior of unsymmetric laminates.

Mattioni *et al.* [30] proposed using bistable panels manufactured by combining symmetric and unsymmetric layups. These panels were to be used as spars of a variable sweep wing. As was pointed out in [30] the suggested design requires accommodating constraints related to the assembly of wing parts including the wing box and ribs. The concept of combining different stacking sequences within the same panel is investigated in [51] and continued in the current work as a means for achieving a UAV wing with morphing capabilities.

Numerical predictions of the cured shapes and stability characteristics of different panels with bistable behavior follow the methodology provided in Chapters 2 and 3.

5.2 Candidate Designs

In this section two candidate designs are presented. These designs combine symmetric as well as unsymmetric layups within the same panel to produce various camber effects. Cross-ply stacking sequences are employed in both symmetric and unsymmetric portions of a panel. The first model, referred to as the Winglet-like I model, has one equilibrium shape straight in the span-wise direction and another with the tip curved up. In Winglet-like I model the chord is maintained constant throughout the wing-

span. Meanwhile, Winglet-like II model, while possessing similar equilibrium shapes to that of Winglet-like I model, is introduced to study the effect of wing taper. In this section the main focus is devoted towards describing their manufacturing, and predicting their cured shapes and stability characteristics.

Winglet-like Designs

A rectangular panel, referred to as Winglet-like I, is manufactured by stacking four cross-plies as shown in Figure 5-3. The panel has three sections: the root section has a symmetric $[0°, 90°]_S$ layup, the middle section has an unsymmetric balanced $[0°_2, 90°_2]$ layup, and the tip section has an unsymmetric unbalanced $[0°_3, 90°]$ layup. When curing the panel, only the unsymmetric balanced portion will exhibit bistable behavior. Meanwhile, the unsymmetric unbalanced tip section will possess a permanent curvature (camber) due to the curing thermal stresses. On the other hand, the cured shape of the symmetric cross-ply section enforces a zero curvature at the root section.

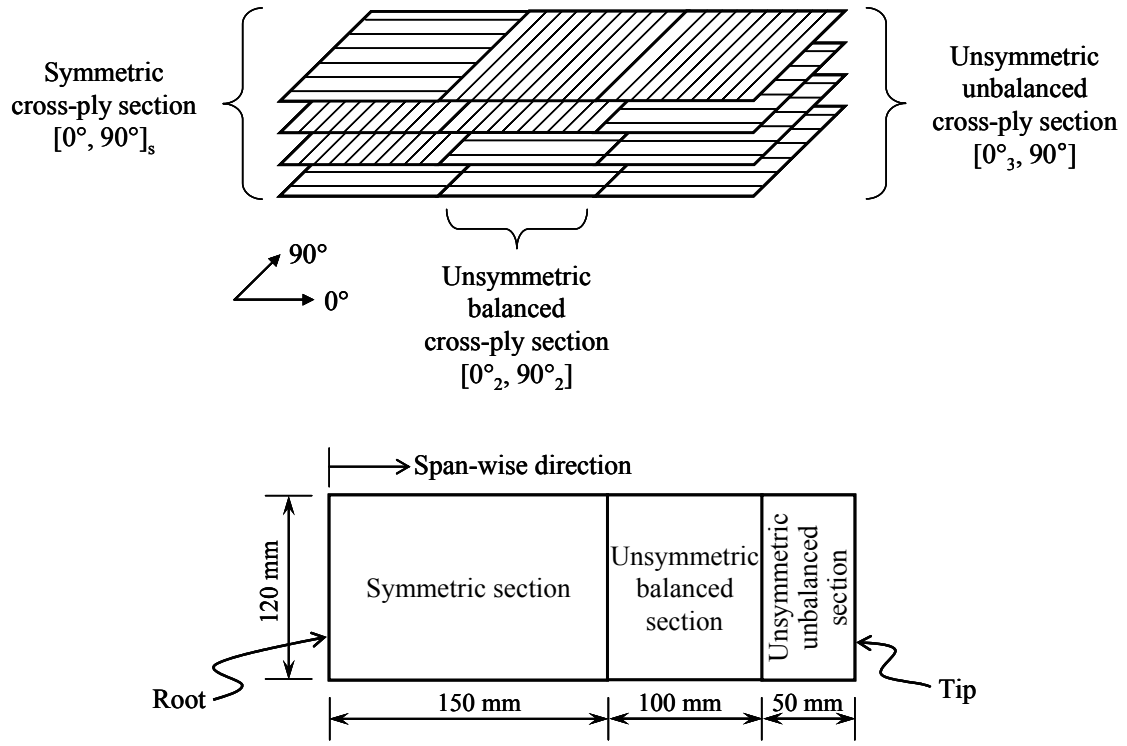

Figure 5-3. Winglet-like I: Rectangular panel with symmetric/unsymmetric balanced/unbalanced cross-ply layups

Chord, span, and size ratios of different panel sections of the Winglet-like I model are initial suggested values. A taper can be introduced into the rectangular planform as shown in Figure 5-4. In this case the design is referred to as the Winglet-like II. Taper ratio represents a design parameter that can be used jointly with other parameters, i.e. Chord, span, size ratios of different panel sections, for design optimization. This Chapter investigates the aerodynamic benefits associated with the proposed bistable wing planform. Design optimizations based on certain aerodynamic requirements is outside the focus of the current work and suggested for future work.

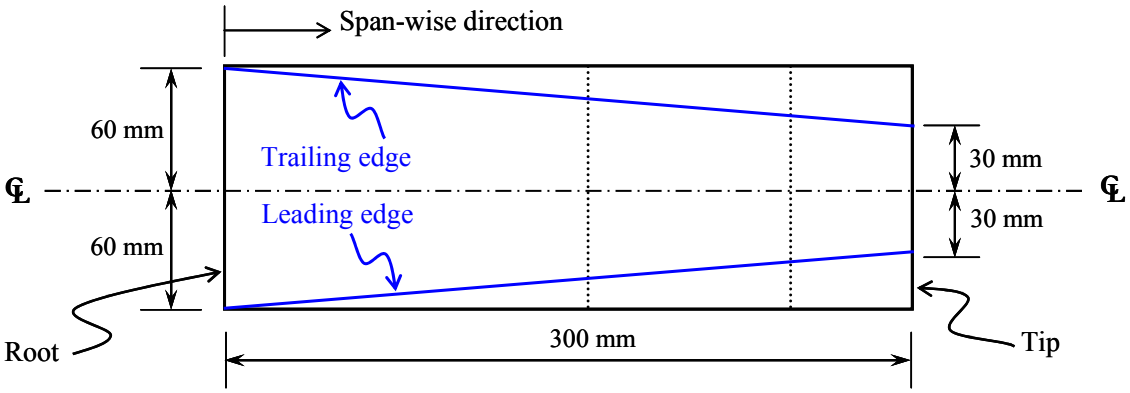

Figure 5-4. Winglet-like II: Tapered panel with symmetric/unsymmetric balanced/unbalanced cross-ply layups

Cured shape and stability characteristics

The stacking sequence used for Winglet-like I and II panels are modeled using the developed ABAQUS FE methodology to predict the cured shapes and stability characteristics. The same size FE element model is employed in both panels, using 230 eight-node, reduced integration, doubly curved shell elements (S8R). The total number of nodes for the model is 757, and the total number of degrees of freedom is 4542. During the cure simulation all degrees of freedom were restrained at the center point of the unsymmetric balanced section of the panel. The two stable configurations of the manufactured Winglet-like I model are shown in Figure 5-5. The corresponding predicted equilibrium configurations are shown in Figure 5-6.

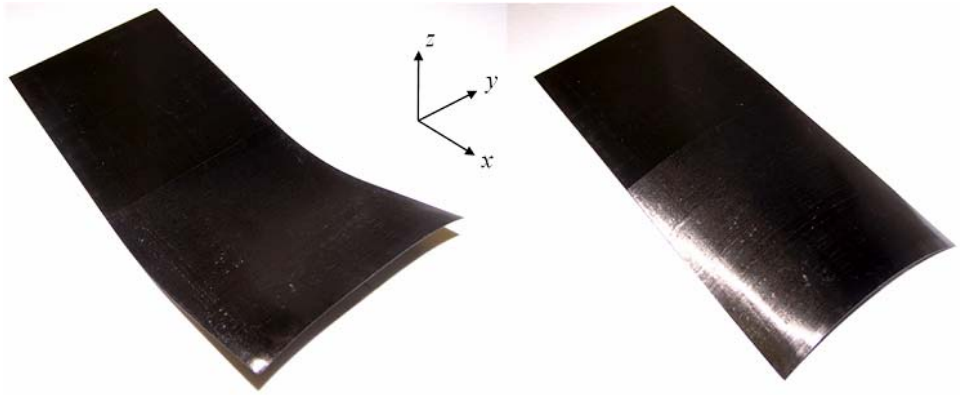

Figure 5-5. Winglet-like I: Manufactured panel showing associated equilibrium configurations

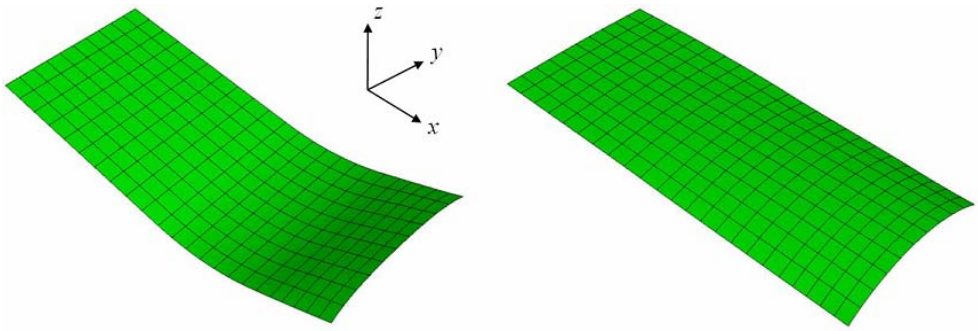

Figure 5-6. Winglet-like I: Predicted equilibrium configurations using ABAQUS FEA software

Both equilibrium shapes of, Winglet-like I, exhibit tip camber due to the unsymmetric unbalanced section of the panel. The first equilibrium shape is characterized by curved-upward surface generators in the span-wise direction while the chord-wise surface generators are straight within the symmetric section and increasingly curved ones towards the tip edge within the unsymmetric balanced and unbalanced sections of the panel. The second equilibrium shape is characterized by straight surface generators in the span-wise direction while the chord-wise surface generators are straight within the symmetric section and slightly increasing curved ones towards the tip edge within the unsymmetric balanced and unbalanced sections. The equilibrium shapes of the Winglet-

like II model are similar to those ones of Winglet-like I. Figures 5-7 and 5-8 provide the cured shapes of the manufactured panel and the corresponding FEA predictions, respectively.

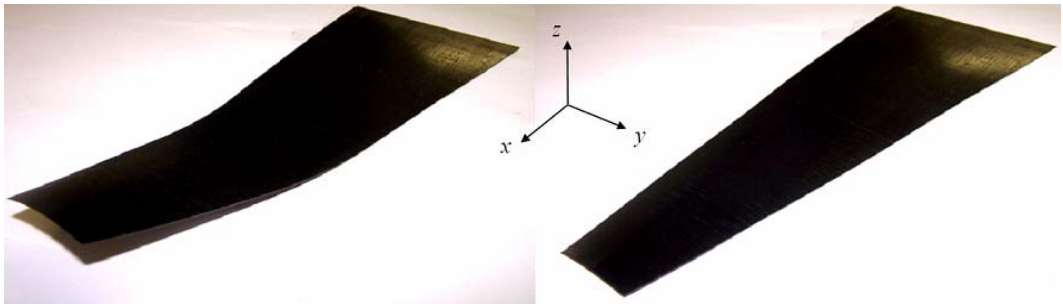

Figure 5-7. Winglet-like II: Manufactured panel showing associated equilibrium configurations

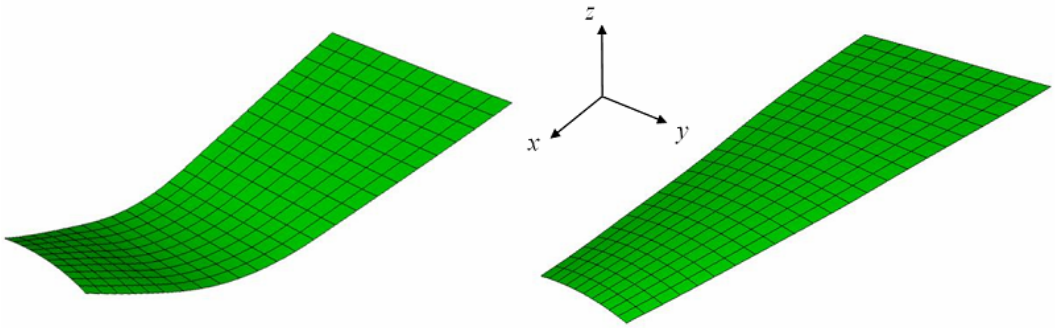

Figure 5-8. Winglet-like II: Predicted equilibrium configurations using ABAQUS FEA software

To predict the stability characteristics, all corner points of the panel are restrained from movement in the z direction while the center point of the unsymmetric section is restricted from movement in both *x* and *y* directions. A concentrated load is applied at the middle point of the unsymmetric section to force the laminate to snap-though, the load is reversed to force the laminate to snap-back. Snap-through and snap-back of model Winglet-like I and II are shown in Figure 5-9 and Figure 5-10, respectively.

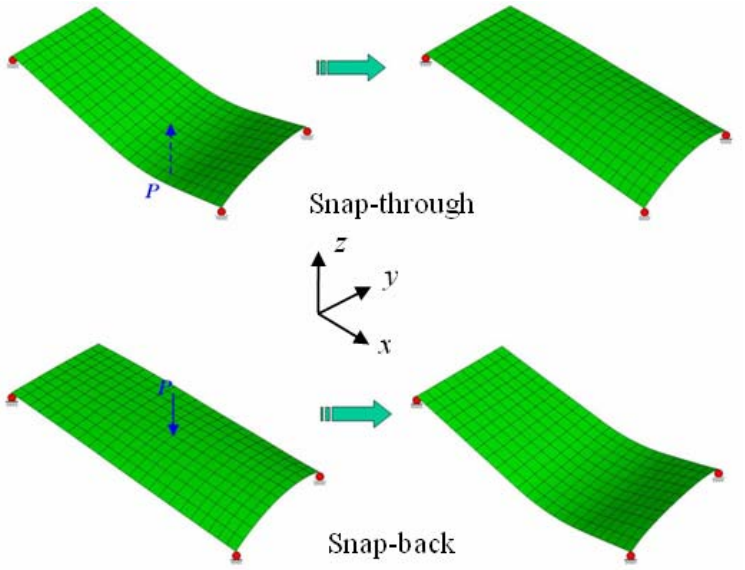

Figure 5-9. Snap-through and snap-back of the Winglet-like I model

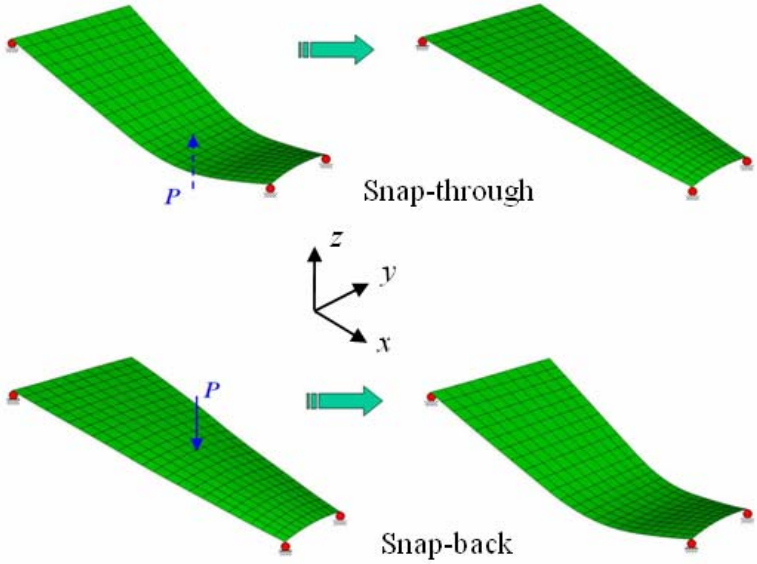

Figure 5-10. Snap-through and snap-back of the Winglet-like II model

A comparison of the required load to cause Winglet-like I and II panels to snap-through or snap-back, is provided in Table 5-1. The 70.1% reduction in snap-back load (from 7.39 N to 2.15 N) for the trimmed panel is indicative of the influence of the taper. The influence of taper parallels the study of trapezoidal panels of Chapter 3. It can also be

noted that if such a panel is used as the wing of a UAV, snap-through will be aerodynamically opposed by the lifting force while snap-back will be the aerodynamically assisted. In this respect, a limitation on the taper ratio is required to avoid accidentally triggering the snap-back behavior by the aerodynamic loads.

Table 5-1 Stability characteristics of the Winglet-like models

	Required Concentrated Load (N)	
	Winglet-like I	Winglet-like II
Snap-through	1.05	1.11
Snap-back	7.39	2.15

5.3 Preliminary Aerodynamic Analysis

In order to capture the aerodynamic benefits of suggested panel designs full 3-D computational fluid dynamics model and wind tunnel testing should be carried out. Performing these of analytical and/or testing is beyond the scope of the current research concern. Consequently a preliminary aerodynamic analysis is performed using a vortex-lattice analysis and applied to the composite panel to investigate the aerodynamic characteristics of its equilibrium configuration. The simple geometry of Winglet-like designs, whether rectangular or tapered, qualifies them for using a simplified preliminary aerodynamic study.

Vortex-lattice analysis

The software Athena Vortex-Lattice (AVL) is an aerodynamic analysis code developed by Mark Drela, at MIT, and Harold Youngren [14]. AVL code is best suited for aerodynamic configurations consisting mainly of a thin lifting surface at a small angle of attack and side slip. The code does not determine the stall boundary of the analyzed surface. A single layer vortex sheet is used to represent the surface. The vortex sheet is discretized into horseshoe vortex filaments whose trailing legs are parallel to the flow direction. AVL assumes quasi-steady flow and unsteady vorticity shedding is neglected. Accordingly, the models analyzed in the current study are pertinent to the panel/wing in one or the other of its equilibrium shapes. The transient motion occurring during snap-through is not addressed. AVL accounts for compressibility effects using Prandtl-Galuert (PG) transformation, limiting the validity of the solution to values of freestream Mach number less than 0.7, i.e. transonic regime.

According to the flight mission of the UAV, the morphed wing is desired to eliminate the use of control surfaces such as flaps and ailerons. To this end, the wing sides are set in non-similar configurations, as one side maintains the planar configuration while the other is forced to the non-planar configuration, the desired control e.g. roll and/or yaw could be effected. Comparison in terms of aerodynamic forces and moments coefficients is sought to determine the aerodynamics benefits of the suggested designs.

Let ρ_∞ and V_∞ be the density and velocity of the freestream, respectively. The dynamic pressure is $q = \frac{1}{2}\rho_\infty V_\infty^2$ and the lift, drag and side force coefficients are

$$C_L = \frac{L}{q\ S}$$
$$C_D = \frac{D}{q\ S} \qquad (5.1)$$
$$C_Y = \frac{F_y}{q\ S}$$

for L, D and F_y are the lift, drag and side force, respectively and, S is the surface area of the lifting surface. Similarly the coefficients of roll and yaw moments can be written as

$$C_l = \frac{M_x}{q\ S\ B}$$
$$C_n = \frac{M_z}{q\ S\ B} \tag{5.2}$$

for M_x, M_z are the roll and yaw moments, and B is the wing span.

The Winglet-like I model

AVL is used to calculate the lift and drag coefficients of the wing being in either one of its bistable configuration, i.e. planar and non-planar as shown in Figure 5-11.

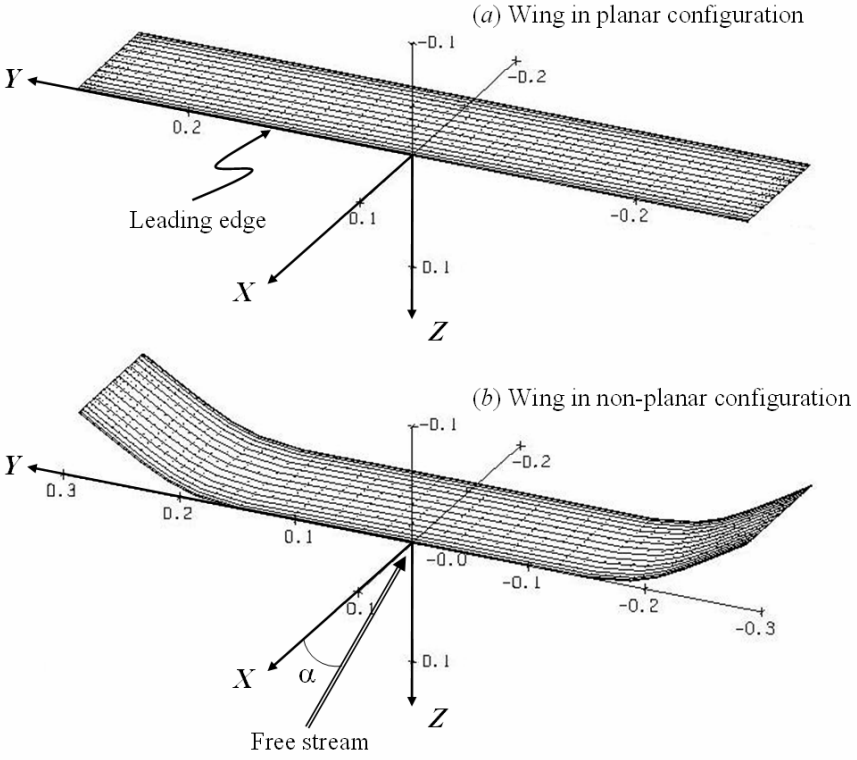

Figure 5-11. Winglet-like I model in planar and non-planar configurations

Although the Winglet-like models possess one stable shape similar to the conventional winglet wing their targeted performance results from the difference in camber between their planar and non-planar configurations. The effect of camber change is more pronounced than introducing winglet shape wing to minimize the tip vortex effect. That is, higher lift is developed in the wing being in the planar configuration due its higher camber. Consequently, the induced drag generated on the wing in the planar configuration is higher. The camber in each configuration is normalized with respect to the wing chord and reported at different wing stations normalized by the half span, denoted by B*, and shown in Figures 5-12 and 5-13.

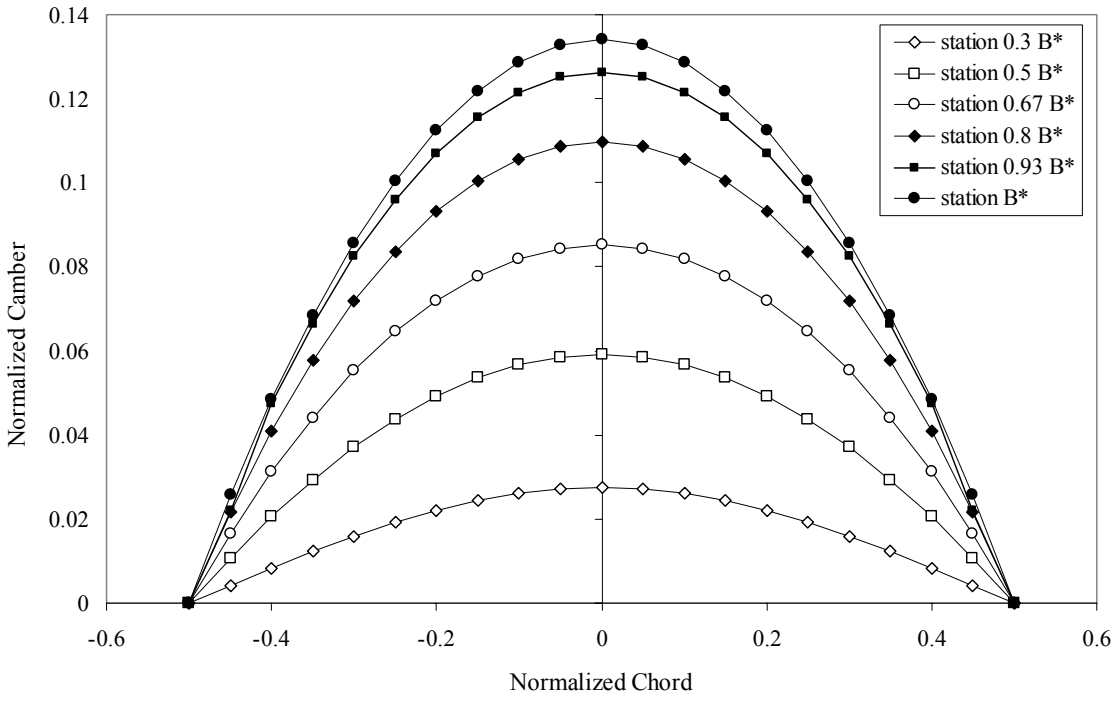

Figure 5-12. Normalized camber of the Winglet-like I model in planar configuration

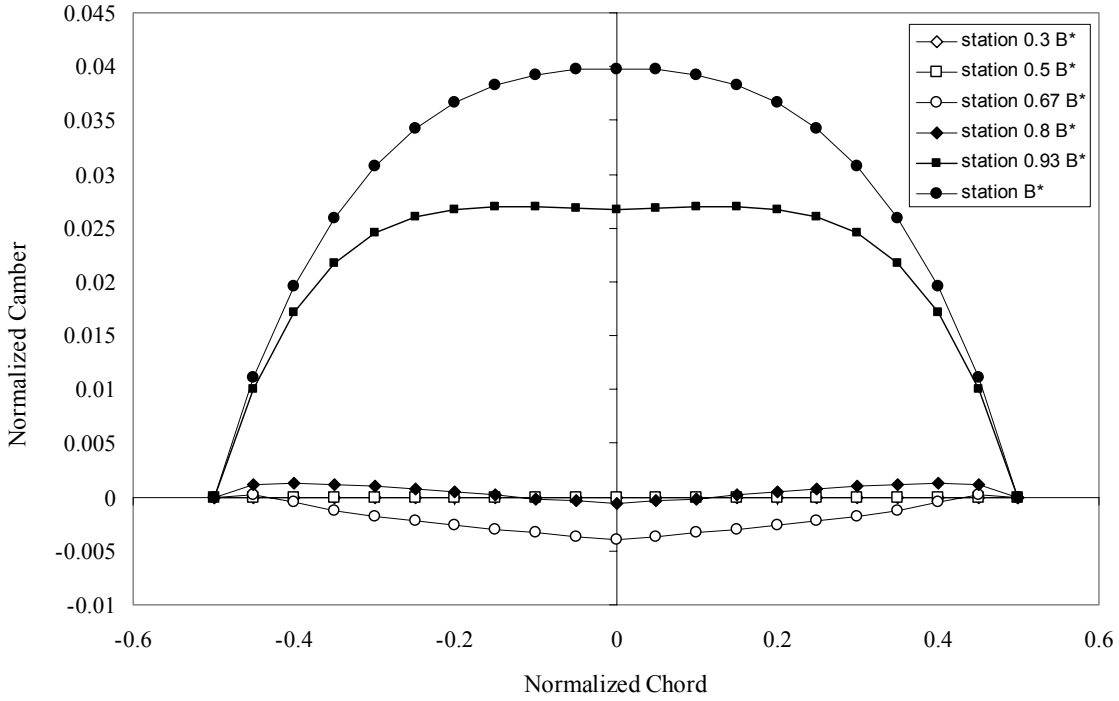

Figure 5-13. Normalized camber of the Winglet-like I model in non-planar configuration

It can be noticed by comparing Figures 5-12 and 5-13 that the camber is nearly zero throughout the majority of the chord-length except at the tip. Also, the tip camber in the planar configuration is nearly three times larger than in the case of non-planar configuration.

The lift and drag coefficient are obtained at angles of attack α ranging form 0º to 15º, and provided in Table 5-2. Also C_L and C_D versus α, and C_L versus C_D curves are presented in Figure 5-14 through Figure 5-116, respectively.

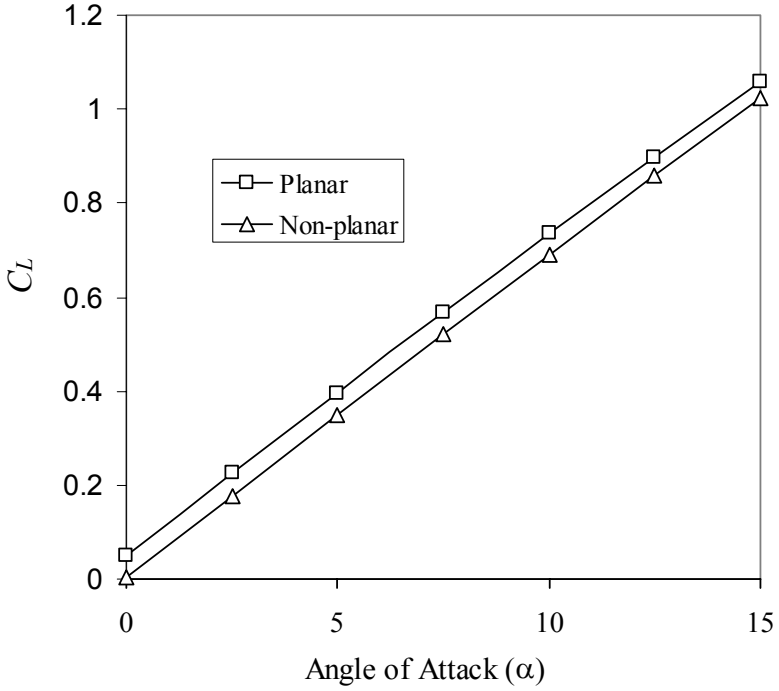

Figure 5-14. Winglet-like I model: C_L versus α (planar and non-planar configurations)

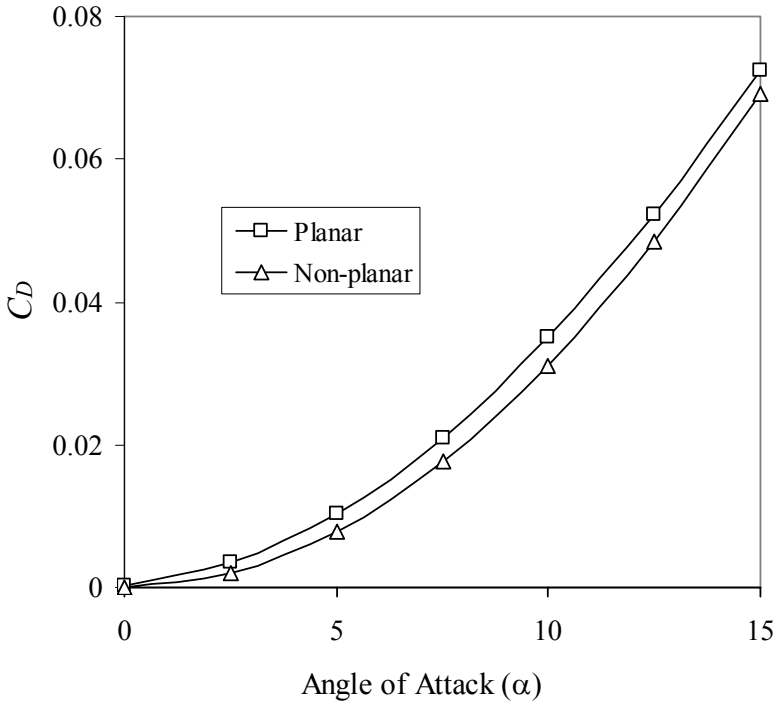

Figure 5-15. Winglet-like I model: C_D versus α (planar and non-planar configurations)

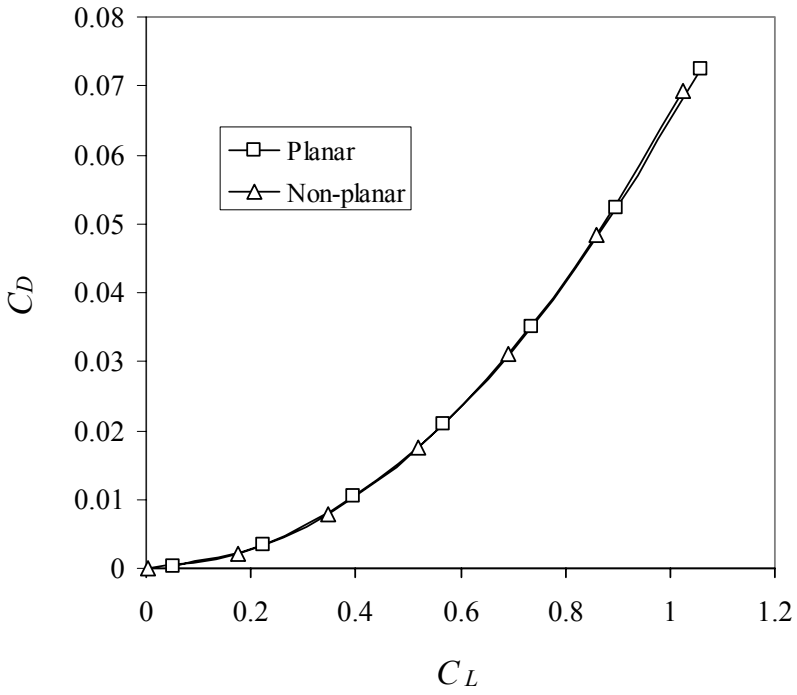

Figure 5-16. Winglet-like I model: $C_L - C_D$ (planar and non-planar configurations)

Figure 5-15 provides the effect of camber on the lift coefficient. The predicted developed lift on the wing in its planar configuration is higher. Similar observations regarding the drag coefficient can be concluded from Figure 5-15. Meanwhile, Figure 5-16 shows that the drag polar of the entire wing in both the planar and non-planar configurations nearly coincide.

Table 5-2 Lift and Drag coefficients for Winglet-like I (planar and non-planar)

α (degree)	Lift Coefficient C_L		Drag Coefficient C_D	
	Planar	Non-planar	Planar	Non-planar
0.00	0.05107	0.00292	0.00035	0.00001
2.50	0.22429	0.17536	0.0035	0.00199
5.00	0.39648	0.348	0.01044	0.00784
7.50	0.56681	0.51998	0.02103	0.01757
10.00	0.7345	0.69048	0.03509	0.03114
12.50	0.89878	0.85867	0.05235	0.04841
15.00	1.05892	1.02374	0.07249	0.06921

Due to the effect of camber on the lift coefficient, four modes of flight can be suggested. Two modes are symmetric as shown in Figure 5-11, namely the whole wing being in either planar or non-planar configuration. The other two modes correspond to asymmetric configuration, i.e. one half of the wing is in planar configuration while the other is in non-planar configuration as shown in Figure 5-17.

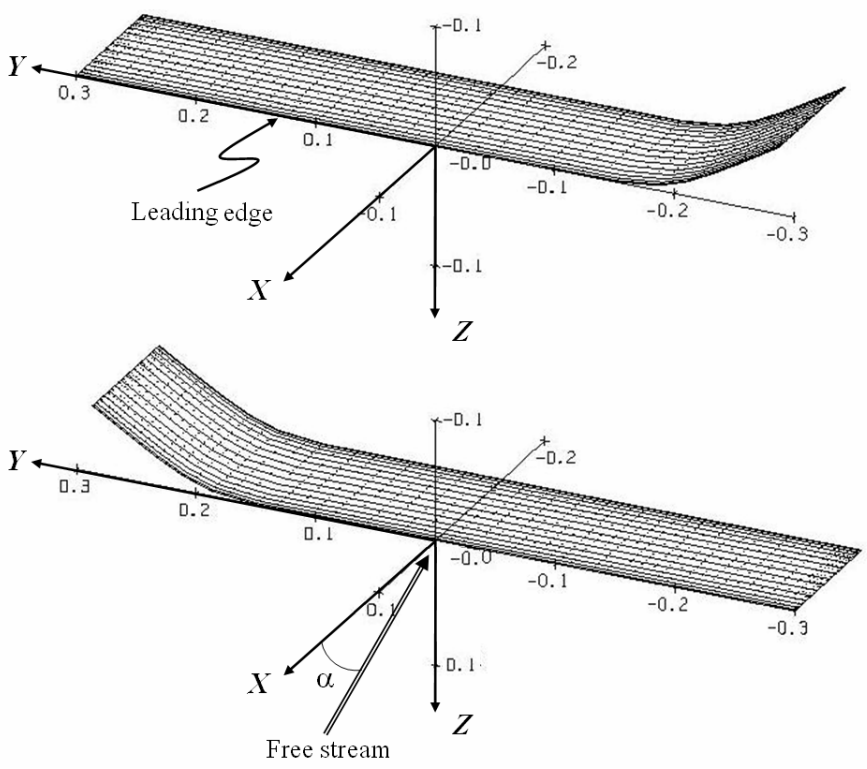

Figure 5-17. Winglet-like I model in asymmetric modes

The lift and drag forces resulting on the asymmetric wing sides are different and hence it can be expected that roll moment will develop. Consequently, the roll moment coefficient is calculated using AVL for one of the asymmetric configurations, e.g. only the left side "port-side" is in the non-planar configuration as shown in Figure 5-18. The roll moment coefficient as a function of the angle of attack is presented in Figure 5-19.

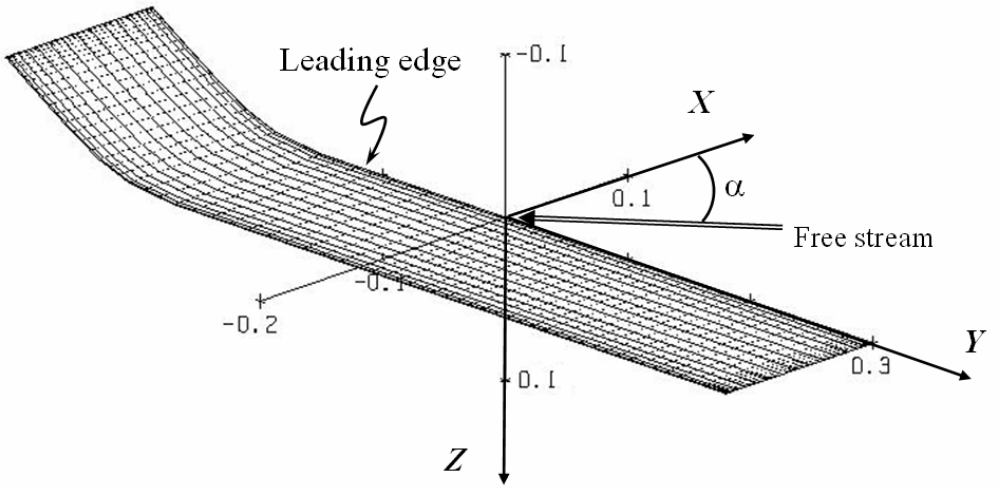

Figure 5-18. Winglet-like I model in "port-side" asymmetric mode

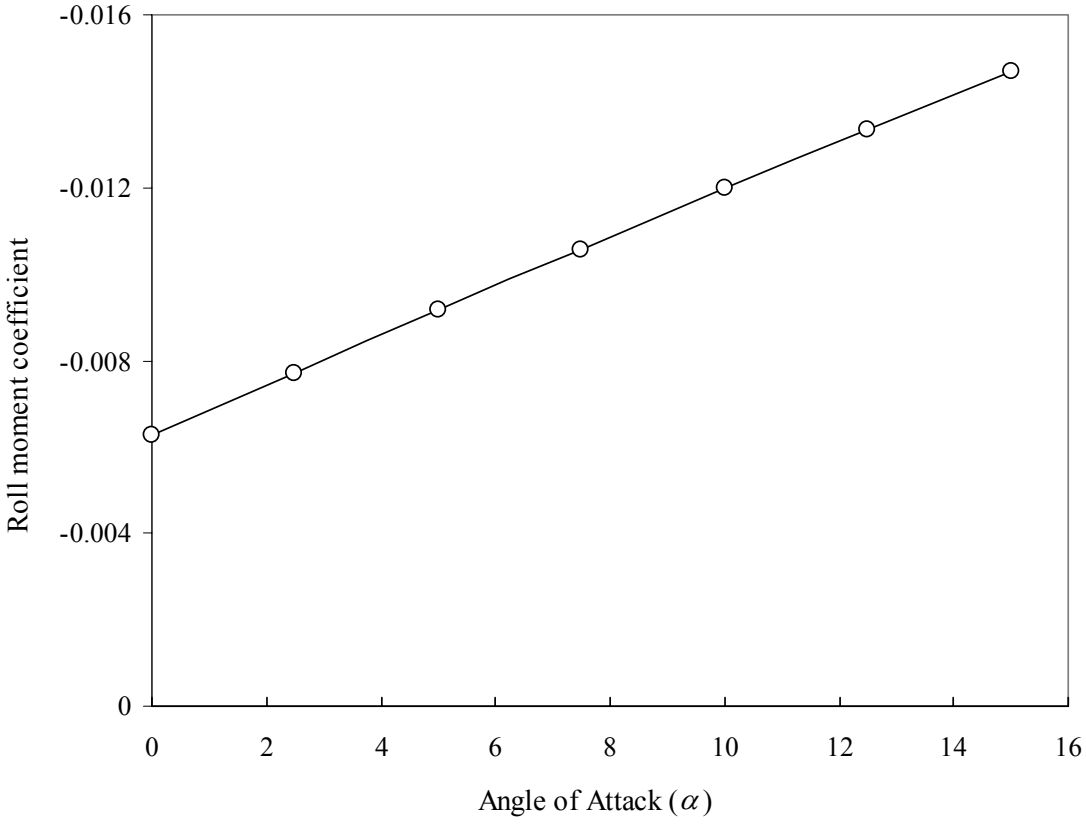

Figure 5-19. Winglet-like I model: Roll moment coefficient in "port-side" asymmetric mode

A negative roll moment coefficient is predicted in this asymmetric configuration. This negative roll moment is expected in the currently studied asymmetric mode of flight due to higher camber of the planar side of the wing.

The Winglet-like II model

AVL code is used in similar analysis procedure to study the Winglet-like II model. First the difference of camber in planar and non-planar configurations is shown. Second the effect of camber on lift and drag coefficients is provided. Finally, the roll moment coefficient of the wing in asymmetric mode is investigated.

The camber of the tapered wing in planar and non-planar configurations is normalized with respect to the root chord and reported at different wing stations normalized by the half span, denoted by B*, and shown in Figures 5-20 and 5-21, respectively.

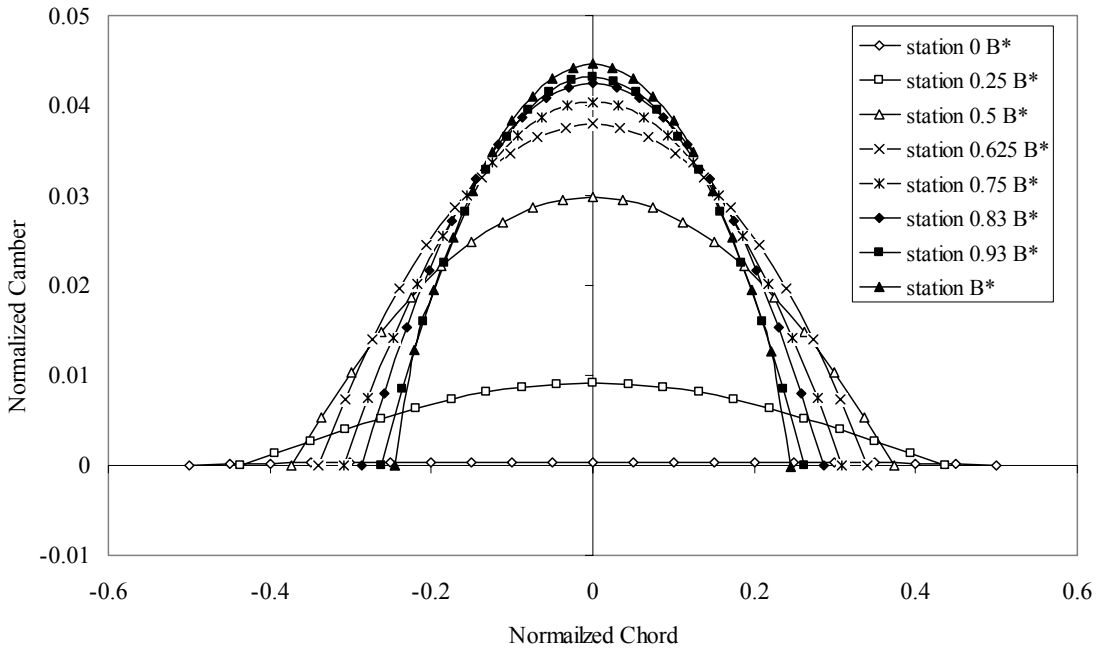

Figure 5-20. Normalized camber of the Winglet-like II model in planar configuration

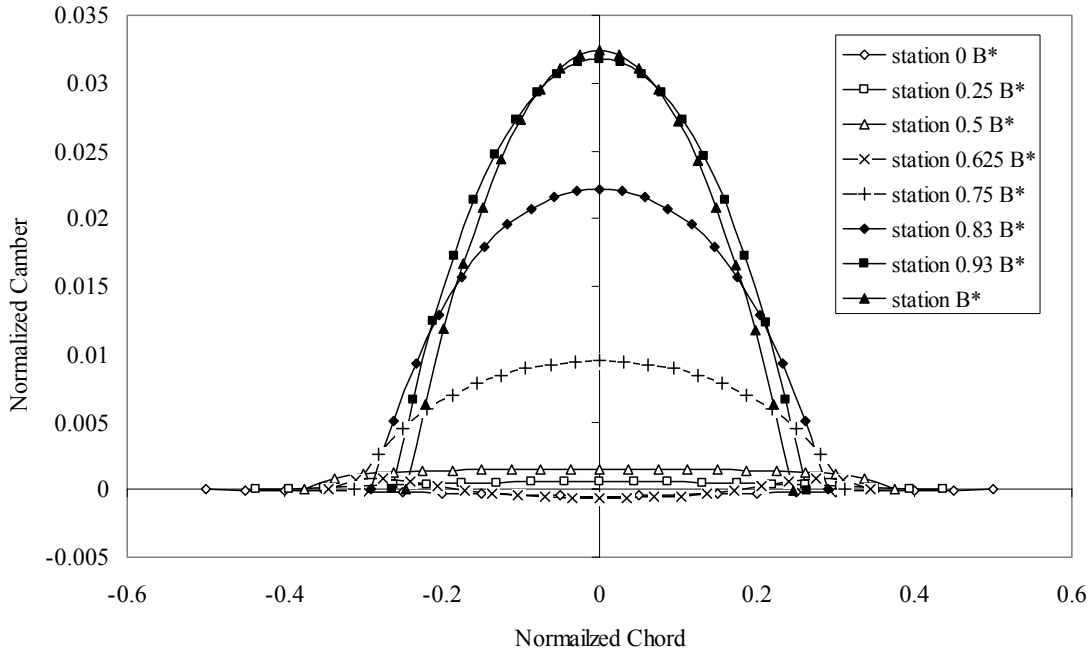

Figure 5-21. Normalized camber of the Winglet-like II model in non-planar configuration

When comparing the Winglet-like models it can be observed that introducing taper, as shown in Figure 5-4, mainly results in reducing the difference in camber between the two equilibrium configurations. The tip curvature, i.e. camber, of the wing in the non-planar configuration is only 25% less than in the planar configuration. Also the effect of changing wing configuration on camber is less pronounced in the span-wise direction than in the case of Winglet-like I model.

The analysis starts by calculating the lift and drag coefficients with the entire wing in either the planar or non-planar configurations, i.e. symmetric modes. The lift and drag coefficients versus the angle of attack, in degrees, is provided in Figures 5-22 and 5-23, respectively. While the drag polar is shown in Figure 5-24.

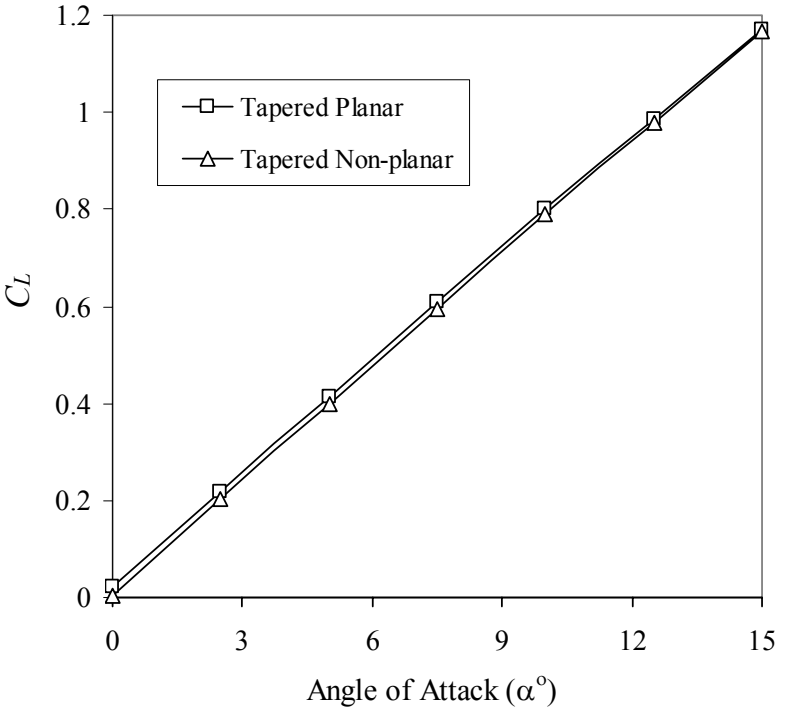

Figure 5-22. Winglet-like II model: C_L versus α (planar and non-planar configurations)

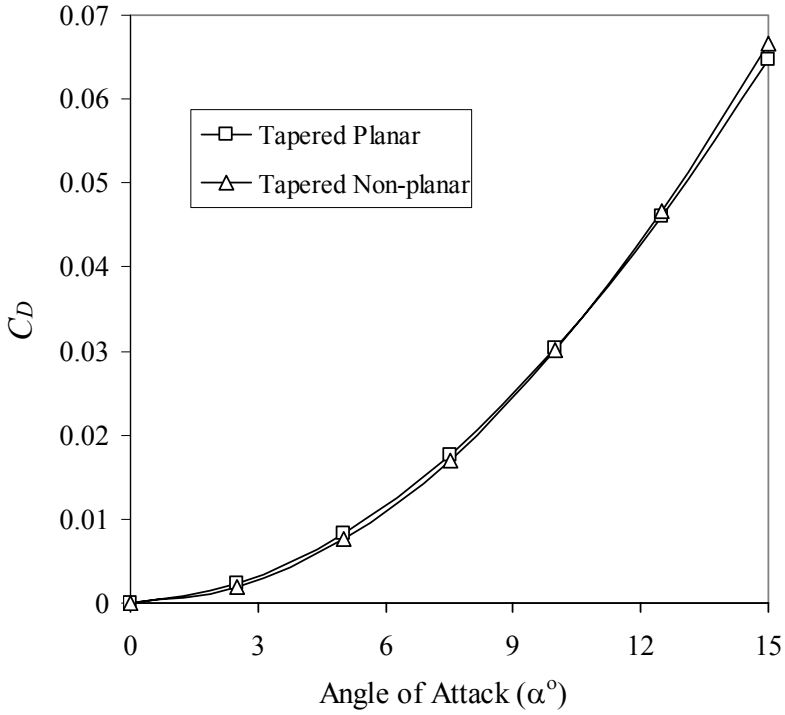

Figure 5-23. Winglet-like II model: C_D versus α (planar and non-planar configurations)

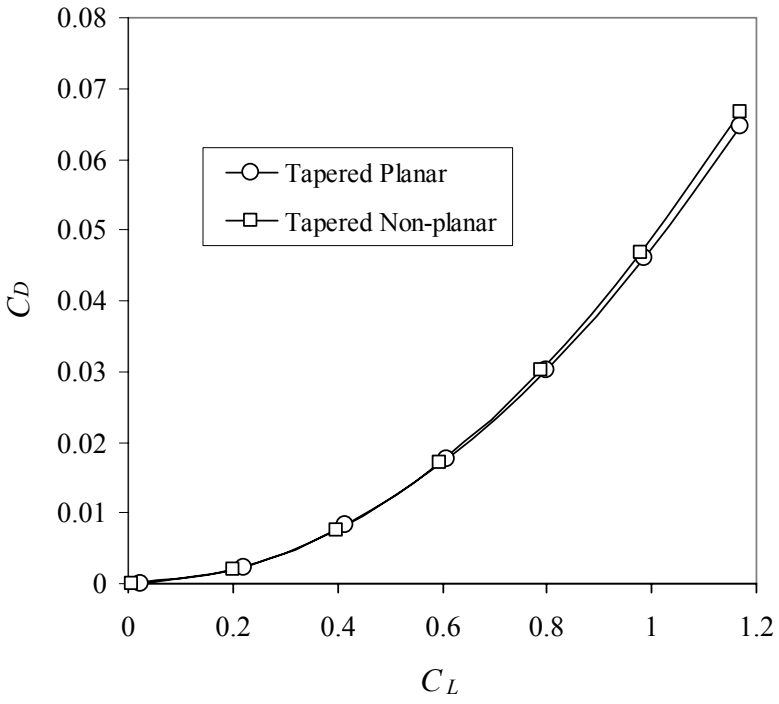

Figure 5-24. Winglet-like II model: $C_L - C_D$ (planar and non-planar configurations)

The developed lift on the wing in its planar configuration is slightly higher throughout all values of angle of attach as shown in Figure 22. While the drag coefficient for the wing in planar configuration is higher till the angle of attach of nearly 10° then the drag coefficient of the non-planar wing becomes higher. Meanwhile, Figure 5-16 shows that the drag polar of the entire wing in the planar and non-planar configurations do not coincide as in the case of Winglet-like I model.

Table 5-3 provides the obtained values of lift and drag coefficients as the angle of attack increases from 0º to 15º.

Table 5-3 Lift and Drag coefficients for Winglet-like II (planar and non-planar)

α (degree)	Lift Coefficient C_L		Drag Coefficient C_D	
	Tapered planar	Tapered non-planar	Tapered planar	Tapered non-planar
0.00	0.02286	0.00525	0.00004	0.00001
2.50	0.2193	0.20197	0.00231	0.00196
5.00	0.41481	0.39867	0.00819	0.00763
7.50	0.60854	0.5945	0.01758	0.01703
10.00	0.79968	0.7886	0.0303	0.0301
12.50	0.98744	0.98012	0.04612	0.04671
15.00	1.17105	1.16823	0.06473	0.06664

Investigating the effect of an asymmetric mode of operation, as shown in Figure 5-25, provides an insight regarding to the roll moment. In the case, Winglet-like II model, the camber difference effect is less pronounced than for the Winglet-like I model.

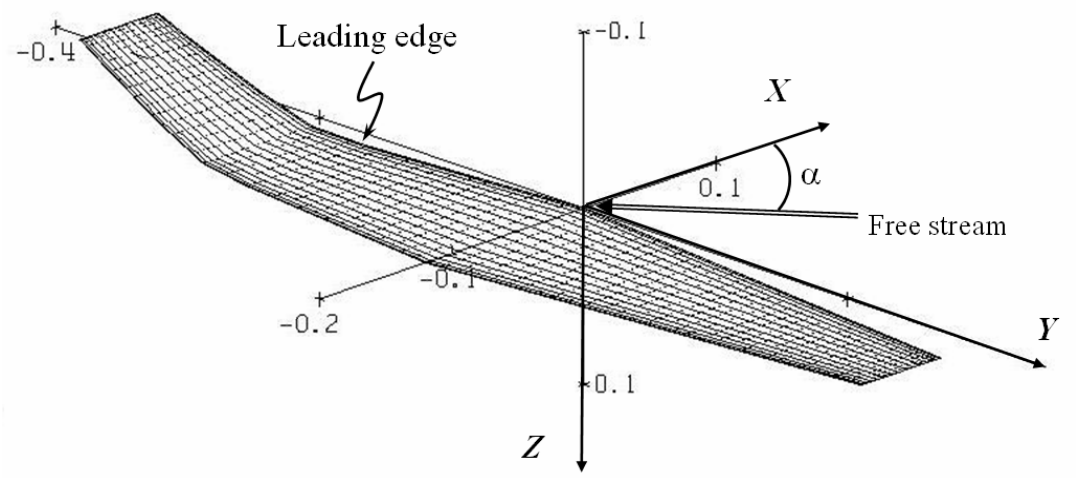

Figure 5-25. Winglet-like II model in “port-side” asymmetric mode

The associated roll moment coefficient in the case of "port-side" asymmetric mode is obtained from AVL and shown in Figure 5-26 at different angles of attack.

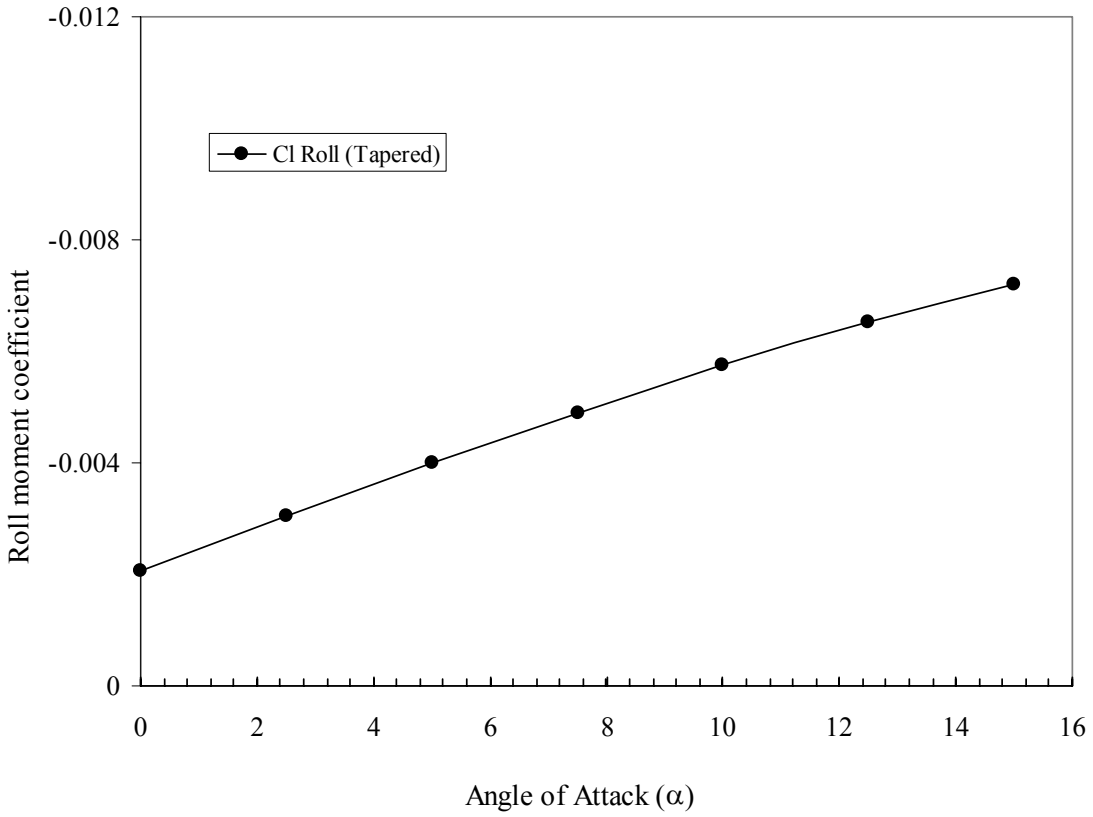

Figure 5-26. Winglet-like II model: Roll moment coefficient in "port-side" asymmetric mode

Inspecting the results presented in Figure 5-26, it is noticed that negative roll moment will develop on the wing in this asymmetric mode of operation. Comparing the results presented in Figure 5-26 and 5-19, provides understanding into the effect of taper on the aerodynamic performance. Figure 5-27 is constructed to provide the comparison between Winglet-like I and II models in terms of roll moment coefficients.

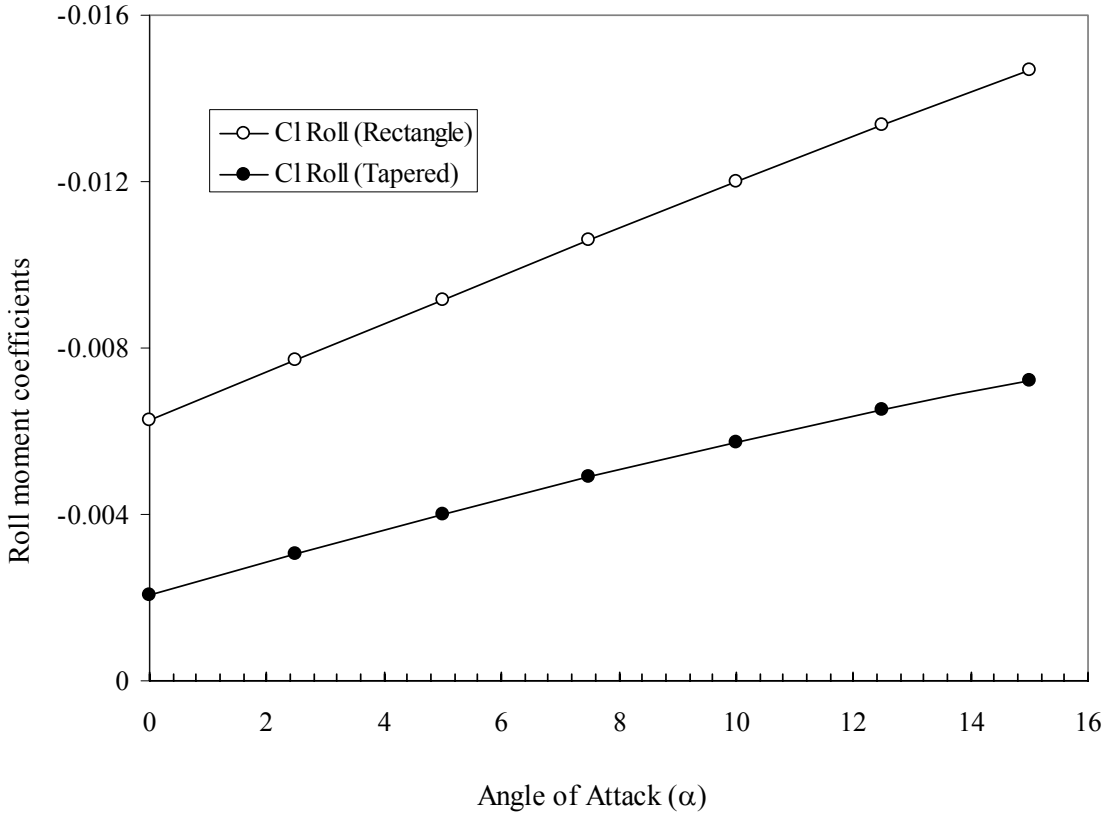

Figure 5-27. Winglet-like I&II models: Roll moment coefficients "port-side" asymmetric mode

Roll moment coefficient, as shown in Figure 5-27, is affected by introducing a taper in the panel. The taper ratio can be determined based on the required roll moment as a function of the angle of attack.

Employing Winglet-like design as a UAV wing could eliminate the need of ailerons. This advantage can be achieved by using a morphing panel as proposed in Chapter 4.

5.4 Discussion and Conclusions

New wing planform design combining both unsymmetric and symmetric cross-ply layups are introduced. Their stability characteristics provide an efficient means for achieving morphed wings. The commercial ABAQUS finite element code is used to predict the cured panel shapes and bistable equilibrium configurations. Two panels combining symmetric, unsymmetric balanced and/or unbalanced sections are manufactured. Both panels exhibit two equilibrium configurations, a planar configuration and a non-planar one similar to a conventional winglet configuration wing used for induced drag reduction. Both panels were designed are suitable as UAV wings.

A preliminary aerodynamic analysis is performed using the software Athena Vortex-Lattice (AVL). The results from this study provide evidence of the aerodynamic benefits associated with the proposed bistable wing planform. A major benefit is gained by bringing the wing in asymmetric modes to create roll moment and hence eliminate the use of ailerons.

Future work is not restricted to the optimization problem based on aerodynamic limitations. A more suitable application can be a wing for MAV (Micro Aerial Vehicle). Further steps of development involve applying aerodynamic loads to the structural model to guarantee inadvertent triggering of snap-through behavior and effective piezoelectric actuation. It is also suggested to perform wind-tunnel testing supported by 3-D computational fluid mechanics models. These tests and analyses should also be performed during actuation to capture the dynamic effects during transition.

CHAPTER 6

DISCUSSION AND RECOMMENDATIONS

6.1 Discussion

This dissertation presented a commercial Finite Element model for predicting the response of unsymmetric cross-ply laminated composites which include predicting their cured shapes, their stability characteristics due to a concentrated force and piezoelectric actuation leading to establishing the requirements to trigger snap-through behavior of bistable panels. The finite element methodology is developed to predict the cured shape of square cross-ply laminates. Investigation is carried out employing the temperature-curvature relationship and the curvature as a function of the sidelength and design curve for square panels in terms of pertinent non-dimensional parameters.

A new apparatus and test method are presented to provide quantitative estimates of the forces for snap-though and snap-back behavior. The influence of friction at the supports is minimized via air cushion and the measured forces enabled validation of the analytical predictions.

Through a parametric study for actuation requirements a new method is developed to optimally attach piezoelectric actuators to a bistable panel. The method is applied by bonding two MFC actuators to a bistable panel and measuring the required voltage to trigger snap-though behavior of the bonded assembly. The Finite Element methodology is extended to predict actuator requirements to trigger snap-through behavior. Analytical predictions from the FE methodology are found to be in agreement with test data.

Finally, an investigation of the viability of bistable panels for use as wings for Uninhabited Aerial Vehicle (UAV) was presented. Examples of morphing panels suitable for UAV wing application are manufactured by combining symmetric and unsymmetric balanced and unbalanced stacking sequence within the same panel. A preliminary aerodynamic analysis is performed and evidential aerodynamic benefits are provided. The morphed capabilities of the proposed concept could effect roll moment and accordingly lead to simplified designs by eliminating control surface, such as ailerons.

6.2 Recommendations

The developed Finite Element methodology proved useful in predicting cured shapes of unsymmetric cross-ply composites. This methodology can be used to predict the cured shapes of unsymmetric angle-ply composites. A major investigation is suggested to be conducted in which analytical predictions are compared to experimental measurements. Curvatures of angle-ply composites can be measured by making the use of simple dial gauge(s), LVDT(s) and/or image processing techniques [33].

The developed methodology is based on assuming that material properties are independent of temperature change during the curing cycle. A more realistic analysis will account for thermo-chemical interactions, void formation and resin flow. The one-dimensional model developed by Loos and Springer [27] to describe the curing process of unidirectional epoxy matrix composites can be used to develop a user-defined material model in ABAQUS. This one-dimensional user defined material model will be employed to describe the curing kinematics of individual layers. Obtaining the material properties as a function of curing cycle temperature and pressure will not entail other changes to the general procedures followed in the methodology to determine the cured shape or the

stability characteristics. Developing a refined material model will also allow other investigations such as post-curing hygrothermal stability of bistable panels.

Regarding unsymmetric cross-ply panels, the conducted experiments can be slightly modified to provide the force-displacement curves. Figure 6-1 provides a schematic drawing of the load measurement apparatus with the required modification to provide the load-displacement curves. A set of two LVDT(s) are installed between the load measurement and load application frames. This setup eliminates any possible contribution resulting from the spring loaded LVDT to the applied load on the curved panels. This setup requires synchronization of signal reading from the LVDT(s) and load cell.

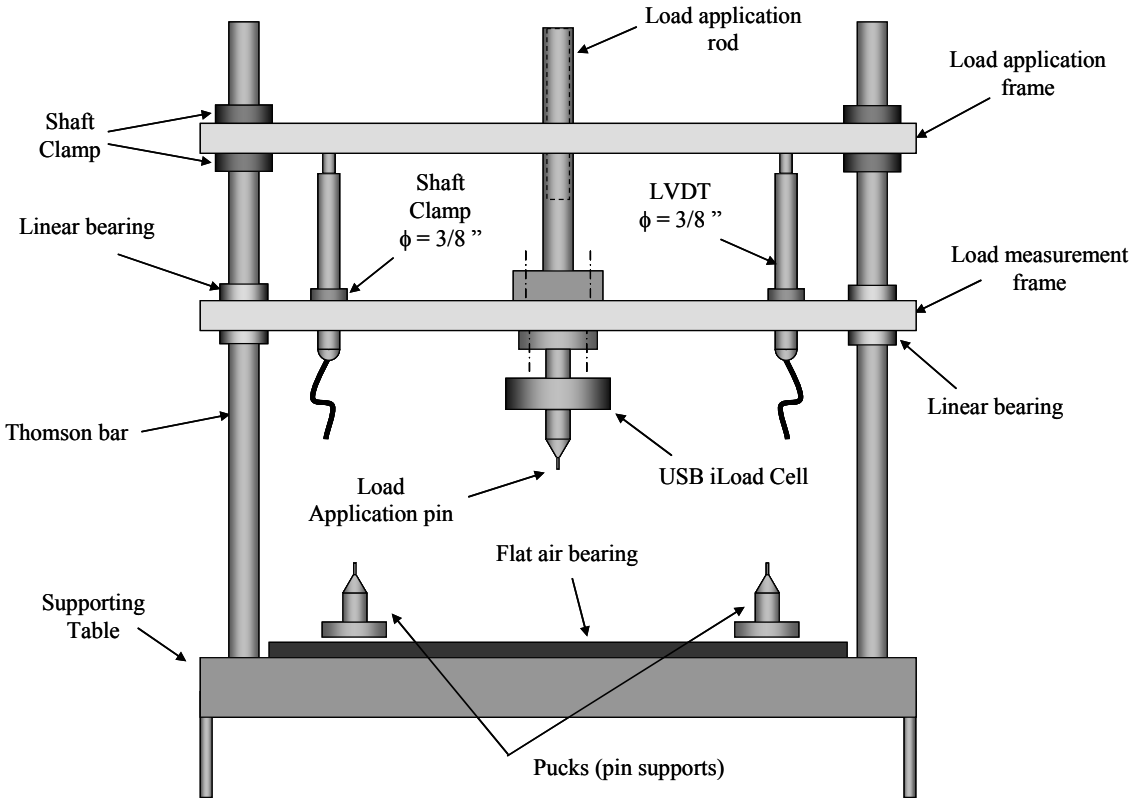

Figure 6-1. Modified load measurement apparatus

The stability characteristics of unsymmetric angle-ply panels can be determined using the same load measurement apparatus. It is suggested to first determine the principal directions of curvatures of the tested panels. Once these directions are determined they can be utilized to identify reference points for panel support and/or load application. Studying the stability characteristics of unsymmetric angle-ply composites provide additional twisting degrees of freedom to meet the design requirements for morphed applications. Enhancing the suggested UAV wing by introducing unsymmetric angle-ply stacking sequence within the panel is a possible option. Moreover, wider range of potential applications can be provided by expanding the design space to include the unsymmetric stacking angle as one of the design parameters.

Wind tunnel tests of the morphed panels suggested for the UAV wing application are recommended. These would verify the results of the preliminary aerodynamic analysis and the effectiveness of the maneuver capabilities for the morphed designs. Another aspect is to examine the wing performance at the moment of snap-through. The elastic behavior of the wing and the amount of flow disturbance contribute to the aerodynamic stability of the UAV. Therefore, measuring the developed aerodynamic forces/moments in case of both symmetric and asymmetric configurations of the wing is essential to account for three-dimensional effects and time dependent behavior. Moreover, quantitative measure of the aerodynamic forces and moments are needed to determine actuator size and power requirements in flight as well as the dynamic effects associated with the transition to an from snap-through and snap-back.

REFERENCES

1. "Standard In-Plane Shear Response of Polymer Matrix Composite Materials by Tensile Test of a 45° Laminate", American Society for Testing and Materials, 2001.
2. "Standard Test Method for Tensile Properties of Polymer Matrix Composite Materials", D 3039/D 3039M, American Society for Testing and Materials, 2002.
3. "Macro Fiber Composite Datasheet", Smart Material Corp., 2004.
4. "Piezo Film Sensors Technical Manual", Measurement Specialties, Inc., 2006.
5. "Air Bearing Application and Design Guide", New Way Air Bearings, 2006.
6. "Miniature DC to HV DC Converters - G Series Datasheet", EMCO High Voltage Corp., 2008.
7. Crisfield, M.A., "A Fast Incremental/Iterative Solution Procedure that Handles Snap-Through", *Journal of Computers and Structures*, Vol. 13, 1981, p. 55-62.
8. Dang, J. and Tang, Y., "Calculation of the Room-Temperature Shapes of Unsymmetric Laminates", *International Symposium on Composite Materials and Structures*, People's Republic of China, 1986, p. 201-206.
9. Dano, M. and Hyer, M.W., "The Response of Unsymmetric Laminates to Simple Applied Forces", *Mechanics of Composite Materials and Structures*, Vol. 3, 1996, p. 65-80.
10. Dano, M., "SMA-Induced Deformations in General Unsymmetric Laminates", Ph.D. Dissertation, 1997, Engineering Science and Mechanics, Virginia Polytechnic Institute and State University, Blacksburg, Virginia.
11. Dano, M. and Hyer, M.W., "Thermally-Induced Deformation Behavior of Unsymmetric Laminates", *International Journal of Solids and Structures*, Vol. 35, 1998, p. 2101-2120.
12. Dano, M. and Hyer, M.W., "Snap-Through of Unsymmetric Fiber-Reinforced Composite Laminates", *International Journal of Solids and Structures*, Vol. 39, 2002, p. 175-198.
13. Dong, X.-J. and Meng, G., "Dynamic Analysis of Structures with Piezoelectric Actuators Based on Thermal Analogy Method", *International Journal of Advanced Manufacturing Technology*, Vol. 27, No. 9/10, 2006, p. 841-844.
14. Drela, M. and Youngren, H. "Athena Vortex Lattice (AVL) code", http://web.mit.edu/drela/Public/web/avl/ [Last accessed on April 27, 2008].
15. Gude, M. and Hufenbach, W., "Design of Novel Morphing Structures Based on Bistable Composites with Piezoceramic Actuators", *Mechanics of Composite Materials*, Vol. 42, No. 4, 2006, p. 339-346.
16. Hamamoto, A. and Hyer, M.W., "Non-linear Temperature-Curvature Relationships for Unsymmetric Graphite-Epoxy Laminates", *International Journal of Solids and Structures*, Vol. 23, No. 7, 1987, p. 919-935.
17. Hufenbach, W., Gude, M. and Kroll, L., "Design of Multistable Composites for Application in Adaptive Structures", *Composites Science & Technology*, Vol. 62, No. 16, 2002, p. 2201.
18. Hufenbach, W., Gude, M. and Czulak, A., "Actor-initiated Snap-through of Unsymmetric Composites with Multiple Deformation States", *Journal of Materials Processing Technology*, Vol. 175, No. 1-3, 2006, p. 225-230.

19. Hyer, M.W., "Calculations of the Room-temperature Shapes of Unsymmetric Laminates", *Journal of Composite Materials*, Vol. 15, 1981, p. 296-310.
20. Hyer, M.W., "Some observations on the cured shape of thin unsymmetric laminates", *Journal of Composite Materials*, Vol. 15, 1981, p. 175-194.
21. Hyer, M.W., "The Room-Temperature Shapes of Four-Layer Unsymmetric Cross-Ply Laminates", *Journal of Composite Materials*, Vol. 16, 1982, p. 318-340.
22. Jun, W.J. and Hong, C.S., "Effect of Residual Shear Strain on the Cured Shape of Unsymmetric Cross-Ply Thin Laminates", *Journal of Composite Science and Technology*, Vol. 38, No. 1, 1990, p. 55-67.
23. Jun, W.J. and Hong, C.S., "Cured Shape of Unsymmetric Laminates with Arbitrary Lay-Up Angles", *Journal of Reinforced Plastics and Composites*, Vol. 11, No. 12, 1992, p. 1352-1366.
24. Kim, I., "Development and analysis of elastically tailored composite star shaped beam sections", Ph.D. Dissertation, 2003, School of Aerospace Engineering, Georgia Institute of Technology, Atlanta, Georgia.
25. Koiter, W.T., "On the Stability of Elastic Equilibrium", Ph.D. Thesis, 1945, Polytechnic Institute Delft, NASA TTF-10833, 1967.
26. Lazos, B.S. and Visser, K.D., "Aerodynamic Comparison of Hyper-Elliptic Cambered Span (HECS) Wings with Conventional Configurations", *Proceedings of the 24th Applied Aerodynamics Conference*, San Francisco, California, June 5-8, 2006.
27. Loos, A.C. and Springer, G.S., "Curing of Epoxy Matrix Composites", *Journal of Composite Materials*, Vol. 17, 1983, p. 135-169.
28. Luo, J. and Daniel, I.M., "Thermally-Induced Deformation of Asymmetric Composite Laminates", *Proceedings of the 18th Annual Technical ASC Conference*, University of Florida, Gainesville, Florida, 2003.
29. Marshall, I.H., Rhodes, J. and Banks, W.M., "Experimental Snap-Buckling Behavior of Thin GRP Curved Panels under Lateral Loading", *Composites*, Vol. 8, No. 4, 1977 p. 81-86.
30. Mattioni, F., Weaver, P., Potter, K., Friswell, "Multi-stable Composites Application Concept for Morphing Aircraft", *16th International Conference on Adaptive Structures and Technologies*, ICAST, 2005.
31. McGowan, A.-M.R., Washburn, A.E., Horta, L.G., Bryant, R.G., Cox, D.E., Siochi, E.J., Padula, S.L. and Holloway, N.M., "Recent Results from NASA's Morphing Project", *SPIE Proceedings of SPIE's 9th Annual International Symposium on Smart Structures and Materials, Electroactive Polymer Actuators and Devices Conference*, 2002, p. 97-111.
32. McGowan, A.-M.R., Cox, D.E., Lazos, B.S., Waszak, M.R., Raney, D.L., Siochi, E.J. and Pao, S.P., "Biologically Inspired Technologies in NASA's Morphing Project", *Proceedings of SPIE's 10th Annual International Symposium on Smart Structures and Materials, Electroactive Polymer Actuators and Devices Conference*, 2003, p. 1-13.
33. Nixon, M.S. and Aguado, A.S., *Feature Extraction and Image Processing*, 2nd edition, 2008, Academic Press.

34. Ochinero, T.T., "Deformations of Unsymmetric Composite Panels", Ph.D. Dissertation, 2001, Engineering Science and Mechanics, Virginia Polytechnic Institute and State University, Blacksburg, Virginia.
35. Pellegrino, S., Soykasap, O. and Yee, J.C.H., "Carbon Fiber Reinforced Plastic Tape Springs", *45th AIAA/ASME/ASCE/AHS/ASC Structures, Structural Dynamics and Materials Conference*, Palm Springs, CA, 2004.
36. Powell, G. and Simons, J., "Improved Iterative Strategy for Nonlinear Structures", *International Journal for Numerical Methods in Engineering*, Vol. 17, 1981, p. 1455–1467.
37. Ramm, E., "Strategies for Tracing the Nonlinear Response near Limit Points", *Nonlinear Finite Element Analysis in Structural Mechanics: Proceedings of the Europe-U.S. Workshop*, Ruhr-Universitat Bochum, Germany, 1981, p. 63-89.
38. Ramrakhyani, D.S., "Morphing Aircraft Structures Using Tendon Actuated Compliant Cellular Truss", Ph.D. Dissertation, 2005, Department of Aerospace Engineering, Pennsylvania State University, University Park, Pennsylvania.
39. Riks, E., "The Application of Newton's Methods to the Problem of Elastic Stability", *Journal of Applied Mechanics*, Vol. 39, 1972, p. 1060-1065.
40. Riks, E., "An Incremental Approach to the Solution of Snapping and Buckling Problems", *International Journal of Solids and Structures*, Vol. 15, 1979, p. 529-551.
41. Schlecht, M., Schulte, K. and Hyer, M.W., "Advanced Calculations of the Room-Temperature Shapes of Thin Unsymmetric Composite Laminates", *Journal of Composite Structures*, Vol. 32, 1995, p. 627-633.
42. Schlecht, M. and Schulte, K., "Advanced Calculation of the Room-Temperature Shapes of Unsymmetric Laminates", *Journal of Composite Materials*, Vol. 33, No. 16, 1999, p. 1472-1490.
43. Schultz, M.R. and Hyer, M.W., "Snap-through of Unsymmetric Cross-ply Laminates using Piezoceramic Actuators", *Journal of Intelligent Material System and Structures*, Vol. 14, 2003, p. 795:814.
44. Schultz, M.R., "Use of Piezoelectric Actuators to Effect Snap-Through Behavior of Unsymmetric Composite Laminates", Ph.D. Dissertation, 2003, Engineering Science and Mechanics, Virginia Polytechnic Institute and State University, Blacksburg, Virginia.
45. Schultz, M.R. and Hyer, M.W., "A Morphing Concept Based on Unsymmetric Composite Laminates and MFC Piezoceramic Actuators", *45th AIAA/ASME/ASCE/AHS/ASC Structures, Structural Dynamics and Materials Conference*, Palm Springs, California, 2004.
46. Silver, M.J., Hinkle, J.D. and Peterson, L.D., "Controlled Displacement Snap-Through of Tape Springs - Modeling and Experiment", *46th AIAA/ASME/ASCE/AHS/ASC Structures, Structural Dynamics, and Materials Conference*, Austin, Texas, 2005.
47. Simitses, G. and Hodges, D., *Fundamentals of Structural Stability*, 2005, Elsevier Science & Technology Books.
48. Soderkvist, J., "Similarities between Piezoelectric, Thermal and other Internal Means of Exciting Vibrations", *Journal of Micromechanics and Microengineering*, Vol. 3, 1993, p. 24-31.

49. Stubbs, M.D., "Kinematic design and analysis of a morphing wing", M.S. Thesis, 2003, Materials Science and Engineering, Virginia Polytechnic Institute and State University, Blacksburg, Virginia.
50. Tawfik, S., Tan, X., Ozbay, S. and Armanios, E., "Modeling of Anticlastic Stability in Elastically Tailored Composites", *Proceedings of the 20th Annual Technical ASC Conference*, Drexel University, Philadelphia, Pennsylvania, 2005.
51. Tawfik, S. and Armanios, E., "Preliminary Investigation of a Morphing Wing Design Concept Employing Unsymmetric Cross-ply Composites Stability Characteristics", *Proceedings of the 21st Annual Technical ASC Conference*, University of Michigan-Dearborn, Dearborn, MI, 2006.
52. Tawfik, S., Xinyuan, T., Ozbay, S. and Armanios, E., "Anticlastic Stability Modeling for Cross-ply Composites", *Journal of Composite Materials*, Vol. 41, No. 11, 2007, p. 1325-1338.
53. Wempner, "Discrete Approximations Related to Nonlinear Theories of Solids", *International Journal of Solids and Structures*, Vol. 7, 1971, p. 1581-1599.
54. Wiggins, L.D., "Structural Design and Analysis of a Kinematic Mechanism for a Morphing Hyper-Elliptic Cambered Span (HECS) wing", M.S. Thesis, 2004, Materials Science and Engineering, Virginia Polytechnic Institute and State University, Blacksburg, Virginia.
55. Wilkie, K.W., Bryant, R.G., High, J.W., Fox, R.L., Hellbaum, R.F., Jalink, A., Jr., Little, B.D. and Mirick, P.H., "Low-cost piezocomposite actuator for structural control applications", *SPIE Proceedings of SPIE's 7th International Symposium on Smart Structures and Materials*, 2000, p. 323-334.
56. Wilkie, W.K., Bryant, R., Fox, R.L., Hellbaum, R.F., High, J.W., Jalink, A., Jr., Little, B.D. and Mirick, P.H., "Method of Fabricating a Piezoelectric Composite Apparatus", United States Patent and Trademark Office, US Patent No. 6,629,341 (2003).